Study on magneto-sensitive solids : Experiments, Theory and Numerics

Erato Psarra

université PARIS-SACLAY

NNT : 2018SACLX094

Thèse de doctorat

A study on magnetosensitive solids: Experiments, Theory and Numerics

Thèse de doctorat de l'Université Paris-Saclay
préparée à l'École Polytechnique

Ecole doctorale n°579 Sciences mécaniques et énergétiques, matériaux et géosciences (SMEMAG)
Spécialité de doctorat : Mécanique des Solides

Thèse présentée et soutenue à Palaiseau, le 07/12/2018, par

ERATO PSARRA

Composition du Jury :

Marc-André KEIP Associate Professor, University of Stuttgart (Institute of Applied Mechanics)	Rapporteur
Benoît ROMAN Directeur de Recherche CNRS, ESPCI	Rapporteur
Basile AUDOLY Directeur de Recherche CNRS, Professeur Ecole Polytechnique (LMS)	Président
Corrado MAURINI Professeur, Université Pierre et Marie Curie (Institut Jean Le Rond d'Alembert)	Examinateur
Philippe PERNOD Professeur, École Centrale de Lille (IEMN)	Examinateur
Laurence BODELOT Professeur Assistante, Ecole Polytechnique (LMS)	Co-directeur de thèse
Konstantinos DANAS Chargé de Recherche CNRS, Professeur Chargé des Cours Ecole Polytechnique (LMS)	Directeur de thèse

A study on magnetosensitive solids: Experiments, Theory and Numerics

Erato Psarra

PhD advisors: Laurence Bodelot, Konstantinos Danas

Laboratory of Solid Mechanics

Ecole Polytechnique, Palaiseau

October 2018

CONTENTS

ABSTRACT

The present work deals with the stability and post-bifurcation response of isotropic magnetorheological elastomers (MREs). MREs are elastomers comprising a finite volume fraction of magnetizable iron particles distributed randomly in the volume. A nonlinear magnetoelastic film/substrate system is experimentally, numerically and theoretically exploited to obtain active control of surface roughness. The non-intuitive interplay between magnetic field and elastic deformation owes to material and geometry selection, namely, a ferromagnetic particle composite film bonded on a compliant passive foundation. Cooperation of two otherwise independent loading mechanisms–mechanical pre-compression and magnetic field–allows to bring the structure near a marginally stable state and then destabilize it with either magnetic or mechanical fields. We demonstrate for the first time that the critical magnetic field is a decreasing function of pre-compression and vice versa. The experimental results are probed successfully with full-field finite element simulations at large strains and magnetic fields. A theoretical magnetomechanical bifurcation analysis on an infinite magnetoelastic system is employed to explore the effect of the interlayer combined properties on the critical response and is compared with the available numerical results.

With the perspective of applying the principle of surface actuation to new magnetomechanically triggered patterns, we further investigate the post-bifurcation of an entirely magnetorheological bilayer block. The underlying idea is to create different interlayer contrasts of magnetic and mechanical properties allowing us to trigger a larger range of surface patterns than that already obtained when using a MRE film on a passive (magnetically insensitive) foundation. Post-bifurcation calculations of MRE films bonded on MRE substrates allow to reveal novel patterns that lead to significant curvature localisation and crinkling. In all cases studied, the magnetoelastic coupling allows for the reversible on/off control of surface patterning under adjustable critical magnetic and mechanical fields for a single specimen and thus, this study constitutes a first step towards realistic active haptic and morphing devices.

RESUMÉ

Cette étude traite de la stabilité et la post-bifurcation des élastomères magnétorhéologiques isotropes (MRE). Les MRE sont des élastomères comprenant une fraction volumique finie de particules de fer magnétisables, réparties de façon aléatoire dans le volume. Plus précisément, un système de film/substrat magnéto-élastique non linéaire est étudié expérimentalement, numériquement et théoriquement pour obtenir un contrôle actif de la rugosité de la surface du film. L'interaction non-intuitive entre le champ magnétique et la déformation élastique est due au choix des matériaux et de la géométrie du système, à savoir un film composite de particules ferromagnétiques lié à un substrat passif souple. La coopération de deux mécanismes qui sont par ailleurs indépendants, la pré-compression mécanique et le champ magnétique, permet de rapprocher la structure d'un état marginalement stable et puis de la rendre instable par des champs magnétiques ou mécaniques. Nous démontrons pour la première fois que le champ magnétique critique est une fonction décroissante de la pré-compression et vice versa. Les résultats expérimentaux sont ensuite sondés avec succès par des simulations à champs complets par éléments finis en grandes déformations et champs magnétiques.

Une analyse théorique de bifurcation magnéto-mécanique sur un système magnéto-élastique infini est également utilisée pour explorer l'effet des propriétés combinées sur la réponse critique. En utilisant différents matériaux mous allant du MPa (caoutchoucs) au kPa (gels), nous constatons que l'augmentation de la douceur du matériau permet de déclencher des instabilités avec des champs magnétiques nettement plus faibles et à l'intérieur de la sensibilité des configurations de compression réalistes. Cela s'explique par le fait que plus les couches sont molles, plus elles se déforment sous le même état de magnétisation. Par conséquent, la façon la plus efficace possible de réduire les champs critiques et d'élargir la gamme des pré-compressions appliquées est d'utiliser des matériaux aussi souples que possible, par exemple des gels polymères de module de cisaillement de l'ordre du kPa. En outre, nous montrons que lorsque on utilise la nature magnéto-élastique des matériaux sous une forme combinée, le contraste de rigidité entre les couches G_s/G_f n'est plus suffisant pour déterminer la charge critique et les modes de bifurcation. Dans la bifurcation magnéto-mécanique, le flambement dépend du G_s/G_f, ainsi que sur les valeurs absolues des modules de cisaillement, G_s et G_f. Ceci contraste avec le flambement purement mécanique sous incompressibilité, où seul le rapport G_s/G_f relatif entraîne la réponse.

Dans la perspective d'élargir l'activation de surface à de nouveaux motifs magnéto-mécaniques, nous étudions plus en détail la post-stabilité d'un système film/substrat entièrement magnéto-rhéologique. L'idée sous-jacente est de créer différents contrastes de propriétés magnétiques/mécaniques entre les couches afin de déclencher une gamme de motifs de surface plus riche que celle déjà obtenue en utilisant un film MRE sur un substrat passif. Les calculs post-bifurcation des films MRE liés à des substrats MRE permettent de mettre en évidence de nouveaux motifs qui conduisent à une localisation de courbure très importante et à du "crinkling" (gondolement). Pour ce faire, nous effectuons une analyse de localisation de courbure dans l'espace de double paramètre de pré-compression et de champ magnétique appliqué et nous montrons qu'il s'agit d'une caractéristique intrinsèque des MRE. Le mécanisme de formation du crinkling est fortement lié à la répulsion des interactions magnéto-élastiques. Si on tient compte de l'accouplement magnéto-élastique, l'accouplement entre la courbure de la surface et la polarisation macroscopique magnétique, conduit à l'émergence d'une couche (largeur de bande) dans laquelle la courbure est très concentrée.

Dans tous les cas étudiés, le couplage magnéto-élastique permet le contrôle réversible de l'apparition (/disparition) de motifs de surface sous des champs magnétiques et mécaniques critiques ajustables. Par conséquent, cette étude constitue un premier pas vers des dispositifs haptiques et morphiques actifs.

CHAPTER I

INTRODUCTION

Interest in the buckling behavior of soft materials has grown in the recent years, with a particular focus on the potential of creating controllable meta-materials with tunable properties. Inspired by natural and biological processes, such as naturally occuring photonic structures in butterflies (see Vukusic and Sambles, 2003) and wetting properties of lotus leaves (see Bhushan and Jung, 2011), attention has been drawn to the use of hierarchical architectures, spanning several length scales from nanometer to centimeter sizes. Such a concept has been further developed by the technological improvements in lithography for fabrication of small length periodic structures (e.g., Lai et al., 2005, Moon et al., 2005). The hierarchical buckling behavior results from geometrical effects coupled with the material properties of the structural members. Composite materials, such as micron-sized magnetic particles embedded in polymeric-based soft matrices (see Fig.I.1), give rise to a magnetoelastic macroscopic response when subjected to combined magnetomechanical external stimuli (e.g., see Bodelot et al., 2016, Danas et al., 2012). In particular, the magnetorheological elastomers (MRE), i.e., ferromagnetic particle-impregnated elastomers, exhibit relatively large deformations (in the order of $10-40\%$), while their response is extremely fast upon application of a magnetic field (in order of milliseconds) (e.g., see Coquelle et al., 2006, Vidal-Verdu and Hafez, 2007). Under appropriate material design, internal reorganization of the fields occurs as the magnetization vectors of the particles tend to align with an externally applied magnetic field, see Fig.I.2. Hence, magnetically triggered instabilities emerge in a reversible and repeatable fashion if the particle microstructure and macroscopic geometry is unfavorably oriented with respect to the applied magnetic field (e.g., see Danas and Triantafyllidis, 2014, Huang et al., 2016).

From a novel perspective and by taking advantage of the magnetomechanical coupling, such material-systems are potentially capable of operating near and beyond "marginally stable" regimes (e.g., Grabovsky and Truskinovsky, 2013). Such a response leads us to attempt controlling MREs shape when combined with an appropriate geometry, similarly to most biological systems, e.g., skin wrinkles, contraction of muscles etc. Our deep interest lies in developing magnetosensitive material-structures whose shape can be remotely controlled by external magnetic fields (e.g., see Kankanala and Triantafyllidis, 2008, Oukhaled et al., 2012, Wilhelm et al., 2003). Such magnetomechanical instabilities can later be exploited in surface patterning for haptic applications (e.g., Horii et al.,

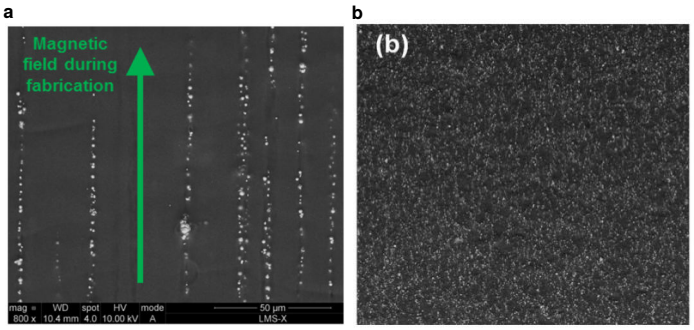

Figure I.1: Scanning Electron Micrograph (200x) of **a**, particle chain alignment in 10% particle volume fraction MRE, **b**, randomly distributed particles in 30% particle volume fraction MRE (Pössinger et al., 2014).

2018, Kawasetsu et al., 2018a, Streque et al., 2010), actively controlled stiffness for cell-growth (e.g., Wang and Stamenovic, 2000), as well as tunable optical (e.g., Zhang et al., 2008b), auxetic (e.g., Bertoldi et al., 2008, Danas, 2017) and acoustic (e.g., Bertoldi and Boyce, 2008) properties under marginal changes in the applied magnetic fields. However, unlike the current modeling of hierarchical composites, MREs require the development of novel experimental techniques and advanced nonlinear magnetomechanical models. In this way, one could tailor the desired macroscopic instability response at finite strains and large magnetic fields.

The motivation of this study thus lies in the magnetomechanical coupling for tailored instabilities. The properties of the magnetorheological elastomers are of main interest here and thus, require a thorough review. MREs belong to the class of the so-called "active" smart materials, i.e., materials that respond in a pre-determined manner to given environmental stimulations, reverting back to their original state as soon as the stimulus is removed (Takagi, 1990). Such external stimuli include stress, temperature, pH, moisture, electric or magnetic fields. Available active materials include piezoelectric ceramics, shape memory alloys, electroactive polymers and magnetostrictive materials.

The first magnetically active materials reported in literature were fluid-state analogues of MREs. The magnetorheological fluids (MRF) typically consist of (sub-)micron magnetically susceptible particles randomly dispersed in a fluid (Rabinow, 1948). When such a suspension is subjected to a magnetic field, the particles acquire a magnetic polarization and form chains. To that end, the system increases its effective viscosity two or three orders of magnitude, while changing from Newtonian to non-Newtonian fluid to the point of becoming a viscoelastic solid (e.g., see Ginder, 1996, 1998, Jolly et al., 1999). The physical mechanism behind viscosity increase owes to the alignment of the microscopic (in the range of $0.1 - 10\mu$m) particles along the lines of the magnetic flux. However, a distinction has to be made between MR fluids and ferrofluids. Ferrofluids contain nanoparticles suspended by Brownian motion (e.g., see Fannin et al., 1987). In contrast, the particles of MRF are primarily on the micrometre-scale and thus, are too dense for Brownian motion to keep them suspended (Lemaire et al., 1995).

I.1 Fabrication and behavior of MREs

Particle sedimentation of MRFs has been an obstacle to their rapid emergence in engineering applications, but see recent advances in Feng et al. (2015), Liu et al. (2015). Such a drawback is well overcome by replacing the fluid matrix with a solid matrix. In this way, magnetic particles of larger size are able to be used (Davis, 1999). The particles can be either randomly distributed within the composite or aligned in chain-structures by curing the composite in the presence of a magnetic field, see Fig.I.1. Indeed, when crosslinking the elastomer under an applied magnetic field, field-induced interparticle interactions promote the formation of particle chains aligned along the field direction (e.g., see Bunoiu and Bica, 2016, Pössinger et al., 2014). That leads to a transversely isotropic macroscopic response (e.g., see Carlson and Jolly, 2000, Chen et al., 2007).

To enhance particle dispersion and structuring, low viscosity polymeric matrices are preferred. Several research groups have made use of gels, silicones and rubbers as soft matrices (e.g., see Ginder et al., 1999, Psarra et al., 2017, Wang et al., 2006), easily processed from liquid pre-polymers combined with the appropriate hardeners. Natural or nitrile rubbers have also been used in biomechanical applications (e.g., see Gong et al., 2005). The effective behavior of MREs depends on fabrication and material parameters, such as: the matrix composition (e.g., Lokander and Stenberg, 2003, Tian et al., 2013), the initial magnetization state of the particles (e.g., Mitsumata et al., 2002, Shiga et al., 1995), their size and shape (e.g., Demchuk and Kuzmin, 2002, Peng et al., 2009), the filler volume fraction (e.g., Bednarek, 1999, Zhu et al., 2012), the particle/matrix adhesion (e.g., Damiani and Sun, 2017, Qin and Peng, 2013, Qing et al., 2010), the particle microstructure generated during curing (e.g., Bossis and Lemaire, 1991, Ginder et al., 1999). A recent work of Wang et al. (2013) on conductive MREs also indicated that the curing temperature affects the electrical conductivity of the composites.

The main mechanisms resulting in MREs magnetoelastic coupling combine the magnetic dipole-dipole (polarization) interactions between particles and, in certain cases, the magnetostrictive properties of the particle materials (Shiga et al., 1995). Frequently used magnetic materials are the carbonyl iron and nickel; examples of more exotic inclusions are the Terfenol-D and Ni_2MnGa. Among them, iron is the most common filler material for its high saturation magnetization, high susceptibility and low remnant magnetization (Kusakawa and Otani, 1964). High saturation magnetization and susceptibility lead to high interparticle interactions and thereby, to strong magnetomechanical coupling. Such a coupling can be macroscopically manifested in terms of effective stiffness increase as the magnetic forces shorten the average particle distance. The macroscopic deformation of MREs when placed within a uniform magnetic field is termed “magnetostriction” and shall not be confused with the magnetostriction refering to very small strains induced by a magnetic field in bulk magnetostrictive materials.

For inclusion materials with very small magnetostriction, such as carbonyl iron, nickel or cobalt, the particles are effectively rigid and the principal mechanisms of magnetomechanical coupling include magnetic torques and magnetic interactions between particles (Galipeau and Ponte Cas-

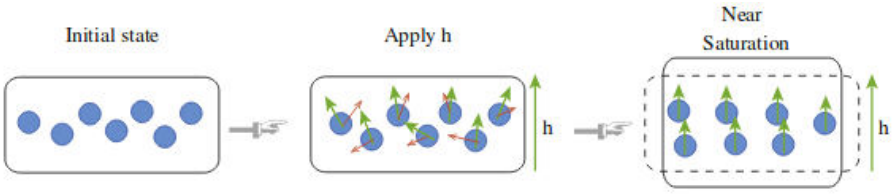

Figure I.2: Mechanism of MREs deformation upon application of an external magnetic field. The large (green-color) arrows indicate the direction of the effective magnetic dipoles, i.e., from south to north pole. The small (red-color) arrows indicate the direction of the particle motion caused by the magnetic forces (Danas et al., 2012).

tañeda, 2012). For MREs containing particles of giant magnetostrictive materials, such as Terfenol-D and Ni_2MnGa, the magnetostriction of the particle materials also contributes to the coupling (Duenas and Carman, 2000). Several experimental works have been concentrated on the optimal particle volume fraction of iron fillers. That has been found 27-30% for the largest relative change in stiffness when the particles reach magnetization saturation (e.g., see Davis, 1999, Shiga et al., 1995). A higher concentration leads to rapid deterioration of the mechanical properties, as well as to material stiffening that is greater than the increase in magnetostriction (e.g., see Lokander and Stenberg, 2003, Shiga et al., 1995). This optimal volume fraction is also taken into account when fabricating MREs with bimodal iron particles (e.g., see Li and Zhang, 2010). To increase their electrical conductivity, graphite can be introduced to conventional MREs (e.g., see Tian et al., 2011). That permits MREs to be used as sensing materials in force and magnetic field sensors (e.g., see Li et al., 2009).

MREs as typical particle reinforced elastomers exhibit the Payne and the Mullins (e.g., see Diani et al., 2009) effect at small and high deformations, respectively. Since their static and cyclic behavior is dependent on the microstructural bonding, an adequate adhesion between the rigid particles and the soft matrix is important. Several studies have been dedicated to the improvement of the interfacial adhesion by modifying the chemical interaction between the matrix and the fillers (e.g., see Damiani and Sun, 2017, Pössinger et al., 2014, Qin and Peng, 2013, Qing et al., 2010, Wang et al., 2013, 2006). Additives are also commonly used to adjust the mechanical and chemical properties or electrical performance of MREs (e.g., see Leblanc, 2002, Zhang et al., 2008a). Silicone oil is an additive to increase the distance between the macro-molecules of the matrix (e.g., see Gong et al., 2005). Graphite powder is an additive that affects the magnetostriction and electrical conductivity of MREs (e.g., see Bica, 2009, Li et al., 2009). The volume resistivity, crosslink density, tensile strength, elongation at break, shore hardness and morphology structure are the main parameters investigated in these works.

I.2 Experimental characterization and applications of MREs

The micromagnetic interactions under an externally applied magnetic field result in field- dependent mechanical properties. The resulting effective response has been experimentally investigated under

both steady-state (e.g., Shiga et al., 1995, Wang et al., 2006) and dynamic (e.g., Norouzi et al., 2016, Tian et al., 2011, Zhu et al., 2012) loading conditions. Jolly et al. (1996) performed quasi-static shear tests on chain-structured MREs and showed that the magnetic field increases the effective shear modulus of the composite. Bednarek (1999) measured the magnetostriction of composites made with randomly distributed particles subjected to very high magnetic fields. Ginder et al. (2002) and Guan et al. (2008) determined experimentally the magnetostriction of random and chain structured MREs. Lanotte et al. (2003) investigated the effect of particle rotation on the average magnetization of the composite. More recently, Diguet et al. (2010) have provided experimental and theoretical results for the magnetostriction and magnetic saturation of composite samples formed into a cylindrical shape and exposed to a remotely applied magnetic field. In the absence of a mechanical loading, the length of the cylindrical specimen reduces when subjected to a magnetic field along its axial direction. Using a theoretical framework for finitely strained MREs, Danas et al. (2012) were the first to probe the experimentally measured magnetization and magnetostriction. The experimental characterization under tension and simple shear (including the effect of pre-stress) was novel for having minor shape effects, i.e., the specimens were close to the poles of the magnet. Taking into account the interfacial adhesion between the particles and the matrix, Bodelot et al. (2016) characterized MRE composites under large deformations and magnetic fields. Such materials have been found to have a small hysterisis in magnetostriction and none in magnetization (e.g., see Bodelot et al., 2018, Danas et al., 2012, Yin et al., 2006).

The majority of studies on the dynamic viscoelastic behavior of MREs measure the shear deformations (e.g., Chen et al., 2005, Eem et al., 2012, Norouzi et al., 2016, Zhu et al., 2012); that is a common mode of operation of MRE materials in structural engineering. Such works mainly focus on the identification of the frequency and strain amplitude effect on the dynamic stiffness (e.g., shear storage modulus) and vibration damping properties (e.g., loss factor). The experimental findings are usually fitted by modified simple viscoelastic models (e.g., the Maxwell (Eem et al., 2012), the Kelvin-Voigt (Norouzi et al., 2016) and the four-parameter (Li et al., 2010) model) that include the loading history on rate-dependent constitutive relationships. Li et al. (2010) performed dynamic tests on particle-column MREs under various harmonic loadings by means of a parallel-plate rheometer, demonstrating that such MREs behave as linear visocoelastic materials. Zhu et al. (2012) and Norouzi et al. (2016) studied MREs dynamic viscoelastic properties under varying fabrication parameters, magnetic fields and frequencies in the shear mode. Kallio et al. (2007) tested spring elements consisting of aligned and isotropic MREs in cyclic compression. Eem et al. (2012) carried-out combined compression-shear type tests on aligned MREs by varying the distance between the magnets among other parameters. Chen and Jerrams (2011) modeled the hysteresis obtained from substituting cyclic loadings into constitutive relationships. Ha et al. (2016) also provided a method to model the nonlinear hysteresis of MREs by means of describing functions used in structural frequency analysis. Tiercelin et al. (2011a)a performed vibrating magnetometer and magneto-optical Kerr effect measurements on a magnetoelastic nanostructured multilayer deposited onto a piezoelectric actuator. Demonstrating the magnetoelectric switching of magnetization, that was exploited

by Tiercelin et al. (2011b)b in the creation of a memory cell, based on a magnetic element with giant magnetostriction embedded in a piezoelectric matrix. Such multiferroic memory-nanostructures were found to exhibit magneto-electro-elastic coupling in dynamical behavior (e.g., see Giordano et al., 2012, 2014).

On the basis of such results, MREs are interesting candidates for vibration control of structural systems, similar to piezoelectric elements (e.g., see Celli et al., 2018, dell'Isola et al., 2004, Gripp and Rade, 2018, Lossouarn et al., 2018, Qiu et al., 2004). Variable stiffness control and magnetostriction take place quickly and reversibly, paving the way for tunable dampers and magnetomechanical (micro-)actuators (e.g., see Liu et al., 2018) and (micro-)motors (e.g., see Ren and Gerhard, 1997). In virtue of their damping properties under harmonic loadings, MREs are used in the automotive industry (e.g., see Ginder et al., 1999) and architecture (e.g., see Carlson and Jolly, 2000). A variable-rate automotive suspension bushing of concentric sleeves made of MREs is currently used by Ford (Ginder et al., 1999). Other technological advances include ferromagnetic elastomer microwires in structural health monitoring, stress sensing, invisible cloaking, microwave absorption and biomedical applications (e.g., see Qin and Peng, 2013, Qing et al., 2010). The strong field dependence of the effective permittivity and transmission/reflection parameters (in the Gigahertz range) indicates wire-arrays filler MREs as promising candidates for a variety of self-sensing applications (e.g., see Peng et al., 2009). To that end, Hage-Ali et al. (2009) made use of PDMS substrates in the fabrication of reconfigurable microwave devices in high frequency bands. However, albeit potentially applicable in sensors, actuators and haptic devices (e.g., Ginder et al., 2000, Lanotte et al., 2003), a non-linear magnetoelastic system for active control of surface roughness has not been devised yet. Moreover, most efforts have been concentrated in maximizing the magnetostrictive coupling in MREs to increase the resulting deformations, with little success so far (e.g., see Bellan and Bossis, 2002, Carlson and Jolly, 2000, Coquelle et al., 2006, Ginder et al., 2002, 2000, Gong et al., 2005).

I.3 Theoretical frameworks and modeling of MREs

In the past two decades, there has been an increasing technological interest on MRE solids for both their magnetostrictive response, as well as the instabilities they undergo. To that end, theoretical frameworks have been developed to describe their behavior of strong magnetoelastic coupling. The very first theoretical formulations of the magnetoelastic response date back to the 1950s and 1960s and are classified into two main categories: (i) an Eulerian-based approach considering conservation laws of continuum mechanics (e.g., see Maugin and Eringen, 972a, Pao, 1978, Pao and Yeh, 1973, Tiersten, 1965, Truesdell and Toupin, 1960) and (ii) a Lagrangian-based approach considering the minimization of potential energy functionals (e.g., see Brown, 1966, Maugin and Eringen, 972b, Tiersten, 1965). Such approaches were developed independently of each other and give different results correspondingly to the assumptions each one adopted. The main differences refer to the background (Maxwell) stresses defined in the entire space, the mechanical jump (surface traction) condition at discontinious interfaces and the potential energy of the applied loads. However, a recent

study of Kankanala and Triantafyllidis (2004) came to embrace all different frameworks under two equivalent formulations (a Eulerian and a Lagrangian) that were proven to yield the same governing equations and boundary/interface conditions.

In turn, the development of Lagrangian variational formulations under finite strains is more recently evidenced in a series of papers by Dorfmann and coworkers (e.g., see Brigadnov and Dorfmann, 2003, Dorfmann and Ogden, 2003, 2004, 2005), Kankanala and Triantafyllidis (e.g., see Kankanala and Triantafyllidis, 2008, Kankanala, 2007, Kankanala and Triantafyllidis, 2004) and Steigmann (2004) among others. On account of numerical solutions of boundary-value problems, the proposed continuum formulations may be different but also equivalent. Their main distinction lies on the choice of the independent magnetic variables. Dorfmann and coworkers (e.g., see Bustamante et al., 2007, Dorfmann and Ogden, 2004) developed variational principles directly related to the primary field equations, satisfied by the constitutively related magnetic field $\mathbf{H}$ and magnetic induction $\mathbf{B}$. The free-energy densities used in their work are purely phenomenological, avoiding to use the magnetization vector as an independent variable or to decouple the magnetic quantities into an "applied" and "perturbed"[1] component. In contrast, Kankanala and Triantafyllidis (2004) make use of two magnetic independent variables: the magnetization vector $\mathbf{m}$ and a magnetic vector potential $\mathbf{A}$ (such as $\mathbf{B} = \mathbf{Curl}\mathbf{A}$). The magnetization $\mathbf{m}$ is regarded, however, as a secondary quantity that can be defined in terms of the primary $\mathbf{B}$ and $\mathbf{H}$ fields. It is noted that the magnetic potential $\mathbf{A}$ is a continuous admissible vector field defined over the entire space, while the magnetization $\mathbf{m}$ vector is defined only within the finite volume and is zero elsewhere. That should not rise frustration however, but be used correspondingly to the needs of the problem at hand. Additionally, the decoupling approach in the work of Kankanala and Triantafyllidis (2008) is found very convenient when solving bifurcation problems. There, the presence of the magnetoelastic solid does not perturb the magnetic field of the free space along the principal solution, i.e., constant magnetic fields equal to the applied (see contact with Section IV.1).

Regardless of the choise of the independent magnetic variables $\{\mathbf{H}, \mathbf{B}, \mathbf{M}\}$, the proposed variational principles derive the same governing equations, boundary/continuity conditions. Yet, differences have been observed on the magnetic counterpart of the potential energy. Using the $(\mathbf{F}, \mathbf{M})$ formulation ($\mathbf{F}$ is the deformation gradient tensor such as $\mathbf{F} = \nabla\mathbf{u} + \mathbf{I}$, with $\mathbf{u}$ the displacement field and $\mathbf{I}$ the identity tensor) requires the magnetic loading to be treated as a body force whose potential is added to the total energy[2] (e.g., see Kankanala and Triantafyllidis, 2008). In contrast, the $(\mathbf{F}, \mathbf{B})$ formulation is able to derive the governing equations in the absence of body forces. In the latter case, the loading potential consists only of the contribution of the mechanical surface traction, see Section III.1. Very recently, Danas (2017) established connections between different variational formulations and Helmoltz free-energy expressions in both Eulerian and Lagrangian frameworks.

Such density functions at the heart of the variational formulations provide principles that are

[1] Perturbed in the sense of how a magnetoelastic solid interferes with the external magnetic field applied somewhere far.

[2] It is noted that the potential energy is the sum of the solid's free energy, plus the magnetic energy of the entire space, and the work done from the external loadings.

adapted for finite element implementation of the magnetoelastostatic theory. In that way, the governing equilibrium equations of nonlinear magnetoelasticity can be solved for non-trivial boundary value problems, where there is little prospect of obtaining analytical solutions. Such examples of numerical solutions can be found in the work of Bustamante et al. (2007) in which a finite-difference method is proposed, in that of Barham et al. (2007) on membrane problems, as well as in that of Lefèvre et al. (2017) on constitutive modeling of ferrofluids versus iron particle reinforced rubbers. The constitutive response of MRE composites changes when different microstructures are taken into account. In the work of Danas et al. (2012), a phenomenological transversly isotropic free-energy density, dependent on a supplementary variable of particle chain orientation, was used to model the experimental characterization of aligned MREs.

In addition to the continuum-based approaches, macroscopic constitutive models have been derived from micromechanical considerations of homogenization theories (e.g., see Borcea and Bruno, 2001, Liu et al., 2006, Yin et al., 2006). Nevertheless, the intrinsic mathematical challenges of carrying out the homogenization limit of the magnetoelastic equations have hindered the construction of homogenization-based models, save for the results of Lefèvre et al. (2017). Also, the experimental challenges in testing the material without the structural response of specimens favors the development of phenomenological energy densities. Using simplifying assumptions about the local strains and magnetization fields, Jolly et al. (1996) provided a model based on the dipolar interaction of particles. The work of Liu et al. (2006) is on the effective properties of a magnetostrictive composite in the dilute limit. The work of Borcea and Bruno (2001) is on small strain elastic response of isotropic elastomers filled in with ferromagnetic particles by considering particle-particle forces. The work of Corcolle et al. (2008) is on small strain Hashin-Shtrikman homogenization. Such analytical homogenization results are restricted in the limit of small deformations. An approximate estimate of the effective free-energy of an incompressible and isotropic MRE under finite deformations can be found in the work of Galipeau and Ponte Castañeda (2013).

More recently, Keip and Rambausek (2015, 2017) conducted computational characterization of MREs effective response with arbitrary microstructures, while investigating the prescription of magnetic boundary conditions and macroscopic shape effects, respectively. Rambausek and Keip (2018) have further provided a constrained minimization formulation of incompressible finite-strain magneto-electro-elasticity, implemented on a microscopic boundary value problem that retrieves the effective constitutive response of a MRE. Another recent work of Lefèvre et al. (2017) on the effective free-energy of isotropic suspensions of (either iron or ferrofluid) particles in finite deformations and large magnetic fields provides comparison with 2D and 3D finite element simulations. An effective variational formulation can also be found in the work of Danas (2017) with applications on auxetic and chiral isotropically distributed microstructures.

I.4 Magnetoelastic buckling instabilities

Such frameworks can be implemented in variational potentials when a buckling instability analysis is also required. In its simplest form, the magnetoelastic buckling refers to the sudden bending transition of an elastic rod under the influence of a uniform magnetic field applied in the direction of its thickness (e.g., see Miya et al., 1978, Wallerstein and Peach, 1972). This fundamental physical phenomenon was initially conceived by Moon and Pao (1968). Moon's work on metallic plates paved the way for both experiments and theory, although the measures showed a critical field twice lower than expected. Later studies reduced that gap down to 15% by considering edge effects on the magnetic field. Such effects can be avoided in cylindrical geometries, considered in the works of Moon and Hara (1982) and Lefèvre et al. (2017). Recently, Gerbal et al. (2015) developed an analytical model on the magnetoelastic buckling of a rod. The model considers the variational minimization of a functional, containing the contribution of a local bending energy and the free magnetic enthalpy, under the assumptions that the magnetization is constant and mostly axial (i.e., perpendicular to the external magnetic field) at the post-bifurcation.

Singh *et al.* (2013) similarly carried-out buckling experiments on a clamped beam with a magnet attached at its end. Such a system undergoes Euler buckling when placed within an external magnetic field. The post-instability can be innovatively controlled by switching to a secondary subcritical mode when an attracting magnet approaches the beam. The experiments were modeled combining Euler elastica and dipole magnetic interactions analysis. Tipton et al. (2012) similarly investigated the elastic buckling of a soft cellular solid under magnetostatic loadings. The system consisted of a passive elastomer square array with embedded earth magnets in circular holes. Past a critical value of the external field, the sample rapidly rotates in alternate directions, switching into an astroid-like shape. However, it has to be noted that in the last two works the magnetomechanical coupling does not arise from the properties of the material itself, but from the combination of different systems (purely elastic bodies with magnets attached). To conclude on the studies dedicated to the magnetoelastic buckling, Huang et al. (2016) conducted buckling experiments on paramagnetic particle chains embedded in a soft polymer gel. In that work, the instability occurs at the level of the individual particle chains and not at that of the macroscopic body. As a result, the findings were modeled by means of a coarse-grained molecular dynamics simulations.

The complexity of the solution under a continuum mechanics framework justifies that a comprehensive description is restrained to some trivial geometries, such as rods with large aspect ratios (e.g., see Gerbal et al., 2015, Neukirch et al., 2012) thin plates (e.g., see Moon and Pao, 1968) and thin film/substrate bilayer blocks (e.g., see Danas and Triantafyllidis, 2014, Kankanala and Triantafyllidis, 2008, Psarra et al., 2017).

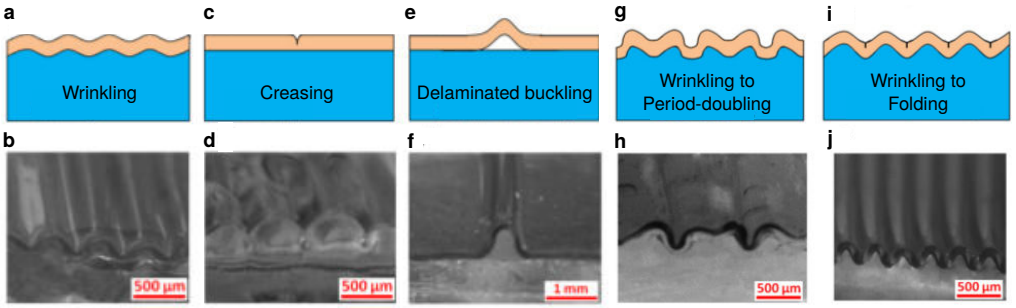

Figure I.3: Schematic illustration of a film/substrate system under plane-strain deformation along with optical microscopic images of **a**-**b**, wrinkling mode **c**-**d**, creasing mode **e**-**f**, delaminated buckling mode as primary instabilities; and **g**-**h**, period-doubling mode **i**-**j**, folding mode as secondary instabilities evolving from wrinkling (Wang and Zhao, 2013b).

I.5 Mechanically triggered instabilities on film/substrate systems

Mechanically stiff films or layers resting on passive compliant substrates are known to undergo mechanical instabilities under uniaxial compressive loads. The principal solution of such material systems is unique and stable until the load exceeds a critical value, which causes the film to bifurcate into a geometric mode influenced by the (visco-)elastic nature of the substrate (e.g., see Huang, 2005, Hutchinson, 2013, Jin and Suo, 2015). The resulting critical buckling mode is determined by the stiffness contrast, or in simple cases, the substrate-to-film shear moduli ratio G_s/G_f, as well as the geometrical constraints of the stucture (e.g., see Jin et al., 2015a, Kim et al., 2011, Lee et al., 2008, Wang and Zhao, 2013b). In the post-bifurcation regime, periodic wrinkling is observed within a G_s/G_f range that is lower than a threshold ~ 0.6 (e.g., see Auguste et al., 2017, Cai et al., 2011, 2012). Upon further compression, wrinkles evolve into more complex morphologies, e.g., folds, creases, ridges (see Auguste et al., 2017, Budday et al., 2015, Jin et al., 2015b, Lestringant et al., 2017, Pocivavsek et al., 2008, Sun et al., 2012, Wang and Zhao, 2013b).

In recent decades, extensive experimental, numerical and theoretical studies have been conducted on various one-dimensional modes of mechanically-triggered instabilities in film/substrate systems, such as wrinkling (e.g., see Huang and Im, 2006, Huang et al., 2005), period-doubling (e.g., see Cao and Hutchinson, 2012b), creasing (e.g., see Chen et al., 2014, Jin and Suo, 2015), folding (e.g., see Shan et al., 2014, Sun et al., 2012), localized ridging (e.g., see Cao et al., 2014, Zang et al., 2012), crinkling (e.g., see Kothari *et al.*, 2018) and delaminated buckling (e.g., see Wang and Zhao, 2013b). The coexistence and coevolution of different modes has also been observed and analyzed, see Fig.I.3. Mechanically induced instabilities in planar geometries find application in strechable electronics, controllable stiffness devices, sensors and actuators (e.g., Bhattacharya and James, 1999, Lacour et al., 2004). The multistable behaviour of non-planar thin structures has also gained attention for shape-changing structural control, see the works of Freund (2000), Vidoli and Maurini (2008) and Stoop et al. (2015).

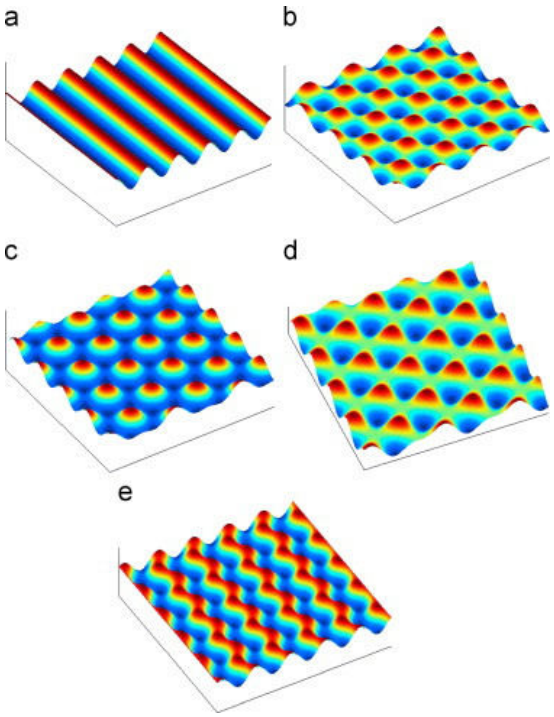

Figure I.4: Schematics of mode shapes: **a**, 1D mode **b**, square checkerboard mode **c**, hexagonal mode **d**, triangular mode and **e**, herringbone mode (Chen and Hutchinson, 2004).

Surface instabilites can also be triggered by (equi-)biaxial in-plane compression leading to intriguing two-dimensional patterns (e.g., Cai et al., 2011, Cao et al., 2014, Huang et al., 2005, Kim et al., 2011). In the range of moderate to large overstress, Chen and Hutchinson (2004) computed the energy in the buckled state of the one-dimensional stripes, two-dimensional square checkboard and two-dimensional herringbone wrinkling modes (see Fig.I.4) and showed that the latter has the lowest energy. Audoly and Boudaoud (2008a)a studied the post-buckling behavior of the same modes plus the hexagonal pattern, including the range in which the one-dimensional wrinkling is stable and transits into the herringbone mode under biaxial (but not equi-biaxial) stress states. The authors showed that the square mode has the lowest energy in the range of small overstress. In sequential studies, Audoly and Boudaoud (2008b)b,c used asymptotic methods to explore nonlinear aspects of the buckling behavior of the herringbone mode, as expected in the range of very large overstress.

I.6 Multiphysically triggered instabilities

The purely mechanical actuation of wrinkling/creasing in film/substrate systems does not allow for an efficient active control of such surface patterns. Therefore, the interest in buckling instabilities under multiphysical coupled stimuli gained ground in the recent years. Bilayer surface patterning and stiffness control can be actively obtained by thermal expansion mismatch (e.g., see Bowden et al., 1998, Huck et al., 2000, Pye and Roth, 2013), differential growth/swelling (e.g., see Chan et al., 2008, Trujillo et al., 2008, Zhao et al., 2015), as well as electroactive wrinkling and creasing (e.g., see Bense et al., 2017, Wang and Zhao, 2013a, Wang et al., 2016). Such externally applied

stimuli induce a biaxial compressive stress state within the film, which leads in turn to buckling patterns (2D wrinkles or creases) (e.g., see J. Yoon, 2010, Park et al., 2013, Wang et al., 2014, 2011). Albeit effective as a method of pattern control, differential swelling requires large times of exposure to the absorbed water/solvents, thus leading to slow on/off pattern switching. On the other hand, electro(-mechanical) actuation is extremely fast but requires complex experimental setups, e.g., dielectrics in conductive solutions and fairly high voltages. In both types of actuation systems, the proposed setups are not straightforward for use in haptic devices. However, the interested reader can refer to the work of Frediani et al. (2014) for recent advances.

Currently exploited in actuators design, piezoelectric materials have been the most popular active materials for shape patterning of flexible structures. This is mainly attributed to the linearity of their response for a large bandwidth of frequencies. Layered structures made of metamaterials, such as phononic crystals (PnC) on piezoelectric substrates (e.g., Yankin et al., 2014), are prominent in surface acoustic wave propagation for imaging and non destructive control. Nevertheless, piezoelectric elements produce limited displacements and strains, triggered by either a voltage or a transverse force. An adapted solution to produce high displacements with moderate actuation loads is provided by the use of bistable structures, such as buckled beams (e.g., see Cottone et al., 2012, Qiu et al., 2004, Ren and Gerhard, 1997, Vangbo, 1998) or shallow arches (e.g., see Chen and Lin, 2005, Hsu, 1967). In virtue of the instability, a rather small amount of actuating energy can induce relatively large deformations. While the majority of the works on the field have been concentrated on a single-parameter actuation, Maurini et al. (2007, 2009) investigated the multi-parameter active (post-)buckling of a bistable three-layered piezoelectric beam.

In such surface instability problems, the interplay between each multiphysical coupling is related to geometry and material system selection. In simple words, the loadings are applied on materials with given properties coupled with structures under given boundaries conditions. Thus, it is clear that the instability occurs from the coupling between the material properties and the structure.

I.7 Scope of the thesis work

Challenged by the reduction of the actuation fields and the fast on/off control of surface patterns with the view of a realistic haptic device (Fig.I.5), we propose the use of novel polymeric-based soft materials that exhibit magnetoelastic coupling and become unstable at small (practically attainable) magnetic fields. In this work, following a less common approach, we exploit experimentally and numerically the stability and post-bifurcation response of a novel MRE film/substrate material system by proper control of magnetomechanically induced surface patterns. Precisely, we combine cooperative instabilities in such a way that surface wrinkles can be triggered by successively smaller magnetic fields as a result of increasing mechanical pre-compression and vice versa.

To explore the impact of the magnetomechanical loading on the critical loads and bifurcation modes, we present stability phase diagrams of the system in the parameters space of mechanical pre-compression and applied magnetic field. The task is carried out first experimentally by intro-

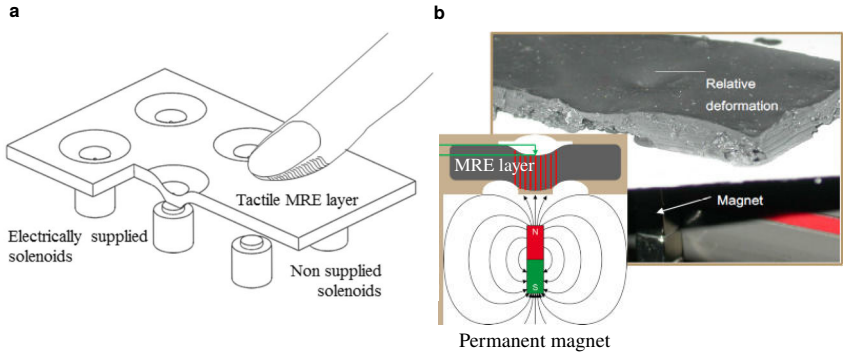

Figure I.5: Schematics of the working principle for tactile interfaces with patterns created by **a**, a matrix of solenoids, **b**, a permanent magnet placed underneath a MRE layer (Pössinger et al., 2014).

ducing an innovative fabrication for perfectly-bonded MRE film/substrate polymer blocks and then numerically by employing a user-defined finite element full-field approach. A theoretical analysis of the bloch-wave bifurcation problem permits to further investigate the influence of the material parameters on the critical response. Intriguing post-instability crinkling modes are experimentally and numerically captured and further investigated through a curvature localization analysis. In virtue of these novel localized modes, the study is expanded to the numerical investigation of MRE films bonded on MRE substrates in an attempt to further enrich the range of the obtained surface patterning.

Overall, we present a combined experimental, numerical and theoretical study on various modes of instabilities on film/substrate systems under a combined magnetomechanical loading. The variety of surface patterns owes to coupling between the bilayer structure, the magnetoelastic properties of the layers and the loading. More specifically:

In the second chapter, we present in detail the fabrication of the MRE film/substrate blocks, the material properties of the system and the experimental process to obtain the magnetomechanically triggered surface instabilities. An image processing analysis to assess the post-bifurcation amplitudes of the surface patterns is then presented. Measurements and theoretical estimates are employed to determine the material properties of the system at hand. Subsequently, the experimental findings of the magnetomechanical (post-)bifurcation response of a MRE film/passive substrate system (with given material properties and geometry) are presented. A morphological map provides experimental evidence of different surface patterns formed with the same material system at different pre-compressions and magnetic fields. The corresponding stability phase diagram in the two-field parameter space is then built, revealing the monotonic tendency of the critical magnetic field to decrease with increasing pre-compression (and vice versa). The experimental findings are followed by a discussion on possible strategies to enrich the experimentally obtained patterns by exploring the material properties of the system.

To gain better understanding of the experiment, we investigate numerically the boundary value problem of the MRE film/substrate block by means of a user-element routine implemented in the general purpose finite element code FEAP (Taylor, 2011). In the third chapter, we present the

non-trivial boundary value problem along with the numerical solution of the governing equations and the stability criterions, obtained from the theory of magnetoelasticity. First, we discuss the variational formulation within a Lagrangian setting, used in the finite element method algorithms. Explicit expressions are given for the first variation (i.e., force vector) of the variational principle that yields the equilibrium and Maxwell equations. Similarly, the second variation (i.e., stiffness matrix) is derived to form the stability condition. Subsequently, we present the phenomenological magnetoelastic energy used in the variational continuum formulation and we show an equivalence between expressions considering different independent magnetic variables. In the following sections, we describe the finite element discretization method, as well as the numerical mesh and the applied magnetic boundary conditions. In the last part, we present a brief mesh convergence study on the purely mechanical and magnetomechanical problem.

In the fourth chapter, we solve the theoretical bifurcation problem of a semi-infinite MRE film/passive substrate (plus the semi-infinite air) system and we investigate the influence of the material properties on the critical response. The first section presents the variational magnetoelastic formulation used in the bifurcation analysis. The second section outlines the principal (non-diverging) solution of the plane-strain solid subjected to in-plane compression and a transverse magnetic field. The third section demonstrates the bifurcation analysis. Such an analysis is an incremental approach that does not incorporate the effects of a boundary-value system (it considers idealized boundary conditions). The last section presents the results from the purely mechanical and magnetomechanical bifurcation. The model aims at determining the critical load for the onset of wrinkling and the associated wavelengths.

In the fifth chapter, we initially present a stiffness sensitivity study on the primary and secondary bifurcation modes of a MRE film/passive substrate block under a) a purely mechanical, b) a purely magnetic and c) a combined magnetomechanical loading. Subsequently, we properly probe the experimental findings of Chapter II with full-field finite element simulations at large strains and magnetic fields. The influence of friction on the experimental setting needs to be taken into account. Thus, it is investigated by applying variable shear forces at the lateral edges of the virtual specimen. The full-field numerical analysis reveals the complexity of the coupled fields within the film in the post-bifurcation and thus, justifies the need of numerical treatment of the problem at hand. In the last part, we investigate the influence of the film slenderness on the critical loads and modes. The results correspond to two chosen film thicknesses: $\mathrm{H}_f = 0.2$ and 0.8mm in a 40×40 (mm^2) bilayer block. The geometry with the thicker film is used to fit the experimental data. The thinner film geometry is used for connection with the theoretical problem in Chapter IV considering an infinitesimally thick MRE layer.

In the last chapter, we present a study on post-bifurcation crinkling patterns emerged from harmonic (wrinkling) modes. Such patterns are obtained by further exploiting the magnetoelastic coupling of the film/substrate structure. First, we carry out a curvature localization analysis at the post-bifurcation regime of the experimental and numerical MRE film/passive substrate system. Such an analysis reveals that curvature localization is an intrinsic feature of MRE instabilities that

leads to crinkling under the given boundary conditions. Next, we investigate the formation and post-stability evolution of crinkles on MRE films bonded on MRE substrates. The underlying idea is to create different interlayer contrasts of magnetic/mechanical properties and thus, trigger a richer range of surface modes than that already obtained when using a MRE film on a passive (magnetically insensitive) foundation. Subsequently, the study is expanded to higher slenderness ratios. We vary the magnetic properties of the substrate and we obtain an extremely large range of unique crinkled surface patterns tuned by the magnetomechanical loading. A full-field numerical analysis of the fields is presented and accompanied by preliminary experiments. The curvature localization analysis on a MRE film/MRE substrate is followed by an insight on the magnetization spatial distribution and how that contributes to the evolution of crinkling.

CHAPTER II

FABRICATION AND EXPERIMENTS

Summary of the Chapter. In this chapter, we present in detail the fabrication of the MRE film/-substrate blocks, the material properties of the system and the experimental process to obtain the magnetomechanically triggered surface instabilities. An image processing analysis to assess the post-bifurcation amplitudes of the surface patterns is then presented. Measurements and theoretical estimates are employed to determine the material properties of the system at hand. Subsequently, the experimental findings of the magnetomechanical (post-)bifurcation response of a MRE film/passive substrate system (with given material properties and geometry) are presented. A morphological map provides experimental evidence of different surface patterns formed with the same material system at different pre-compressions and magnetic fields. The corresponding stability phase diagram in the two-field parameter space is then built, revealing the monotonic tendency of the critical magnetic field to decrease with increasing pre-compression (and vice versa). The experimental findings are followed by a discussion on possible strategies to enrich the obtained patterns by exploring the material properties of the system.

Contents

The experimental system consists of an elastomeric cube of 40mm edge, in which an isotropic MRE film of thickness $H_f = 0.8$ (or 0.2) mm and shear modulus G_f rests on a (non-)magnetic substrate of thickness $H_s = 39.2$ (or 39.8) mm and shear modulus G_s, Fig.II.1. The two layers are made of elastomers of the same family that are cured simultaneously to prevent film delamination. The elastic nature of such soft and nearly incompressible materials is fairly approximated by the neo-Hookean law for uniaxial (tensile) stretches within the range $1 \leq \lambda \leq 1.25$. Nevertheless, challenges occur when needed to characterize a composite film under compression. Thus, a combined method of experiments and FE implementations is later employed in Section V.2 to evaluate the stiffness of the material-layers by numerically probing the amplitudes of the experimental surface patterns. Measurements and theoretical estimates are also employed to determine the magnetic properties of the film for later use in a magnetoelastic phenomenological constitutive law.

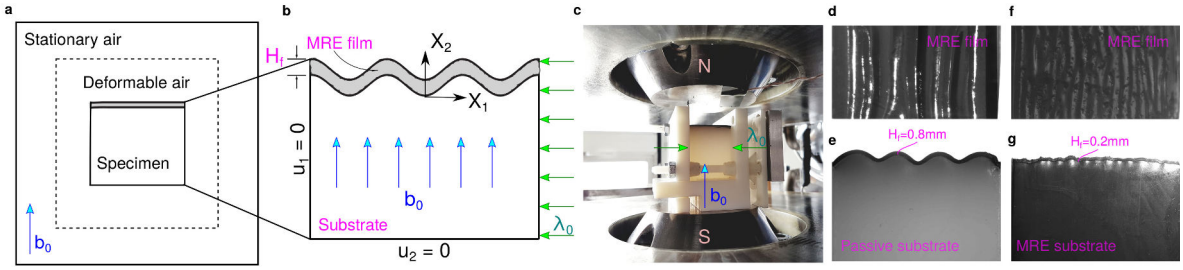

Figure II.1: **a**-**b**, Schematics of the boundary value problem under plane-strain conditions: **a**, Stress-free state of the magnetoelastic specimen surrounded by air. **b**, Bifurcated specimen of a MRE film bonded on a substrate. **c**, Experimental magnetomechanical setup. The loading consists of uniaxial pre-compression λ_0, followed by the application of a magnetic field b_0 in the direction of film thickness. The substrate can be either magnetically insensitive (**d**-**e**) or a MRE (**f**-**g**). The film thickness can be either $H_f = 0.8$mm (**d**-**e**) or 0.2mm (**f**-**g**).

The system is subjected to in-plane uniaxial compression perpendicular to the film thickness denoted by the stretch measure $\lambda_0 = 1 + \varepsilon_0$ such that $0 < \lambda_0 < 1$ (or $-1 < \varepsilon_0 < 0$). The magnetic field b_0 is then linearly increased beyond the bifurcation point to obtain well-formed wrinkling. We capture the morphological side patterns of the film using a digital camera system with 12μm/pixel resolution and we trace the out-of-plane surface displacements as a function of the magnetic field, after image processing and analysis (see Section II.4). The images are recorded during testing at a rate of 17 frames per 0.1T. To verify repeatability of the experimental evidences, three specimens of the same materials and geometry are fabricated and tested under the same conditions.

II.1 Material selection

In the perspective of fabricating a magnetoelastic film bonded on a softer elastic substrate structure of adequate magnetomechanical coupling, the family of Ecoflex silicones from Smooth-On Inc.,USA, is a suitable choice. The substrate material Ecoflex 00-10 is a soft and stretchable silicone elastomer (see manufacturer's specifications in Table II.1 and mechanical characterization in Section II.5). The elastomeric film matrix Ecoflex 00-50 is chosen to be stiffer than the substrate, so as to create

a stiffness interlayer contrast that yields one-dimensional wrinkles (if materials incompressible), see Fig.II.2. When cured, the hyperelastic material-layers are nearly incompressible and isotropic, undergoing nonlinear stress-strain response at large deformations.

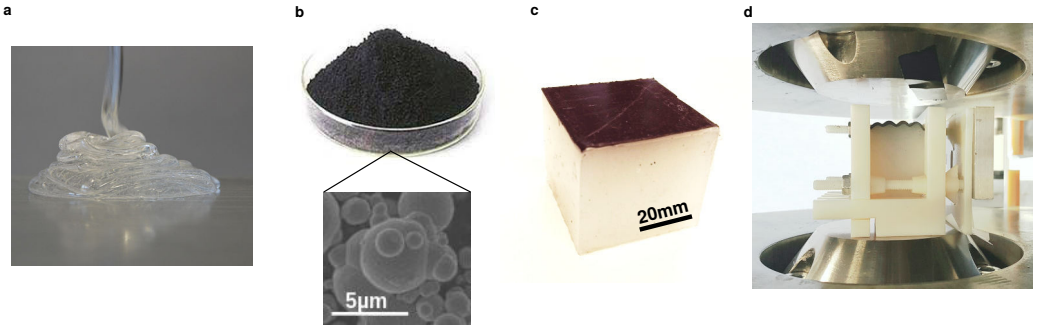

Figure II.2: From fabrication to testing: **a**, Silicone polymer in liquid state. **b**, Carbonyl iron powder comprising spherical particles of median diameter at 5μm. **c**, Fabricated MRE film/silicone substrate specimen. **d**, Wrinkled MRE film/silicone substrate specimen under the magnetomechanical loading.

Ecoflex elastomers are two-part addition-cured platinum-catalyzed systems (RTV-2), mixed at room temperature. The mixed viscosity of the liquid Ecoflex-0010 (substrate material) allows for manageable material pouring even at large times close to the pot life[1] of 18 min. For the film, it is not straightforward to achieve a compromise between pot life limit (18 min) and adequate dispersion when mixing at high particle volume fractions ($c \approx 25\%$). More specifically, the intrinsic viscosity of the film matrix (8000 cps) increases when adding the iron particles, while the degassing process warms up the composite material speeding the polymerization up. As a result, the pot life noticeably decreases to 10 min and thus, prompt handling is required when fabricating the film. In order to eliminate the air entrapped during mixing, an adequate film degassing is carried out at least for 5 min. In view of that, providing a material quality that respects both isotropy (perfectly-dispersed film) and incompressibility (full degassing) is a true challenge for the film polymer, which has 10 min pot life under real operating conditions. The physical and mechanical properties of the bi-material are shown in Table II.1 as provided by the manufacturer.

Properties	Substrate	Film
Shore hardness	00-10	00-50
Elongation at break(%)	800	980
Density [kg/m^3]	1.040	1.170
Mixed viscosity [cps]	4000	8000

Table II.1: Material properties of the silicone substrate and silicone film matrix provided by the manufacturer.

The filler phase is carbonyl iron powder (CIP) SM from BASF Germany. This powder is made of spherical particles with a median diameter of 5μm, containing up to 99.8% of Fe with low amounts

[1]Pot life: Period for which two mutually reactive chemicals remain usable when mixed. Two Ecoflex components (i.e., polymer and hardener) polymerize within about 18 min upon mixing and become useless.

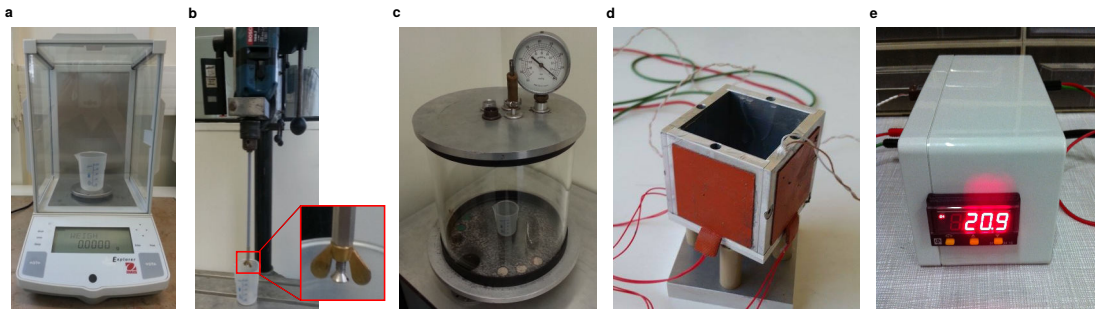

Figure II.3: Fabrication process steps: **a**, Weighting **b**, Mixing **c**, Degassing **d**, Molding **b**, Curing

of C, N and O. Soft iron is defined by low coercitivity and magnetic saturation $\mu_0 m^s = 0.8\text{T}$ (Haynes, 2013). Hence, the particles are good candidates for active MRE applications without permanent magnetization requirements. According to the manufacturer, the iron bulk density is within the range of $1.5 - 2.5\ \text{kg/m}^3$ in the form of powder and $7.874\ \text{kg/m}^3$ in the form of a bulk metal. The bulk density takes into account the presence of air gaps between the particles, when occupying a given volume in the form of powder. However, this becomes irrelevant once the particles are mixed in a viscous liquid elastomer. Hence, the density commonly regarded in the MRE literature is taken either as that of the bulk iron (e.g., Schubert, 2014), or slightly lower (e.g., Gorodkin et al., 2009) so as to account for the minute air gaps that can be retained between adjacent particles in interaction with the polymeric chains.

II.2 Fabrication of the MRE film/substrate block

The substrate is fabricated from silicone elastomer Ecoflex 00-10, mixed in a 1:1 weight ratio (polymer: hardener) for 4 min and degassed inside a vacuum chamber for 6 min, Fig.II.3c. While the substrate is under vacuum, the film matrix Ecoflex 00-50 is similarly mixed for 3 min, after adding 5μm-diameter iron particles at 20% volume fraction. To ensure proper particle dispersion before polymerization, the carbonyl powder is first mixed with the polymer and the semi-blend is then mixed with the hardener. The mixing process is performed at 400rpm by means of a rotating drill-type tool, Fig.II.3b. The film material is then degassed for 5 min and directly casted into the mold, so as its intrinsic curing does not prevent pouring. The film compound is poured into a metallic $40 \times 40 \times H_f\ (\text{mm}^3)$, $H_f = 0.2, 0.8\text{mm}$, mold base previously cleaned and polished. Scraping the top surface of the material leads its excess quantity to flow out of the mold base, thus creating a flat film surface. To build the whole $40 \times 40 \times 40\ (\text{mm}^3)$ system, four metallic walls are mounted onto the aforementioned base to form a taller mold, Fig.II.3d. The substrate material is then poured on the top of the film. The soft silicone is casted into a thick layer of thickness $H_s (= 40 - H_f) \gg H_f$.

Heating resistors, encapsulated in silicone and attached to each of the walls (Fig.II.3d), are connected to a temperature on/off PID regulation system, Fig.II.3e. The PID system delivers current so that the temperature measured by a thermocouple (inserted in one of the walls) matches the programmed heating schedule. By virtue of this system, the film/substrate block is subjected to

a 60 min curing process at 70°C with a 5°C/min rate of temperature rise (drop) from (to) ambient. The polymerization is carried out in the absence of a magnetic field, thus leading to an isotropic MRE film. Ecoflex silicones can also be cured at room temperature within 24h, though the external heating prevents the gravitational movement of the particles towards the bottom of the mold. The specimen is unmolded after 24h.

Observations of a cross-section of the bilayer material with a VHX-5000 series Keyence Digital Microscope confirm a nearly constant film thickness (0.8 ± 0.04 mm) and absence of film delamination, Fig.II.4d. This owes to material selection with respect to curing conditions; the film and the substrate are polymers of the same family, simultaneously cured in a joint fashion.

We note that the proposed fabrication process is independent of the tensile pre-stretching of the substrate, required in a well-known fabrication technique to produce compression in the surface layer (e.g., see Cao and Hutchinson, 2012a, Sun et al., 2012, Wang and Zhao, 2013b, Wang et al., 2016). In the latter technique, a thin unstretched film is bonded to a thick pre-stretched substrate. When such a system is set free, the stretch in the substrate is relaxed, leading to film compression that triggers wrinkling. As a result, the incremental anisotropy induced to the substrate becomes an inevitable parameter to be considered. In our case, the film and substrate are jointly compressed from a stress-free state where the material-layers are isotropic. Hence, the critical response does not depend on another supplementary field-parameter. To that end, the proposed fabrication process permits to perform a large range of adjustable loadings in-situ with only one specimen.

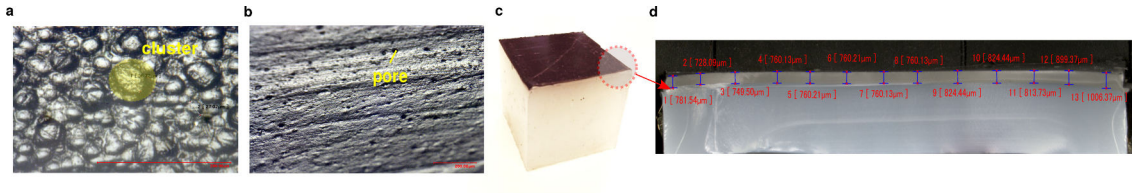

Figure II.4: VHX-5000 series Keyence Digital Microscope observations of **a**, Ecoflex 00-50 silicone film reinforced with 5μm-diameter carbonyl iron particles at volume fraction $c = 25\%$ (particle aggregation observed); **b**, Ecoflex 00-10 silicone substrate. **c**, Cubic specimen made of carbonyl iron particle-impregnated Ecoflex 00-50 film adhered on Ecoflex 00-10 substrate. **d**, A well-bonded interface of controllable thickness $H_f = 0.8 \pm 0.04$ mm is observed.

II.3 Magnetomechanical experiment

The compression device is 3D-printed in Verowhite polymeric material so as not to interfere with the magnetic field during the experiments, Fig.II.5. It is fabricated in a shiny and smooth finish of injection molded plastic, delimited by the print quality of EDEN260VS Stratasys printer at sub-0.16mm layer height. The setup consists of three orthogonal walls forming a U shape. As seen in Fig.II.5b, one of the walls in parallel is able to slide on the bottom wall, while the other at the opposite is fixed. A non-magnetic screw-driven system controls the distance between the two parallel walls and thus defines the applied pre-compression stretch ratio λ_0 within the range $\lambda_0 \in [0.7, 1)$.

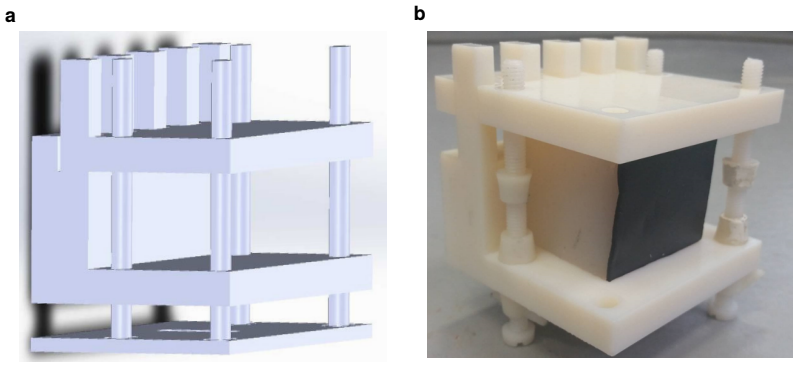

Figure II.5: **a**, Solidworks 3D CAD design of the compression device. **b**, 3D printed compression device with specimen.

Before compression, silicone oil is applied onto the lateral faces of the film/substrate block in contact with the setup walls to decrease friction. However, the friction developed at these regions is not negligible at large pre-compressions. Thus, such boundary effects need to be taken into account in the numerical analysis to reach a quantitative agreement with the experiments (see Section V.3). The bottom part of the block remains uncoated to prevent pronounced translations at the bottom of the substrate. The specimen is placed at the center of the setup and the system is properly assembled to apply the prescribed pre-compression. The bilayer structure is compressed from a stress-free state where both materials are isotropic.

Keeping the pre-compression fixed, the entire system is installed onto an aluminum plate with the MRE layer perpendicular to the external magnetic field. The system is placed within a 82mm-air gap that separates two 90mm-diameter poles of a two-coil electromagnet, Fig.II.6. The custom-built electromagnet consists of two current conducting water-cooled copper coils mounted on a C-frame, each bearing at its center a truncated conical iron pole. In this way, a nearly homogeneous field is concentrated across the air gap between the two poles without induced heating during the experiments. The electromagnet is connected to a four-quadrant bipolar water-cooled power supply of $\pm$70V and $\pm$70A nominal voltage and intensity, respectively. Generation of the magnetic field is current-controlled (precision $\pm$50mA), but can also be field-controlled when a magnetic probe is installed within the air gap. The intensity delivered by the power supply can be varied either manually or through an analogic entry. A field intensity of $b_0 = 0.8$T is obtained at the center of the air gap for a current of 68A. The magnetic field b_0 is homogeneous within the central zone of the air gap along all three principal directions ($\pm$1mT at $\pm$3mm from the center).

After installation within the electromagnet, the compressed specimen is aligned at the center of the poles $(X_1, X_2, X_3) = (0,0,0)$. For a given pre-stretch λ_0, the screw-driven system properly adjusts the height of the compression setup, so that the center of the sample along the direction of the applied stretch, X_1, is at $X_1 = 0$ of the poles. Non-magnetic centering pins hold the compression device on the aluminum stand at $X_3 = 0$ of the poles. However, centering the sample at $X_2 = 0$ of the poles (X_2 is the direction of the applied magnetic field in parallel to the film thickness) is in fact a spatial

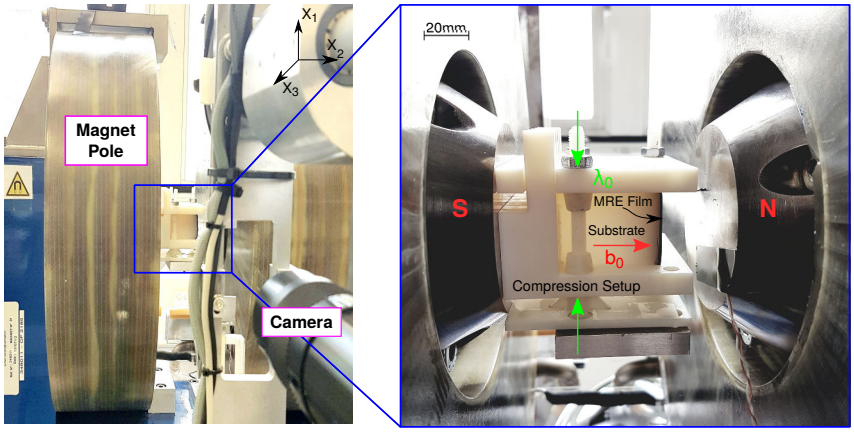

Figure II.6: Custom-made setup for the magnetomechanical experiment. The specimens are uniaxially compressed by means of a non-magnetic screw-driven device. The pre-stretch λ_0 is fixed and the system enters within the two poles of the electromagnet. The magnetic field b_0 is applied along the film thickness in a linear increasing fashion. A camera records the profile of the specimen and thus the surface patterns of the film.

compromise between the thickness of the specimen after compression at H$\simeq 40\lambda_2$ (mm) [2] and the air-gap distance between the two poles at 82mm.

The installation holds a 5 Megapixels Tokina camera for optical diagnostics opposite to the profile of the bilayer, Fig.II.6a. Images of 12μm/pixel resolution of the film/substrate specimen are recorded during testing at a rate of 17 frames per 0.1T. Given the dimensions of the specimen, the optimal working distance is 173mm, the field of view is 16mm $\times$ 20mm and the depth of field is 8mm. The camera is connected to the custom-designed software Sylvie for image acquisition. The software is both a camera monitor and a digital controller of photo recording. Setting the acquisition frequency, the camera software is synchronized with the custom-designed software Agnes, which is a digital interface of the electromagnet's hardware. The signals of the external magnetic probe generated by an encoder are taken to a NI 9215 (BNC) data acquisition card connected to the digital monitor. The measurement type is in voltage and the sensitivity of data acquisition of the external magnetic probe is 0.3T/V. The analog signals received from the electromagnet are logged into a sensor amplifier. The signals are filtered, digitized and sent to the data acquisition card (sensitivity 7A/V) for current control/measurement. The speed control unit of the applied current intensity is controlled by the computer software using the data acquisition card. Once the experiment has started, the data acquisition interface monitors the outputs and the signal generator. The progress of the test is displayed in real time through the plots of the current vs. time and magnetic field vs. time.

To reduce hysteresis and anisotropic material behaviors during the experiment, the specimens are subjected to a pre-conditioning loading at prescribed stretch $\lambda_0 = 0.85$. Such a procedure also serves in eliminating pre-stresses that may be present after clamping. To that end, the specimens are both mechanically and magnetically pre-cycled to reach a stabilized (quasi-equilibrated) state

[2] The elastomeric cube displays a nearly incompressible response expressed by the constraint equation $\lambda_1\,\lambda_2\,\lambda_3 = 1$, where $\lambda_1 = \lambda_0, \lambda_2 \simeq \lambda_3 \simeq 1/\sqrt{\lambda_0}$ are the principal stretches.

before data recording. The magnetic field is increased linearly from 0 to 0.6T at a rate of 0.002T/s. The unloading is carried out under the same magnetic rate until the field attains 0T. The external sensor measures the amplitude of the applied magnetic field as far as possible from the boundary of the specimen. Data recording acquisition considers 1 measurement per 0.5s (2Hz). The specimen is magnetically and mechanically unloaded and then retested under an increased pre-compression value.

While magnetomechanically testing the specimens under twelve pre-stretches within the range $\lambda_0 \in [0.7, 1)$, we capture the morphological side patterns of the film using a digital camera system. Subsequently, we trace the out-of-plane surface displacements versus the magnetic field by means of image processing and analysis, see Section II.4. To ensure repeatability of the experimental evidence, three specimens are fabricated and tested under the same conditions, see Fig.II.16,II.19a.

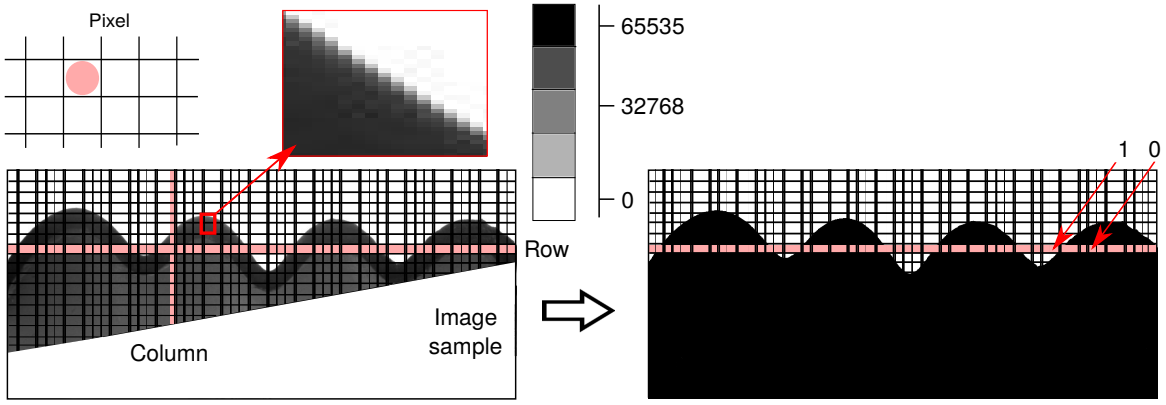

Figure II.7: A grayscale image corresponds to a 2D matrix of pixels with grascaling values within [0,65535] for uint-16 type. Each entry (i,j) represents the color value at the corresponding pixel (location). The gray levels can be transformed into a binary system, based on a threshold of pixel intensity that sets all the values lower to that equal to 0 and the rest equal to 1. The jump in [0,1] along the film thickness direction corresponds to the interface between the black film and the white background, thus making the out-of-plane trajectories of the film pixels trackable. The process followed requires scanning in rows and storing the location of the matrix cells in which the jump occurs (per column).

II.4 Post-processing via image analysis

The bifurcation curves are obtained by image processing of 12μm/pixel resolution images, recorded during testing at a rate of 17 frames per 0.1T magnetic field increment. Due to tight spacing between the magnetic poles, the current setup does not allow the direct visualization and measurement of wrinkling from the top of the film. However, such a visualization is carried out by means of a mirror, placed in 45° angle with the camera, see Figs.II.19b,c,d. Future work in different setups is underway and will allow the quantitative analysis of more complex magnetomechanical wrinkling patterns, such as those obtained for small pre-compressions in Figs.II.19d,g,j.

The digital images are processed in Matlab so as to obtain the bifurcation amplitude A curves

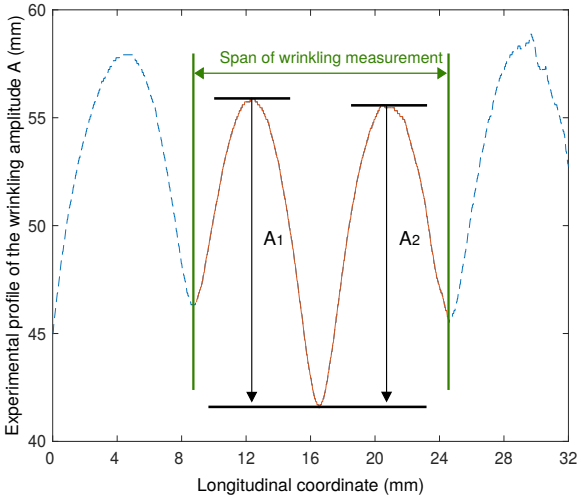

Figure II.8: Detection of the film-background interface corresponding to the film profile at $\lambda_0 = 0.8$ and $b_0 = 0.2$T. Our image analysis excludes the external wrinkles to avoid measurements affected by friction. The current amplitude of film deflection A is determined as the average value of the two middle wrinkle amplitudes, $A = (A_1 + A_2)/2$.

of three different specimens under the range of pre-compressions $\lambda_0 \in [0.7, 0.98]$ tested. Grayscale images (e.g., Figs.II.16 and II.18) are first normalized so that pixel values in the range of [0,1] represent their brightness. Each image is a 2D array (or a matrix) with a given number of pixels, i.e., spatial discretization elements. The experimental images are specified as (29100×24000) pixel numeric matrices. The measured color intensity at the sampled points is given by an integer that represents the number of bits per pixel. The data matrix has class uint16 (16-bit intensity) meaning that the range of pixel intensity is within $[0, 65535]$. Such a range of grayscaling is not handy to work with when adequate pixel contrast is needed and thus, matrix conversion to binary images takes place.

In order to detect the film profile evolution versus the applied magnetic field, the contrast between the dark film and the light background is enhanced and the images are binarized. To convert the 2D grayscale images from uint16 to double image arrays, two methods are followed: Otsu's method using a global image thresholding (e.g., see Fan and Zhao, 2007) and another using a user-defined threshold of pixel intensity. In particular, the first method calls the function *graythresh* that computes a global threshold (i.e., level=*graythresh*(I)), used to convert the intensity I to binary images with *im2bw* function. By means of Otsu's method, the threshold is chosen so as to minimize the intraclass variance of the black and white pixels (Fan and Zhao, 2007). In turn, the function *im2bw*(I,level) replaces the pixels of the input image with luminance greater than the level with the value 0 (white) and the rest with the value 1 (black). The luminance threshold, returned as a positive scalar, is a normalized intensity value within the range [0,1]. The default level value of 0.5 corresponds to an intensity halfway between the minimum and maximum value of the double image array class.

The second method considers an user-defined thresholding in order to test the range of validity of the binarization matlab functions. In particular, one can treat the input image as a numeric

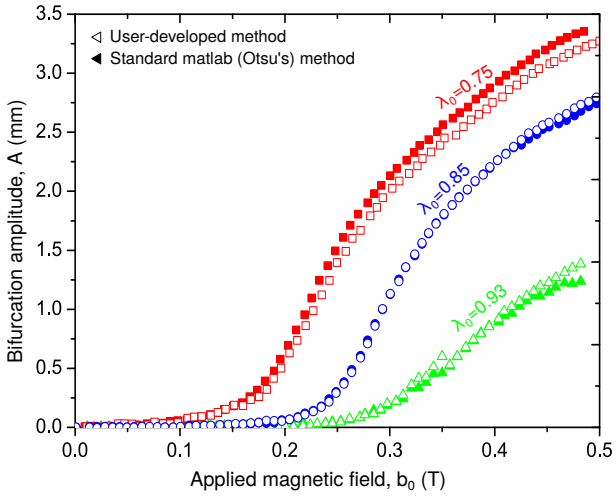

Figure II.9: Measurements of the experimental bifurcation amplitude A as a function of the magnetic field b_0 under three compressive pre-stretch ratios $\lambda_0 = 0.75, 0.85, 0.93$. The bifurcation amplitude is assessed from the wrinkled film deflection profile, detected from the experimental images by means of the standard Matlab binarization (Otsu's) method and a user-developed method. For $\lambda_0 = 0.75, 0.85$, the bifurcation curve corresponding to the user-defined method is obtained by detection of the film/air interface. For $\lambda_0 = 0.93$, the relevant curve is obtained by detection of the film/substrate interface.

matrix and convert it to an intensity image containing values within the range [0,1] (*mat2gray*). The binarization takes place by a user-developed loop, setting a threshold (~ 0.3) that defines whether a pixel intensity corresponds to the film or to the lighter background close to the film. In both methods, the position vector of the pixels located at the film/background interface (jump from 1 to 0) is stored for the initial (i.e., zero magnetic field) and magnetically loaded film configurations. However, for low pre-compressions within the range [0.9,1), the surface patterns are two-dimensional, growing in several in-plane directions and thus, cannot be accurately measured from the film/air interface side profile (see Figs.II.19d,g,j). Here, a more rigorous approach would require the detection of the interface between the film and the substrate by means of the user-defined binarization. To do so, the luminance threshold is set lower (~ 0.23), so as to convert white the higher intensity gray pixels of the substrate. Then, the first occurence of the jump from 0 to 1 is stored while scanning, i.e., position of the first cell value that is found one per image row.

We consider that clear wrinkling occurs away from the contact boundaries at which the pre-stretch is applied and thus, both edge wrinkles are excluded from the bifurcation analysis, see Fig.II.8. The absolute amplitude of the edge wrinkles tends to be higher than those in the middle of the specimen due to friction effects (discussed in Section V.3), as well as due to magnetic field concentration near the corners of the specimen (shown in Figs.V.7,V.12d). The global maximum (peak) and minimum (valley) of the central wrinkles are then tracked and the corresponding vertical displacements u_2 (along the field direction) are measured from the trajectories of the extreme points. The amplitude of film deflection A is quantified as the average distance between the peak and the valley of the two wrinkles, see Fig.II.8. The pixel coordinate system is then transformed into the laboratory Cartesian system. The difference between the current average amplitude A_i at a

given magnetic field and the initial (reference) average film amplitude A_0, $A = A_i - A_0$, is evaluated in Figs.II.18q,V.9a. The same process is followed to obtain the numerical bifurcation curves, as discussed in the context of Fig.V.9.[3]

Fig.II.9 presents the bifurcation amplitude A measured by means of the standard Matlab binarization (Otsu's) method and the user-developed one. The amplitude is traced as a function of the magnetic field for three pre-stretch values $\lambda_0 = 0.75, 0.85, 0.93$. For $\lambda_0 = 0.93$, the bifurcation curve corresponding to the user-developed method is obtained by detecting the film/substrate interface. As observed, the two methods converge on the initial post-instability regime, while slight discrepancies appear deep in the post-bifurcation. Since no significant differences are found to affect the critical loads, the methods are considered equivalent. To that end, Otsu's method is chosen to be used throughout the present study.

II.5 Mechanical characterization

For incompressible elastic materials, the critical buckling strain upon uniaxial compression is obtained for substrate/film shear moduli ratios G_s/G_f that range from the limit in which the film and the substrate have the same modulus to a very stiff film on a compliant substrate, $G_s/G_f \in (0, 1]$. An important limiting case is surface instabilities analyzed by Biot (1965) setting a threshold from smooth wrinkling to localized patterns. Past that threshold at $G_s/G_f \simeq 0.6$, morphologies more complex than wrinkling appear, e.g., creases, folds, ridges etc (see a relevant numerical analysis in Section III.5.1). The mechanical characterization aimed at mapping the ground moduli contrast G_s/G_f of our elastomeric bilayer with its critical behavior under pure compression. In that way, the critical buckling load can be predicted in the absence of a magnetic field, which is useful when creating a magnetomechanical phase diagram. Moreover, knowing the bifurcation mode (i.e., morphology of the surface pattern) yielded from one independent field, one can get more information on the contribution of each loading counterpart (mechanical or magnetic) on coupled-triggered localizations.

However, since the film/substrate is a structure, a stress-strain curve would inevitably depend upon the geometrical parameters of the system. For the MRE characterization, it is not straightforward to have direct access to the properties when deposited as a film. Measuring the response of a film is possibly not identical to that of a dogbone specimen, due to fabrication uncertainties and possible particle clustering while depositing the film. Since it is of no use to subject the MRE material to a standard tensile test, the mechanical characterization concentrated on the substrate material.

Cyclic tension tests in independent dog-bone specimens were carried out under different strain rates $\dot{\varepsilon}$ to characterize the substrate material, $G_s \simeq 3.5$kPa at $\dot{\varepsilon} = 5 \cdot 10^{-6}\,(s^{-1})$. A quasi-static characterization of very low strain rate is needed to overcome the inelastic effects of such soft materials,

[3]The numerical surface layer is free from structural fluctuations (experimentally coming from the fabrication) and thus, the initial amplitude corresponding to the stress-free state is $A_0 = 0$, i.e., perfectly flat film. Therefore, the considered numerical amplitude is equal to the average current $A = A_i$.

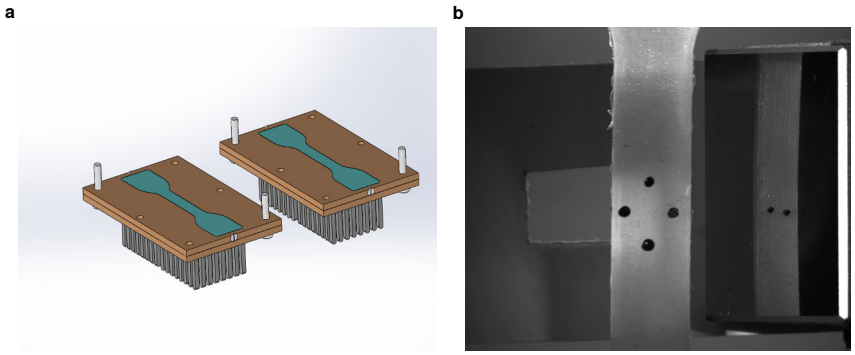

Figure II.10: **a**, Schematics of the molds for fabrication of the dogbone specimens. **b**, Black acrylic paint dots are drawn with 4 mm distance along the longitudinal direction of the specimen, in order to track the logarithmic strains by means of video extensometry.

e.g., Mullin's effects, creep behavior, stress relaxation, inertia phenomena, hysteresis etc (e.g., see Karadeniz et al., 2011). The uniaxial tensile test gave a neo-Hookean response up to $\sim 30\%$ nominal axial strain. The film modulus $G_f = 1$MPa was fitted directly from the magnetomechanical experiment. Consequently, for substrate-to-film shear moduli ratio $G_s/G_f = 0.3$, the critical behavior of the system under uniaxial compression is wrinkling, numerically verified in Fig.V.4. For later use, it is noted that the mechanical buckling stretch is $\lambda_0^c \simeq 0.76$ for such nearly incompressible neo-Hookean systems.

Albeit supplementary progress is required in the area of elastomer testing, our experimental trials will be subsequently presented. The fabrication of dog-specimens and the characterization process of the substrate material, as well as the challenges faced in order to provide reliable data will be discussed in the following.

II.5.1 Fabrication of dogbone specimens

The mechanical characterization of the substrate considers flat dogbone specimens based on the ISO 37-2 standard. The standards (protocols) provide guidelines for sample shape design, so as to ensure repeatability in material testing. The shape of the sample depends on both the tested material and the type of loading. When the tensile specimen is long, the stress field is uniform within the gage area far away from the clamping (Saint Venant's principle). However, if the sample is to be shorter, stress localization at the clamping needs to be attenuated by smooth root-corner radii from the sample's head to its gage area. This yields the well-known dogbone (or dumbbell) samples for tensile testing. For elastomers tested in tension, the corresponding standards are the American ASTM D412 and the equivalent European counterpart ISO 37. The span region of the specimen is $25 \times 4 \times 2.5$ (mm^3) based on ISO 37-2. Nonetheless, this thickness is small for purposes of video extensometry (i.e., calculation of transverse stretch along thickness) and thus, our molds were designed to provide specimens of 3 mm thickness, still respecting a good length L to thickness H ratio, $L \gg H$, for uniform strain state.

For the fabrication of Ecoflex-0010 dogbone specimens, the material parts are weighted out in

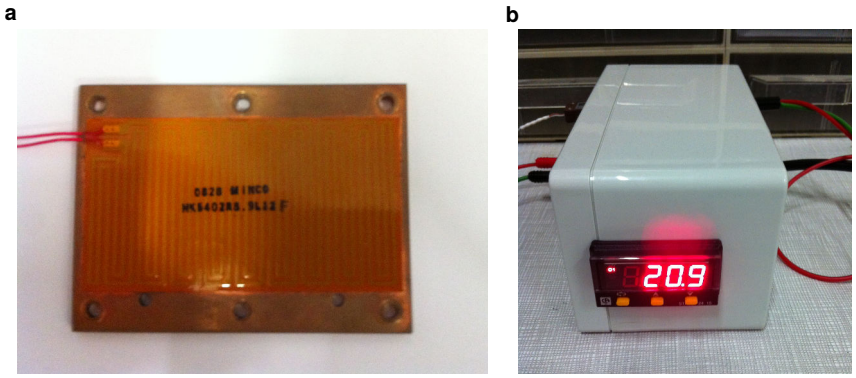

Figure II.11: **a**, Thermal resistors attached on the surfaces of the copper molds for curing. **b**, Temperature on/off PID regulation system.

Sartorius TE612 0.01 g-precision scale and catalyzed in a ratio 1:1 (hardener:polymer). The mass quantities are those of the block substrate, i.e., 50g per part, so as to reproduce the mixing and degassing quality of the cubic sample. The polymer mixture is degassed in a vacuum chamber for 6 min. Copper molds with thermal resistors attached on them are carefully cleaned. Copper is selected because of its high thermal conductivity at $390\,\mathrm{W\,m^{-1}K^{-1}}$, which ensures optimized thermal exchanges through a significant thickness of 4 mm. The inner mold surfaces are then sprayed with the commercial Mann Ease 2OO mold release wax. The mold consists of three plates with dimensions $81 \times 60 \times 2\,(\mathrm{mm}^3)$, providing a full sandwich-like mold when assembled. Two of the plates are innerly curved with the negative imprint of the dogbone specimen (Fig.II.10a), where a flat plate comes in between to connect them. The liquid material is poured into the first imprint and the flat plate comes upon it to seal the material after assembling. The second negative imprint is filled again with the material and assembled with the previous half-mold. The assembling is guided by pins that transversely interconnect the plates for proper alignment. The thermal resistors are attached on the external plates (Fig.II.11a) and connected to a thermal source through a temperature regulation system Statop 2415 (on/off PID regulator, Fig.II.11b), which correlates the temperature seen by a thermocouple attached on the inner flat plate and the scheduled heating program of the source. The selected thermocouple is of type T, providing a 0.5°C precision (in class 1). The system is subjected to a 60 min thermal process at 70°C with a 5°C/min rate of temperature rise (drop) from (to) ambient. The cycle of the curing process is that of the cubic specimen for the magnetomechanical test. The specimens are removed from the mold after 24h so as to have the thermal stresses relaxed.

Once the specimens are prepared, black acrylic paint dots are drawn with a sharp tip along the longitudinal direction having 4 mm distance, in order to track the logarithmic strains by means of video extensometry, see Fig.II.10b. The dots are painted within the central parallel portion of the specimen with relatively uniform stress and strain distributions. This type of specimen is difficult to grip and the non-uniform elongations near the jaws do not allow to determine the stretch ratios by simply considering the change in distance between them. This is the reason why the elongation measurements are concentrated within the span by tracking the motion of the black dots.

II.5.2 Mechanical cyclic tests

Symmetric tension is applied to the dogbone samples by means of a custom-made setup consisting of two motors (from Oriental Motor) installed in opposition, see Fig.II.12a. The motors are attached on long cylindrical axes. At the opposite side of the motors, each axis has mounted custom-designed clamps to hold the sample during testing. The rectangular heads are 3D printed in thermoset in dimensions $37.5 \times 17.5 \times 3$ (mm^3), see Fig.II.12b. Each pair of clamps consists of two plates with curved at their inner side a rectangle of dimensions $12.5 \times 12.5 \times 1.5$ (mm^3) to locate the head of the specimen. The motors can bear very small loads up to 10N.

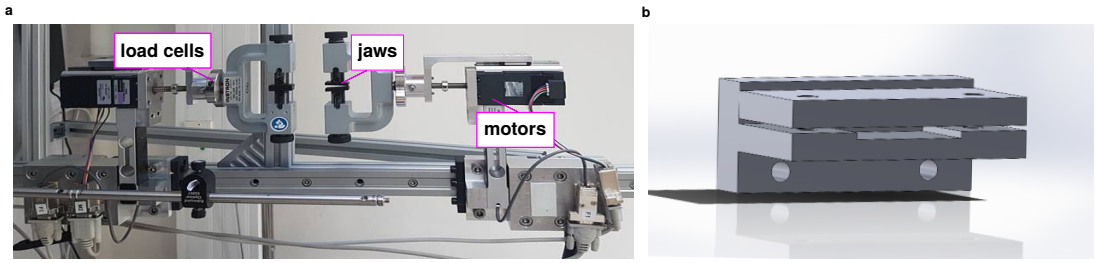

Figure II.12: **a**, Setup for uniaxial tension tests. **b**, Solidworks 3D CAD design of the 3D-printed jaws.

The experimental characterization is carried out under ambient conditions. Strains in the gage area of the samples are measured via non-contact video extensometry. Owing to the large stretch ratios and Poisson's ratio values, attention must be paid to how the sample is clamped so as to obtain valid data (Karadeniz et al., 2011). A 5 Megapixels camera, connected to the custom-made image acquisition software Sylvie for elongation recording, is initially used to align the sample. The sample is first placed on the clamps without being locked in place. Then, the load cell force is imposed to be zero by means of the custom-made software Agnes that controls the loading process. Having removed the gravitational forces from the system, the specimen is fixed on the clamps. A proper lighting and background setting are required for clean data recording. A mirror in 45° angle with the camera reflects the image of its side (in the perpendicular plane to its front plane) towards the camera. In this way, the mirror guides the alignment of the specimen as it is being stretched at 0.05 mm/s displacement rate. The focus of the camera is subsequently adjusted as a tradeoff between the front and the side profile view. The camera shutter is then adapted based on the lighting conditions.

The longitudinal stretch is measured by extensometry of two boxes, tracking the position of the black dots at 4 mm distance. The transverse stretches are measured by incremental detection of the edges. Ten cycles are performed under displacement-controlled sinusoidal signal stimulation of 0.01 Hz, 270° phase and 15 mm total amplitude. A single image from the camera provides both the front and side view of the sample, giving access to the strains along the three principal directions of the sample. The displacement, strain and force are recorded as a function of the time by means of the digital data acquisition software (synchronized with the digital camera system). The data recording rate is set at 0.1 data/sec. Zero displacement and force are set zero both in load frames and extensiometers. Plots of force vs. time, displacement vs. time and force vs. displacement monitor during cycling the loading conditions. A tracking algorithm implemented in LabView follows in real

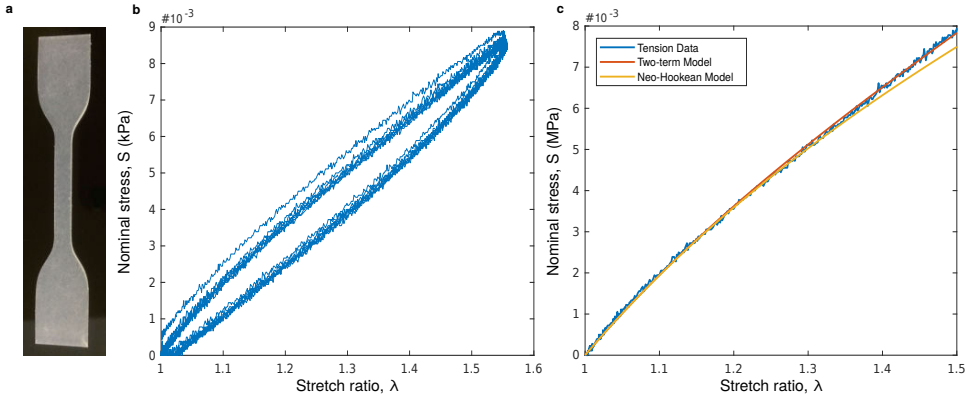

Figure II.13: **a**, Substrate dogbone specimen for uniaxial tensile tests. Nominal stress versus stretch curve for Ecoflex-0010 elastomeric substrate material under uniaxial tension at strain rate $\dot{\varepsilon} = 10^{-3}$ (s^{-1}). **b**, The loading-unloading test consists of 10 cycles of sinusoidal signal with 15mm amplitude, 0.01Hz frequency and 270°C phase; **c**, The fifth stabilized cycle is fitted by the neo-Hookean and the two-term model of Lopez-Pamies (2010). The entire range of tested stretches (up to 1.5) is fitted by the two-term model, measuring at uniaxial stretching ($\lambda_1 = \lambda$, $\lambda_2 = \lambda_3 = \lambda^{1/2}$ the principal stretches and $t_1 \neq 0$, $t_2 = t_3 = 0$ the tractions): $S_{un} = \lambda^{-1} t_1 = \frac{\lambda^3 - 1}{2\lambda + \lambda^4} \cdot 3^{1-a} G(\lambda^2 + 2\lambda^{-1})^a$ the scalar Piola–Kirchhoff stress, with $a = 1.25$ and $G = 7$kPa. When the stretch is lower than 1.25, the Ecoflex 00-10 follows the neo-Hookean law: $S_{nH} = S_{un}$ for $a = 1$ and $G = 7$kPa under the given strain rate.

time the longitudinal and the caliper boxes, thus giving access to the principal Eulerian logarithmic strains

$$\varepsilon_i = \int_{l_i^0}^{l_i} \frac{1}{l_i} dl_i = ln \frac{l_i}{l_i^0} = ln\lambda_i,$$

$i = 1,2,3$ along the three fixed laboratory axis e_i. The force exerted on the sample during loading is measured by the two LCAE-600G single-point load cells from OMEGA.

Fig.II.13 shows the experimental uniaxial nominal stress-stretch curve of the silicone substrate, together with two fitting hyperelastic models. The shear modulus of the material is found $G_s = 7$kPa at strain rate $\dot{\varepsilon} = 10^{-3}$ s^{-1} by fitting the stress-stretch data of the fifth loading stabilized cycle. In Fig.II.13c, the two-term model of Lopez-Pamies (2014) probes the entire stretch ratio range, $1 \leq \lambda \leq 1.5$, with strain-stiffening constant $a = 1.25$. Instead, the incompressible neo-Hookean model is fitted to the experimental data points within the range of stretch ratio $1 \leq \lambda \leq 1.25$. For incompressible isotropic materials, the neo-Hookean strain energy function writes

$$W(I_1) = \frac{G}{2}(I_1 - 3) = \frac{G}{2}(\lambda_1^2 + \lambda_2^2 + \lambda_3^2 - 3), \tag{II.1}$$

with $\lambda_1 \lambda_2 \lambda_3 = 1$, G the small-strain shear modulus, $I_1 = \mathbf{tr}\mathbf{C}$ the first invariant of $\mathbf{C}$ the right Cauchy-Green strain tensor and $\lambda_1, \lambda_2, \lambda_3$ the principal stretches. The neo-Hookean constitutional law is based on statistical thermodynamics of cross-linked polymer chains. Initially, cross-linked polymers (such as elastomers and thermosets) behave in a neo-Hookean manner, since the polymeric chains can move relatively to each other when a force (seen as stress by the solid) is applied. When the load reaches a certain value, the chains are stretched to the maximum length that the covalent bonds allow. That causes a dramatic increase in the incremental elastic modulus of the material.

Such an inrease in modulus cannot be captured by the neo-Hookean model and thus, the two-term model of Lopez-Pamies (2010), also belonging to the class of incompressible isotropic stored-energy functions, is used. In practice, the two-term model is a generalized version of the neo-Hookean, since it a) depends on the first invariant I_1 but not on the second $I_2 = \frac{1}{2}\{(\mathrm{tr}\mathbf{C})^2 - \mathrm{tr}\mathbf{C}^2\}$ (similar to the neo-Hookean law); b) is adequate not only for uniaxial stress states (in contrast to the neo-Hookean) and c) contains a second variable, the real number a, that controls the incremental modulus in large deformations. The two-term model is a linear combination of the invariants $\frac{3^{1-a}}{a} \cdot (I_1^a - 3^a)$ instead of $(I_1 - 3)$ and writes

$$W(I_1;a) = \sum_{r=1}^{M} \frac{3^{1-a_r}}{2a_r} \cdot G_r(I_1^{a_r} - 3^{a_r}), \tag{II.2}$$

where the integer M denotes the number of terms included in the summation. The small-strain shear modulus G_r and the strain-stiffening shear modulus a_r ($r = 1, 2...M$) are real-valued material parameters that need to be determined ultimately from macroscopic experiments (or possibly from microstructural considerations (Lopez-Pamies, 2010)).

The stress-stretch curve of the Ecoflex-0010 (substrate material) uniaxial tensile test closely matches the neo-Hookean curve up to $\sim 30\%$ stretching. To this extent, the mechanical constitutive behavior of the substrate bulk material can adequately be described as neo-Hookean and thus, we assume for simplicity such a response for our Ecoflex silicones. In Section V.2, we show that the neo-Hookean behavior is sufficient to probe the experimental bifurcation curves up to the level of the current analysis, Figs.V.9,V.10. However, a more elaborated energy should be taken into account when huge magnetomechanical coupling is regarded. Such a case is when considering a nonlinear magnetoelastic substrate, instead of a purely elastic one.

II.5.3 Challenges in characterization

Elastomers show large variations in physical properties based on the weight ratio of the ingredients (polymer:crosslinkler), strain rate, temperature and humidity conditions, inertia phenomena, stress relaxation, creep behavior, Mullin's effect etc. Indeed, a parametric study carried-out by means of an INSTRON machine, shows a strong dependence of the elastic modulus on the strain rate.

Since the experiment is displacement controlled, the strain is derived as $\varepsilon = \Delta l/l_0$ with l_0 the initial span length at 25 mm and Δl the displacement of the jaws at 30mm. For a given strain rate $\dot{\varepsilon}$, the (un-)loading time is then $\Delta t = \varepsilon/\dot{\varepsilon}$ and the displacement rate is given as $\dot{\Delta l} = \Delta l/\Delta t$. The displacement rate $\dot{\Delta l}$ is given as input in the INSTRON machine. The true strain is measured by means of the tensile machine and video extensometry. The encoder of the machine understimates the engineering strain by 12%. This is because it measures the changes in distance (displacement) between the grips and thus, takes into account the nonuniform elongations near the grips. Such a measurement is correct only when no slipping occurs at the grips. Nevertheless, relatively uniform stress and strain distributions occur throughout its central parallel region. Thus, the elongation measured within this portion by means of video extensometry is far more accurate.

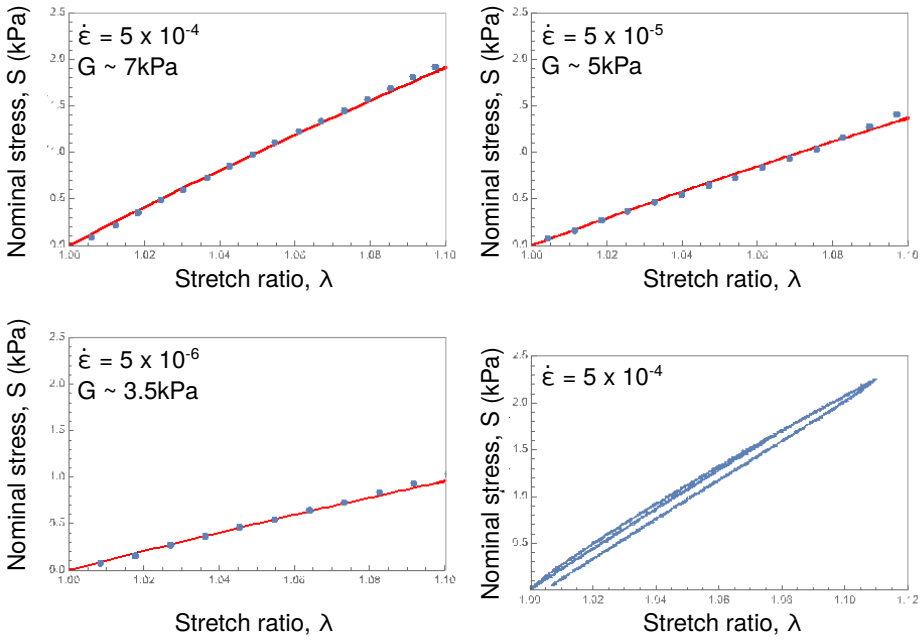

Figure II.14: Nominal stress-stretch curves for Ecoflex-0010 elastomeric substrate material under uniaxial tension for different strain rates. The dependence of the elastic modulus on the strain rate is shown. The discrete values represent the experiments and the continuous lines the neo-Hookean fitting. The film/substrate system is pre-compressed in a fixed setup and thus, is in a fully relaxed state. By contrast, a tension experiment has intrinsic rate effects. As a result, the uniaxial tension test is used as a guide and not as an independent fitting process.

The validity of our custom-made tensile machine was verified by the INSTRON machine, confirming a substrate shear modulus $G_s = 7$kPa at strain rate $\dot{\boldsymbol{\varepsilon}} = 10^{-3}\, s^{-1}$. Subsequently, lower strain rates were employed to study their effect on the tensile response. Fig.II.14 shows representative nominal stress-stretch tensile curves for three strain rates $\dot{\boldsymbol{\varepsilon}} = 5\cdot 10^{-4}, 5\cdot 10^{-5}, 5\cdot 10^{-6}\, s^{-1}$. A significant decrease of the shear modulus G_s is observed with decreasing strain rate. When $\dot{\boldsymbol{\varepsilon}} = 5\cdot 10^{-6}\, s^{-1}$, the shear modulus is found $G_s = 3.5$kPa, unlike $G_s = 7$kPa found under $\dot{\boldsymbol{\varepsilon}} = 10^{-3}\, s^{-1}$. Since the response of such soft material depends on temperature, strain rate and strain measurements[4], these stress-strain curves can provide only a range of values for the substrate shear modulus. The tensile stretching is not necessarily the best independent experiment to recover the response under compression due to the tension-compression asymmetry.[5] In addition, the curing process of a standard thin-section dogbone sample leads to different polymerization time/process than in a 40mm edge cubic block. To that end, we make use of bifurcation diagrams together with full-field (magneto)mechanical simulations, so as to obtain a precise estimate of the moduli for the application at hand.

In a number of recent papers studying film/substrate buckling (e.g., see Sun et al., 2012), the material parameters are obtained from bifurcation diagrams. In our problem, the numerical fitting

[4]Instead, the film/substrate system is pre-compressed in a fixed setup, fully relaxed before compression.
[5]We recall that the magnetomechanical experiment considers strains up to 30% under compression.

assessment of the experimental wrinkling curves (12 tested pre-compressions × 3 specimens) can be done independently, see Fig.V.9a. The setup of the magnetomechanical experiment does not allow for in-situ force measurements. The measurable quantities are the far-applied magnetic field and the observable patterns and pattern-amplitudes. To identify the material properties, we use two bifurcation curves experimentally obtained at pre-compression $\lambda_0 = 0.8$ and 0.85 (see Fig.V.9 for a detailed discussion). Given that the material layers are nearly incompressible, we consider Lamé compressibility moduli about 100 times larger than the shear moduli. From the fitting of the experimental bifurcation curves, we obtain the shear moduli for the substrate $G_s = 3$KPa and for the MRE film $G_f = 10$KPa, leading to a substrate-to-film ratio of $G_s/G_f = 0.3$. The substrate modulus is in agreement with the independent uniaxial tensile test at strain rate $\dot{\varepsilon} = 5 \cdot 10^{-6}\ s^{-1}$. These values are shown in Sections V.2 and V.3 to be sufficient to accurately probe the rest of the experimental curves.

II.6 Magnetic measurements

The MRE permeability μ_f is measured with a Bartington MS3/MS2G sensor and is used to obtain the relative film susceptibility χ_f from the relation $\chi_f = (\mu_f - \mu_0)/\mu_f$, with $\mu_0 = 4\pi 10^{-7}$ NA^{-2} the susceptibility of the air. Temperature compensated high precision measurements of the initial volume susceptibility χ_f are performed on cylindrical MRE samples. The sensor of the device is a very high thermal stability oscillator, having a wound inductor as a frequency-determining component (resolution: 10^{-6}[–] SI). This technique consists in generating a known alternative low-intensity magnetic field in a coil. When the inductor contains only air, the value of μ_0 determines the frequency of the oscillation. When the inductor is within the influence of the MRE sample, the value of μ_f determines the frequency of the oscillation. This is attributed to a perturbation of current that is created when the sample is placed inside the coil. The μ_0 and μ_f dependent frequency values are then digitized with a resolution of better than 10^{-6} and the initial susceptibility is measured such that $\chi_f^* = (\mu_f - \mu_0)/\mu_0$.

A new magnetic susceptibility quantity χ_f is however defined as $\chi_f^* = \chi_f/(1-\chi_f)$, $0 \leq \chi_f \leq 1$ and thus, combining it with the previous expression, one obtains $\chi_f = (\mu_f - \mu_0)/\mu_f$. The expression is also valid for the effective properties of the film writing $\widetilde{\chi}_f = (\widetilde{\mu}_f - \mu_0)/\widetilde{\mu}_f$. In the absence of interphases, the macroscopic permeability reduces to the Maxwell-Garnett (MG) estimate

$$\widetilde{\mu}_f = \mu_0 + \frac{3c(\mu_p - \mu_0)\mu_0}{(2+c)\mu_0 + (1-c)\mu_p} \xrightarrow{\mu_p \to \infty} \widetilde{\mu}_f = \mu_0 + \frac{3c}{(1-c)}\mu_0 = \frac{1+2c}{1-c}\mu_0, \tag{II.3}$$

where c denotes the particle volume fraction, μ_0 and μ_p the matrix (equal to that of the air) and particles (infinite) permeability, respectively. When $\mu_0 \geq \mu_p$ ($\mu_0 \leq \mu_p$), this result agrees with the Hashin-Shtrikman upper (lower) bound for a two-phase medium with arbitrary (not necessarily particulate) isotropic microstructures. In the case of particle composites, the spherical inclusions model the isotropic repartition of the phases and not the inclusion shape, i.e., they do not have to be spherical. While the result in (II.3) is not appropriate to describe the permeability of nanoparticle

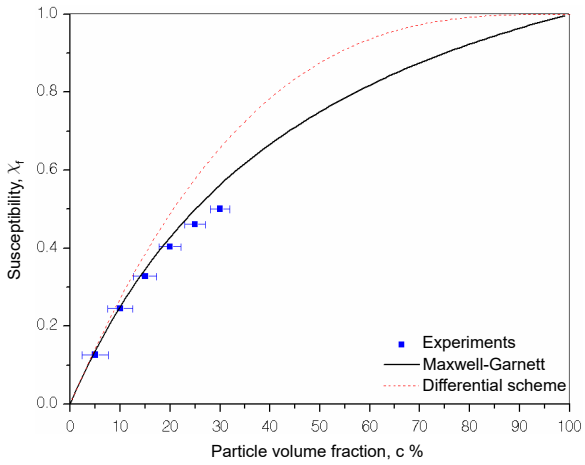

Figure II.15: Experimental measurements and analytical estimates of the MRE film relative susceptibility $\chi_f = (\mu_f - \mu_0)/\mu_f$, with μ_f and μ_0 denoting the magnetic permittivity of the film and the air, respectively. The analytical homogenization Maxwell-Garnett and differential scheme curves are included for comparison.

composites observed in experiments, it does describe reasonably well the macroscopic permeability of mediums filled with micron-sized spherical particles over large ranges of volume fractions of particles (Lopez-Pamies, 2014).

An alternative estimation of the effective permeability $\widetilde{\mu}_f$ of the film can be given by the differential scheme that writes: if the volume fraction of the matrix is decreased from c to $c-\delta$ by carving out of the composite a volume fraction δ/c of large spherical cavities and inserting large solid spheres of permeability μ_p into these cavities, then the medium surrounding these new inclusions can be treated as homogeneous with permeability $\mu_*(c)$, provided that a) the cavities are placed well apart from each other and b) their radius is chosen to be sufficiently large compared to the scale of inhomogeneities present in the original composite. To calculate the effective permeability $\mu_*(c-\delta)$ of the new suspension, one can treat it as a dilute suspension of large spheres of permeability μ_p, occupying a volume fraction δ/c in a matrix of permeability $\mu^*(c)$. At the next step, one can increase the volume from $c_1 - \delta$ to $c_1 - 2\delta$ by inserting even larger spheres of permeability μ_p. By iterating this procedure, starting from a homogeneous medium with permeability μ_0 containing no spherical inclusions, i.e., $c = 1$, we build up a material with any desired volume fraction of spheres of permeability μ_p, for which the effective permeability can be estimated by (Milton, 2002)

$$\left(\frac{\mu_p - \mu_*}{\mu_p - \mu_0}\right)\left(\frac{\mu_0}{\mu_*}\right)^{1/3} = c. \tag{II.4}$$

To solve for the effective susceptibility $\widetilde{\chi}_f$, one should go back to the relation of the effective properties $\widetilde{\chi}_f = (\widetilde{\mu}_f - \mu_0)/\widetilde{\mu}_f$, where $\widetilde{\mu}_f = \mu_*$.

The effect of the iron-particle volume fraction c on the overall magnetic susceptibility (or permittivity) of the MRE composite film is shown in Fig.II.15. For completeness, the two homogenization estimates are presented, obtained by considering air permittivity μ_0 for the silicone matrix and infinite permittivity for the iron particles (that is a good assumption since results do not change

significantly if one considers a permittivity 100 times or more than that of the air). The Maxwell-Garnett estimate is given by $\widetilde{\mu}_f/\mu_0 = (1+2c)/(1-c)$, whereas the differential scheme is given by $\widetilde{\mu}_f/\mu_0 = (1-c)^{-3}$. In Fig.II.15, one can observe that the Maxwell-Garnett is in better agreement with experiments. Since μ_0 denotes the matrix and μ_p the rigid particles permeability, then $\mu_0 \leq \mu_p$ and thus, $\mu_f^{MG}(\mu_0) \leq \mu_f^h$, where μ_f^{MG} (or $\widetilde{\mu}_f$) the homogenized permeability of the Maxwell-Garnett estimate and μ_f^h (or μ_f) the real effective permeability (if we are able to compute it exactly). The latter relations lead to a lower bound for the effective permeability μ_f^h. As a result, a lower bound for the effective susceptibility χ_f should also follow. The estimation of the volume fraction from an alleged bulk density can be a source of error. Moreover, manufacturing based parameters, such as debonding (Mullin's effect), aggregation of particles, and trapped air of zero susceptibility within the polymer (see Figs.II.4c,d) could explain why the experimental findings slightly violate the bound. By setting $c = 0.2$ (i.e., 20%), one finds $\chi_f = 0.4$, which is the value used in the subsequent numerical simulations.

The saturation magnetization of the MRE material is independent of the mechanical properties and the microstructure and is obtained by the simple rule of mixtures (see Danas, 2017). By using earlier experimental results in similar materials (see Danas et al., 2012), we use for the carbonyl iron a saturation magnetization in the order of $\mu_0 m_s^{iron} \sim 2.5$T. That gives $\mu_0 m_f^s = 0.5$T for the MRE film if mixed at $c = 20\%$ with a non-magnetic polymeric matrix.

II.7 Magnetomechanical experimental observations

The experimental system consists of an elastomeric cube of 40mm edge, in which an isotropic MRE film of thickness $H_f = 0.8$mm and shear modulus $G_f = 10$kPa rests on a non-magnetic substrate of thickness $H_s = 39.2$mm and shear modulus $G_s = 3$kPa. The two layers are made of elastomers of the same family and are cured simultaneously to prevent film delamination. The system is subjected to in-plane uniaxial compression perpendicular to the film thickness denoted by the stretch measure $\lambda_1 \equiv \lambda_0 = 1+\varepsilon_0$ such that $0 < \lambda_0 < 1$ (or $-1 < \varepsilon_0 < 0$). The magnetic field b_0 is then linearly increased beyond the bifurcation point to obtain well-formed wrinkling. We capture the morphological side patterns of the film using a digital camera system with 12μm/pixel resolution and we trace the out-of-plane surface displacements as a function of the magnetic field, after image processing and analysis (see Section II.4). The images are recorded during testing at a rate of 17 frames per 0.1T. The experimental process considers three specimens of the same geometry, fabricated under the same conditions.

A representative post-analysis of the experimental measurements is shown in Fig.II.16. Subjected to a compressive pre-stretch $\lambda_0 = 0.78$, the three specimens buckle under a 1D sinusoidal mode at $b_0 \approx 0.2$T external magnetic field, Figs.II.16b,f,j. From the profile of the wrinkled film in the inset of Fig.II.16a, we measure the average deflection of the film–referred as bifurcation amplitude A–as a function of the magnetic field, b_0. In Fig.II.16a, we then summarize the supercritical amplitude A with increasing applied magnetic field b_0 for the three specimens. Repeatability in response is

illustrated for both amplitude measurements (Fig.II.16a) and morphological patterns (Figs.II.16b-m). Standard deviation of measurements is later included in the experimental phase diagram of Figs.II.19a,V.9b, for the entire range of tested pre-compressions λ_0. As observed in Figs.II.16b-m, the wavelength of the wrinkles is susceptible to local defects, inherent from the experimental boundary conditions (lateral friction modeled in Section V.3) and the fabrication. Geometrical imperfections of the structural properties, such as film thickness, lead to variations in film stiffness and to non-uniformity of the wrinkles. As the magnetic field increases, the deflection of the wrinkled film $+A/2$ $(-A/2)$ in the peaks (valleys) evolves asymmetrically and progressively gives rise to a curvature localization mode. When $b_0 = 0.3$T, the curvature at the central valley is notably larger than that of the peaks aside, implying that the film might have asymmetric bending stiffness. Asymmetric bending stiffness[6] (due to fluctuations of the structural properties) of the surface layer produce bending configurations with high contrast of curvatures[7] between the valley and the peak of the wrinkle, which seem to promote localizations (Sun et al., 2012). The curvature contrast is growing larger with increasing magnetic field, leading to a paired-wrinkle pattern of dual period. While the curvature localization evolves, the wrinkles aside get unloaded in the most favorable fashion to create the minimum magnetoelastic configuration given the imperfections (see inset of Fig.II.16a). The post-buckling evolution manifests nonlinear growth of the localization (Figs.II.16c-e,g-i,k-m) that can be assessed by the second derivative of the out-of-plane displacement (see relevant analysis in Chapter VI).

The coexistence and coevolution of wrinkling and curvature localization is observed and further analyzed in Fig.II.17. Here, we plot the bifurcation amplitude A versus the applied magnetic field b_0 for the central (green) and the right (red) valley. When the applied field is relatively low $b_0 < 0.1$T, the flat state of film/substrate system gives the global minimum of the potential energy. As the applied field reaches a critical value $b_0^c \simeq 0.1$T, the potential energy of a new state (i.e., wrinkling) becomes equal to that of the flat state. The system then transits (smoothly due to material imperfections) into a uniform wrinkling state; all wrinkles have the same amplitude. We note that a state switched from the non-diverging (flat) one is defined as the primary bifurcation mode. The pre-compression $\lambda_0 = 0.78$ is such that brings the structure near (but not at) the critical mechanical buckling $\lambda_0^c \simeq 0.76$ [8]. In virtue of that, the instability is triggered by a small magnetic field $b_0 \simeq 0.1$T. In this way, one could possibly make use of ordinary magnets to actively control such magnetoelastic blocks as real haptic devices.

At a higher applied magnetic field $b_0 \simeq 0.32$T, the central wrinkle diverges from the primary bifurcated branch, displaying curvature localization. The formation of the secondary pattern is

[6] Asymmetric bending stiffness occurs when the top and bottom surface of a thin layer object have different local stiffness due to different types of inhomogeneities at each side. Not to be confused with bending of asymmetrical sections.

[7] High contrast for Sun et al. (2012) implies $k_1 \gg k_2$, with k_1 and k_2 the curvature of the valley and the peak, respectively.

[8] For a substrate-to-film shear moduli ratio $G_s/G_f = 0.3$, smooth one-dimensional wrinkling of $(\omega =)4$ wrinkles is triggered when the bilayer is mechanically buckled at $\lambda_0^c = 0.76$. This bifurcation mode, found by a relative numerical analysis under purely mechanical compression (i.e., $b_0 = 0$) in agreement with the theoretical results of Danas and Triantafyllidis (2014) (see Fig.V.4 for later use), progressively evolves into a double-wrinkle-pair at $\lambda_0^{c_2} = 0.69$.

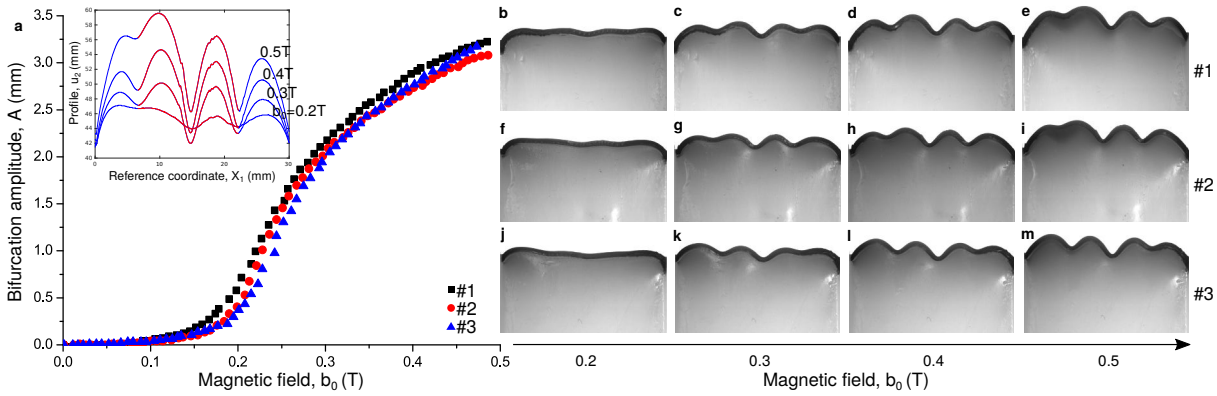

Figure II.16: **a**, Measurement of the bifurcation amplitude A versus the magnetic field b_0 at pre-stretch ratio $\lambda_0 = 0.78$ (orelse pre-strain $\varepsilon_0 = 22\%$). The bifurcation amplitude is assessed from the film deflection profile (seen in the inset), extracted from the experimental images by means of image processing. A in mm denotes the average distance between the peaks and valleys of the two central wrinkles. Three specimens are considered. **b-m**, Optical images of the morphological patterns versus the magnetic field b_0 at pre-stretch $\lambda_0 = 0.78$. The bilayer systems undergo an out-of-plane deformation, manifesting curvature localization at the middle of the surface layer as the magnetic field increases. Despite the imperfections of the pattern coming from the fabrication, the three specimens show repeatability in response in terms of morphology **(b-m)**, as well as in terms of wrinkling amplitude **(a)**.

illustrated by the shape configurations in Figs.II.16b-m. A localization develops within the uniform undulations of the sinusoidal mode, as the neighboring wrinkles grow relatively to each other. Upon further increase of the magnetic field, the localization process continues with the central undulation becoming dominant, in the form of a double-wrinkle-pair. The amplitude (depth) of the central valley grows much larger than that at its right side for $b_0 > 0.35$T, Fig.II.17. This behavior results from the incompatibility of the bifurcation modes triggered by the two independent fields under finite strains, coupled with the experimental boundary conditions (later interpreted against numerical results in Section V.3). Under such finite stretch $\lambda_0 = 0.78$, the friction developed between the lateral faces of the specimens and the walls of compression device is not negligible. That is manifested by a noticeable curvature at the corners of the surface layer (see Figs.II.18i,m). The corresponding curvature affects, in turn, the morphology of the surface pattern by pulling the corners of the film towards the substrate. Within such finite strain regime, the incremental moduli of the neo-Hookean substrate is different from the ground state and becomes anisotropic. In turn, a higher interlayer stiffness contrast might be formed, known (e.g., see Cao and Hutchinson, 2012b) to yield mechanically localized instabilities when $G_s/G_f \geq 0.6$ (see context of Figs.V.4,V.5). By contrast, the film/substrate magnetic contrast is infinite (i.e., $\chi_s/\chi_f = 0$) and thus, triggers single-period wrinkling. Consequently, the morphological pattern is a tradeoff between the purely mechanical and purely magnetic loading contributions.

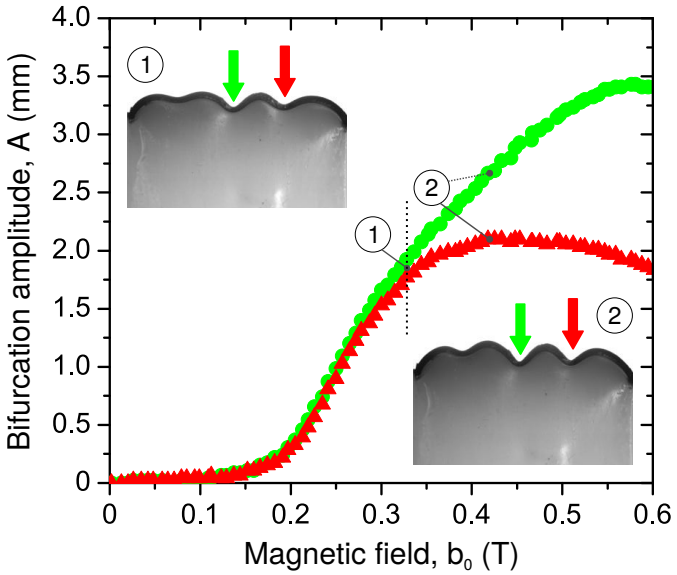

Figure II.17: Measurement of the bifurcation amplitude A versus the magnetic field b_0 of the central (green) and the right (red) wrinkle, for pre-stretch value $\lambda_0 = 0.78$. The primary instability mode of the bilayer-system is wrinkling, which soon manifests curvature localization at the center of the film. When the applied field is relatively low $b_0 < 0.1$T, the film/substrate system is at the flat state. As the applied field reaches a critical value $b_0^c \simeq 0.1$T, the system transits (smoothly due to material imperfections) into a uniform wrinkling state; all wrinkles have the same amplitude. At a higher applied magnetic field $b_0 \simeq 0.32$T, the central wrinkle diverges from the primary bifurcated branch, displaying curvature localization. Asymmetric bending stiffness (due to fluctuations of the structural properties) of the surface layer produce bending with high contrast of curvatures between the valley and the peak of the wrinkles, which seem to promote localizations (Sun et al., 2012). This behavior may also result from the incompatibility of the bifurcation modes triggered by the two independent fields under finite strains, combined with the experimental boundary conditions.

II.7.1 Morphological patterns

The morphological response of the MRE film/substrate system is summarized in Figs.II.18a-p. Therein, the block, initially pre-compressed with $\lambda_0 = 0.95, 0.85, 0.8$ and 0.75 (Figs.II.18a,e,i,m), bifurcates as a result of the applied magnetic field b_0. The post-buckling evolution of the modes versus the applied magnetic field is also considered for the aforementioned λ_0 (Figs.II.18c-d,g-h,j-l,n-p). This magnetomechanical morphological map provides experimental evidence of different surface patterns formed with the same material system at different pre-compressions and magnetic fields. The morphology of the critical modes evolves more drastically with increasing pre-compression, while it remains almost unchanged with increasing magnetic field once in the post-bifurcation regime. The magnetoelastic properties of such a structure allow for bifurcation modes of sinusoidal type (wrinkles) within a large range of pre-compressions, even when λ_0 is significantly higher (i.e., compressive strain is lower) than the theoretical mechanical bifurcation point for a substrate-to-film shear moduli ratio of $G_s/G_f = 0.3$, denoted as $\lambda_0^c \simeq 0.76$ (Figs.II.18a-l). For small pre-compressions, e.g., $\lambda_0 = 0.95$ (Figs.II.18a-d), the wrinkling patterns are complex and two-dimensional (2D) as a consequence of the high in-plane symmetries of the cubic block, i.e., almost square top surface of the

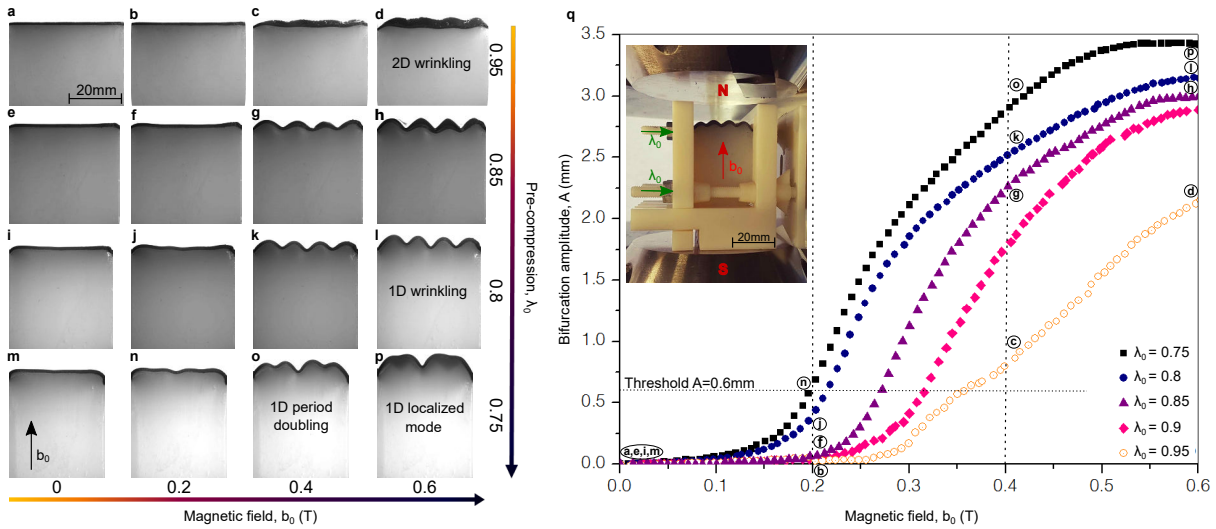

Figure II.18: Experimental influence of the magnetomechanical coupling on bifurcation and post-bifurcation. **a-p**, Optical images of the morphological pattern evolution versus the magnetic field b_0 under different pre-compressions λ_0. Scale bar, 20mm. Bifurcation patterns and critical loads depend on coupling: (**a-d**) For small pre-compressions, two-dimensional (2D) wrinkling patterns (see inset of Fig.V.9b blue region) are mainly controlled by the magnetic field, e.g., $\lambda_0 = 0.95$, $b_0^c < 0.4$T; (**e-l**) For moderate pre-strains, one-dimensional (1D) wrinkling pattern of stable wavenumber $\omega(=4)$ is obtained. The single-period wrinkling is the most preferable buckling mode in the range of pre-compressions tested. As pre-compression increases, wrinkling is triggered at smaller magnetic fields, e.g., $\lambda_0 = 0.85$, $b_0^c > 0.2$T and $\lambda_0 = 0.8$, $b_0^c \approx 0.2$T; (**m-p**) For high pre-compressions, period-doubling is observed while the critical magnetic fields do not decrease further, e.g., $\lambda_0 = 0.75$, $b_0^c < 0.2$T. **q**, Measurements of the bifurcation amplitude A as a function of the magnetic field b_0, for different pre-compressions λ_0. A in mm denotes the average distance between peaks and valleys of the two central wrinkles. For small pre-compressions (e.g., $\lambda_0 = 0.95$), the amplitude measurements should be analyzed with caution since the camera has no access to the internal part of the film surface, where higher wrinkling amplitude is developed (see Fig.V.9b-inset of blue regime).

film at small pre-compression (but see also Audoly and Boudaoud (2008a), Stoop et al. (2015)). By further pre-compressing, e.g., $\lambda_0 = 0.85, 0.8$ (Figs.II.18e-l), the cubic symmetry breaks, leading to a one-dimensional (1D) sinusoidal wrinkling pattern of single period and stable wavenumber $\omega(=4)$. This mode governs the post-bifurcated response for a wide range of $\lambda_0 \in [0.75, 0.9]$, illustrating the similarity and cooperation of the magnetic and mechanical primary bifurcation modes. This similarity results from the substrate-to-film infinite magnetic susceptibility contrast ($\chi_s/\chi_f = 0$) and moderate mechanical moduli ratio ($G_s/G_f = 0.3$), respectively.

Further pre-compression beyond $\lambda_0 = 0.75$ (Figs.II.18m-p) causes single-period wrinkling to evolve into period-doubling. The double-period pair bifurcates from the flat state by varying the amplitude of the middle valley, leading to a period twice of the wrinkles aside. In this latter regime, the film/substrate block is under the influence of finite strains and significant friction at its lateral faces in contact with the mechanical compression device. The friction is manifested by the presence of a non-negligible curvature at the extremal sides of the film (see Figs.II.18i,m). Such a curvature tends to inhibit the full formation of mechanical wrinkling on the film, even though one reaches the

point of mechanical wrinkling ($\lambda_0^c \simeq 0.76$)[9]. In view of that, the applied stretch exceeds the point of mechanical buckling, $\lambda_0 < \lambda_0^c$, without undergoing a clear instability, see Fig.II.18m. Instead, it promotes a mechanical localized mode that resembles closely a crease mode but without self-contact of the free surface. By contrast, the application of the magnetic field gives rise to pure wrinkles. This possibly suggests that the mechanical and magnetic bifurcation modes become different in high pre-compressions and thus, their cooperative nature is lost. Within such finite strain regime, the incremental moduli of the neo-Hookean substrate is also different from the ground state and becomes anisotropic, see Fig.II.13b for the substrate stress-strain (tensile) response. In turn, a higher interlayer stiffness contrast is formed, $G_s/G_f \geq 0.6$, known (e.g., see Cao and Hutchinson, 2012b) to yield mechanically localized instabilities (see context of Figs.V.4,V.5). As a consequence, the critical magnetic field saturates as a function of pre-compression, whereby its quantitative interpretation can already be observed in Figs.II.18q and II.19 (it is also discussed in detail in the context of Fig.V.9b). Further increase of the magnetic field leads to large out-of-plane deformations that relaxes the neighboring wrinkles and promotes a single localized pre-crease mode, as shown in Fig.II.18p.

II.7.2 Bifurcation amplitudes

In the morphological map, one can qualitatively observe a monotonic tendency of the critical magnetic field to decrease with increasing pre-compression (and vice versa) (Figs.II.18c,f-g,j,n). To further explore quantitatively the influence of magnetomechanical coupling over the critical loads, we measure the evolution of the out-of-plane deflection of the film–referred in this work as bifurcation amplitude A–as a function of the applied magnetic field b_0 (see image processing method in Section II.4). In Fig.II.18q, we summarize the supercritical bifurcation amplitude curves for different pre-compressions, which plainly depict the decreasing trend of the critical magnetic field as a function of pre-compression. The transition from the principal solution ($A = 0$) to the supercritical bifurcated branch is smooth and increases gradually with the magnetic field, indicating the presence of unavoidable geometrical and material imperfections deriving from the fabrication process. For later use, we define the bifurcation transition points (λ_0, b_0^c) by setting a threshold over the amplitude A, as seen in Figs.II.18q and II.19. The threshold here is chosen so that clear wrinkles have been formed and is in the same range of the film thickness H_f.

Selecting two thresholds $A = 0.4$ and $0.6\,\mathrm{mm}$ for comparison, the two-field stability diagram is built in Fig.II.19a and divided in three domains based on pattern distinction: two-dimensional (2D) wrinkles (pink), one-dimensional (1D) wrinkles (white) and a double-wrinkle-pair (blue) regime that is sequenced by a mechanically triggered crease at $\lambda_0 = 0.7$. The graph reveals that pattern switching is controlled by pre-compression λ_0 when the substrate is magnetically insensitive. The reduction of the critical magnetic load b_c with applying pre-compression λ_0 is now evident. This reduction is a direct consequence of the proper cooperation of the magnetic and mechanical wrinkling instabilities. A qualitative explanation behind this decreasing trend is the following: the elastic energy stored by

[9]That will be discussed in detail in Section V.3, after having solved numerically the problem at hand.

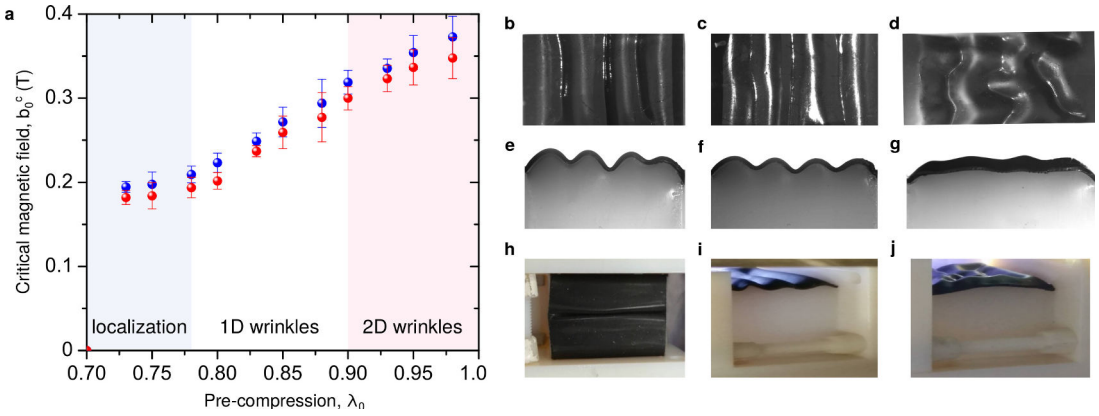

Figure II.19: **a**, Identification of bifurcation in the two-field parameter space: mechanical pre-compression λ_0 and magnetic field b_0. A decreasing trend of the critical magnetic field b_0^c as a function of the applied pre-stretch λ_0 is observed in the two-field stability phase diagram of morphological patterns. Experimental (λ_0, b_0^c) critical points for 2D wrinkling (pink), 1D wrinkling (white) and wrinkling followed by curvature localization patterns (blue) are defined from the bifurcation curves (in Figs.II.18q, V.9a and V.10a) by considering thresholds of macroscopically observed bifurcation amplitude at $A = 0.4$ and 0.6 mm. Standard deviation of measurements among three specimens is included in the experimental data points. **b-d**, Top view; **e-g**, side view; **h-j**, overall view of localizations, 1D wrinkling and 2D wrinkling, respectively.

compressive pre-straining λ_0 brings the system closer to a mechanically critically stable state. Such a state subsequently contributes in triggering a cooperative magnetic instability at a lower magnetic field b_c.

At smaller pre-compressions (pink region), we observe morphological 2D effects since there is no bias to plane strain modes, shown in Figs.II.19d,g,j. Here, the local variation of thickness and stiffness in the film highly affects the morphological paths, i.e., defect-sensitive pre-compression regime. At high pre-compressions, the magnetic field saturates in an asymptotic response with no further reduction of the b_c. It is noted that this latter regime is under the influence of finite strains and boundary friction at the side walls of our specimen (later treated in Section V.3) that leads to a pronounced curvature at the edges of the block, see Figs.II.16b,f,j and II.18m. Nevertheless, the maximum field reduction achieved because of the magnetomechanical coupling is up to 50% versus the almost purely magnetic case. More specifically, the critical magnetic field when the block is under significant pre-compression, $\lambda_0 = 0.75$, reduces to half with respect to that in the presence of small pre-compression, $\lambda_0 = 0.98$.

The variety of surface patterns owes to coupling between the magnetoelastic properties of the layers, the structure and the combined loading. In the present experiment, we use polymers to fabricate the film and the substrate and systematically vary the pre-compression of the joint bilayer from a stress-free state. Given the magnetic film is stiffer than the passive substrate (perfect interfacial adhesion), the experiment demonstrates a systematic set of instabilities: (i) If the in-plane symmetry of the square film surface is strong, then 2D labyrinth-like patterns are formed, Figs.II.19d,g,j. (ii) If the in-plane symmetry is broken due to (moderate-to-high) pre-compression, then 1D smooth wrinkling is formed, Figs.II.19c,f,i. (iii) If the system is under high pre-compressions, then the co-

existence of wrinkling and localizations is observed, Figs.II.19b,e. (iv) Further pre-compressing at $\lambda_0 = 0.7$ gives a mechanical crease, Fig.II.19h. To our knowledge, this is the first time in literature that such experimental results are shown in a two-field stability diagram. The interplay between the two fields (magnetics and mechanics) in surface pattern tuning is generally non-intuitive. The proper combination of the coupled loading allows for the observation of various surface patterns, as well as the reduction of the critical fields. However, this is the case only when one has cooperative instabilities, i.e., both of the fields have to trigger the same bifurcation modes. Otherwise, the solution bypasses the mechanical primary mode and is driven directly to later advanced bifurcations.

A general and quantitative understanding of the various modes of instabilities given the material properties of the layers is of significant importance. The proposed fabrication technique provides a single material that serves as a magnetomechanical device for the active control of surface patterns and critical loads. In this way, the need for multiple material-specimens under different pre-loads, such as other fabrication techniques do (e.g., substrate tension prior to film attachment) is overcome.

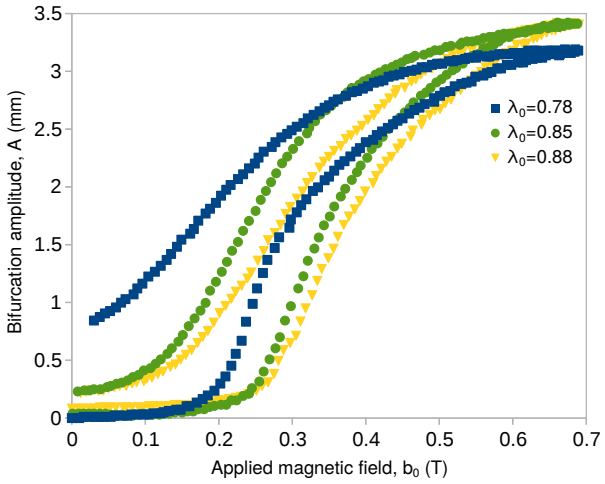

Figure II.20: Measurement of the bifurcation amplitude A versus the magnetic field b_0 under compressive pre-stretch values $\lambda_0 = 0.78, 0.85, 0.88$. Both magnetic loading and unloading are regarded to show the size of the hysteresis effect on the response.

All the above-discussed morphological patterns reversibly vanish with slight hysteresis after magnetic loading removal. Without including a dissipative rate-dependent magnetoelastic theory, it is not possible to identify what part of the hysteresis owes to the viscoelasticity of the polymer and/or to the magnetic hysteresis of the MRE film. However, most of the hysteresis should be due to the polymer viscosity, since for the magnetic part we use magnetically soft iron. Danas et al. (2012) have shown that soft particle MREs exhibit very small hysteresis in magnetostriction and none in magnetization. To provide an idea of the size of the effect, we show in Fig.II.20 three experimental magnetomechanical (un-)loading bifurcation curves versus the applied magnetic field at applied pre-stretch $\lambda_0 = 0.78, 0.85, 0.88$. The effect of hysteresis increases with increasing pre-compression, growing large as high pre-compressions are reached. A light magnetomechanical cyclic loading is applied before measurements to relax residual stresses in the specimens coming from the fabrication. However, the magnetic loading rate effects are not studied in the present study (we use a fixed one

at 0.17A/min).

II.8 Perspectives: material design

With the perspective of designing new materials having unique prescribed magnetoelastic responses, we make use of combined material properties on an entirely magnetorheological bilayer block. In that way, we could possibly create different interlayer contrasts of magnetic/mechanical properties and widen the range of surface patterns that are triggered by using a MRE film on a passive (i.e., magnetically insensitive) substrate. As already mentioned in Section II.2, the two polymers have been chosen from the same family, so as to obtain an adequate adhesion while jointly cured. In addition, the film Ecoflex 00-50 has been chosen for having the highest shore hardness, while the substrate 00-10 for having the lowest among the family products. This material selection serves in obtaining a stiff film on a highly compliant substrate and thus, the mechanical interlayer contrast to be moderate-to-low (indeed, $G_s/G_f = 0.3$). For incompressible elastic materials, this contrast given in terms of the substrate-to-film shear moduli ratio G_s/G_f (i.e., neglecting the compressibility Lamé constants since $\lambda_1\lambda_2\lambda_3 = 1$, see constitutive models in Section II.5) yields 1D smooth wrinkling when the bilayer is subjected to uniaxial in-plane compression.

However, when we make use of the magnetoelastic nature of the materials under a combined magnetomechanical loading, the ratio G_s/G_f is no longer sufficient in determining the critical loads and bifurcation modes. In virtue of this coupling in material properties, geometry and loading, new contrasts between the mechanical and magnetic properties of the layers take the lead in bifurcation. It is noted that these contrasts cannot be written in form of ratios if the constitutive behavior of the materials is non-linear in magnetic properties (see relevant analysis in Section VI.2). After all, the goal is set to keep the G_s/G_f shear moduli ratio low (so as to avoid the mechanical actuation of localizations) and test a range of finite magnetic interlayer contrasts, expressed as ratios of composite substrate-to-film particle volume fraction c_s/c_f. In that way, we can potentially trigger a richer range of surface patterns and study the contribution of the magnetic substrate to actuation of localizations by use of a magnetic field.

Given the material parameters of the layers used in the magnetomechanical experiment, the mechanical and magnetic properties of the elastomers are estimated versus the particle concentration c by means of homogenization estimates and bounds. It is noted that the mechanical parameters are assessed after numerical (FE) fitting of the experimental bifurcation curves that considers small magnetoelastic coupling in the energy functional (see Section III.2 eq.(III.34)). However, having identified the shear modulus of the composite film $G_f = 10$kPa at $c = 20\%$ from the buckling analysis, we use the homogenization differential scheme to identify the shear modulus of the film matrix $G_f^0 = 5.7$kPa. The differential scheme reads $G_f/G_f^0 = 1/(1-c)^{5/2}$ for an incompressible matrix (i.e., bulk modulus $K^0 \to \infty$) filled with mechanically rigid particles (i.e., shear modulus $G^p \to \infty$ and bulk modulus $K^p \to \infty$, implying a stiffness $\mathbf{C}^p \to \infty$ since $\mathbf{C} = 2G\mathbb{K} + 3K\mathbb{J}$, with $\mathbb{K}$ and $\mathbb{J}$ the fourth-order deviatoric and volumetric unit tensors, respectively). The approximation of rigid particles is quite

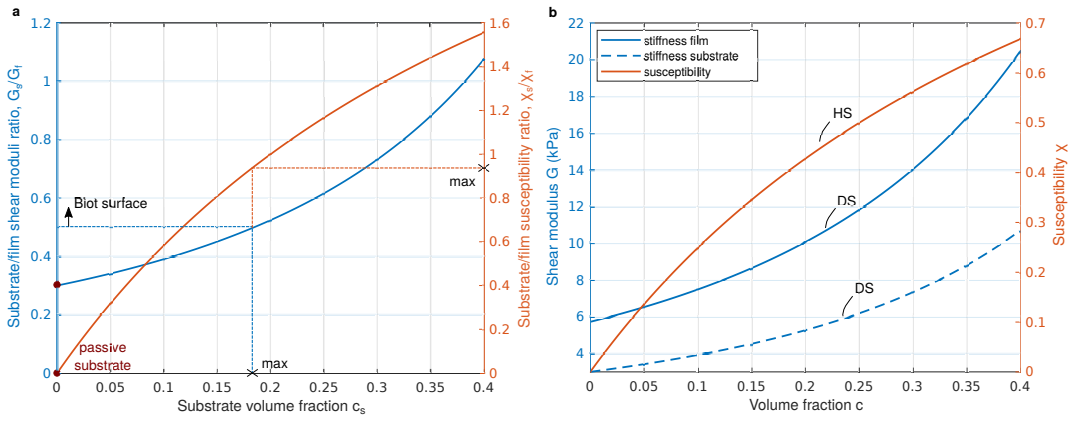

Figure II.21: Analytical homogenization estimates for isotropic incompressible elastomers filled with random isotropic distributions of rigid particles considering **a**, the substrate-to-film shear moduli ratio G_s/G_f and susceptibility ratio χ_s/χ_f; **b**, the susceptibility χ and the shear modulus G of a composite film and substrate versus the concentration of particles. The plots consider **(i)** the Hashin–Shtrikman lower bound (or Maxwell–Garnett scheme) for the magnetic permettivity, $\mu/\mu_0 = (1+2c)/(1-c)$, with μ and μ_0 the permittivity of the filled and the pure polymer, taken the latter (i.e., the matrix) to be equal to that of the air. The relative susceptibility is then given by $\chi = (\mu-\mu_0)/\mu$. **(ii)** the differential scheme for the shear modulus giving $G/G^0 = (1-c)^{-5/2}$, with G and G^0 the shear modulus of the composite and the matrix, respectively. The selection of the estimates is based on better agreement with experimental results, i.e., Fig.II.15 for magnetics and Lopez-Pamies (2010) for mechanics. The plots refer to a composite film of elastic modulus $G_f = 10$kPa and magnetic susceptibility $\chi_f = 0.43$ at volume fraction $c_f = 20\%$. Given the material properties of the film used in the magnetomechanical experiment, we explore the maximum particle concentration in the substrate (and the corresponding magnetic and mechanical properties) in order to prevent Biot's instabilities, $c_s^{max} = 18\%$ from **(a)** giving $G_s = 5.5$kPa and $\chi_s = 0.4$ from **(b)**.

accurate for MREs, since the modulus of the particles is several orders of magnitude higher than that of the soft elastomeric matrix.

For the mechanical properties, the differential scheme has been found in better agreement with experiments (Lopez-Pamies et al., 2013) than the Hashin-Strikman lower bound that reads $G_f/G_f^0 = (2+3c)/(2-2c)$. When the matrix is softer than the particles $G^0 \leq G^p$, with G^0 the matrix and G^p the particle modulus, the Hashin-Shtrikman bound gives $G^{HS}(G^0) \leq G^h$, with G^{HS} the estimated and G^h the effective stiffness. It has been shown that the Hashin-Shtrikman bound significantly underestimates the effective response for particle volume fractions $c \geq 0.1$ (Lopez-Pamies et al., 2013), while the differential scheme result is in between the bounds. On the other hand, when the particles are magnetically rigid, the Hashin-Shtrikman is in better agreement with the experiments, as seen from the susceptibility measurements versus the analytical estimates in Fig.II.15. Here, the approximation of magnetically rigid particles (albeit soft magnets) is quite accurate for MREs, since the elastomeric matrix is magnetically insensitive. Consequently, the mechanical properties of the composite elastomers are estimated by means of the differential scheme, while the magnetic properties are estimated by means of the Hashin-Shtrikman bound.

From Fig.II.21, it is straightforward that given the properties of the film already fabricated and used in the magnetomechanical experiment, i.e., $G_f = 1$MPa and $\chi_f = 0.43$ at volume fraction

$c_f = 20\%$, the magnetic substrate can be reinforced up to a maximum concentration $c_s = 18\%$ if mechanical wrinkling is preferable, i.e., $G_s/G_f \in (0, 0.6]$ to prevent surface localizations (see more in Figs.V.4,V.5). The corresponding maximum magnetic contrast in terms of susceptibility ratio is then $\chi_s/\chi_f = 0.9$ from Fig.II.21a, with $G_s = 5.5$kPa and $\chi_s = 0.4$ from Fig.II.21b.

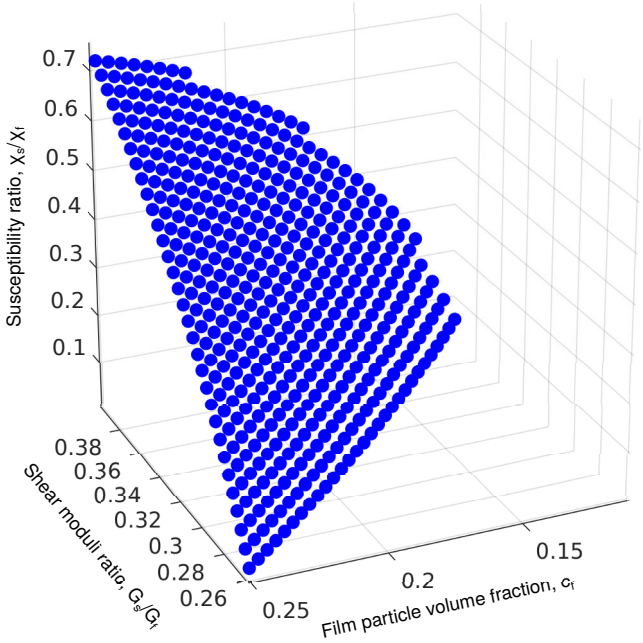

Figure II.22: A surface including all the possible combinations of film/substrate magnetomechanical material properties versus the film particle volume fraction c_f, given as base materials the Ecoflex 00-10 and 00-50 for the substrate and the film, respectively. Limitations: the particle volume fraction of the film should be $c_f \leq 0.25$ (fabrication-wise) and the interlayer shear moduli ratio should be within the range (0,0.6] (so as to avoid the actuation of localizations due to mechanical compression).

Fabrication-wise, the highest particle concentration that can be achieved is $c \approx 25\%$. Beyond that threshold, the viscosity of the material prevents pouring in the mold and diminishes the pot life. Therefore, given that (i) the moduli ratio G_s/G_f should be within the range $(0, 0.6]$ to prevent surface localizations (Cao and Hutchinson, 2012b); (ii) the mechanical properties of Ecoflex 00-10 and 00-50 for the substrate and the film, respectively, have been assessed from the magnetomechanical experiment, given the restrictions of the numerical fitting is terms of energy densities and (iii) the particle volume fraction for both layers should be c_f,$c_s \leq 0.25$ experiment-wise, we design a map of all the feasible combinations of material properties that respect the above mentioned specifications. As seen in Fig.II.22, this map represents a surface in the three-parameter space of substrate-to-film shear moduli ratio G_s/G_f, substrate-to-film susceptibility ratio χ_s/χ_f and film particle volume fraction c_f. The bounds of the plot prevent increasing the shear moduli ratio above $G_s/G_f = 0.395$ for a composite film at maximum reinforcement $c = 25\%$ and that provides a magnetic contrast of $\chi_s/\chi_f = 0.73$. Numerical simulations of the magnetoelastic bilayer block under magnetomechanical buckling will be subsequently presented in Chapters V and VI.

In the present experiment, we use polymers to fabricate the film and the substrate and systematically vary the film thickness, the elastic moduli, the susceptibility and the saturation magnetization of the magnetoelastic layers, as well as the pre-compression of the joint bilayer from a stress-free state. This analysis reveals the surface patterns obtained by the contribution of a magnetized substrate in bifurcation and map the limitations of our experimental materials. After all, in case the base materials cannot manifest new surface patterns but wrinkling due to their intrinsic properties, then modified ones can be obtained by changing the weight ratio of polymer-to-crosslinker.

II.9 Concluding remarks

In this chapter, we present in detail the fabrication of the MRE film/substrate blocks, the material properties of the system and the experimental process to obtain the magnetomechanically triggered surface instabilities. We note that the present work does not address the development of silicone-based MREs fabrication. Such a process serves only in the implementation of our proof of concept. However, the proposed fabrication technique is novel and brings an advantage: it is independent of the substrate tensile pre-stretching, which is required in a well-known fabrication technique to produce compression in the surface layer (e.g., see Cao and Hutchinson, 2012a, Sun et al., 2012, Wang and Zhao, 2013b, Wang et al., 2016). In the latter technique, the incremental anisotropy induced to the substrate becomes an inevitable parameter to be considered. In our case, the surface patterns do not depend on any supplementary field-parameter, apart from the applied loading that triggers the instabilities. In that way, we succeed to perform magnetomechanical tests under in-situ adjusted loadings with only one specimen.

The mechanical properties of the materials at hand are identified from tensile tests under a low strain rate in combination (and agreement) with the experimental and numerical buckling analysis in Section V.2. The uniaxial tensile tests are used as a guide and not as an independent fitting procedure. The magnetic properties of the film are obtained from measurements versus theoretical estimates. Such estimates and bounds are useful in designing new responses of tunable magnetomechanical properties for the substrate.

The morphological response of a MRE film/passive substrate system (with film thickness $H_f = 0.8$mm) under the magnetomechanical loading is presented. Repeatability in response is illustrated for both amplitude measurements and morphological patterns. The coexistence and coevolution of wrinkling and curvature localization is observed and analyzed. A morphological map provides experimental evidence of different surface patterns formed with the same material system at different pre-compressions and magnetic fields. To further explore quantitatively the influence of magnetomechanical coupling over the critical loads, we measure the evolution of the out-of-plane deflection of the film–referred in this work as bifurcation amplitude A–as a function of the applied magnetic field. Then, we summarize the supercritical bifurcation amplitude curves for different pre-compressions, which plainly depict the decreasing trend of the critical magnetic field b_c as a function of pre-compression λ_0.

The corresponding two-field parameter space stability phase diagram is built, illustrating that pattern switching is controlled by pre-compression when the substrate is passive. The reduction of the critical magnetic field b_c with applying pre-compression λ_0 is now quantified. This reduction is a direct consequence of the proper cooperation of the magnetic and mechanical wrinkling instabilities. A qualitative explanation behind this decreasing trend is the following: the elastic energy stored by pre-straining λ_0 brings the system closer to a mechanically critically stable state. Such a state subsequently contributes in triggering a cooperative magnetic instability at a lower magnetic field.

The proposed fabrication technique provides a single material-structure that serves as a magnetomechanical device for the active control of surface patterns. The variety of surface patterns owes to coupling between the magnetoelastic properties of the layers, the structure and the combined loading. In the present experiment, we use soft silicones to fabricate the film and the substrate and we systematically vary the pre-compression of the joint bilayer from a stress-free state. Given that the magnetic film is stiffer than the passive substrate, the experimental findings demonstrate a systematic set of instabilities: (i) If the in-plane symmetry of the square film surface is strong, then 2D labyrinth-like patterns are formed, Figs.II.19d,g,j. (ii) If the in-plane symmetry is broken due to pre-compression, then 1D smooth wrinkling is formed, Figs.II.19c,f,i. (iii) If the system is under high pre-compressions, then the coexistence of wrinkling and localizations is observed, Figs.II.19b,e. (iv) Further pre-compressing at $\lambda_0 = 0.7$ gives a mechanical crease, Fig.II.19h.

The experimental findings are followed by a closing discussion on the possible strategies to enrich the experimentally obtained patterns by exploring the material properties of the system. With the perspective of designing new materials having unique prescribed magnetoelastic responses, we discuss the potential of making use of combined material properties on an entirely magnetorheological bilayer block. In that way, we could possibly create different interlayer contrasts of magnetic/mechanical properties and widen the range of surface patterns that are triggered by using a MRE film on a passive (i.e., magnetically insensitive) substrate.

CHAPTER III

THEORETICAL FRAMEWORK AND NUMERICAL IMPLEMENTATION

Summary of the Chapter. In this chapter, we present the non-trivial boundary value problem of a MRE film/substrate plane-strain block, along with the numerical solution of the governing equations and the stability criterions arised from the theory of magnetoelasticity. First, we discuss the variational formulation within a Lagrangian setting, used in the finite element method algorithms. Explicit expressions are given for the first variation (i.e., force vector) of the variational principle that yields the equilibrium and Maxwell equations. Similarly, the second variation (i.e., stiffness matrix) is derived to form the stability condition. Subsequently, we present the phenomenological magnetoelastic energy used in the variational continuum formulation and we show an equivalence between expressions considering different independent magnetic variables. In the following sections, we describe the finite element discretization method, as well as the numerical mesh and the applied magnetic boundary conditions. In the last part, we present a brief mesh convergence study on the purely mechanical and magnetomechanical problem.

Contents

To systematically account for the various bifurcations modes, we regard the film/substrate structure as a thermodynamically energetic (reversible) system and we consider its potential energy. The potential energy evolves in the parameter space of uniaxial pre-compression and transverse magnetic field. In the undeformed configuration, the experimental system is an incompressible cube of 40mm side length, in which an isotropic magnetoelastic film of thickness $H_f(=0.8\text{mm})$ and shear modulus $G_f(=10\text{kPa})$ rests on a (non-)magnetic substrate of thickness $H_s(=39.2\text{mm}) \gg H_f$ and shear modulus $G_s(=3\text{kPa}) \ll G_f$. The neo-Hookean law applies to the substrate under uniaxial tensile stretch within the range $1 \leq \lambda_1 \leq 1.25$ (Fig.II.13). The system is subjected to in-plane uniaxial compression perpendicular to the film thickness denoted by the stretch measure $\lambda_1 \equiv \lambda_0 = 1+\varepsilon_0$ such that $0 < \lambda_0 < 1$ (or $-1 < \varepsilon_0 < 0$). The magnetic field b_0 is then linearly increased beyond the bifurcation point to obtain well-formed wrinkling.

To gain better understanding of the experiment, we investigate numerically the boundary value problem of the MRE film/substrate block by means of a user-element routine implemented in the general purpose finite element code FEAP (Taylor, 2011). The geometry of the thin film/substrate is designed in Abaqus and imported to FEAP. We consider a two-dimensional plane-strain (i.e., the stretch $\lambda_3 = 1$ in direction X_3) block surrounded by air, as shown in Fig.III.1. The film and the substrate are taken to have the dimensions of the experimental bilayer. The size of the surrounding air region ensures magnetic field uniformity far from the specimen in the free air space (Fig.III.1a). Due to the finite strains, a significant part of the air needs to be deformed via a penalty-function method, in order to avoid severe mesh distortion near the film/air interfaces (see Section III.4).

To numerically mimic the experimental procedure, we first apply a pre-compressive stretch $\lambda_0 \equiv \lambda_1$ in direction X_1 on the vertical right side of the block, i.e., a displacement-controlled loading $u_1 = 40\,(\lambda_1 - 1)$. Then, we linearly increase the magnetic field $b_0 \equiv b_2^0$ in direction X_2, Fig.III.1b. The magnetic loading is applied on the external boundary of the air domain (see context of Fig.III.2) via the magnetic vector potential $A_3(X_1,X_2) = -B_2^0 X_1$, with $B_2^0 = \lambda_1\, b_2^0$ the magnetic field and (X_1,X_2) the global coordinates in the reference configuration, respectively. Zero normal displacement u_1 is prescribed on the vertical left side of the block. Normal displacement u_2 and shear traction t_1 are also taken to be zero on the bottom side. Tangential forces f_2 are prescribed to approximately model the experimentally observed friction at the lateral faces between the block and the walls of the compression device (see Fig.III.1). The shear forces increase linearly with the applied normal compressive stretch λ_0. This applied non-zero shear traction t_2 results in a curvature at the lateral face of the MRE film, similar to the experimental observations in Figs.II.18j,m. This point is rather technical and is further detailed in V.3.

Continuity of the displacements across the film/substrate and film/air interfaces is automatically satisfied by use of nodal elements, while the tangential component of the magnetic vector field $\mathbf{b}$ is allowed to jump at these interfaces. In the present boundary value problem, the non-uniformity of the magnetic field at the corners of the film geometry, as well as the applied friction, are unavoidable sources of imperfections, leading to the numerical bifurcation curves in Fig.V.9a without any need for user-defined geometrical imperfections. Since the experiments have been carried-out in air,

the surface energies of the polymers have been neglected due to their small values and negligible effect in the current system (Wang and Zhao, 2013b). The length of the film is found to be on the magnitude of 4-20 wavelengths of the sinusoidal (wrinkling) pattern, based on two film thicknesses tested: $H_f = 0.2$ and 0.8mm. The thickness of the substrate is taken to be 199 times greater than the film thickness for $H_f = 0.2$mm and 49 times greater for $H_f = 0.8$mm. As a result, the substrate is adequately (or theoretically-considered infinetely) deep, so as to ensure that the surface modes will not interact with the bottom of the structure (bottom of the substrate). This is later verified in Sections V.1.1, V.1.3 and V.5 via comparison of the numerical results with the theoretical predictions of Section IV.4.

The numerical calculations are carried out by use of standard four-node quadrilateral bilinear isoparametric elements, with 3 degrees of freedom per node: the displacements $\mathbf{u} = \{u_1(X_1,X_2), u_2(X_1,X_2), 0\}$ and the magnetic vector potential $\mathbf{A} = \{0,0,A_3(X_1,X_2)\}$, where (X_1,X_2) denote the global reference coordinates. The nonlinear solutions of the field equations were obtained incrementally with the use of a standard Newton-Raphson scheme. A more detailed description of the numerical algorithms and meshes is presented in Section III.3 and III.4, respectively.

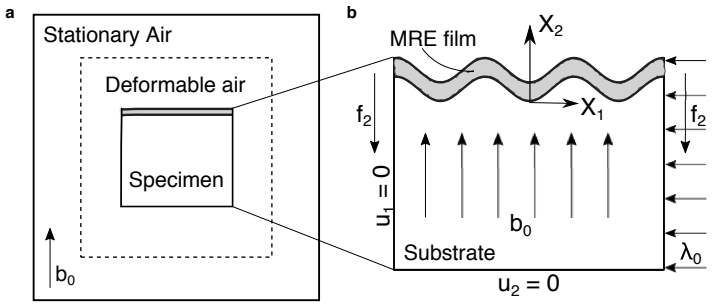

Figure III.1: Schematics of the numerical boundary value problem. **a**, MRE film adhering to a substrate under plane strain conditions, surrounded by deformable and stationary air. **b**, The block is subjected to uniaxial pre-compression λ_0 and tangential forces f_2 to mimic friction between the specimen and the compression device. Subsequently, the magnetic field b_0 is uniformly applied at the exterior boundary of the air, i.e., far from the block, and perpendicular to the film, i.e., along direction X_2.

III.1 Variational formulation for finite magnetoelasticity

In order to deal with the finite strains and large magnetic fields, we work in a Lagrangian setting and define the deformation gradient $\mathbf{F} = \mathrm{Grad}\mathbf{x} = \mathbf{I} + \mathrm{Grad}\mathbf{u}$ and its determinant $J = \det\mathbf{F} > 0$, with $\mathbf{x} = \mathbf{X} + \mathbf{u}(\mathbf{X})$ denoting the position vector of a material point in the deformed configuration, $\mathbf{X}$ the position vector of the same point in the reference configuration and $\mathbf{u}$ the displacement vector. This implies that the reference density of the solid ρ_0 is related to the current density ρ by $\rho_0 = \rho J$. We recall that the deformation gradient $\mathbf{F}$ (we use standard notation $\mathrm{grad} \equiv \mathrm{Grad}$ in the reference configuration) is a two-point tensor describing the transformation of a material point from the reference Ω_i to the deformed Ω configuration. We also note for later use that the polar decomposition of the deformation gradient is $\mathbf{F} = \mathbf{RU}$, where $\mathbf{R}$ is the rotation and $\mathbf{U}$ is the stretch tensor. Since

the rotation $\mathbf{R}$ (that is an orthogonal tensor $\mathbf{R}^{-1} = \mathbf{R}^T$) induces no stress during transformation, we define the right Cauchy-Green tensor such as $\mathbf{C} = \mathbf{U}^2 = \mathbf{R}^{-1}\mathbf{R}^T\mathbf{F}^T\mathbf{F} = \mathbf{F}^T\mathbf{F}$. We also define the relation between the current (Eulerian) magnetic field $\mathbf{b}$ and reference (Lagrangian) one $\mathbf{B}$ via $\mathbf{b} = J^{-1}\mathbf{F}\mathbf{B}$. Using the minimum energy formulation of Dorfmann and Ogden (2003) (but see also Danas and Triantafyllidis (2014), Kankanala and Triantafyllidis (2004)) and neglecting the purely mechanical body (gravity) forces, the potential energy $\mathscr{P}$ of the system may be expressed in terms of the displacement field $\mathbf{u}$ and the magnetic vector potential $\mathbf{A}$ ($\mathbf{B} = \mathbf{Curl}\mathbf{A}$) such that

$$\mathscr{P}(\mathbf{u},\mathbf{A}) = \int_{\Omega_i} \rho_0^i \Phi_i(\mathbf{F},\mathbf{B})\, \mathrm{d}\Omega + \int_{\Re^3} \frac{1}{2\mu_0 J} \|\mathbf{F}\cdot\mathbf{B}\|^2\, \mathrm{d}\Omega - \int_{\partial\Omega_i^t} \mathbf{T}\cdot\mathbf{u}\, \mathrm{dS}, \tag{III.1}$$

for $i =$ film (f), substrate (s). Here, $\|.\|$ denotes the standard Euclidean norm, ρ_0^i is the reference density and Φ_i denotes the Helmholtz free energy of the solids in the reference volume Ω_i. The second term in (III.1) serves to describe the background magnetic (Maxwell) energy in the entire space $\Re^3$ and thus it accounts for all three phases, i.e., film, substrate and air. $\mathbf{T}$ is the mechanical surface traction vector applied at the traction part of the boundary of the reference volume $\partial\Omega_i^t$. It is noted that in order to model the air domain, it suffices to set $\rho_0^{air} = 0$. As a consequence, all subsequent expressions are valid for all phases (i.e., MRE film, substrate and air).

In pure magnetics and in the absence of deformation ($\mathbf{F} = \mathbf{I}$), the current (Eulerian) magnetic field $\mathbf{b}$ is divergence-free ($\nabla\cdot\mathbf{b} = 0$), the current h-field $\mathbf{h}$ is curl-free ($\nabla\times\mathbf{h} = 0$) and the magnetization per unit current volume $\mathbf{m}$ is defined by

$$\mathbf{b} = \mu_0(\mathbf{h}+\mathbf{m}) \quad \text{on } \Omega, \tag{III.2}$$

where μ_0 is the magnetic permeability in vacuum and Ω is the volume in the current configuration. This equation is used to identify one out of the three vector fields, when one vector is used as an independent variable and the other two are constitutively related. The relation between the current $\mathbf{h}$ field and reference one $\mathbf{H}$ is defined via $\mathbf{H} = \mathbf{F}^T\mathbf{h}$, see Dorfmann and Ogden (2003), Kankanala and Triantafyllidis (2008). In finite magnetoelasticity ($\mathbf{F} \neq \mathbf{I}$), this relation is valid in the absence of material or when the material is non-magnetic, see also eq.(III.17). It should be noted that the Eulerian magnetization $\mathbf{m}$ does not need to satisfy any differential constraints or boundary/interface conditions, in contrast to $\mathbf{b}$ (or $\mathbf{B}$) and $\mathbf{h}$ (or $\mathbf{H}$) magnetic fields. The Lagrangian magnetization is defined via a non-unique form $\mathbf{M} = \mathbf{m}/\rho$, see Danas (2017). The magnetization is a field determined by the material occupying a given space. In the present analysis, it is not constitutively related with any magnetic field. In virtue of that, the magnetic field $\mathbf{H}$ (h-field pulled back in Ω_i) is a function of the magnetic induction $\mathbf{B}$ and the deformation $\mathbf{F}$ that serve as independent variables, see eq.(III.17). However, alternative but equivalent formulations exist and later presented in Sections III.2.2 and IV.1.

III.1.1 First variation of the potential energy and force vector

In equation (III.1), $\mathbf{u}$ and $\mathbf{A}$ serve as independent variables with respect to which the potential energy in (III.1) is minimized. This is achieved first by considering the first variation of $\mathscr{P}$ with respect to the independent variables that yields the force vector in the numerical implementations. The stationarity of the first variation of the potential energy (III.1) with respect to the independent variables $\mathbf{u}$ and $\mathbf{A}$ reads

$$\delta\mathscr{P} = \mathscr{P}_{,\mathbf{u}}\,\delta\mathbf{u} + \mathscr{P}_{,\mathbf{A}}\,\delta\mathbf{A} = 0, \tag{III.3}$$

with ',' denoting partial derivation. We note that the magnetic vector potential $\mathbf{A}$ is a continuous admissible vector field defined over $\Re^3$ (while the magnetization vector $\mathbf{M}(\mathbf{X})$ is defined only on the volume Ω_i, $\mathbf{M}(\mathbf{X}) = 0$ for $\mathbf{X} \in \Re^3\backslash\Omega_i$). The admissible displacements $\mathbf{u}(\mathbf{X})$ can also continuously extend over $\Re^3$ without loss of generality, although they make physical sense only within the material volume, $\mathbf{X} \in \Omega_i$. In theory, the deformation in the air is $\mathbf{F}(\mathbf{X}) = \mathbf{I}$, $\mathbf{X} \in \Re^3\backslash\Omega$. Writting the first variation with respect to the deformation gradient tensor $\mathbf{F}$ and the Lagrangian magnetic field $\mathbf{B}$, we obtain the equivalent form

$$\delta\mathscr{P} = \frac{\partial\mathscr{P}}{\partial\mathbf{F}}\frac{\partial\mathbf{F}}{\partial\mathbf{u}}\delta\mathbf{u} + \frac{\partial\mathscr{P}}{\partial\mathbf{B}}\frac{\partial\mathbf{B}}{\partial\mathbf{A}}\delta\mathbf{A} = \mathscr{P}_{,\mathbf{F}}\,\delta\mathbf{F} + \mathscr{P}_{,\mathbf{B}}\,\delta\mathbf{B} = 0, \tag{III.4}$$

with $\mathbf{F}$ and $\mathbf{B}$ serving as independent variables. To be more specific, it is helpful to define the following variations, where $\mathbf{C} = \mathbf{F}^T \cdot \mathbf{F}$ denotes the right Cauchy-Green tensor such that[1]

$$\begin{aligned} &\delta\mathbf{F} = \delta(\mathbf{u}\nabla), \qquad \delta\mathbf{C} = 2\,\mathbf{F}^T \cdot \delta(\mathbf{u}\nabla), \qquad \delta\mathbf{B} = \nabla \times \delta\mathbf{A} \\ &\delta\rho = -\rho\,\mathbf{F}^{-T} : \delta(\mathbf{u}\nabla), \qquad \delta\left(J^{-1}\right) = -J^{-1}\,\mathbf{F}^{-T} : \delta(\mathbf{u}\nabla) = \frac{\delta\rho}{\rho_0}. \end{aligned} \tag{III.5}$$

Then, dropping for simplicity the indexes i referring to material properties and using (III.3) together with (III.5), one gets

$$\begin{aligned} \delta\mathscr{P} = &\int_\Omega \rho_0 \left\{ \frac{\partial\Phi}{\partial\mathbf{F}} : \delta(\mathbf{u}\nabla) + \frac{\partial\Phi}{\partial\mathbf{B}} \cdot (\nabla \times \delta\mathbf{A}) \right\} \mathrm{d}\Omega \\ &+ \int_{\Re^3} \left\{ \frac{\delta\left(J^{-1}\right)}{2\mu_0} (\nabla \times \mathbf{A}) \cdot \mathbf{C} \cdot (\nabla \times \mathbf{A}) + \frac{1}{\mu_0 J} (\nabla \times \mathbf{A}) \cdot \mathbf{C} \cdot (\nabla \times \delta\mathbf{A}) \right. \\ &\left. + \frac{1}{2\mu_0 J} (\nabla \times \mathbf{A}) \cdot \delta\mathbf{C} \cdot (\nabla \times \mathbf{A}) \right\} \mathrm{d}\Omega - \int_{\partial\Omega^t} \mathbf{T} \cdot \delta\mathbf{u}\,\mathrm{d}S, \end{aligned} \tag{III.6}$$

[1] We use the following vector-tensor product notation. For two second-order tensors, $\mathbf{A}$ and $\mathbf{B}$, we define the operations $\mathbf{A} \cdot \mathbf{B} = A_{ik}B_{kj}$, $\mathbf{A} : \mathbf{B} = A_{ij}B_{ji}$. For a second-order tensor $\mathbf{A}$ and a vector $\mathbf{v}$, we denote $\mathbf{A} \cdot \mathbf{v} = A_{ij}v_j$, $\mathbf{v}\mathbf{v} = v_i v_j$ and $\mathbf{v} \cdot \mathbf{v} = v_i v_i$.

which can be rewritten in terms of $\delta\mathbf{F}$ and $\delta\mathbf{B}$ by use of definitions (III.5) as

$$\begin{aligned}\delta\mathscr{P} = &\int_\Omega \rho_0 \left\{ \frac{\partial\Phi}{\partial\mathbf{F}} : \delta\mathbf{F} + \frac{\partial\Phi}{\partial\mathbf{B}} \cdot \delta\mathbf{B} \right\} \mathrm{d}\Omega \\ &+ \int_{\Re^3} \left\{ -\frac{1}{2\mu_0 J} \|\mathbf{F}\cdot\mathbf{B}\|^2 \mathbf{F}^{-T} : \delta\mathbf{F} + \frac{1}{\mu_0 J} (\mathbf{F}\cdot\mathbf{B}) \cdot [\mathbf{F}\cdot(\delta\mathbf{B})] + \frac{1}{\mu_0 J} [(\mathbf{F}\cdot\mathbf{B})\,\mathbf{B}] : \delta\mathbf{F} \right\} \mathrm{d}\Omega \\ &- \int_{\partial\Omega^t} \mathbf{T}\cdot\delta\mathbf{u}\,\mathrm{d}S. \end{aligned} \tag{III.7}$$

The variations $\delta\mathbf{u}$ and $\delta\mathbf{A}$ (or equivalently $\delta\mathbf{F}$ and $\delta\mathbf{B}$ from (III.4)) are arbitrary and thus, $\mathscr{P}_{,\mathbf{u}}\,\delta\mathbf{u} = \mathscr{P}_{,\mathbf{A}}\,\delta\mathbf{A} = 0$. To derive the equilibrium equation and the corresponding tractions, we consider the minimization of $\mathscr{P}$ in (III.7) with respect to the displacement field $\mathbf{u}$

$$\begin{aligned}\mathscr{P}_{,\mathbf{u}}\delta\mathbf{u} = &\int_\Omega \left\{ \rho_0 \frac{\partial\Phi}{\partial\mathbf{F}} : \delta(\mathbf{u}\nabla) \right\} \mathrm{d}\Omega + \int_{\Re^3} \left\{ -\frac{1}{2\mu_0 J} \|\mathbf{F}\cdot\mathbf{B}\|^2 \mathbf{F}^{-T} + \frac{1}{\mu_0 J} (\mathbf{F}\cdot\mathbf{B})\,\mathbf{B} \right\} : \delta(\mathbf{u}\nabla)\,\mathrm{d}\Omega \\ &- \int_{\partial\Omega^t} \mathbf{T}\cdot\delta\mathbf{u}\,\mathrm{d}S = 0. \end{aligned} \tag{III.8}$$

Use of integration of (III.8) by parts for the terms involving $\delta\mathbf{u}\nabla$

$$\begin{aligned}&\int_\Omega \left\{ \left(\rho_0 \frac{\partial\Phi}{\partial\mathbf{F}} - \frac{1}{2\mu_0 J} \|\mathbf{F}\cdot\mathbf{B}\|^2 \mathbf{F}^{-T} + \frac{1}{\mu_0 J} (\mathbf{F}\cdot\mathbf{B})\,\mathbf{B} \right) \delta\mathbf{u} \right\} \cdot \nabla\,\mathrm{d}\Omega \\ &- \int_\Omega \nabla\cdot \left\{ \rho_0 \frac{\partial\Phi}{\partial\mathbf{F}} - \frac{1}{2\mu_0 J} \|\mathbf{F}\cdot\mathbf{B}\|^2 \mathbf{F}^{-T} + \frac{1}{\mu_0 J} (\mathbf{F}\cdot\mathbf{B})\,\mathbf{B} \right\} \delta\mathbf{u}\,\mathrm{d}\Omega \\ &+ \int_{\Re^3\setminus\Omega} \left\{ -\frac{1}{2\mu_0 J} \|\mathbf{F}\cdot\mathbf{B}\|^2 \mathbf{F}^{-T} + \frac{1}{\mu_0 J} (\mathbf{F}\cdot\mathbf{B})\,\mathbf{B} \right\} : \delta(\mathbf{u}\nabla)\,\mathrm{d}\Omega - \int_{\partial\Omega^t} \mathbf{T}\cdot\delta\mathbf{u}\,\mathrm{d}S = 0 \end{aligned} \tag{III.9}$$

and subsequent application of Gauss' divergence theorem on the first term of (III.9) [2] yield the strong form of the equilibrium equation, $\mathrm{Div}\mathbf{S} = \nabla\cdot\mathbf{S} = \mathbf{0}$, in the absence of mechanical body forces. The operator Div is identified with respect to reference position $\mathbf{X}$. The corresponding traction (see page footnote) is

$$\mathbf{T} = \left[\left[\rho_0 \frac{\partial\Phi}{\partial\mathbf{F}} - \frac{1}{2\mu_0 J} \|\mathbf{F}\cdot\mathbf{B}\|^2 \mathbf{F}^{-T} + \frac{1}{\mu_0 J} (\mathbf{F}\cdot\mathbf{B})\,\mathbf{B} \right] \right] \cdot \mathbf{N} \quad (\text{on } \partial\Omega_i^t), \tag{III.10}$$

where $[[\cdot]]$ denotes the jump condition and $\mathbf{N}$ the outward normal to the boundary in the reference configuration. The total first Piola-Kirchoff stress $\mathbf{S}$, such that $\mathbf{T} = [[\mathbf{S}]]\cdot\mathbf{N}$, is given from the combination of (III.9) with Gauss' theorem (footnote) and is in form of indexes i referring to material properties

$$\mathbf{S} = \rho_0^i \frac{\partial\Phi_i}{\partial\mathbf{F}} - \frac{1}{2\mu_0 J} \|\mathbf{F}\cdot\mathbf{B}\|^2 \mathbf{F}^{-T} + \frac{1}{\mu_0 J} \mathbf{B}\,(\mathbf{F}\cdot\mathbf{B}) \quad (\text{on } \Omega_i) \tag{III.11}$$

By use of the relation between the stress in the initial and current configurations, $\boldsymbol{\sigma} = \frac{1}{J}\mathbf{S}\cdot\mathbf{F}^T$, acting

[2] writing $\int_\Omega \left\{ \left(\rho_0 \frac{\partial\Phi}{\partial\mathbf{F}} - \frac{\|\mathbf{F}\cdot\mathbf{B}\|^2}{2\mu_0 J} \mathbf{F}^{-T} + \frac{1}{\mu_0 J} (\mathbf{F}\cdot\mathbf{B})\,\mathbf{B} \right) \delta\mathbf{u} \right\} \cdot \nabla\,\mathrm{d}\Omega = \int_{\partial\Omega^t} \left\{ \rho_0 \frac{\partial\Phi}{\partial\mathbf{F}} - \frac{\|\mathbf{F}\cdot\mathbf{B}\|^2}{2\mu_0 J} \mathbf{F}^{-T} + \frac{1}{\mu_0 J} (\mathbf{F}\cdot\mathbf{B})\,\mathbf{B} \right\} \delta\mathbf{u} \cdot \mathbf{N}\,\mathrm{d}S$

on (III.11), we obtain the total Cauchy stress

$$\boldsymbol{\sigma} = \rho^i \frac{\partial \Phi_i}{\partial \mathbf{F}} : \mathbf{F}^T \underbrace{- \frac{1}{2\mu_0 J^2} \|\mathbf{F}\cdot\mathbf{B}\|^2 + \frac{1}{\mu_0 J}(\mathbf{F}\cdot\mathbf{B})(\mathbf{F}\cdot\mathbf{B})}_{\text{maxwell stress } \boldsymbol{\sigma}^{maxw}} \quad (\text{on } \Omega), \tag{III.12}$$

which satisfies the governing equation $\mathrm{div}\boldsymbol{\sigma} = 0$ at static equilibrium and in the absence of mechanical body forces, as well as the symmetry condition $\boldsymbol{\sigma} = \boldsymbol{\sigma}^T$ due to angular momentum balance. In this expression, div is the divergence operator with respect to current position vector $\mathbf{x}$. The Cauchy-stress includes both mechanical and magnetic contributions and can be decoupled into a solid and a background (Maxwell) counterpart, $\boldsymbol{\sigma}^{maxw}$. It is noted that the Maxwell stress is defined in every material point (solid and air) within $\Re^3$. Thus, in the absence of a material or when the material is non-magnetic, there is still a stress that is induced by the magnetic field.

For the case of a magnetoelastic solid, equation (III.12) must be replaced by the continuity condition $[[\boldsymbol{\sigma}]]\cdot\mathbf{n} = \mathbf{t}$ at an interface, where $\mathbf{n}$ is the Eulerian normal to the interface. The corresponding traction is given by the jump condition for the total Cauchy stress along the solid/air boundary $\mathbf{t} = [\boldsymbol{\sigma}^+ - \boldsymbol{\sigma}^-]\cdot\mathbf{n} = [\boldsymbol{\sigma}^+ - \boldsymbol{\sigma}^{maxw}]\cdot\mathbf{n}$, with $\boldsymbol{\sigma}^+$ the stress within the solid. In the view of (III.12), the traction gets

$$\mathbf{t} = \left\{ \rho^i \left(\frac{\partial \Phi_i^{mec}}{\partial \mathbf{F}} + \frac{\partial \Phi_i^{mag}}{\partial \mathbf{F}} \right) : \mathbf{F}^T \right\} \cdot \mathbf{n} \quad (\text{on } \partial\Omega^t), \tag{III.13}$$

with Φ_i^{mec} the purely mechanical component and Φ_i^{mag} the magnetic component of the material free energy density, $\rho_i\Phi_i = \rho_i\left(\Phi_i^{mec} + \Phi_i^{mag}\right)$ (see discusion in Section III.2). It follows that the energy function fully describes the behavior of the magnetoelastic materials when combined with the Maxwell energy density. To be more specific, the magnetic fields are not only stored within the solid but they extend into the air (or another non-magnetic medium). When a non-magnetic material is within the magnetic field, the magnetic stresses are self-equilibrated and magnetic fields have no effect on the traction, $\mathbf{t} = \rho^i \left(\frac{\partial \Phi_i^{mec}(\mathbf{F})}{\partial \mathbf{F}} : \mathbf{F}^T \right) \cdot \mathbf{n}$. We recall that in pure elasticity, the traction is just the normal component of the total Cauchy stress, $\mathbf{t} = \boldsymbol{\sigma}^{mec}\cdot\mathbf{n}$, since the vacuum induces no stress, $\boldsymbol{\sigma}^{maxw} = 0$. However, when the material is magnetic, the Maxwell stresses (i.e., stresses induced by the magnetic field) affect the mechanical traction measured on the boundary of the specimen. In view of that, the internal stresses equilibrate the external traction and hence, the equilibrium equations.

Use of the vector potential $\mathbf{A}$, such that $\mathbf{B} = \nabla\times\mathbf{A}$, together with the stationarity conditions in (III.3) yield the strong form of the Maxwell field equations

$$\nabla\cdot\mathbf{B} = 0 \quad (\text{on } \Re^3) \tag{III.14}$$

(automatically satisfied) and the Lagrangian magnetic H-field. In view of arbitrariness of $\delta\mathbf{A}$ in

(III.3), we consider from (III.6) and (III.7)

$$\begin{aligned}\mathscr{P}_{,\mathbf{A}}\delta\mathbf{A} &= \int_\Omega \left\{\rho_0\frac{\partial\Phi}{\partial\mathbf{B}}(\nabla\times\delta\mathbf{A})\right\}\mathrm{d}\Omega + \int_{\Re^3}\left\{\frac{1}{\mu_0 J}(\mathbf{F}\cdot\mathbf{B})\cdot\mathbf{F}\,(\nabla\times\delta\mathbf{A})\right\}\mathrm{d}\Omega \\ &= \int_\Omega \left\{\nabla\times\left(\rho_0\frac{\partial\Phi}{\partial\mathbf{B}}+\frac{1}{\mu_0 J}(\mathbf{F}\cdot\mathbf{B})\cdot\mathbf{F}\right)\delta\mathbf{A}\right\}\mathrm{d}\Omega + \int_{\Re^3\setminus\Omega}\left\{\nabla\times\left(\frac{1}{\mu_0 J}(\mathbf{F}\cdot\mathbf{B})\cdot\mathbf{F}\right)\delta\mathbf{A}\right\}\mathrm{d}\Omega = 0.\end{aligned} \tag{III.15}$$

Recalling the relation between the reference and current magnetic field $\mathbf{b} = J^{-1}\mathbf{F}\mathbf{B}$ and the definition of the right Cauchy-Green tensor $\mathbf{C} = \mathbf{F}^T\mathbf{F}$, the vector field appearing in the volume integrals in (III.15) is

$$\rho_0\frac{\partial\Phi}{\partial\mathbf{B}} + \frac{1}{\mu_0}\left(\frac{1}{J}(\nabla\times\mathbf{A})\cdot\mathbf{C}\right) = \rho_0\frac{\partial\Phi}{\partial\mathbf{B}} + \left(\frac{1}{\mu_0}\mathbf{b}\right)\cdot\mathbf{F} = \mathbf{h}\cdot\mathbf{F} = \mathbf{H} \tag{III.16}$$

or else the Lagrangian H-field is

$$\mathbf{H} = \rho_0\frac{\partial\Phi}{\partial\mathbf{B}} + \frac{1}{\mu_0 J}\mathbf{F}^T\cdot(\mathbf{F}\cdot\mathbf{B}) \quad (\text{on } \Re^3), \tag{III.17}$$

and $\mathbf{m} = -\rho_0\dfrac{\partial\Phi_i}{\partial\mathbf{B}} : \mathbf{F}^{-T}$. In view of arbitrariness of the vector field $\mathbf{A}$, one can restate (III.15) in view of (III.17) as the Euler-Lagrange differential equation

$$\nabla\times\mathbf{H} = 0 \quad (\text{on } \Re^3). \tag{III.18}$$

In other words, under quasi-static conditions, the magnetic induction $\mathbf{B}$ and the magnetic field $\mathbf{H}$ satisfy the conservation equations. The corresponding continuity conditions at an interface are given by $[[\mathbf{B}]]\cdot\mathbf{N} = 0$ and $[[\mathbf{H}]]\times\mathbf{N} = 0$, respectively.

III.1.2 Second variation of the potential energy and Jacobian matrix

Similarly, the second variation of the potential energy (III.1), which forms the Jacobian of the numerical system of equations can be written in the form

$$\Delta\delta\mathscr{P} = (\mathscr{P}_{,\mathbf{uu}}\delta\mathbf{u})\Delta\mathbf{u} + (\mathscr{P}_{,\mathbf{Au}}\delta\mathbf{A})\Delta\mathbf{u} + (\mathscr{P}_{,\mathbf{uA}}\delta\mathbf{u})\Delta\mathbf{A} + (\mathscr{P}_{,\mathbf{AA}}\delta\mathbf{A})\Delta\mathbf{A}, \tag{III.19}$$

The second-order variation is evaluated by direct derivation of the potential energy ((III.7) that is equivalent to (III.6)) in the view of (III.4), such that

$$\begin{aligned}\Delta\delta\mathscr{P} = &\left(\frac{\partial^2\mathscr{P}}{\partial \mathrm{F_{kl}}\partial \mathrm{F_{ij}}}\delta \mathrm{F_{ij}} + \frac{\partial^2\mathscr{P}}{\partial \mathrm{F_{kl}}\partial \mathrm{B_i}}\delta \mathrm{B_i}\right)\Delta \mathrm{F_{kl}} \\ &+ \left(\frac{\partial^2\mathscr{P}}{\partial \mathrm{B_k}\partial \mathrm{F_{ij}}}\delta \mathrm{F_{ij}} + \frac{\partial^2\mathscr{P}}{\partial \mathrm{B_k}\partial \mathrm{B_i}}\delta \mathrm{B_i}\right)\Delta \mathrm{B_k},\end{aligned} \tag{III.20}$$

or in matrix notation (and by use of definitions (III.5)) as

$$\Delta\delta\mathscr{P} = \{\Delta\mathbf{F} \quad \Delta\mathbf{B}\} \begin{bmatrix} \dfrac{\partial^2\mathscr{P}}{\partial\mathbf{F}\partial\mathbf{F}} & \dfrac{\partial^2\mathscr{P}}{\partial\mathbf{F}\partial\mathbf{B}} \\ \dfrac{\partial^2\mathscr{P}}{\partial\mathbf{B}\partial\mathbf{F}} & \dfrac{\partial^2\mathscr{P}}{\partial\mathbf{B}\partial\mathbf{B}} \end{bmatrix} \begin{Bmatrix} \delta\mathbf{F} \\ \delta\mathbf{B} \end{Bmatrix}. \tag{III.21}$$

Considering direct derivation of (III.8) and (III.15) with respect to the independent variables $\mathbf{u}$ and $\mathbf{A}$ and recalling that $\delta F_{ij} = \delta u_{i,j}$ and $\frac{\partial F_{ji}^{-1}}{\partial F_{kl}} = -F_{jk}^{-1}\cdot F_{li}^{-1}$ (also note that [3]), the two terms of the $\delta\mathbf{u}$ component get

$$\begin{aligned}\mathscr{P}_{,\mathbf{uu}}\Delta\mathbf{u}\delta\mathbf{u} = \int_\Omega \delta F_{ij}\left\{\rho_0\frac{\partial^2\Phi}{\partial F_{ij}\partial F_{kl}}\right\}\delta F_{kl}\,\mathrm{d}\Omega + \int_{\Re^3}\delta F_{ij}\left\{\frac{1}{2\mu_0 J}\|\mathbf{F}\cdot\mathbf{B}\|^2\left[F_{lk}^{-1}F_{ji}^{-1} - F_{jk}^{-1}F_{li}^{-1}\right]\right. \\ \left. - \frac{1}{\mu_0 J}\left[F_{ks}B_sB_lF_{ji}^{-1} + F_{im}B_mF_{lk}^{-1}B_j - \delta_{ik}B_lB_j\right]\right\}\delta F_{kl}\,\mathrm{d}\Omega\end{aligned} \tag{III.22}$$

and

$$\mathscr{P}_{,\mathbf{Au}}\Delta\mathbf{A}\delta\mathbf{u} = \int_\Omega \delta B_i\left\{\rho_0\frac{\partial^2\Phi}{\partial B_i\partial F_{kl}}\right\}\delta F_{kl}\,\mathrm{d}\Omega + \int_{\Re^3}\delta B_i\left\{\frac{1}{\mu_0 J}\left[-F_{lk}^{-1}C_{ip}B_p + B_lF_{ki} + F_{kp}B_p\delta_{il}\right]\right\}\delta F_{kl}\,\mathrm{d}\Omega, \tag{III.23}$$

while the two terms of the $\delta\mathbf{A}$ component are

$$\mathscr{P}_{,\mathbf{AA}}\Delta\mathbf{A}\delta\mathbf{A} = \int_\Omega \delta B_i\left\{\rho_0\frac{\partial^2\Phi}{\partial B_i\partial B_k}\right\}\delta B_k\,\mathrm{d}\Omega + \int_{\Re^3}\delta B_i\left\{\frac{1}{\mu_0 J}F_{rk}F_{ri}\right\}\delta B_k\,\mathrm{d}\Omega \tag{III.24}$$

and

$$\mathscr{P}_{,\mathbf{uA}}\Delta\mathbf{u}\delta\mathbf{A} = \int_\Omega \delta F_{ij}\left\{\rho_0\frac{\partial^2\Phi}{\partial F_{ij}\partial B_k}\right\}\delta B_k\,\mathrm{d}\Omega + \int_{\Re^3}\delta F_{ij}\left\{\frac{1}{\mu_0 J}\left[-C_{kq}B_qF_{ji}^{-1} + F_{ik}B_j + F_{im}B_m\delta_{jk}\right]\right\}\delta B_k\,\mathrm{d}\Omega. \tag{III.25}$$

It is straightforward in view of (III.23) and (III.25) that $\mathscr{P}_{,\mathbf{uA}} = \mathscr{P}_{,\mathbf{Au}}$.

III.2 Material selection: magnetoelastic energy density functions for MREs

To restate the problem for connection with the previous sections, we are interested in a system of a magnetoelastic film/substrate block surrounded by air. At the boundaries of the air, i.e., far away from the solid, a Eulerian magnetic field $\mathbf{b}$ is applied. Each constituent layer material can be either purely elastic or magnetoelastic. For the latter case, the material at hand is a two-phase composite, consisting of ferromagnetic particles in a magnetically insensitive and hyperelastic

[3] $\frac{\partial(F_{ws}B_sF_{wq}B_q)}{\partial F_{kl}} = \delta_{wk}\delta_{sl}B_sF_{wq}B_q + F_{ws}B_s\delta_{wk}\delta_{ql}B_q = \delta_{wk}B_lF_{wq}B_q + F_{ws}\delta_{kw}B_sB_l = 2F_{ks}B_sB_l$
and $\frac{\partial(F_{ws}B_sF_{wq}B_q)}{\partial B_k} = F_{ws}\delta_{sk}F_{wq}B_q + F_{ws}B_sF_{wq}\delta_{qk} = 2F_{ws}F_{kw}B_s = 2C_{kq}B_q$

matrix. The particles are considered mechanically stiff but magnetically soft. Instead of making use of homogenization, the approach followed is phenomenological accounting for both the magnetic field effects and the finite strains. The constitutive behavior of the materials is defined by an energy density function, or potential, W_i ($i =$ film, substrate), which is taken to be a function of the deformation gradient tensor $\mathbf{F}$ and the Lagrangian magnetic field $\mathbf{B}$

$$W_i(\mathbf{F},\mathbf{B}) = \rho_0^i \Phi_i(\mathbf{F},\mathbf{B}) + \frac{1}{2\mu_0 J}(\mathbf{FB})\cdot(\mathbf{FB}) \quad \text{in } \Omega_i. \tag{III.26}$$

As equation (III.26) implies, we make use of a "decoupling" approximation, splitting the magnetoelastic energy into a material component $\rho_0^i \Phi_i$, together with a magnetostatic component evaluated in the undeformed configuration. In turn, the Helmoltz free-energy $\Phi_i(\mathbf{F},\mathbf{B})$ reads

$$\Phi_i(\mathbf{F},\mathbf{B}) = \Phi_i^{mec}(\mathbf{F}) + \Phi_i^{mag}(\mathbf{F},\mathbf{B}), \tag{III.27}$$

where $\Phi_i^{mec}(\mathbf{F})$ the purely mechanical component and $\Phi_i^{mag}(\mathbf{F},\mathbf{B})$ the coupled magnetoelastic component, denoting stored-energy functions for the (magnetic) elastomer i in the absence and presence of a magnetic field, respectively. Without loss of generality, this free-energy function can be extended to vacuum, recalling that $\rho_0^{air} = 0$. Assuming no dissipative effects under fixed temperature, i.e., there is no strain or magnetization hysteresis, we recall from Section III.1.1 that the constitutive response of the (magneto)elastic material i is defined by the energy-density function W_i, such that the first Piola-Kirchhoff stress $\mathbf{S}$ and the Lagrangian magnetic field $\mathbf{H}$ in material are respectively given by (see in Section III.1.1, eq.(III.11) and (III.17))

$$\mathbf{S} = \frac{\partial W_i(\mathbf{F},\mathbf{B})}{\partial \mathbf{F}} = \rho_0^i \frac{\partial \Phi_i}{\partial \mathbf{F}} - \frac{1}{2\mu_0 J}\|\mathbf{F}\cdot\mathbf{B}\|^2 \mathbf{F}^{-T} + \frac{1}{\mu_0 J}\mathbf{B}(\mathbf{F}\cdot\mathbf{B}) \quad (\text{in } \Omega_i) \tag{III.28}$$

and

$$\mathbf{H} = \frac{\partial W_i(\mathbf{F},\mathbf{B})}{\partial \mathbf{B}} = \rho_0^i \frac{\partial \Phi_i}{\partial \mathbf{B}} + \frac{1}{\mu_0 J}\mathbf{F}^T\cdot(\mathbf{F}\cdot\mathbf{B}) \quad (\text{in } \Omega_i). \tag{III.29}$$

III.2.1 F-B formulation

After a push-forward to the current configuration and recalling the relation between the applied Eulerian $\mathbf{b}$ and the Lagrangian $\mathbf{B}$ magnetic field, $\mathbf{b} = \frac{1}{J}\mathbf{F}\cdot\mathbf{B}$, as well as the mass conservation equation, $\rho_0 = \rho J$, the free-energy (III.26) in view of (III.27) can be written as

$$w_i(\mathbf{F},\mathbf{b}) = \rho^i \phi_i^{mec}(\mathbf{F}) + \frac{1}{2\mu_0}\mathbf{b}\cdot\mathbf{b} + \rho^i \phi_i^{mag}(\mathbf{F},\mathbf{b}) \quad (\text{in } \Omega), \tag{III.30}$$

where the first term describes a purely mechanical contribution in the absence of magnetic field and the sum of the two last terms describe the magnetoelastic contribution to the total energy. From (III.26), (III.30) and the previous definitions, it is straightforward to state that

$$w_i(\mathbf{F},\mathbf{b}) = \frac{W_i(\mathbf{F}, J\mathbf{F}^{-1}\mathbf{b})}{J}, \tag{III.31}$$

where w_i the energy-density in the current configuration, or else for the magnetic Helmoltz-free energy in the reference Φ^{mag} and current ϕ^{mag} configuration respectively

$$\phi_i^{mag}(\mathbf{F},\mathbf{b}) = \Phi_i^{mag}(\mathbf{F},\mathbf{B}) = \Phi_i^{mag}(\mathbf{F},J\mathbf{F}^{-1}\mathbf{b}). \tag{III.32}$$

Now, mathematical expressions should be assigned to the magnetic and mechanical components of the energy functions, so as to form a derivable total potential and to solve for the unknowns (admissible displacement field $\mathbf{u}$ and magnetic vector potential $\mathbf{A}$) of the problem in the pre- and post-bifurcation, as discussed in Sections III.1.1 and III.1.2. To begin with, we consider the film and/or the substrate to be magnetically isotropic but nonlinear. Thus, we make use of a Langevin function to phenomenologically describe the magnetic behavior of the magnetically sensitive elastomers, based on macroscopically measured properties. Although other models could be used (e.g., see Danas, 2017), the Langevin model should be adequate to approximately describe a magnetic behavior that exhibits saturation but no hysteresis in magnetization, such that of magnetically soft iron (e.g., see Galipeau and Ponte Castañeda, 2012). The model accounts for the initial (linear) susceptibility χ^i and saturation magnetization $\mu_0 m_s^i$ of the material i, so that the isotropic magnetic energy in the current configuration is given by

$$\rho^i \phi_i^{mag}(\mathbf{b}) = \frac{\mu_0 (m_s^i)^2}{3\chi^i}\left[\ln\left(\frac{3\chi^i\|\mathbf{b}\|}{\mu_0 m_s^i}\right) - \ln\left(\sinh\left(\frac{3\chi^i\|\mathbf{b}\|}{\mu_0 m_s^i}\right)\right)\right] \quad (\text{in } \Omega), \tag{III.33}$$

where μ_0 the magnetic permeability in vacuum and $\|\mathbf{b}\| = \sqrt{\mathbf{b}\cdot\mathbf{b}} = J^{-1}\sqrt{(\mathbf{F}\cdot\mathbf{B})\cdot(\mathbf{F}\cdot\mathbf{B})}$ the standard Euclidean norm of the Eulerian magnetic field, so that the magnetic function is independent of the deformation of the elastomer, $\phi_i^{mag}(\mathbf{F},\mathbf{b}) = \phi_i^{mag}(\mathbf{b})$. After a pull-back to the reference configuration and in view of mass conservation $\rho_0 = \rho J$, the Langevin fuction gives the magnetoelastic contribution to the coupled energy

$$\rho_0^i \Phi_i^{mag}(\mathbf{F},\mathbf{B}) = \frac{J\mu_0 (m_s^i)^2}{3\chi^i}\left[\ln\left(\frac{3\chi^i\|\mathbf{b}\|}{\mu_0 m_s^i}\right) - \ln\left(\sinh\left(\frac{3\chi^i\|\mathbf{b}\|}{\mu_0 m_s^i}\right)\right)\right] \quad (\text{in } \Omega_i). \tag{III.34}$$

For the case of nearly-incompressible elastomers, this magnetomechanical coupling denoted by ($J = \det\mathbf{F}, b = \|\mathbf{b}\|$) is very small. This could be a possible drawback of the model when characterizing MREs with strong coupling. After all, the energy approximation (as the sum of a purely mechanical and a magnetoelastic contribution to the energy) exploits the fact that the magnetic energy of the composite depends only on the applied magnetic field and not on the deformation of the material.[4] In the limit of small magnetic fields $\mathbf{B} \to 0$, the defined energy-density (III.33) becomes quadratic in $\mathbf{B}$ (or $\mathbf{b}$), such that

$$\rho_0^i \Phi_i^{mag}(\mathbf{F},\mathbf{B}) = -\frac{\chi^i}{2\mu_0 J}\mathbf{F}\mathbf{B}\cdot\mathbf{F}\mathbf{B} = -\frac{J\chi^i}{2\mu_0}\mathbf{b}\cdot\mathbf{b} = \rho_0^i \phi_i^{mag}(\mathbf{F},\mathbf{b}). \tag{III.35}$$

This last expression of actual linearization of (III.33) outlines the behavior of an ideal material

[4] Considering an elastomeric but passive material, we note that the mechanical component is independent of $\mathbf{B}$ and the magnetostatic energy is self-equilibrated, just as it is in vacuum $W_i(\mathbf{F},\mathbf{B}) = \rho_0^i \Phi_i^{mec}(\mathbf{F}) + \frac{1}{2\mu_0 J}(\mathbf{F}\mathbf{B})\cdot(\mathbf{F}\mathbf{B})$ in Ω_i and $w_i(\mathbf{F},\mathbf{b}) = \rho^i \Phi_i^{mec}(\mathbf{F}) + \frac{\mathbf{b}\mathbf{b}}{2\mu_0}$ in Ω

with no saturation. For the definition of the mechanical component of the energy, a constitutive law for hyperelastic isotropic materials should be a fair approximations for MREs, upon comparison with experimental measurements in large deformations. In the present study, it suffices to propose a neo-Hookean law as discussed in Section II.5 such that

$$\rho_0^i \Phi_i^{mec}(\mathbf{F}) = \frac{G^i}{2}\left(\mathbf{F}^T : \mathbf{F} - 3 - 2\ln J\right) + \frac{G'^i}{2}(J-1)^2, \tag{III.36}$$

where G_i is the shear modulus and $G_i'(=100G_i)$ the second Lamé compressibility constant. As discussed in Section II.5.2, the use of a simple neo-Hookean mechanical response for the MRE material constitutes a fair approximation, which accurately probes the experimental post-bifurcation amplitudes for the entire range of the loading states considered in this study. In turn, a non-magnetic substrate leads to the vanishing of the last term in (III.27) and thus, is simply described by the purely mechanical neo-Hookean model. The nearly incompressible response of the film/substrate system imply an out-of-plane deformation $\lambda_2 \simeq 1/\lambda_0$, in accordance with the experimental measurements. This is satisfied via a large Lamé compressibility constant in the above-described constitutive laws of the solids.

III.2.2 From F-B to F-M formulation

In this section, we show that working with the continuum framework of the deformation gradient tensor $\mathbf{F}$ and the Lagrangian magnetic field $\mathbf{B}$ as independent variables of the potential energy is equivalent to working with the deformation gradient tensor $\mathbf{F}$ and the Lagrangian magnetization $\mathbf{M}$ as an alternative set of independent variables. From Section III.2, we recall that the energy-density functions used to describe the magnetoelastic response of the materials, considering both the magnetic field effects and the finite strains in the reference and current configuration, are equivalent such that

$$\begin{aligned} W_i(\mathbf{F},\mathbf{B}) &= \rho_0^i \Phi_i(\mathbf{F},\mathbf{B}) + \frac{1}{2\mu_0 J}(\mathbf{FB})\cdot(\mathbf{FB}) \\ &= \rho_0^i \Phi_i(\mathbf{F}, J\mathbf{F}^{-1}\mathbf{b}) + \frac{J}{2\mu_0}\mathbf{b}\cdot\mathbf{b} \\ &= J\left(\rho^i \phi_i(\mathbf{F},\mathbf{b}) + \frac{1}{2\mu_0}\mathbf{b}\cdot\mathbf{b}\right) = J w_i(\mathbf{F},\mathbf{b}). \end{aligned} \tag{III.37}$$

By use of the partial Legendre-Fenchel transform on the augmented variational formulation with respect to $\mathbf{H}$, reading[5] for a function $W_i(\mathbf{F},\mathbf{B}) : \mathbb{R}^3 \to [0,+\infty)$ with $\mathbf{H}(\mathbf{B}) = \frac{\partial W_i(\mathbf{F},\mathbf{B})}{\partial \mathbf{B}}$ (see eq.(III.29)) that $\mathbf{B} = \mathbf{H}^{-1}(\mathbf{H}(\mathbf{B})) = \frac{\partial \hat{W}_i(\mathbf{F},\mathbf{H})}{\partial \mathbf{H}}$, we obtain

$$\begin{aligned} W_i(\mathbf{F},\mathbf{B}) &= \mathbf{H}\cdot\mathbf{B} - \hat{W}_i(\mathbf{F},\mathbf{H}) \\ &= J\mathbf{b}\cdot\mathbf{h} - \hat{W}_i(\mathbf{F},\mathbf{h}), \end{aligned} \tag{III.38}$$

[5] Let's consider a convex function $f(x) : A \to \mathbb{R}$, with $p(x) = \frac{df(x)}{dx}$ such that $p(x) : 1-1$ (*i.e.*, $\frac{d^2 f}{dx^2} \neq 0$). Then, $x(p) = p^{-1}(p(x)) = \frac{dg(p)}{dp}$ and $\frac{dx}{dp} = \frac{d^2 g}{dp^2} \neq 0$. The Legendre transformation of $f(x)$ and $g(p)$ read $g(p) = px - f(x)$ and $f(x) = px - g(p)$ respectively, with $x = f(p)$.

in view of $\mathbf{H}=\mathbf{F}\cdot\mathbf{h}$ (see eq.(III.15)) and $\mathbf{b}=J^{-1}\mathbf{F}\cdot\mathbf{B}$, which are the relations between the reference and current magnetic h- and b-field, respectively. Next, we write the total potential $\hat{W}_i(\mathbf{F},\mathbf{h})$ by use of a partial decoupling approach, defined as the sum of the material-volume stored energy and the free-space energy component (Kankanala and Triantafyllidis, 2008), such as

$$\hat{W}_i(\mathbf{F},\mathbf{h})=\rho_0^i\hat{\phi}_i(\mathbf{F},\mathbf{h})+\frac{J\mu_0}{2}\mathbf{h}\cdot\mathbf{h}. \tag{III.39}$$

The energy function $\hat{\phi}_i(\mathbf{F},\mathbf{h})$ can be subsequently defined by use of inversion with respect to $\mathbf{m}$ such that

$$\rho_0^i\hat{\phi}_i(\mathbf{F},\mathbf{h})=J\mu_0\mathbf{m}\cdot\mathbf{h}-\rho_0^i\check{\phi}_i(\mathbf{F},\mathbf{m}). \tag{III.40}$$

The total potential $W(\mathbf{F},\mathbf{B})$ in (III.37) can be then written with combination of (III.38), (III.39), (III.40) and the relation $\mathbf{b}=\mu_0(\mathbf{h}+\mathbf{m})$ as

$$\begin{aligned}W_i(\mathbf{F},\mathbf{B})&=\rho_0^i\check{\phi}_i(\mathbf{F},\mathbf{m})-J\mu_0\mathbf{m}\cdot\mathbf{h}-\frac{J\mu_0}{2}\mathbf{h}\cdot\mathbf{h}+J\mathbf{b}\cdot\mathbf{h}\\&=\rho_0^i\check{\phi}_i(\mathbf{F},\mathbf{m})-J\mu_0\mathbf{m}\cdot\mathbf{h}-\frac{J\mu_0}{2}\mathbf{h}\cdot\mathbf{h}+J\mu_0\mathbf{m}\cdot\mathbf{h}+J\mu_0\mathbf{h}\cdot\mathbf{h}\\&=\rho_0^i\check{\phi}_i(\mathbf{F},\mathbf{m})+\frac{J\mu_0}{2}\mathbf{h}\cdot\mathbf{h}=\check{W}(\mathbf{F},\mathbf{m},\mathbf{h}).\end{aligned} \tag{III.41}$$

Combining (III.37) and (III.40), the material potential $\check{\phi}_i(\mathbf{F},\mathbf{m})$ is written as

$$\rho_0^i\check{\phi}_i(\mathbf{F},\mathbf{m})=\rho_0^i\phi_i(\mathbf{F},\mathbf{b})+\frac{J}{2\mu_0}\mathbf{b}\cdot\mathbf{b}-\frac{J\mu_0}{2}\mathbf{h}\cdot\mathbf{h}. \tag{III.42}$$

We recall from (III.5) that the relation between the magnetization in the reference and current configuration is defined by $\mathbf{m}=\rho\mathbf{M}$ and thus, the energy-density with respect to $\mathbf{M}$ can be written in view of (III.37) and (III.32) as

$$\rho_0^i\check{\Phi}_i(\mathbf{F},\mathbf{M})=\rho_0^i\check{\Phi}_i(\mathbf{F},\frac{\mathbf{m}}{\rho})=\rho_0^i\phi_i(\mathbf{F},\mathbf{b}^*)+\frac{J}{2\mu_0}\mathbf{b}^*\cdot\mathbf{b}^*-\frac{J\mu_0}{2}\mathbf{h}^*\cdot\mathbf{h}^*, \tag{III.43}$$

with $\mathbf{b}^*=\mathbf{b}(\frac{\mathbf{m}}{\rho})$ and $\mathbf{h}^*=\mathbf{h}(\frac{\mathbf{m}}{\rho})$.

A simple example of energy conversion from $W(\mathbf{F},\mathbf{B})$ to $\check{W}(\mathbf{F},\mathbf{m},\mathbf{h})$ will be now given, as illustrated in Danas (2017). To avoid complexity in derivations, we will work with linearized energies that correspond to ideal materials, i.e., no saturation. This conversion in the space of independent variables will be subsequently used in Chapter IV for comparison between magnetoelastic variational frameworks, used in the bifurcation analysis of film/substrate systems (e.g., see Danas and Triantafyllidis, 2014, Dorfmann and Ogden, 2003). So, in the limit of small magnetic fields, $\mathbf{B}\to 0$, the defined magnetoelastic energy becomes quadratic in $\mathbf{B}$ or $\mathbf{b}$, such that

$$\rho_0^i\Phi_i^{mag}(\mathbf{F},\mathbf{B})=-\frac{\chi^i}{2\mu_0 J}\mathbf{F}\,\mathbf{B}\cdot\mathbf{F}\,\mathbf{B}=-\frac{J\chi^i}{2\mu_0}\mathbf{b}\cdot\mathbf{b}=\rho_0^i\phi_i^{mag}(\mathbf{F},\mathbf{b}). \tag{III.44}$$

We recall from (III.35) that this expression is the zero order term of Taylor expansion series about $\mathbf{B}$ of the Langevin magnetoelastic energy, which is non-linear in $I_5=(\mathbf{FB})\cdot(\mathbf{FB})$, as seen in (III.34). Simirarly, the eq.(III.44) can be obtained by the first derivative of the energy with respect to I_5

(see (IV.10) for the definition of invariants). In view of the energy decoupling $\phi_i(\mathbf{F},\mathbf{b}) = \phi_i^{mec}(\mathbf{F}) + \phi_i^{mag}(\mathbf{F},\mathbf{b})$, the magnetization is subsequently defined by derivation of (III.44) as[6]

$$\mathbf{m} = -\frac{\rho_0}{J}\frac{\partial \phi}{\partial \mathbf{b}} = -\frac{\rho_0}{J}\frac{\partial \phi^{mag}}{\partial \mathbf{b}} = -\frac{\rho_0}{J}\frac{\partial \phi^{mag}}{\partial \mathbf{B}} : \mathbf{F}^{-T}, \tag{III.45}$$

which yields from (III.44) in combination with the relation $\mathbf{b} = \mu_0(\mathbf{h}+\mathbf{m})$ (see Section III.1)

$$\mathbf{b} = \frac{\mu_0}{\chi^i}\mathbf{m} \quad \text{or} \quad \mathbf{h} = \frac{1-\chi^{\mathrm{i}}}{\chi^{\mathrm{i}}}\mathbf{m}, \quad \chi^{\mathrm{i}} > 0. \tag{III.46}$$

Substituting the above expressions in (III.42) in combination with (III.44) gives

$$\begin{aligned}
\rho_0^i \check{\phi}_i(\mathbf{F},\mathbf{m}) &= \rho_0^i \phi_i^{mec}(\mathbf{F}) + \frac{J\mu_0(1-\chi^i)}{2\chi^i}\mathbf{m}\cdot\mathbf{m} \\
&= \rho_0^i \phi_i^{mec}(\mathbf{F}) + \frac{J(\rho^i)^2\mu_0(1-\chi^i)}{2\chi^i}\mathbf{M}\cdot\mathbf{M} \\
&= \rho_0^i \phi_i^{mec}(\mathbf{F}) + \frac{(\rho_0^i)^2\mu_0(1-\chi^i)}{2J\chi^i}\mathbf{M}\cdot\mathbf{M}.
\end{aligned} \tag{III.47}$$

For test purposes presented in Chapter IV, we use the neo-Hookean model for the mechanical component of the energy function writing the potential in $\mathbf{F}-\mathbf{M}$

$$\rho_0^i \Phi_i(\mathbf{F},\mathbf{M}) = \frac{G^i}{2}\left(\mathbf{F}^T:\mathbf{F}-3-2\ln J\right) + \frac{G'^i}{2}(J-1)^2 + \frac{(\rho_0^i)^2\,\mu_0(1-\chi^i)}{2J\chi^i}\mathbf{M}\cdot\mathbf{M} \tag{III.48}$$

versus the augmented potential in $\mathbf{F}-\mathbf{B}$

$$\rho_0^i \Phi_i(\mathbf{F},\mathbf{B}) = \frac{G^i}{2}\left(\mathbf{F}^T:\mathbf{F}-3-2\ln J\right) + \frac{G'^i}{2}(J-1)^2 - \frac{\chi^i}{2\mu_0 J}(\mathbf{F}\,\mathbf{B})\cdot(\mathbf{F}\,\mathbf{B}), \tag{III.49}$$

which will be used with the subsequent material parameters corresponding to soft Ecoflex silicones as presented in Table III.1.

	$\rho_0(\mathrm{g}\cdot\mathrm{cm}^{-3})$	G (kPa)	χ	$\mu_0 m_s$ (T)	μ_0 ($\mu\mathrm{N}\cdot\mathrm{A}^{-2}$)
Film	1.1	10	0.4	0	$4\pi 10^{-1}$
Substrate	1.07	3	0	0	$4\pi 10^{-1}$

Table III.1: Material properties of the film/substrate system in experimental, numerical and theoretical analysis.

[6] Note that $\frac{\partial \phi^{mag}}{\partial \mathrm{B_i}} < 0$, so as $\mathrm{m_i} > 0$, ($i = 1,2$ in plane-strain problems).

III.3 Finite element discretization in two-dimensions

One can discretize the above equations by discretizing the total volume Ω in N_e discrete finite elements (and N_n nodes) by

$$\Omega = \sum_{I=1}^{N_e} \Omega_e^I, \tag{III.50}$$

with Ω_e^I denoting the volume of each element. Then, the element vector of unknowns $\delta\mathbf{q}_e$ is given readily by

$$\delta\mathbf{q}_e = \{\delta\mathbf{u}, \delta\mathbf{A}\}. \tag{III.51}$$

Next, we define (in a general fashion) the discretized form of the unknown variables, i.e., $\mathbf{u}$ and $\mathbf{A}$, using standard notation

$$\delta\mathbf{u} = \mathbf{N}_u \cdot \delta\mathbf{q}_e, \qquad \delta\mathbf{A} = \mathbf{N}_\alpha \cdot \delta\mathbf{q}_e, \tag{III.52}$$

where $\mathbf{N}_{q_e}$ are the matrices associated with the element shape functions. In order to compute the gradients, one has

$$\delta(\mathbf{u}\nabla) = \mathbf{G}_u \cdot \delta\mathbf{q}_e, \qquad \nabla \times \delta\mathbf{A} = \mathbf{G}_\alpha \cdot \delta\mathbf{q}_e, \tag{III.53}$$

with $\mathbf{G}_{q_e}$ denoting the gradient of the $\mathbf{N}_{q_e}$ matrices. This allows for the definition of the element force vector $\mathbf{f}_e$ conjugate to the element vector of unknowns $\delta\mathbf{q}_e$ and it is given readily by

$$\mathbf{f}_e \cdot \delta\mathbf{q}_e = \int_{\Omega_e} \delta\mathscr{P}\, \mathrm{d}\Omega = \left[\int_{\Omega_e} \left\{ \frac{\partial\mathscr{P}}{\partial\mathbf{F}} : \mathbf{G}_u + \frac{\partial\mathscr{P}}{\partial\mathbf{B}} \cdot \mathbf{G}_\alpha \right\} \mathrm{d}\Omega\right] \cdot \delta\mathbf{q}_e. \tag{III.54}$$

Gathering the variations with respect to $\delta\mathbf{F}$ and $\delta\mathbf{B}$, one obtains the following quantities in index notation

$$\begin{aligned} \frac{\partial\mathscr{P}}{\partial F_{ij}} &= \rho_0 \frac{\partial\Phi}{\partial F_{ij}} - \frac{1}{2\mu_0 J} \|\mathbf{F}\cdot\mathbf{B}\|^2 F_{ji}^{-1} + \frac{1}{\mu_0 J} F_{im} B_m B_j \quad (\text{in } \Re^3), \\ \frac{\partial\mathscr{P}}{\partial B_i} &= \rho_0 \frac{\partial\Phi}{\partial B_i} + \frac{1}{\mu_0 J} F_{rp} B_p F_{ri} \quad (\text{in } \Re^3), \end{aligned} \tag{III.55}$$

where,

$$\frac{\partial\Phi}{\partial F_{ij}} = \sum_{P=1}^{n_{inv}} \frac{\partial\Phi}{\partial I_P} \frac{\partial I_P}{\partial F_{ij}} \tag{III.56}$$

$$\frac{\partial\Phi}{\partial B_i} = \sum_{P=1}^{n_{inv}} \frac{\partial\Phi}{\partial I_P} \frac{\partial I_P}{\partial B_i}. \tag{III.57}$$

Similarly, the element stiffness matrix $\mathbf{k}_e$ is defined by

$$\Delta\mathbf{q}_e\cdot\mathbf{k}_e\cdot\delta\mathbf{q}_e=\int_{\Omega_e}\Delta\delta\mathscr{P}\,\mathrm{d}\Omega=\Delta\mathbf{q}_e\cdot\left\{\int_{\Omega_e}\begin{bmatrix}\mathbf{G}_u^T & \mathbf{G}_\alpha^T\end{bmatrix}\begin{bmatrix}\dfrac{\partial^2\mathscr{P}}{\partial\mathbf{F}\partial\mathbf{F}} & \dfrac{\partial^2\mathscr{P}}{\partial\mathbf{F}\partial\mathbf{B}}\\[2ex] \dfrac{\partial^2\mathscr{P}}{\partial\mathbf{B}\partial\mathbf{F}} & \dfrac{\partial^2\mathscr{P}}{\partial\mathbf{B}\partial\mathbf{B}}\end{bmatrix}\begin{bmatrix}\mathbf{G}_u\\[2ex]\mathbf{G}_\alpha\end{bmatrix}\mathrm{d}\Omega\right\}\cdot\delta\mathbf{q}_e. \tag{III.58}$$

The second-order derivatives are evaluated by direct derivation of the potential energy (III.1), such that

$$\begin{aligned}\frac{\partial^2\mathscr{P}}{\partial F_{ij}\partial F_{kl}}=&\rho_0\frac{\partial^2\Phi}{\partial F_{ij}\partial F_{kl}}+\frac{1}{2\mu_0 J}\|\mathbf{F}\cdot\mathbf{B}\|^2\left[F^{-1}_{lk}F^{-1}_{ji}-F^{-1}_{jk}F^{-1}_{li}\right]\\&-\frac{1}{\mu_0 J}\left[F_{ks}B_sB_lF^{-1}_{ji}+F_{in}B_nF^{-1}_{lk}B_j-\delta_{ik}B_lB_j\right]\quad(\text{in }\Re^3),\end{aligned} \tag{III.59}$$

and

$$\frac{\partial^2\mathscr{P}}{\partial F_{ij}\partial B_k}=\rho_0\frac{\partial^2\Phi}{\partial F_{ij}\partial B_k}+\frac{1}{\mu_0 J}\left[F_{ik}B_j+F_{in}B_n\delta_{jk}-C_{kr}B_rF^{-1}_{ji}\right]\quad(\text{in }\Re^3), \tag{III.60}$$

and

$$\frac{\partial^2\mathscr{P}}{\partial B_i\partial B_j}=\rho_0\frac{\partial^2\Phi}{\partial B_i\partial B_j}+\frac{1}{\mu_0 J}C_{ij}\quad(\text{in }\Re^3). \tag{III.61}$$

The above equations will also need the evaluation of

$$\frac{\partial^2\Phi}{\partial F_{ij}\partial F_{kl}}=\sum_{P=1}^{n_{inv}}\sum_{Q=1}^{n_{inv}}\frac{\partial^2\Phi}{\partial I_P\partial I_Q}\frac{\partial I_P}{\partial F_{ij}}\frac{\partial I_Q}{\partial F_{kl}}+\sum_{P=1}^{n_{inv}}\frac{\partial\Phi}{\partial I_P}\frac{\partial^2 I_P}{\partial F_{ij}\partial F_{kl}}, \tag{III.62}$$

$$\frac{\partial^2\Phi}{\partial F_{ij}\partial B_k}=\sum_{P=1}^{n_{inv}}\sum_{Q=1}^{n_{inv}}\frac{\partial^2\Phi}{\partial I_P\partial I_Q}\frac{\partial I_P}{\partial F_{ij}}\frac{\partial I_Q}{\partial B_k}+\sum_{P=1}^{n_{inv}}\frac{\partial\Phi}{\partial I_P}\frac{\partial^2 I_P}{\partial F_{ij}\partial B_k}, \tag{III.63}$$

$$\frac{\partial^2\Phi}{\partial B_i\partial B_j}=\sum_{P=1}^{n_{inv}}\sum_{Q=1}^{n_{inv}}\frac{\partial^2\Phi}{\partial I_P\partial I_Q}\frac{\partial I_P}{\partial B_i}\frac{\partial I_Q}{\partial B_j}+\sum_{P=1}^{n_{inv}}\frac{\partial\Phi}{\partial I_P}\frac{\partial^2 I_P}{\partial B_i\partial B_j}. \tag{III.64}$$

The invariants I_p $(p=1,..,6)$ of the problem are defined such as

$$I_1=C_{ii}=F_{ki}F_{kj},\qquad I_2=\frac{1}{2}\left[C^2_{rr}-C_{ik}C_{ki}\right],\qquad J=I_3=\det\mathbf{F}, \tag{III.65}$$

$$I_4=B_iB_i,\qquad I_5=B_iC_{ij}B_j,\qquad I_6=B_iC_{ik}C_{kj}B_j. \tag{III.66}$$

We write the force vector and stiffness matrix in index notation and we define the local-to-global coordinate transformation by the Jacobian matrix, denoted as $[\mathscr{J}]=\partial X_i/\partial\xi_j=\sum_{I=1}^{N_n}(\partial N_I/\partial\xi_j)X_i^I$, $i=$

1,2, pertinent to the shape functions N. Subsequently, we evaluate the quantities $\mathbf{u}\nabla$ and $\nabla\times\mathbf{A}$ by

$$\underbrace{\begin{bmatrix} \partial u_1/\partial X_1 \\ \partial u_1/\partial X_2 \\ \partial u_2/\partial X_1 \\ \partial u_2/\partial X_2 \\ \partial A_3/\partial X_2 \\ -\partial A_3/\partial X_1 \end{bmatrix}}_{[\mathbf{dqdx}]} = \underbrace{\begin{bmatrix} \mathscr{J}_{11}^{-1} & \mathscr{J}_{12}^{-1} & 0 & 0 & 0 & 0 \\ \mathscr{J}_{21}^{-1} & \mathscr{J}_{22}^{-1} & 0 & 0 & 0 & 0 \\ 0 & 0 & \mathscr{J}_{11}^{-1} & \mathscr{J}_{12}^{-1} & 0 & 0 \\ 0 & 0 & \mathscr{J}_{21}^{-1} & \mathscr{J}_{22}^{-1} & 0 & 0 \\ 0 & 0 & 0 & 0 & \mathscr{J}_{21}^{-1} & \mathscr{J}_{22}^{-1} \\ 0 & 0 & 0 & 0 & -\mathscr{J}_{11}^{-1} & -\mathscr{J}_{12}^{-1} \end{bmatrix}}_{[\mathbf{JI}]} \underbrace{\begin{bmatrix} \partial u_1/\partial \xi_1 \\ \partial u_1/\partial \xi_2 \\ \partial u_2/\partial \xi_1 \\ \partial u_2/\partial \xi_2 \\ \partial A_3/\partial \xi_1 \\ \partial A_3/\partial \xi_2 \end{bmatrix}}_{[\mathbf{dqdxi}]}, \tag{III.67}$$

and the vector **dqdxi** by

$$\underbrace{\begin{bmatrix} \partial u_1/\partial \xi_1 \\ \partial u_1/\partial \xi_2 \\ \partial u_2/\partial \xi_1 \\ \partial u_2/\partial \xi_2 \\ \partial A_3/\partial \xi_1 \\ \partial A_3/\partial \xi_2 \end{bmatrix}}_{[\mathbf{dqdxi}]} = \underbrace{\begin{bmatrix} \mathscr{G}_{11} & 0 & 0 & \mathscr{G}_{21} & 0 & 0 & \mathscr{G}_{31} & 0 & 0 & \mathscr{G}_{41} & 0 & 0 \\ \mathscr{G}_{12} & 0 & 0 & \mathscr{G}_{22} & 0 & 0 & \mathscr{G}_{32} & 0 & 0 & \mathscr{G}_{42} & 0 & 0 \\ 0 & \mathscr{G}_{11} & 0 & 0 & \mathscr{G}_{21} & 0 & 0 & \mathscr{G}_{31} & 0 & 0 & \mathscr{G}_{41} & 0 \\ 0 & \mathscr{G}_{12} & 0 & 0 & \mathscr{G}_{22} & 0 & 0 & \mathscr{G}_{32} & 0 & 0 & \mathscr{G}_{42} & 0 \\ 0 & 0 & \mathscr{G}_{11} & 0 & 0 & \mathscr{G}_{21} & 0 & 0 & \mathscr{G}_{31} & 0 & 0 & \mathscr{G}_{41} \\ 0 & 0 & \mathscr{G}_{12} & 0 & 0 & \mathscr{G}_{22} & 0 & 0 & \mathscr{G}_{32} & 0 & 0 & \mathscr{G}_{42} \end{bmatrix}}_{[\mathbf{NG}]} \underbrace{\begin{bmatrix} u_1^{(1)} \\ u_2^{(1)} \\ A^{(1)} \\ u_1^{(2)} \\ u_2^{(2)} \\ A^{(2)} \\ u_1^{(3)} \\ u_2^{(3)} \\ A^{(3)} \\ u_1^{(4)} \\ u_2^{(4)} \\ A^{(4)} \end{bmatrix}}_{\mathbf{q}_e}. \tag{III.68}$$

Then, the derivative matrix $[\mathbf{G}]$ is given by

$$[\mathbf{G}] = [\mathbf{G}_u \quad \mathbf{G}_\alpha] = [\mathbf{JI}]\,[\mathbf{NG}]\,. \tag{III.69}$$

III.4 Mesh and boundary conditions

To solve the boundary value problem of a finite geometry in nonlinear magnetoelasticity, we implement the above described magnetoelastic element in the general code FEAP (Taylor, 2011). We define a simple, but largely sufficient, plane-strain 4-node quadrilateral isoparametric element, with 3 degrees of freedom per node: the displacements $\mathbf{u} = \{u_1(X_1,X_2), u_2(X_1,X_2)\}$ and the magnetic vector potential $\alpha = A_3(X_1,X_2)$, with (X_1,X_2) the global reference coordinates. The (A_1,A_2) compo-

nents are zero since $\mathbf{B} = \{B_1, B_2, 0\} = \{\partial A_3/\partial X_2, -\partial A_3/\partial X_1, 0\}$ (we remind that $\mathbf{B} = \nabla \times \mathbf{A}$). The nodal unknowns $\mathbf{q}_e \equiv \{\delta u_1, \delta u_3, \delta\alpha\}$ were interpolated by $\delta q_i(X_1, X_2) = \sum_{j=1}^{4} \delta q_i^j N_j(X_1, X_2)$ (with δq_i^j denoting the 4 nodal values of the degrees of freedom), using linear shape functions,

$$N_1(\xi_1,\xi_2) = \frac{1}{4}(1-\xi_1)(1-\xi_2), \qquad N_2(\xi_1,\xi_2) = \frac{1}{4}(1-\xi_1)(1+\xi_2),$$
$$N_3(\xi_1,\xi_2) = \frac{1}{4}(1+\xi_1)(1+\xi_2), \qquad N_4(\xi_1,\xi_2) = \frac{1}{4}(1+\xi_1)(1-\xi_2), \tag{III.70}$$

with $(\xi_1, \xi_2) \in [-1, 1]$ denoting the local coordinates.

Following convergence studies, the number of elements in the film is 1200, in the substrate 5200 and in the air 10160. The nonlinear solutions of the field equations are obtained incrementally with the use of a standard Newton-Raphson scheme. However, the air domain needs special treatment, since it has no mechanical energy and thus, the deformation gradient is undefined therein. In view of this, we partitioned the air mesh into two domains: one with a structured mesh and the rest with unstructured mesh, as shown in Fig.III.2.

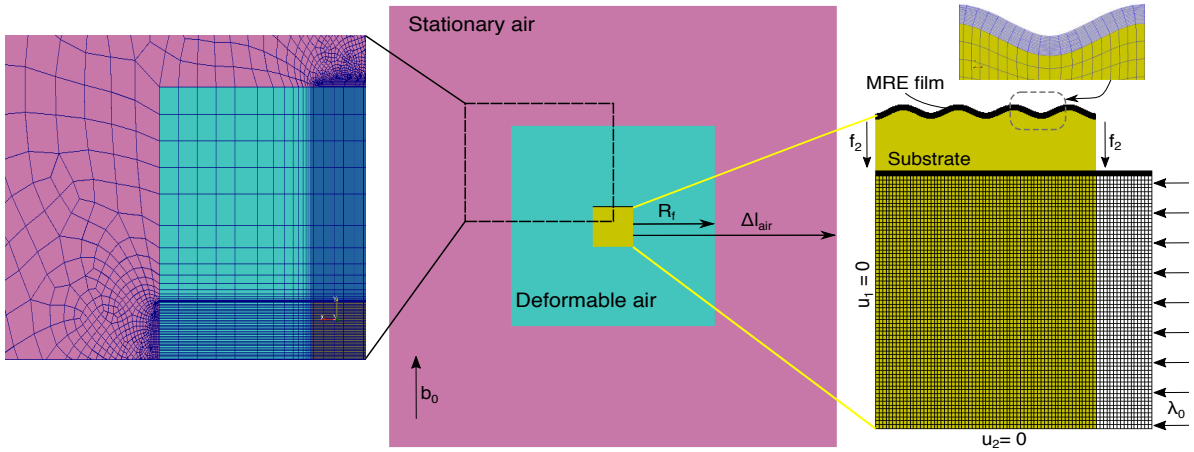

Figure III.2: Mesh of the film/substrate/air system. All regions are meshed with quadrilateral bilinear, 4-node isoparametric, (magneto)mechanical elements. A structured mesh with deformable elements (blue) is defined by the distance R_f from the solid boundary. The rest of the air region, defined by distance Δl_{air} from the solid boundary, is unstructured and stationary (purple).

Specifically, the first structured domain is deformable and spatially defined by a square of side length $2R_f + L$, concentric to the solid square of side length $L(= 40\text{mm})$. We use $R_f = 0.5\Delta L_{air}$, where ΔL_{air} is the half length size of the entire air domain minus the solid domain, see Fig.III.2. The elements within the deformable air domain are forced to deform to avoid severe mesh distortion near the specimen/air interface. This fictitious air deformation does not alter the solution of the problem, since the air density is zero and thus does not contribute to the mechanical energy of the system. To achieve this fictitious deformation, we follow the steps below:

(i) for all nodes lying in the deformable air domain, we find the closest node on the specimen boundary by a simple search algorithm, thus defining a set of pairs of size N_{a-s}.

(ii) for each pair of air-solid nodes, we define the linear constraint function $c_u = (1 - |x_i^{(2)} - x_i^{(1)}|/R_f) \cdot$

$u_i^{(2)} - u_i^{(1)} = 0$, with $i = 1,2$. In this last expression, node (1) belongs to the deformable air and node (2) to the solid domain, respectively.

(iii) the above constraint function can be achieved with either a Lagrange multiplier or a penalty formulation. For simplicity, we choose the second option and we define the penalty energy

$$\Phi_{pen}(u_i) = \sum_{n=1}^{N_{a-s}} \sum_{i=1}^{2} \frac{1}{2\varepsilon} \left[\left(1 - \frac{|x_i^{(n,solid)} - x_i^{(n,air)}|}{R_f} \right) u_i^{(n,solid)} - u_i^{(n,air)} \right]^2 \tag{III.71}$$

which is added to the original variational formulation (III.1).

(iv) we choose a sufficiently small value for $\varepsilon = 10^{-7}$ such that the constraint function is satisfied to a good accuracy. This value and approach leads in general to more accurate results and better convergence than that of using a small but finite shear and bulk moduli for the air domain.

(v) we consider first and second variations in (III.71) with respect to u_i and amend the original force vector and stiffness matrix of the entire system.

Finally, for the undeformable air domain, we apply identically zero displacements $u_i = 0\,(i = 1,2)$. In turn, the magnetic field is applied via the vector potential α by imposing at the outer boundary of the air the following condition

$$\alpha(X_1, X_2) = \varepsilon_{ij} (B_0)_i X_j, \qquad X_i \in \partial\Re^3, \qquad \mathbf{B}_0 = \mathbf{b}_0. \tag{III.72}$$

In the above equation, we have abused the notation $\Re^3$ to denote the boundary of the undeformable (outer) air domain. In addition, the Lagrangian, $\mathbf{B}_0$, and Eulerian, $\mathbf{b}_0$, magnetic fields are equal in the stationary air domain by definition.

III.5 Numerical mesh convergence

In this section, some examples of numerical implementation will be given in order to investigate the mesh sensitivity of the structure.

III.5.1 Mesh sensitivity in the purely mechanical problem

The plane-strain boundary value problem of a thin film of ($\mathrm{H}_f =$)0.2mm thickness and ($G_f =$)10kPa shear modulus bonded on a softer $G_s = 3$kPa substrate of ($\mathrm{H}_s =$)19.8mm thickness, subjected to an in-plane uniaxial compressive stretch $\lambda_1 (= \varepsilon_{11} + 1)$ is adressed by means of the linear buckle analysis in Abaqus and the full-field simulation under finite strains in FEAP.

The eigenvalue buckling problem employed in Abaqus is generally used to estimate the critical (bifurcation) load of linear materials, i.e., stiff structures. It consists of a linear perturbation procedure around equilibrium, where the loads are calculated relatively to the base state, i.e., the unloaded configuration in the present study. Since the eigenvalue buckling process is the first step in

our analysis, the base state of the problem is formed by the initial conditions. The eigenvalue problem reads $\mathbf{Ku} = 0$, where $\mathbf{K}$ is the tangent stiffness matrix and the $\mathbf{u}$ are the nontrivial displacement solutions. In order to find such nontrivial solutions, one needs to search for the loads that cause the model stiffness matrix to become singular, $\det \mathbf{K} = 0$. Since geometric nonlinearities and preloads are omitted, the incremental problem reads $(\lambda_i K_D^{mn}) u_i^m = 0$, where K_D^{mn} the load (tangent) stiffness matrix due to the incremental perturbation loading Q^n, λ_i the eigenvalues and u_i^m the buckling mode shapes (eigenvectors). The critical buckling load is then $\lambda_i Q^n$; the magnitude of Q^n is not important at the eigenvalue prediction step, since it is later scaled by the load factor λ_i extracted from the solution. The corresponding eigenmodes u_i^m are normalized vectors (so as the maximum displacement is 1) and thus, they do not represent actual magnitudes of deformations at the critical load. For choosing an appropriate scale factor, one can set an order of magnitude lower than the film thickness for the first mode, sequentially decreasing it by half at each next eigenmode. The eigensolver used to extract the desired number of eigenvalues, $i = 3$, is the *subspace iteration* method. The maximum number of iterations is set at 1000. Mechanical boundary conditions are prescribed at the initial (base state) step at the left edge of the block, where $u_1 = 0$, and the bottom edge of the block, where $u_2 = 0$. The uniformly applied compressive displacement at the right edge of the block is set at the buckling prediction step, reading $u_1 = -1$. The real magnitude of the loading is not asked to be defined, as discussed before. The buckling eigenmodes are affected by the stresses in the base state (zero in the present case), as well as by the incremental stresses due to the perturbation loading in the buckling step. These stresses depend on the incremental boundary conditions used for "stress perturbation and buckling mode calculation" (i.e., our selected option).

Linear, quadrilateral plane-strain elements with hybrid formulation and high incompressibility are selected; the element type is CPE4H (4-node bilinear, hybrid with constant pressure). Note that these elements can only be used with the subspace iteration eigensolver and not the Lanczos. Edge biased seeding is also employed, as convergence studies indicate (Fig.III.5b). This is because a finer mesh is required close to the film/substrate interface, relaxing towards the bottom bulk mass of the substrate. For a given bias ratio B and a given number of elements N, the length ratio of an element (i+1) to its previous element (i) along the biasing direction is $\frac{l_{i+1}}{l_i} = B^{\frac{1}{N-1}}$. The element sizes and the nodal spacing can be calculated from this relation.

The constitutive material layers are modeled as linear elastic, which is not the realistic behavior of our soft structure. However, even when the response is nonlinear before bifurcation, a general eigenvalue buckling analysis can provide an estimate of bifurcation critical loads and wavelengths. For the post-buckling regime, higher-order perturbation analysis is necessary to obtain adequate accuracy on the post-buckling wavelength evaluation. A predicted linear buckle load $u_1^c = 9.2183$ for the first mode (i.e., wrinkling) is representatively given in Fig. III.3.

In case the stucture has eigenmodes with closely spaced eigenvalues, it is noted that a preload can be applied. This is very likely in imperfection-sensitive structures. There, one can apply a preload P^n close to the buckling load Q^n and then perform the eigenvalue extraction step. If $P^n = \mu Q^n$, the structural stiffness takes into account the load stiffness K_0^{mn} due to the preload, such

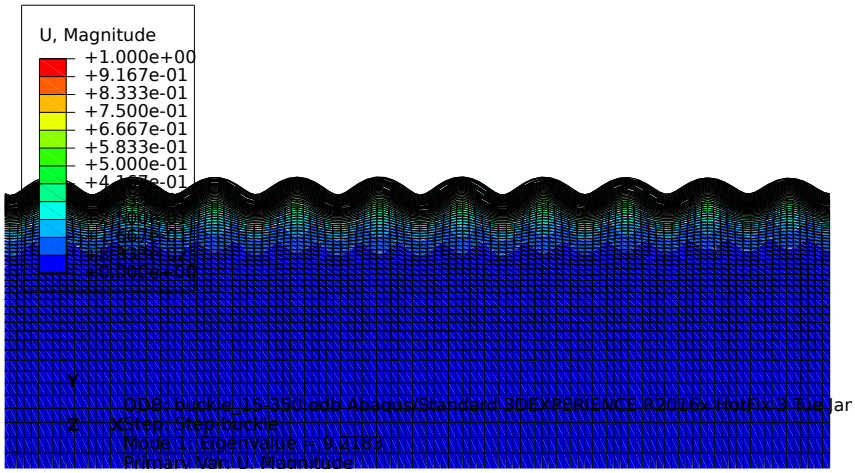

Figure III.3: Results from the linear buckle analysis on a stiff film/substrate block (film thickness $H_f =$ 0.2mm) under Dirichlet boundary conditions and in absence of user-defined geometric nonlinearities. The first mode depicted in half (symmetric) plane is wrinkling, obtained under a critical buckling displacement $u_1^c = 9.2183$ (the value is normalized so that the magnitude of maximum displacement is one) or stretch ratio $\lambda_1^c = 0.7695$. Scale factor used 0.1.

that $K_0^{mn} + \mu K_D^{mn}$, and the buckling load becomes $(\mu + \lambda_i)Q^n$. The process is equivalent to a dynamic eigenfrequency extraction with shift μ. However, the eigensolves do not converge when the preload reaches the buckling load (or give inaccurate predictions). Thus, the static Riks procedure is instead recommended to be employed (Abaqus, 2009, ABAQUS/Explicit, 2005).

A mesh sensitivity study of the purely mechanical problem in Abaqus is presented in Table III.2. There, the first column contains the number of film elements along e_2 direction, the second the number of film elements along e_1 direction, the third the number of substrate elements along e_2 direction, the fourth the bias ratio of the substrate elements (along e_2 direction) and the final the critical buckling stretch. The number of film elements along e_2 direction is set 10, 15 or 20, i.e., a dense choice along film thickness at 0.2mm over total block thickness at 40mm. The number of elements in the substrate along e_2 and the corresponding edge seeding are such that a) the length of the film and the substrate elements at the interface (along e_2) are equal, $l_f^+ = l_s^-$; and b) the aspect ratio of the substrate elements[7] approximates one (i.e., square). In virtue of that, the influence of film meshing along e_1 direction is investigated. It is observed that the greater the mesh refinement, the lower the compressive buckling load. The value of the latter starts converging after 350 elements along e_1 direction. However, in the case of FEAP full-field simulations, the selection of the mesh has to be in a compromise with the computational cost, mostly for the magnetomechanical loading case in which the free space is also modeled in detail.

[7]Rectangles are constructed with edges passing through the element edge midpoints. The aspect ratio of the quadrilateral is the ratio of a longer side to a shorter side of whichever rectangle is the most stretched.

film elements // e_2	film elements // e_1	substrate elements // e_2	bias ratio	λ_1^c
10	80	65	-	0.70915
10	160	65	130	0.752565
15	350	85	160	0.7695425
15	350	160	80	0.769515
10	360	85	160	0.7699325
10	800	80	40	0.7719775
10	1600	160	80	0.7728275
20	1600	160	100	0.7728425
20	2000	160	100	0.7733425

Table III.2: Mesh convergence via Abaqus investigating the critical stretch ratio λ_1^c versus the mesh density in film and substrate. Film thickness $H_f = 0.2$mm and shear modulus $G_f = 10$kPa. Substrate thickness $H_f = 19.8$mm and shear modulus $G_s = 3$kPa. CPE4H high incompressibility elements are used.

Subsequently, a standard static analysis is carried out for the hyperelastic bilayer block in FEAP. Fig. III.4 presents the critical bifurcation point and the subsequent post-bifurcated response of a neo-Hookean film/substrate stucture under uniaxial compression. Here, the mesh of the solid phases have to be designed in combination with the air mesh used in the magnetomechanical loading case. Given the mesh sensitivity study in Table III.2, as well as that in the subsequent Section III.5.2 for the coupled loading case, 15×350 elements is a rational mesh density for the film (0.2×40 mm^2). From Table III.2, one can also tell that the response is already converged for 85×350 substrate mesh elements (bias ratio=160). Thus, one can try to decrease the number of the elements in the substrate.

The curves in Fig. III.4 represent three different meshes of constant film mesh at 15×350 elements and variable substrate and air mesh. The blue and red curve (with film shape configuration also in the same color) correspond to 85×350 elements substrate mesh, but different air box penalty values ε at 1e-6 and 1e-7, respectively (for air box see Section III.4 and eq.(III.71)). We note that $\varepsilon \leq$ 1e-6, so that the calculations for such delicate meshes to run. The yellow curve corresponds to air box penalty $\varepsilon =$ 1e-7 and lighter substrate and air mesh densities (i.e., substrate mesh: 75×350 elements and bias ratio=220, structured air mesh: 45 elements along e_2 direction and bias ratio=330). The three curves converge for the primary critical load $\lambda_1^w = 0.7721$. The air box penalty is found to slightly affect the post-bifurcation response around the secondary bifurcation branch. The second (red) mesh leads to creases deep in the post-bifurcation, in contrast to the other two.

The mesh of the air acts as an inevitable imperfection due to its unstructured elements, which renders the mesh uncontrollable at high strains. More specifically, the free space is distinguished into a deformable and a stationary regime. This is applied by a penalty function that progressively calls-off the nodal deformations from the solid boundaries to a given distance from the center of the rectangular block, i.e., boundaries of the deformable air, see context of Fig.III.2. The deformable regime is modeled with structured elements (area of mesh sensitivity study) and the rest with unstructured. The latter includes 20 nodes per edge at the external air boundaries.

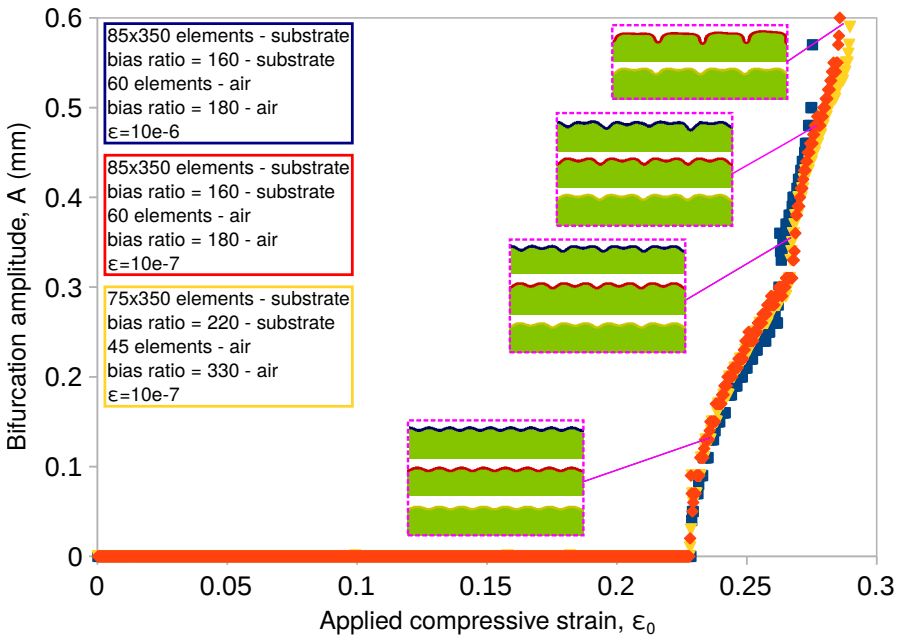

Figure III.4: Mesh sensitivity on substrate and air mesh for fixed film mesh at 15×350 elements (film thickness $H_f = 0.2$mm). Bifurcation amplitude A versus the applied compression ε_0 for: **a**, blue curve/film pattern: substrate mesh 85×350 elements and bias ratio = 160, structured air mesh 60 elements along e_2 direction, bias ratio = 180 and air box penalty ε = 1e-6; **b**, red curve/film: substrate mesh 85×350 elements and bias ratio = 160, structured air mesh 60 elements along e_2 direction, bias ratio = 180 and air box penalty ε = 1e-7; **c**, yellow curve/film: substrate mesh 75×350 elements and bias ratio = 220, structured air mesh 45 elements along e_2 direction, bias ratio = 330 and air box penalty ε = 1e-7. Half (symmetric) plane of the block is shown. The air is not depicted.

The critical load $\lambda_1^w (= 0.7721)$ corresponds to sinusoidal wrinkling as primary buckling mode, which evolves to period-doubling upon further compression, $\lambda_1^{pd} = 0.735$. The primary buckling load found by FEAP is in agreement with the linearized 'buckle' calculation in Abaqus (see Table III.2). This owes to the neo-Hookean behavior of the bilayer, which is close to that of linear materials about the primary buckling point. However, for other nonlinear elastic materials, e.g., with finite strains up to 200%, the incremental moduli are different from the ground state and become anisotropic. In that case, the buckle analysis would not accurately predict the critical response. Generally, the response of the substrate is highly nonlinear and induces an anisotropic elastic state under incremental deformation. Beyond the primary instability point, the post-bifurcation is defined by wrinkles of increasing amplitude that often lead to folding (see Sun et al., 2012). This or other (e.g., creases, ridges, crinkles) higher-order patterns manifest finite strains around localizations. In all these cases, a linear (small deformation) stability analysis is not sufficient to predict the critical eigenvalues/eigenmodes.

III.5.2 Mesh sensitivity in the magnetomechanical problem

The formal method for mesh convergence requires a critical result parameter plotted against some measure of mesh density. This curve is then used to indicate when convergence is achieved, or

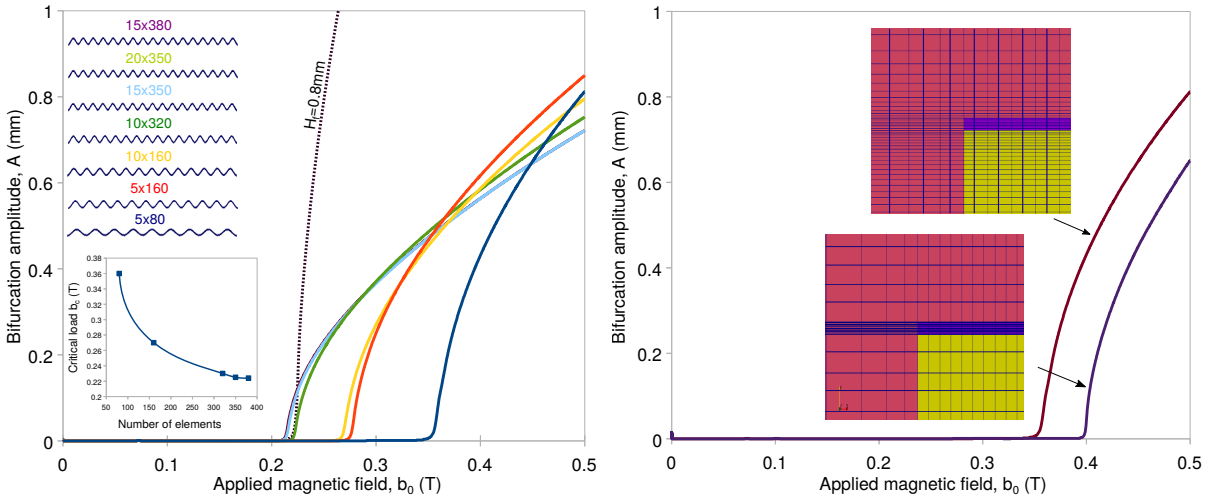

Figure III.5: Mesh sensitivity analysis on wrinkling amplitude and critical wavenumber of a bilayer block of $(H_f =)$0.2mm film thickness subjected to a given pre-compression $\lambda_0 = 0.85$. The average amplitude of the wrinkles A is plotted as a function of the applied magnetic field b_0 for different meshes: **a,** 5×80, 5×160, 10×160, 10×320, 15×350, 20×350, 15×380 elements in the film. That is the number of elements along e_2 direction $\times$ the number of elements along e_1 direction. The surface patterns underneath the labels correspond to the amplitude curves of the same color for $b_0 = 0.45$T. A converged response on the critical modes and amplitudes is obtained for 15×350 film discretization. **b**, biased and unbiased substrate and air meshing for a fixed film mesh at 6 elements along e_2 direction versus 80 elements along e_1 direction. It is straightforward that the critical magnetic field is sensitive to a gradual meshing.

how far the most refined mesh is from full convergence. The present problem is defined by several critical result parameters needed to converge: the critical fields in a two-parameters space, the corresponding wavenumbers, the bifurcation amplitudes. The mesh parameters of the problem are also a few: film, substrate and (un-/)structured air mesh density, penalty function value. As a result, it is not trivial to find a compromise between all these parameters and simultaneously keep low the computational cost, especially since the problem requires direct and detailed air meshing.

In Fig.III.5a, we plot the average amplitude of the wrinkles A as a function of the applied magnetic field b_0 for different film/substrate meshes. The corresponding surface patterns are depicted for applied magnetic field $b_0 = 0.45$T. The labels in color denote the number of film elements along e_2 direction $\times$ the number of film elements along e_1 direction. The surface modes underneath the labels correspond to the amplitude curves of the same color. Following convergence studies corresponding to MRE film thickness at $(H_f =)$0.2mm, one needs at least 350 elements along e_1 direction to guarantee convergence of the critical wavenumber (=17 wrinkles) under a given pre-stretch $\lambda_0 = 0.85$. Given that, the number of film elements along e_2 direction has to be at least 15, in order to obtain convergence on the critical magnetic field (see inset) and uniform post-bifurcated wrinkling amplitudes. The amplitude curve corresponding to the film/substrate geometry of thicker film $(H_f =)$0.8mm is plotted against the curves for $(H_f =)$0.2mm for comparison reasons.

The penalty value ε is found to affect the post-bifurcated behavior under finite strains, but not the critical fields. The solution leads to converged morphological responses for air box penalty value

$\varepsilon \leq$1e-7. The substrate is meshed with 75×350 elements and bias ratio 220 along e_2 (thickness) direction. The structured regime of the air is modeled with 45 elements and bias ratio 330 along e_2 direction, for penalty value $\varepsilon =$ 1e-7. This air mesh converges with the heavier (blue and red) ones presented for the mechanical problem in Fig.III.4. An alternative to the penalty method is to assign elastic properties to the air, so as to activate its deformation. The shear modulus of the air is of order ε. Therefore, relatively large penalty values (e.g., $\varepsilon \geq$1e-4) should be avoided, so that the modulus of the air is not comparable to that of the substrate.

In Fig.III.5b, the influence of gradual meshing of the air and the substrate along both directions is shown for a fixed film mesh with 6 elements along e_2 direction versus 80 elements along e_1 direction. The substrate is meshed with 30×80 elements. The structured (deformable) regime of the air is modeled with 25 elements along e_2 direction for penalty value $\varepsilon =$ 1e-7. One mesh considers a bias ratio (along e_2 direction) with values 120 and 140 for the substrate and the air, respectively. The other mesh considers zero bias ratio between the elements of the film/substrate and the film/air. The wrinkling amplitude curve corresponding to the gradual mesh is shifted to a significantly lower critical magnetic field with respect to the one in the absence of gradual meshing. To conclude, it is clear that gradual meshing (bias) is necessary for mesh convergence of the problem at hand.

III.6 Concluding remarks

To conclude, the present chapter presents the finite element method (FEM) used to numerically investigate the plane-strain boundary value problem of the MRE film/substrate block by means of a user-element routine in FEAP. On account of numerically solving such a non-trivial problem, the proposed continuum formulation by Dorfmann and Ogden (2004) is a Lagrangian variational approach. Such an approach pertains to the minimization of a potential energy with respect to the independent variables: the displacement field $\mathbf{u}$ and the potential vector of the magnetic field $\mathbf{A}$. The potential energy includes the internal elastic energy of the solid bilayer, the work done by the external forces and the Maxwell background energy defined in the entire space. This yields all the appropriate governing equations and boundary/interface conditions.

In the center of the analysis lies a phenomenological isotropic free-energy density that consists of the neo-Hookean combined with the Langevin model. In virtue of such energy function selection, the developed variational principle is directly related to the primary field equations, satisfied by the constitutively related magnetic field $\mathbf{H}$ and magnetic induction $\mathbf{B}$. It follows that the energy function fully describes the behavior of the magnetoelastic materials when combined with the Maxwell energy density. In particular, the magnetic fields are not only stored within the solid but they extend into the air (or another non-magnetic medium). When a non-magnetic material is within the magnetic field, the magnetic stresses are self-equilibrated and magnetic fields have no effect on the traction. However, when the material is magnetic, the Maxwell stresses (i.e., stresses induced by the magnetic field) affect the mechanical traction measured on the boundary of the specimen.

The nonlinear solutions of the field equations are obtained incrementally with the use of a stan-

dard Newton-Raphson scheme. In that way, the governing equilibrium equations can be solved when a buckling instability analysis is also required. The stability criterion derives from the incremental positive definitess of the Jacobian stiffness matrix, i.e., the second derivatives of the potential energy with respect to the independent variables.

A standard static analysis is carried out for a stiff and hyperelastic bilayer block in Abaqus and FEAP, respectively. The mesh of the solid phases have to be designed in combination with the air mesh used for the magnetomechanical loading case. In turn, the air domain needs special treatment, since it has no mechanical energy and thus the deformation gradient is undefined therein. In view of that, we partition the free space into a (structured) deformable and a (unstructured) stationary regime. This is applied by a penalty function that progressively calls-off the nodal deformations from the solid boundaries to a given distance from the center of the rectangular block, i.e., boundaries of the deformable air. The mesh of the air acts as an avoidable imperfection due to its unstructured elements, which renders the mesh uncontrollable at high strains.

A mesh sensitivity study of the combined magnetomechanical problem is also carried-out in FEAP. To obtain convergence of the critical loads, modes and post-bifurcation amplitudes for both purely mechanical and magnetomechanical loadings, the final mesh selection for the geometry of 0.2mm film thickness considers 15 elements along the thickness and 350 elements along the length of the film (15×350). The substrate is meshed with 75×350 elements and bias ratio 220 along the thickness direction. The structured regime of the air is modeled with 45 elements and bias ratio 330 along the thickness direction, for penalty value $\varepsilon =$ 1e-7.

CHAPTER IV

THEORETICAL BIFURCATION MODEL

Summary of the Chapter. In this chapter, we solve the theoretical bifurcation problem of a semi-infinite MRE film/passive substrate (plus the semi-infinite air) system and we investigate the influence of the material properties on the critical response. The first section presents the variational magnetoelastic formulation used in the bifurcation analysis. The second section outlines the principal (non-diverging) solution of the plane-strain solid subjected to in-plane compression and a transverse magnetic field. The third section demonstrates the bifurcation analysis. Such an analysis is an incremental approach that does not incorporate the effects of a boundary-value system (it considers idealized boundary conditions). The last section presents the results from the purely mechanical and magnetomechanical bifurcation. The model aims at determining the critical load for the onset of wrinkling and the associated wavelengths.

Contents

IV.1 Alternative variational formulation: perturbation magnetic field

The potential energy of the entire system – which accounts for the magnetoelastic energy stored within the material volume, as well as the magnetic background energy that is affected by the presence of the solid – can be reformulated taken into account an exact decomposition of the Lagrangian magnetic field $\mathbf{B}$. In virtue of that, the total magnetic field $\mathbf{B}$ can be separated into an externally applied background $\mathbf{B}^0$ and a perturbed (due to the presence of the magnetoelastic solid within the field) $\widetilde{\mathbf{B}}$ component, such that

$$\mathbf{B} = \mathbf{B}^0 + \widetilde{\mathbf{B}}. \tag{IV.1}$$

Both the externally imposed and the background field have to satisfy the divergence-free condition, as well as the corresponding boundary condition[1]

$$\nabla \cdot \mathbf{B}^0 = 0, \quad [[\mathbf{B}^0]] \cdot \mathbf{N} = 0 \quad \text{and} \quad \nabla \cdot \widetilde{\mathbf{B}} = 0, \quad [[\widetilde{\mathbf{B}}]] \cdot \mathbf{N} = 0 \tag{IV.2}$$

and thus, one can express $\mathbf{B}^0$ and $\widetilde{\mathbf{B}}$ in terms of a Lagrangian vector potential $\mathbf{A}^0$ and $\widetilde{\mathbf{A}}$ respectively, such that

$$\mathbf{B}^0 = \nabla \times \mathbf{A}^0 \quad \text{and} \quad \widetilde{\mathbf{B}} = \nabla \times \widetilde{\mathbf{A}}. \tag{IV.3}$$

We note that $\mathbf{A} = \mathbf{A}^0 + \widetilde{\mathbf{A}}$, which in index notation and in view of (IV.3) gets $\varepsilon_{ijk} \mathrm{B_j}\, \mathrm{X_k} = \varepsilon_{\mathrm{ijk}} \mathrm{B^0_j}\, \mathrm{X_k} + \varepsilon_{\mathrm{ijk}} \widetilde{\mathrm{B}}_{\mathrm{j}}\, \mathrm{X_k}$, with ε_{ijk} the Levi-Civita operator and $\mathrm{X_k}$ the reference configuration coordinate of a material point, $i, j, k = 1, 2, 3$.

In view of (IV.1), the potential energy (III.1) can be rewritten as

$$\begin{aligned} \mathscr{P}(\mathbf{u}, \mathbf{A}) = &\int_{\Omega_i} \rho_0^i \Phi_i \left(\mathbf{F}, \mathbf{B}\right) \mathrm{d}\Omega + \int_{\Re^3} \frac{1}{2\mu_0 J} (\mathbf{F}\mathbf{B}^0) \cdot (\mathbf{F}\mathbf{B}^0)\, \mathrm{d}\Omega + \int_{\Re^3} \frac{1}{2\mu_0 J} (\mathbf{F}\mathbf{B}^0) \cdot (\mathbf{F}\widetilde{\mathbf{B}}) \\ &+ \int_{\Re^3} \frac{1}{2\mu_0 J} (\mathbf{F}\widetilde{\mathbf{B}}) \cdot (\mathbf{F}\widetilde{\mathbf{B}})\, \mathrm{d}\Omega - \int_{\partial\Omega_i^t} \mathbf{T} \cdot \mathbf{u}\, \mathrm{d}S. \end{aligned} \tag{IV.4}$$

After neglecting the second (constant) term of the energy, induced by the externally applied magnetic field, and showing[2] that the third term in (IV.4) is zero, since $\widetilde{\mathbf{B}} \to 0$ at $|\mathbf{x}| \to \pm\infty$, the potential energy writes

$$\mathscr{P}(\mathbf{u}, \widetilde{\mathbf{A}}) = \int_{\Omega_i} \rho_0^i \Phi_i \left(\mathbf{F}, \mathbf{B}^0 + \widetilde{\mathbf{B}}\right) \mathrm{d}\Omega + \int_{\Re^3} \frac{1}{2\mu_0 J} (\mathbf{F}\widetilde{\mathbf{B}}) \cdot (\mathbf{F}\widetilde{\mathbf{B}})\, \mathrm{d}\Omega - \int_{\partial\Omega_i^t} \mathbf{T} \cdot \mathbf{u}\, \mathrm{d}S. \tag{IV.5}$$

The energy within the solid volume W_i (i =film, substrate), described by the functional of the first

[1] The following relations are straightforward since the divergence is a linear operator.

[2] $\int_\Omega \frac{1}{2\mu_0} (\mathbf{F}\mathbf{B}^0) \cdot (\mathbf{F}\widetilde{\mathbf{B}})\, \mathrm{d}\Omega = \int_\Omega \frac{\mathrm{J}}{2\mu_0} \mathbf{b}^0 \cdot \widetilde{\mathbf{b}}\, \mathrm{d}\Omega = \int_{\partial\Omega} \frac{\mathrm{J}}{2\mu_0} \mathbf{b}^0 \cdot (\nabla \times \widetilde{\mathbf{a}}) \cdot \mathbf{n}\, \mathrm{d}S = 0$ (divergence theorem) for finite volume $\Omega \to \Re^3$, since $|\widetilde{\mathbf{a}}| \to 0$ at $\mathrm{X}_2 \to \pm\infty$.

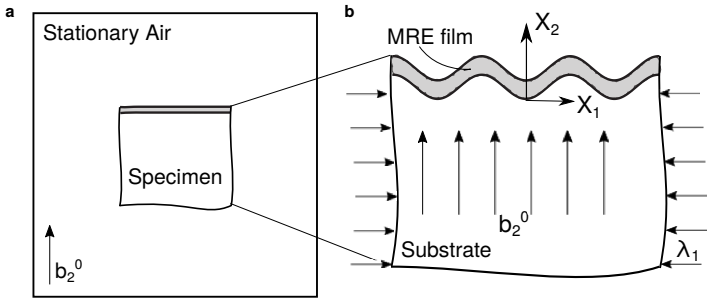

Figure IV.1: Schematics of a plane-strain infinite system. **a**, A MRE film adheres to a substrate that is extended towards negative infinity. On the top of the film, there is air extended to positive infinity. All phases are taken to be infinitely long. **b**, The solid system is initially subjected to uniaxial pre-compression λ_1, followed by a transverse magnetic field b_2^0 of Eulerian nature.

term in combination with the background energy, gets in view of (III.26), (III.27) and (IV.1)

$$W_i(\mathbf{F},\widetilde{\mathbf{B}}) = \rho_0^i \Phi_i^{mec}(\mathbf{F}) + \frac{1}{2\mu_0 J}(\mathbf{F}\widetilde{\mathbf{B}})\cdot(\mathbf{F}\widetilde{\mathbf{B}}) + \rho_0^i \Phi_i^{mag}(\mathbf{F},\mathbf{B}^0+\widetilde{\mathbf{B}}), \tag{IV.6}$$

recalling that $\Phi_i^{mec}(\mathbf{F}) + \Phi_i^{mag}(\mathbf{F},\mathbf{B}) = \Phi_i(\mathbf{F},\mathbf{B})$.

Without loss of generality, the expression (IV.6) can be also extended to air, $\rho_0^{air} = 0$. At the principal solution (i.e., uniform displacements and magnetic fields), the presence of the magnetoelastic solid does not perturb the magnetic field of the free space. Thus, it is more convenient to work on the analytical bifurcation with the perturbed component of the magnetic potential vector $\widetilde{\mathbf{A}}$, instead of the total vector potential $\mathbf{A}$. Indeed, the functions $\Phi_i(\mathbf{F},\mathbf{B})$ and $\Phi_i(\mathbf{F},\widetilde{\mathbf{B}})$ are different. However, their derivatives with respect to $\widetilde{\mathbf{B}}(=0)$ are the same, see Section IV.3. We will subsequently show that the approach with the perturbed and the total field are almost the same and the differences will be given in parallel.

IV.2 Geometry and principal solution

We consider a plane-strain infinite system consisting of a MRE layer bonded on a substrate extended towards negative infinity. On the top of the film, air is extended towards positive infinity, as seen in Fig.IV.1. All phases are taken to be infinitely long. The reference configuration of the (magneto)elastic solid is its stress-free state. Following the experimental and numerical process, the system deforms under plane-strain conditions due to the application of in-plane compression $\lambda_1(=\lambda_0)$, followed by a transverse magnetic field $b_2^0(=b_0)$. Note that the response is path-independent and thus, the application of the loads can be reversed.

The film is made of a nonlinear magnetoelastic, isotropic and nearly incompressible material, as thoroughly discussed in Section III.2. Such a material can be fairly approximated by the simple combination of a Neo-Hookean elastic energy and a Langevin (without hysteresis) magnetic energy

(see (III.34)) such that

$$\rho_0^i\Phi_i(\mathbf{F},\mathbf{B}) = \frac{G^i}{2}(I_1-3-2\ln I_3)+\frac{G'^i}{2}(I_3-1)^2 + I_3\frac{\mu_0(m_s^i)^2}{3\chi^i}\left[\ln\left(\frac{3\chi^i}{I_3\mu_0 m_s^i}\sqrt{I_5}\right)-\ln\left(\sinh\left(\frac{3\chi^i}{I_3\mu_0 m_s^i}\sqrt{I_5}\right)\right)\right], \tag{IV.7}$$

where $i=f,s$ for the film and the substrate, respectively. In equation (IV.7), G^i is the shear modulus, G'^i the second Lamé compressibility constant, χ^i the susceptibility, m_s^i the saturation magnetization and μ_0 the permeability of vacuum. The nearly incompressible response of the bilayer-system up to $O(\delta^2)$ implies an out-of-plane deformation $\lambda_2 \simeq 1/\lambda_1$ that is solved by means of the Newton-Raphson method. This is satisfied via a large Lamé compressibility constant a for $G'^i = aG^i$, $i=f,s$. The effect of the compressibility $a=10,100,1000$ on the critical response is demonstrated in Fig. IV.7b. In the incompressible case, one needs to first map the deformations ($\lambda_2=1/\lambda_1$) and then solve for the hydrostatic pressure independently from the deformation kinematics.

A linear magnetoelastic (without saturation) energy in the augmented variational formulation has also been employed, so as to obtain a direct comparison with the bifurcation analysis in Danas and Triantafyllidis (2014), see the energy potentials in (III.48) and (III.49). To discard Jacobian singularities, one can use a small dependence on I_6 invariant, with the $\mathbf{F}-\mathbf{B}$ potential writing

$$\rho_0^i\Phi_i(\mathbf{F},\mathbf{B}) = \frac{G^i}{2}(I_1-3-2\ln I_3)+\frac{G'^i}{2}(I_3-1)^2-\frac{\chi^i}{2\mu_0 I_3}I_5+\frac{C_6}{2\mu_0 I_3}I_6. \tag{IV.8}$$

.

Due to isotropy, it has been shown by Kankanala and Triantafyllidis (2004) that the free energy depends on the invariants I_1 and I_3 of the rank two right Cauchy-Green deformation tensor, as well as on the magnetoelastic invariant I_5. The invariants I_1,I_3,I_4,I_5 and I_6 of the problem are defined such as

$$I_1 = C_{ii} = F_{ki}F_{kj}, \qquad J = I_3 = \det\mathbf{F} = F_{ii}, \tag{IV.9}$$

$$I_4 = B_iB_i, \qquad I_5 = B_iC_{ij}B_j, \qquad I_6 = B_iC_{ik}C_{kj}B_j. \tag{IV.10}$$

This constitutive laws permit to plug in the material properties i (= film, substrate) from macroscopic measurements and homogenization estimates. As seen in Table IV.1, we use the experimental and numerical material parameters corresponding to soft Ecoflex silicones. A Lamé compressibility constant, 100 times higher than the shear moduli of the materials, leads to nearly incompressible material phases, see Fig. IV.7b.

	$\rho_0(\mathrm{g\cdot cm^{-3}})$	G (kPa)	G'/G	χ	$\mu_0 m_s$ (T)	μ_0 ($\mu\mathrm{N\cdot A^{-2}}$)
Film	1.1	10	100	0.4	0.5	$4\pi 10^{-1}$
Substrate	1.07	3	100	0	0	$4\pi 10^{-1}$

Table IV.1: Material properties of the film/substrate system in numerical and theoretical analysis.

To avoid boundary layer effects, the admissible displacement $\mathbf{u}$ field and the magnetic vector potential $\widetilde{\mathbf{A}} = \widetilde{A}_3 = a$ [3] must also satisfy the continuity conditions at the film/substrate interface $X_2 = 0$ and the film/air boundary $X_2 = H_f = h$ respectively:

$$\begin{aligned} u_1(X_1,0^+)_f &= u_1(X_1,0^-)_s, \qquad & u_1(X_1,h^+)_{air} &= u_1(X_1,h^-)_f, \\ u_2(X_1,0^+)_f &= u_2(X_1,0^-)_s, \qquad & u_2(X_1,h^+)_{air} &= u_2(X_1,h^-)_f, \\ a(X_1,0^+)_f &= a(X_1,0^-)_s, \qquad & a(X_1,h^+)_{air} &= a(X_1,h^-)_f, \end{aligned} \tag{IV.11}$$

with index f for the film and s for the substrate.

For the sake of algebraic simplicity, the principal solution is solved in the current configuration. At the principal solution, the mechanical and magnetic fields are uniform. The perturbed component of the magnetic field thus disappears, $\widetilde{\mathbf{B}} = \widetilde{\mathbf{b}} = 0$, implying from (IV.1) that $\mathbf{B} = \mathbf{B}^0$ and $\mathbf{b} = \mathbf{b}^0$. Due to the transverse nature of the magnetic field, the in-plane component is nonexistent, i.e., $b_1 = b_1^0 = 0$, leaving λ_2 as the unknown quantity. In view of the relation between the magnetic field at the reference and current configuration, $\mathbf{B} = J\mathbf{F}^{-1}\mathbf{b}$, we obtain the vertical component of the Lagrangian applied magnetic field

$$B_2^0 = J\left(F_{21}^{-1}\, b_1^0 + F_{22}^{-1} b_2^0\right) = J\, F_{22}^{-1}\, b_2^0 = \lambda_1\, b_2^0, \tag{IV.12}$$

with the deformation gradient $\mathbf{F} = \lambda_1(e_1 \otimes e_1) + \lambda_2(e_2 \otimes e_2) = \mathbf{F}^T$ or in index notation the corresponding determinant $J = F_{11}\, F_{22} = \lambda_1\, \lambda_2$. Here, the magnetic field that is feasible to be controlled is the Eulerian $b_2 = b_2^0$. This is because the specimens in actual experiments are placed within a field far from the poles of the magnet. The poles are stable and do not follow the transformation of the specimen, setting the problem of Eulerian nature. As a result, what can be actually measured is the current b_2^0 and not the reference B_2^0 magnetic field.

The only existent term of the applied magnetic potential vector $\mathbf{A}^0 (= a^0)$ writes $a^0 = \mathrm{A}_3^0 = \varepsilon_{3jk}\,\mathrm{B}_j^0\,\mathrm{X}_k = -\mathrm{B}_2^0\,\mathrm{X}_1 + \mathrm{B}_1^0\,\mathrm{X}_2$, with ε_{ijk}, $i,j,k = 1,2,3$ the Levi-Civita operator. The unknown principal stretch λ_2 is obtained from the traction condition applied at the film/substrate interface, $X_2 = 0$, for the substrate and the film/air boundary, $X_2 = h$, for the film. Using the expression (III.13) regarded in the current configuration, the vertical component of the traction requires to satisfy

$$t_2 = 0 = \frac{\rho_0^i}{J}\frac{\partial \Phi_i}{\partial F_{2k}}\bigg|_{\widetilde{B}_2=0} F_{lk}\, n_l, \qquad k,l = 1,2, \tag{IV.13}$$

where the energy function $\rho_0^i \Phi_i$ can be replaced by (IV.7) or (IV.8). By means of the Newton-Raphson method, the principal solution, i.e., $F_{22} = \lambda_2$, is solved considering the function t_2, its derivative and an initial value of the variable F_{22} such that

$$F_{22}^{n+1} = F_{22}^n - \underbrace{\frac{t_2(F_{22}^n)}{t_2'(F_{22}^n)}}_{dF_{22}}, \tag{IV.14}$$

[3] Since $\widetilde{\mathbf{B}} = \nabla \times \widetilde{\mathbf{A}}$ and $\widetilde{B}_3 = 0$ giving $\widetilde{B}_1 = \frac{\partial \widetilde{A}_3}{\partial X_2}$ and $\widetilde{B}_2 = -\frac{\partial \widetilde{A}_3}{\partial X_1}$ by ignoring X_3 dependence of the quantities, the only nonzero component of $\widetilde{\mathbf{A}}$ is $\widetilde{A}_3$. For the sake of simplicity in notation, $a \equiv \widetilde{A}_3$.

where n an iteration and $'$ the derivation with respect to the normal component F_{22}. To approximate the root of the nonlinear equation, the quantity dF_{22} needs to decrease towards zero versus the iterations, assuming that the process has worked accurately when $dF_{22}/F_{22} < 10^{-3}$.

IV.3 Bifurcation analysis

Starting from zero fields, the principal solution corresponds to uniform strain and constant magnetic quantities for the flat film. Given a set of loading values $\{\lambda_1, b_2^0\}$, the corresponding out-of-plane stretch λ_2, traction t_1 and magnetic field h_1 are found by minimizing the potential energy $\mathscr{P}(\mathbf{u}, \widetilde{\mathbf{A}})$ in (IV.5) with respect to the independent variables $\mathbf{g} \equiv \mathbf{u}, \widetilde{\mathbf{A}}$, i.e.,

$$\delta \mathscr{P} = \mathscr{P}_{,\mathbf{g}}(\mathbf{g}) \delta \mathbf{g} = 0, \tag{IV.15}$$

or else $\mathscr{P}_{,\mathbf{u}}\, \delta \mathbf{u} = \mathscr{P}_{,\widetilde{\mathbf{A}}}\, \delta \widetilde{\mathbf{A}} = 0$[4].

Considering a given pre-compression λ_1, the principal solution remains stable in the parameter space of the applied magnetic field b_2^0, i.e., $\mathbf{g}_0\left(\lambda_1, b_2^0\right)$ is a local minimizer of the potential energy satisfying $\mathscr{P}_{,\mathbf{gg}}(\mathbf{g}_0) \Delta \mathbf{g} \delta \mathbf{g} > 0$ for any arbitrary perturbation $\delta \mathbf{g} \neq 0$. Upon further increase, the magnetic field reaches a critical value b_2^c, where the solution $\mathbf{g}_0\left(\lambda_1, b_2^c\right)$ is no longer a minimizer of the potential energy. That causes the film to bifurcate under a deformation mode that satisfies the critical condition

$$\mathscr{P}_{,\mathbf{gg}}(\mathbf{g}_0) \delta \mathbf{g} \Delta \mathbf{g} = 0. \tag{IV.16}$$

In virtue of this stability criterion, the present approach aims at exciting the principal solution (i.e., at $\widetilde{B}_i = \widetilde{b}_i = 0, i = 1,2$) [5] and searching for corresponding soft modes, i.e., components of the stiffness matrix that get vanished. To that end, one writes the second variation of the potential energy presented in (III.20) in view of (IV.16) such that

$$\begin{aligned} \Delta \delta \mathscr{P} = & \left(\frac{\partial^2 \mathscr{P}}{\partial F_{kl} \partial F_{ij}} \delta F_{ij} + \frac{\partial^2 \mathscr{P}}{\partial F_{kl} \partial \widetilde{B}_i} \delta \widetilde{B}_i \right) \Delta F_{kl} \\ & + \left(\frac{\partial^2 \mathscr{P}}{\partial \widetilde{B}_k \partial F_{ij}} \delta F_{ij} + \frac{\partial^2 \mathscr{P}}{\partial \widetilde{B}_k \partial \widetilde{B}_i} \delta \widetilde{B}_i \right) \Delta \widetilde{B}_k = 0, \end{aligned} \tag{IV.17}$$

recalling from (III.5) that $\Delta \mathbf{F} = \Delta(\nabla \mathbf{u})$ (or in index notation $\Delta F_{kl} = \Delta u_{k,l}$) and $\Delta \widetilde{\mathbf{B}} = \Delta(\nabla \times \widetilde{\mathbf{A}})$ (or $\Delta \widetilde{B}_k = \Delta \widetilde{A}_{3,l}\, \varepsilon_{3kl} = \Delta a_{,l}\, \varepsilon_{kl}$). Due to the arbitrariness of $\Delta \mathbf{F}$ and $\Delta \widetilde{\mathbf{B}}$, the stability condition in (IV.17)

[4] We also recall the equivalent expressions: $\delta \mathscr{P} = \mathscr{P}_{,\mathbf{u}}\, \delta \mathbf{u} + \mathscr{P}_{,\widetilde{\mathbf{A}}}\, \delta \widetilde{\mathbf{A}} = \frac{\partial \mathscr{P}}{\partial \mathbf{F}} \cdot \frac{\partial \mathbf{F}}{\partial \mathbf{u}} \delta \mathbf{u} + \frac{\partial \mathscr{P}}{\partial \widetilde{\mathbf{B}}} \cdot \frac{\partial \widetilde{\mathbf{B}}}{\partial \widetilde{\mathbf{A}}} \delta \widetilde{\mathbf{A}} = \mathscr{P}_{,\mathbf{F}}\, \delta \mathbf{F} + \mathscr{P}_{,\widetilde{\mathbf{B}}}\, \delta \widetilde{\mathbf{B}} = 0$.

[5] After bifurcation, one can no longer excite the principal solution but the bifurcated one, where $\widetilde{\mathbf{B}} \neq 0$.

reads

$$(\mathscr{P}_{,\mathbf{gu}}\delta\mathbf{g})\,\Delta\mathbf{u} = \left\{ \underbrace{\frac{\partial^2\mathscr{P}}{\partial F_{kl}\partial F_{ij}}}_{\mathscr{P}_{,\mathbf{FF}}}\delta u_{i,j} + \underbrace{\frac{\partial^2\mathscr{P}}{\partial F_{kl}\partial \widetilde{B}_i}}_{\mathscr{P}_{,\widetilde{\mathbf{B}}\mathbf{F}}}\varepsilon_{ij}\,\delta a_{,j} \right\} \underbrace{\Delta u_{k,l}}_{\Delta F_{kl}} = 0 \tag{IV.18}$$

and

$$\left(\mathscr{P}_{,\mathbf{g}\widetilde{\mathbf{A}}}\delta\mathbf{g}\right)\Delta\widetilde{\mathbf{A}} = \left\{ \underbrace{\frac{\partial^2\mathscr{P}}{\partial \widetilde{B}_k\partial F_{ij}}}_{\mathscr{P}_{,\mathbf{F}\widetilde{\mathbf{B}}}}\delta u_{i,j} + \underbrace{\frac{\partial^2\mathscr{P}}{\partial \widetilde{B}_k\partial \widetilde{B}_i}}_{\mathscr{P}_{,\widetilde{\mathbf{B}}\widetilde{\mathbf{B}}}}\varepsilon_{ij}\,\delta a_{,j} \right\} \varepsilon_{kl}\,\underbrace{\Delta a_{,l}}_{\Delta\widetilde{B}_k} = 0. \tag{IV.19}$$

with ',' denoting partial derivation, see full derivations in Sections III.1.1 and III.1.2. Considering the potential energy of the perturbation in (IV.5), the second derivatives with respect to the independent variables $\mathbf{g} \equiv \left\{\mathbf{u}, \widetilde{\mathbf{A}}\right\}$ (or $\left\{\mathbf{F}, \widetilde{\mathbf{B}}\right\}$) can be subsequently assigned to the fourth-order incremental stiffness moduli such that

$$\begin{aligned}\mathscr{L}^{uu}_{ijkl} = \frac{\partial^2\mathscr{P}}{\partial F_{kl}\partial F_{ij}} &= \rho_0\frac{\partial^2\Phi_m(\mathbf{F},\mathbf{B})}{\partial F_{kl}\partial F_{ij}}\Big|_{\widetilde{B}=0} + \frac{1}{2\mu_0 J}\left\|\mathbf{F}\cdot\widetilde{\mathbf{B}}\right\|^2\left(F^{-1}_{lk}F^{-1}_{ji} - F^{-1}_{jk}F^{-1}_{li}\right)\\ &- \frac{1}{\mu_0 J}\left(F_{ks}\widetilde{B}_s\widetilde{B}_l F^{-1}_{ji} + F_{im}\widetilde{B}_m F^{-1}_{lk}\widetilde{B}_j - \delta_{ik}\widetilde{B}_l\widetilde{B}_j\right) = \frac{\partial^2\mathscr{P}}{\partial F_{ij}\partial F_{kl}} = \mathscr{L}^{uu}_{klij}\end{aligned} \tag{IV.20}$$

while the tangential $\Delta\mathbf{u}$ and $\Delta\widetilde{\mathbf{A}}$ components, i.e., third-order incremental moduli, get

$$\begin{aligned}\mathscr{L}^{au}_{jkl} = \frac{\partial^2\mathscr{P}}{\partial F_{kl}\partial \widetilde{B}_i}\varepsilon_{ij} &= \left\{\rho_0\frac{\partial^2\Phi_m(\mathbf{F},\mathbf{B})}{\partial F_{kl}\partial \widetilde{B}_i}\Big|_{\widetilde{B}=0} + \frac{1}{\mu_0 J}\left(-F^{-1}_{lk}C_{ip}\widetilde{B}_p + \widetilde{B}_l F_{ki} + F_{kp}\widetilde{B}_p\delta_{il}\right)\right\}\varepsilon_{ij}\\ &= \frac{\partial^2\mathscr{P}}{\partial \widetilde{B}_k\partial F_{ij}}\varepsilon_{kl} = \mathscr{L}^{u\tilde{b}}_{ijk}\cdot\mathscr{L}^{\tilde{b}a}_{kl} = \mathscr{L}^{ua}_{ijl}\end{aligned} \tag{IV.21}$$

and the remaining term of the $\Delta\widetilde{\mathbf{A}}$ component, i.e., second-order incremental moduli

$$\mathscr{L}^{aa}_{jl} = \varepsilon_{ij}\frac{\partial^2\mathscr{P}}{\partial \widetilde{B}_k\partial \widetilde{B}_i}\varepsilon_{kl} = \varepsilon_{ij}\left\{\rho_0\frac{\partial^2\Phi_m(\mathbf{F},\mathbf{B})}{\partial \widetilde{B}_k\partial \widetilde{B}_i}\Big|_{\widetilde{B}=0} + \frac{1}{\mu_0 J}C_{ki}\right\}\varepsilon_{kl} = \varepsilon_{ij}\frac{\partial^2\mathscr{P}}{\partial \widetilde{B}_i\partial \widetilde{B}_k}\varepsilon_{kl} = \mathscr{L}^{\tilde{a}b}_{ji}\cdot\mathscr{L}^{\tilde{b}\tilde{b}}_{ik}\cdot\mathscr{L}^{\tilde{b}a}_{kl} = \mathscr{L}^{aa}_{lj}, \tag{IV.22}$$

where $m = f, s$ for the film and the substrate, respectively (or else for the air: $\Phi_a = 0$). We also note that the function $\Phi_m(\mathbf{F},\mathbf{B})$ is different from the function $\Phi_m\left(\mathbf{F},\widetilde{\mathbf{B}}\right)$. However, their derivatives [6] are the same since

$$\frac{\partial\Phi_m}{\partial B_i} = \frac{\partial\Phi_m}{\partial \widetilde{B}_j}\frac{\partial \widetilde{B}_j}{\partial B_i} = \frac{\partial\Phi_m}{\partial \widetilde{B}_j}\delta_{ji}. \tag{IV.23}$$

As a result, the first- and second-order derivations of the function $\Phi_m(\mathbf{F},\mathbf{B})$ in (IV.7) with respect to $\mathbf{g} \equiv \{\mathbf{F}, \widetilde{\mathbf{B}}\}$ are given by the relations in (III.57) and (III.62)–(III.64), where $\mathbf{B}$ is substituted by $\widetilde{\mathbf{B}}$.

[6] and thus, $\frac{\partial^2\Phi_m}{\partial F_{kl}\partial B_i} = \frac{\partial}{\partial F_{kl}}\left(\frac{\partial\Phi_m}{\partial B_i}\right) = \frac{\partial}{\partial F_{kl}}\left(\frac{\partial\Phi_m}{\partial \widetilde{B}_i}\right) = \frac{\partial^2\Phi_m}{\partial F_{kl}\partial \widetilde{B}_i}$.

Writing (IV.18) (and (IV.19)) in view of (IV.20) and (IV.21) ((IV.21) and (IV.22)), one gets

$$\begin{aligned}
&(\mathscr{P}_{,\mathbf{g}\mathbf{u}}\delta\mathbf{g})\,\Delta\mathbf{u}=0\Rightarrow\int_{\mathbb{R}^3}\left(\mathscr{L}^{uu}_{ijkl}\delta u_{i,j}+\mathscr{L}^{au}_{jkl}\delta a_{,j}\right)\Delta u_{k,l}\,\mathrm{d}\Omega=0,\\
&\left(\mathscr{P}_{,\mathbf{g}\tilde{\mathbf{A}}}\delta\mathbf{g}\right)\Delta\tilde{\mathbf{A}}=0\Rightarrow\int_{\mathbb{R}^3}\left(\mathscr{L}^{ua}_{ijl}\delta u_{i,j}+\mathscr{L}^{aa}_{jl}\delta a_{,j}\right)\Delta a_{,l}\,\mathrm{d}\Omega=0,
\end{aligned}\tag{IV.24}$$

which yield the Euler-Lagrange differential equations after standard integration by parts,[7] such that

$$\begin{aligned}
&\left\{\left(\mathscr{L}^{uu}_{ijkl}\delta u_{i,j}+\mathscr{L}^{au}_{jkl}\delta a_{,j}\right)_{,l}\right\}_m=0,\quad\mathbf{X}\in\mathbb{R}^3\\
&\left\{\left(\mathscr{L}^{ua}_{ijl}\delta u_{i,j}+\mathscr{L}^{aa}_{jl}\delta a_{,j}\right)_{,l}\right\}_m=0,\quad\mathbf{X}\in\mathbb{R}^3.
\end{aligned}\tag{IV.25}$$

with $m=f,s,a$ for the film, the substrate and the air, respectively. Note that the coupled terms $\mathscr{L}^{au}_{jkl},\mathscr{L}^{ua}_{ijl}$ are zero for the substrate and the air when one works on the perturbation problem, but nonzero when ones uses the total magnetic vector potential $\mathbf{A}$ (instead of $\tilde{\mathbf{A}}$) as independent variable. The absence of deformation in the air is satisfied by setting $\mathbf{F}=\mathbf{I}$ and thus, the magnetic term $\mathscr{L}^{aa}_{jl}$ of the air is indeed existent. These equations need to be supplemented with the appropriate natural boundary/interface conditions at the MRE film/substrate interface and the MRE film/air boundary, which are found to be from (IV.18) and (IV.19)

$$\begin{aligned}
\left\{\mathscr{L}^{uu}_{ijk2}\delta u_{i,j}+\mathscr{L}^{au}_{jk2}\delta a_{,j}\right\}_f&=\left\{\mathscr{L}^{uu}_{ijk2}\delta u_{i,j}\right\}_s,\quad(X_1,X_2)\in\mathbb{R}^3\times\{0\}\\
\left\{\mathscr{L}^{ua}_{ij2}\delta u_{i,j}+\mathscr{L}^{aa}_{j2}\delta a_{,j}\right\}_f&=\left\{\mathscr{L}^{aa}_{j2}\delta a_{,j}\right\}_s,\quad(X_1,X_2)\in\mathbb{R}^3\times\{0\}\\
\left\{\mathscr{L}^{uu}_{ijk2}\delta u_{i,j}+\mathscr{L}^{au}_{jk2}\delta a_{,j}\right\}_f&=\left\{\mathscr{L}^{uu}_{ijk2}\delta u_{i,j}\right\}_a,\quad(X_1,X_2)\in\mathbb{R}^3\times\{h\}\\
\left\{\mathscr{L}^{ua}_{ij2}\delta u_{i,j}+\mathscr{L}^{aa}_{j2}\delta a_{,j}\right\}_f&=\left\{\mathscr{L}^{aa}_{j2}\delta a_{,j}\right\}_a,\quad(X_1,X_2)\in\mathbb{R}^3\times\{h\}.
\end{aligned}\tag{IV.26}$$

Taking the interface conditions at the film/substrate interface (the same is valid for the film/air boundary), one has

$$\begin{aligned}
(k=1)\quad&\left\{\mathscr{L}^{uu}_{1212}\delta u_{1,2}+\mathscr{L}^{uu}_{2112}\delta u_{2,1}+\varepsilon_{12}\mathscr{L}^{\tilde{b}u}_{112}\delta a_{,2}\right\}_f=\left\{\mathscr{L}^{uu}_{1212}\delta u_{1,2}+\mathscr{L}^{uu}_{2112}\delta u_{2,1}\right\}_s,\\
(k=2)\quad&\left\{\mathscr{L}^{uu}_{1122}\delta u_{1,1}+\mathscr{L}^{uu}_{2222}\delta u_{2,2}+\varepsilon_{21}\mathscr{L}^{\tilde{b}u}_{222}\delta a_{,1}\right\}_f=\left\{\mathscr{L}^{uu}_{1122}\delta u_{1,1}+\mathscr{L}^{uu}_{2222}\delta u_{2,2}\right\}_s,\\
&\left\{\mathscr{L}^{u\tilde{b}}_{121}\varepsilon_{12}\delta u_{1,2}+\mathscr{L}^{u\tilde{b}}_{211}\varepsilon_{12}\delta u_{2,1}+\varepsilon_{12}\mathscr{L}^{\tilde{b}\tilde{b}}_{11}\varepsilon_{12}\delta a_{,2}\right\}_f=\left\{\varepsilon_{12}\mathscr{L}^{\tilde{b}\tilde{b}}_{11}\varepsilon_{12}\delta a_{,2}\right\}_s,\ (X_1,X_2)\in\mathbb{R}^3\times\{0\}
\end{aligned}\tag{IV.27}$$

where $\varepsilon_{ij}\equiv\varepsilon_{ij3}$ the Levi-Civita operator, with $i,j=1,2$. To the above natural boundary/interface conditions, one must also add the essential boundary/interface conditions. The latter reflect the continuity of displacement and magnetic perturbation potential, as seen in (IV.11). Here, we should note that the rest of the coupled components are zero and thus, do not appear in the Euler-Lagrange equations or in the boundary conditions, e.g., $\mathscr{L}^{u\tilde{b}}_{111}=\mathscr{L}^{u\tilde{b}}_{221}=\mathscr{L}^{u\tilde{b}}_{122}=\mathscr{L}^{u\tilde{b}}_{212}=0$.

[7] e.g., $\left(\mathscr{L}^{uu}_{ijkl}\delta u_{i,j}+\mathscr{L}^{au}_{jkl}\delta a_{,j}\right)\Delta u_{k,l}=\left[\left(\mathscr{L}^{uu}_{ijkl}\delta u_{i,j}+\mathscr{L}^{au}_{jkl}\delta a_{,j}\right)\Delta u_k\right]_{,l}-\left(\mathscr{L}^{uu}_{ijkl}\delta u_{i,j}+\mathscr{L}^{au}_{jkl}\delta a_{,j}\right)_{,l}\Delta u_k$

MRE film. The Euler-Lagrange equations for the MRE film read

$$\begin{aligned} &\left\{\mathscr{L}^{uu}_{ijkl}\delta u_{i,jl}+\mathscr{L}^{au}_{jkl}\delta a_{,jl}\right\}_f=0\\ \text{and}\quad &\left\{\mathscr{L}^{ua}_{ijl}\delta u_{i,jl}+\mathscr{L}^{aa}_{jl}\delta a_{,jl}\right\}_f=0,\quad (X_1,X_2)\in\mathbb{R}^3\times[0,h]. \end{aligned} \tag{IV.28}$$

The X_2-invariance of the principal solution allows a Fourier decomposition of the eigenmode with ω the corresponding wavenumber, such that

$$\begin{aligned} \Delta u_j(X_1,X_2)&=e^{i\omega X_1}\sum_I \Delta U^I_j e^{J_I\omega X_2}\\ \text{and}\quad \Delta a(X_1,X_2)&=e^{i\omega X_1}\sum_I \Delta\widetilde{A}^I e^{J_I\omega X_2}, \end{aligned} \tag{IV.29}$$

where I the number of independent eigenmodes and J_I the eigenvalues (per material phase). The unknowns of the problem are the $\Delta U^I_1, \Delta U^I_2$ and $\Delta\widetilde{A}^I$. Taking the first and second derivatives of the preferable form of solution (IV.29) with respect to X_1 and X_2 and introducing them into the Euler-Lagrange equations (IV.28), one gets the following algebraic system with constant coefficients in direction X_1 ($l=1$)

$$\begin{aligned} (k=1)\quad &\left(-\mathscr{L}^{uu}_{1111}\sum_I\Delta U^I_1+i\,\mathscr{L}^{uu}_{2211}\sum_I J_I\Delta U^I_2-\varepsilon_{21}\,\mathscr{L}^{\tilde{b}u}_{211}\sum_I\Delta\widetilde{A}^I\right)\omega^2\,e^{i\,\omega X_1}e^{J_I\omega X_2}=0,\\ (k=2)\quad &\left(i\,\mathscr{L}^{uu}_{1221}\sum_I J_I\Delta U^I_1-\mathscr{L}^{uu}_{2121}\sum_I\Delta U^I_2+i\,\varepsilon_{12}\,\mathscr{L}^{\tilde{b}u}_{121}\sum_I J_I\Delta\widetilde{A}^I\right)\omega^2\,e^{i\,\omega X_1}e^{J_I\omega X_2}=0,\\ &\left(-\mathscr{L}^{u\tilde{b}}_{112}\varepsilon_{21}\sum_I\Delta U^I_1+i\,\mathscr{L}^{u\tilde{b}}_{222}\varepsilon_{21}\sum_I J_I\Delta U^I_2-\varepsilon_{21}\,\mathscr{L}^{\tilde{b}\tilde{b}}_{22}\varepsilon_{21}\sum_I\Delta\widetilde{A}^I\right)\omega^2\,e^{i\,\omega X_1}e^{J_I\omega X_2}=0 \end{aligned} \tag{IV.30}$$

and the relevant system of equations in direction X_2 ($l=2$)

$$\begin{aligned} (k=1)\quad &\left(\mathscr{L}^{uu}_{1212}\sum_I J^2_I\,\Delta U^I_1+i\,\mathscr{L}^{uu}_{2112}\sum_I J^I\Delta U^I_2+\varepsilon_{12}\,\mathscr{L}^{\tilde{b}u}_{112}\sum_I J^2_I\,\Delta\widetilde{A}^I\right)\omega^2\,e^{i\,\omega X_1}e^{J_I\omega X_2}=0,\\ (k=2)\quad &\left(i\,\mathscr{L}^{uu}_{1122}\sum_I J_I\,\Delta U^I_1+\mathscr{L}^{uu}_{2222}\sum_I J^2_I\,\Delta U^I_2+i\,\varepsilon_{21}\mathscr{L}^{\tilde{b}u}_{222}\sum_I J_I\,\Delta\widetilde{A}^I\right)\omega^2\,e^{i\,\omega X_1}e^{J_I\omega X_2}=0,\\ &\left(\mathscr{L}^{u\tilde{b}}_{121}\,\varepsilon_{12}\sum_I J^2_I\Delta U^I_1+i\,\mathscr{L}^{u\tilde{b}}_{211}\,\varepsilon_{12}\sum_I J^I\Delta U^I_2+\varepsilon_{12}\,\mathscr{L}^{\tilde{b}\tilde{b}}_{11}\,\varepsilon_{12}\sum_I J^2_I\,\Delta\widetilde{A}^I\right)\omega^2\,e^{i\,\omega X_1}e^{J_I\omega X_2}=0, \end{aligned} \tag{IV.31}$$

which can be written in implicit eigenvalue form for J_I, with $(\Delta U^I_1, \Delta U^I_2, \Delta\widetilde{A}^I)$ the corresponding

amplitudes, such that

$$\underbrace{\begin{bmatrix} -\mathscr{L}^{uu}_{1111}+J_I^2\,\mathscr{L}^{uu}_{1212} & iJ_I(\mathscr{L}^{uu}_{2211}+\mathscr{L}^{uu}_{2112}) & \mathscr{L}^{\tilde{b}u}_{211}+J_I^2\,\mathscr{L}^{\tilde{b}u}_{112} \\ iJ_I(\mathscr{L}^{uu}_{1221}+\mathscr{L}^{uu}_{1122}) & -\mathscr{L}^{uu}_{2121}+J_I^2\,\mathscr{L}^{uu}_{2222} & iJ_I\left(\mathscr{L}^{\tilde{b}u}_{121}-\mathscr{L}^{\tilde{b}u}_{222}\right) \\ \mathscr{L}^{u\tilde{b}}_{112}+J_I^2\,\mathscr{L}^{u\tilde{b}}_{121} & iJ_I\left(-\mathscr{L}^{u\tilde{b}}_{222}+\mathscr{L}^{u\tilde{b}}_{211}\right) & -\mathscr{L}^{\tilde{b}\tilde{b}}_{22}+J_I^2\,\mathscr{L}^{\tilde{b}\tilde{b}}_{11} \end{bmatrix}}_{Q^f(J_I)} \begin{Bmatrix} \Delta U^I_1 \\ \Delta U^I_2 \\ \Delta\widetilde{A}^I \end{Bmatrix} = 0, \tag{IV.32}$$

where J_I the six roots of the bi-cubic characteristic equation, implying that the integer I ranges from 1 to 6. In order to have a non-trivial solution of the system, the determinant of the tensor Q^f must vanish, i.e., $\det Q^f(J_I)=0$, $1\le I\le 6$. In this way, solving for the J_I roots yields 6×3 eigenmodes (or vector of unknowns: $\mathscr{H}^f_q=\Delta U^I_1,\Delta U^I_2,\Delta\widetilde{A}^I$, $1\le I\le 6$).

For each root J_I, one can find from (IV.32) the linear relationship between the corresponding ΔU^I_j and $\Delta\widetilde{A}^I$; $1\le j\le 2, 1\le I\le 6$, such that

$$\Delta U^I_2=\underbrace{\frac{Q^f_{21}Q^f_{13}-Q^f_{11}Q^f_{23}}{Q^f_{11}Q^f_{22}-Q^f_{21}Q^f_{12}}}_{\Delta\mathscr{U}^I_2}\Delta\widetilde{A}^I,\quad \Delta U^I_1=\underbrace{-\frac{Q^f_{12}}{Q^f_{11}}\Delta U^I_2+\frac{Q^f_{13}}{Q^f_{11}}}_{\Delta\mathscr{U}^I_1}\Delta\widetilde{A}^I, \tag{IV.33}$$

where the coefficients Q^f_{ij}, $i,j=1,2,3$ (introduced for convenience in notation) are functions of the constants $\mathscr{L}_{uu},\mathscr{L}_{u\tilde{b}},\mathscr{L}_{\tilde{b}u},\mathscr{L}_{\tilde{b}\tilde{b}}$ defined in (IV.32). As a result, one reduces the equations of the film from 18 to 6, written in terms of $\Delta\widetilde{A}^I$.

Passive substrate. The system of equations for the substrate is significantly simplified since it has no magnetomechanical coupling. The Euler-Lagrange equations for the passive substrate read

$$\left\{\mathscr{L}^{uu}_{ijkl}\delta u_{i,jl}\right\}_s=0\quad\text{and}\quad\left\{\mathscr{L}^{aa}_{jl}\delta a_{,jl}\right\}_s=0,\quad (X_1,X_2)\in\mathbb{R}^3\times(-\infty,0). \tag{IV.34}$$

The form of solution that one searches for is

$$\begin{aligned}\Delta u_j(X_1,X_2)&=e^{i\omega X_1}\sum_I\Delta V^I_j e^{\xi_I\omega X_2}\\ \text{and}\quad\Delta a(X_1,X_2)&=e^{i\omega X_1}\sum_I\Delta\widetilde{A}^I_s e^{\theta_s\omega X_2},\end{aligned} \tag{IV.35}$$

where I the number of independent eigenmodes and ξ_I and θ_s the eigenvalues. The unknowns of the problem are the ΔV^I_1 and $\Delta\widetilde{A}^I_s$. For the Δu component of the eigenmode, substitution of (IV.35) into (IV.34) leads to the following algebraic eigenvalue problem for ξ_I and the corresponding amplitudes

$(\Delta V_1^I, \Delta V_2^I)$:

$$\underbrace{\begin{bmatrix} -\mathscr{L}^{uu}_{1111} + \xi_I^2\,\mathscr{L}^{uu}_{1212} & i\,\xi_I\,(\mathscr{L}^{uu}_{2211} + \mathscr{L}^{uu}_{2112}) \\ i\,\xi_I\,(\mathscr{L}^{uu}_{1221} + \mathscr{L}^{uu}_{1122}) & -\mathscr{L}^{uu}_{2121} + \xi_I^2\,\mathscr{L}^{uu}_{2222} \end{bmatrix}}_{Q^s(\xi_I)} \begin{Bmatrix} \Delta V_1^I \\ \Delta V_2^I \end{Bmatrix} = 0, \tag{IV.36}$$

In the above expression, ξ_I are the four roots of the bi-quadratic characteristic equation. However, the decay condition for the eigenmode $\Delta\mathbf{u}$ reads $\Delta\mathbf{u} \to 0$ as $X_2 \to -\infty$. In order for this conditions to be satisfied, it is straightforward from $(\text{IV.35})_1$ that when $-\infty < X_2 < 0$, then $\xi_I\,\omega > 0$, with $\omega > 0$ and thus, one gets $Re(\xi_I) > 0$. As a result, out of the four complex roots, only the two with positive real part are considered. This implies that I ranges from 1 to 2.

In order to find a non-trivial solution of the system, the following conditions needs to be satisfied: $\det Q^s(\xi^I) = 0$; $Re(\xi^I) > 0, 1 \le I \le 2$. For each root ξ_I of (IV.36), one can find the linear relationship between ΔV_1^I and ΔV_2^I, namely:

$$\Delta V_2^I = \underbrace{-\frac{Q^s_{11}}{Q^s_{12}}}_{\Delta\mathscr{V}_2^I}\,\Delta V_1^I, \tag{IV.37}$$

where the coefficients $Q^s_{ij}\,(i,j=1,2)$ are functions of the constants $\mathscr{L}_{uu}$ defined in (IV.36). For the independent Δa component of the eigenmode, substitution of $(\text{IV.35})_2$ into $(\text{IV.34})_2$ leads to the following algebraic equation, relating θ_s to the corresponding amplitude $\Delta\widetilde{A}_s^I$:

$$\left[-\mathscr{L}^{\widetilde{b}\widetilde{b}}_{22} + \theta_s^2\,\mathscr{L}^{\widetilde{b}\widetilde{b}}_{11}\right]\cdot\Delta\widetilde{A}_s^I = 0, \quad 1 \le I \le 2; \quad \theta_s = \left(\frac{\mathscr{L}^{\widetilde{b}\widetilde{b}}_{22}}{\mathscr{L}^{\widetilde{b}\widetilde{b}}_{11}}\right)^{1/2}. \tag{IV.38}$$

Similarly, out of the two real roots of the above equation (it can be shown that $\mathscr{L}^{\widetilde{b}\widetilde{b}}_{22}/\mathscr{L}^{\widetilde{b}\widetilde{b}}_{11} > 0$), only the positive root is considered in order to satisfy the decay condition $\Delta a \to 0$ for the eigenmode as $X_2 \to -\infty$. Here, we recall that $A_3 = a + A_3^0$ and thus, the eigenmode corresponding to the total magnetic vector is $\Delta A(X_1, X_2) = e^{i\omega X_1}\sum_I \Delta\widetilde{A}_a^I\, e^{\theta_a \omega X_2} + \varepsilon_{ijk} B_j^0 X_k$. Now, if $-\infty < X_2 < 0$ then $\theta_a > 0$, so as to have $\widetilde{B}_i \to 0$ $(1 \le i \le 2)$ as $X_2 \to -\infty$, meaning that $b_i = b_i^0$ at $X_2 \to -\infty$. In this way, the total number of system equations for the substrate is reduced from 5 to 3 considering a vector of unknowns: $\mathscr{H}_q^s = \Delta V_1^I, \Delta\widetilde{A}_s,\ 1 \le I \le 2)$.

Air. The system of equations for the air is also simplified, since $\widetilde{\mathbf{B}} = 0$ vanishes $\mathscr{L}_{uu}, \mathscr{L}_{au}, \mathscr{L}_{ua}$ components in (IV.20) and (IV.21). The Euler-Lagrange equations for the air simply read

$$\left\{\mathscr{L}^{aa}_{jl}\,\delta a_{,jl}\right\}_a = 0, \quad (X_1, X_2) \in \mathbb{R}^3 \times (h, +\infty). \tag{IV.39}$$

As before, the following eigenmode Δa is the solution of the constant coefficient equation (IV.39):

$$\Delta a(X_1,X_2) = e^{i\omega X_1}\sum_I \Delta\widetilde{A}_a^I e^{\theta_a \omega X_2}. \tag{IV.40}$$

Upon substitution of the eigenmode expression (IV.40) into the governing equation (IV.39), one obtains the following relation between θ_a and the corresponding amplitude $\Delta\widetilde{A}_a^I$

$$\left[-\mathscr{L}^{\widetilde{bb}}_{22} + \theta_a^2 \mathscr{L}^{\widetilde{bb}}_{11}\right]\cdot \Delta\widetilde{A}_a^I = 0, \quad 1\le I\le 2; \quad \theta_a = \left(\frac{\mathscr{L}^{\widetilde{bb}}_{22}}{\mathscr{L}^{\widetilde{bb}}_{11}}\right)^{1/2}, \tag{IV.41}$$

where again one can easily show that $\mathscr{L}^{\widetilde{bb}}_{22}/\mathscr{L}^{\widetilde{bb}}_{11} > 0$. Since $\Delta a \to 0$ for the eigenmode as $X_2 \to +\infty$ (so as $\mathbf{B} = \mathbf{B}_0$ at infinity), it is straightforward from (IV.40) that $\theta_a \omega < 0$, with $\omega > 0$ when $0 < X_2 < +\infty$ and thus, $\theta_a < 0$. That implies that only the negative root is considered to satisfy the decay condition. Consequently, only one equation is considered for the air, corresponding to the unknown $\Delta\widetilde{A}_a = \mathscr{H}_q^a$.

Determination of critical loads and corresponding eigenmodes

The critical loads and corresponding eigenmodes can been found upon substitution of the preferable form of (eigenmode) solution on the natural and essential boundary/interface conditions. To this end, recalling from (IV.26) and (IV.11) the natural and essential interface conditions and taking into account the orthotropy of the incremental moduli tensor $\mathscr{L}$, one obtains (see also (IV.27)) at the film/substrate interface, $(X_1,X_2)\in\mathbb{R}^3\times\{0\}$

$$\begin{aligned}
&\left\{\mathscr{L}^{uu}_{1212}\delta u_{1,2} + \mathscr{L}^{uu}_{2112}\delta u_{2,1} + \mathscr{L}^{\widetilde{bu}}_{112}\delta a_{,2}\right\}_f = \left\{\mathscr{L}^{uu}_{1212}\delta u_{1,2} + \mathscr{L}^{uu}_{2112}\delta u_{2,1}\right\}_s,\\
&\left\{\mathscr{L}^{uu}_{1122}\delta u_{1,1} + \mathscr{L}^{uu}_{2222}\delta u_{2,2} - \mathscr{L}^{\widetilde{bu}}_{222}\delta a_{,1}\right\}_f = \left\{\mathscr{L}^{uu}_{1122}\delta u_{1,1} + \mathscr{L}^{uu}_{2222}\delta u_{2,2}\right\}_s,\\
&\left\{\mathscr{L}^{u\widetilde{b}}_{121}\delta u_{1,2} + \mathscr{L}^{u\widetilde{b}}_{211}\delta u_{2,1} + \mathscr{L}^{\widetilde{bb}}_{11}\delta a_{,2}\right\}_f = \left\{\mathscr{L}^{\widetilde{bb}}_{11}\delta a_{,2}\right\}_s,\\
&\{\Delta u_1\}_f = \{\Delta u_1\}_s,\\
&\{\Delta u_2\}_f = \{\Delta u_2\}_s,\\
&\{\Delta a\}_f = \{\Delta a\}_s
\end{aligned} \tag{IV.42}$$

and at the film/air boundary, $(X_1,X_2)\in\mathbb{R}^3\times\{h\}$

$$\begin{aligned}
&\left\{\mathscr{L}^{uu}_{1212}\delta u_{1,2} + \mathscr{L}^{uu}_{2112}\delta u_{2,1} + \mathscr{L}^{\widetilde{bu}}_{112}\delta a_{,2}\right\}_f = 0,\\
&\left\{\mathscr{L}^{uu}_{1122}\delta u_{1,1} + \mathscr{L}^{uu}_{2222}\delta u_{2,2} - \mathscr{L}^{\widetilde{bu}}_{222}\delta a_{,1}\right\}_f = 0,\\
&\left\{\mathscr{L}^{u\widetilde{b}}_{121}\delta u_{1,2} + \mathscr{L}^{u\widetilde{b}}_{211}\delta u_{2,1} + \mathscr{L}^{\widetilde{bb}}_{11}\delta a_{,2}\right\}_f = \left\{\mathscr{L}^{\widetilde{bb}}_{11}\delta a_{,2}\right\}_a,\\
&\{\Delta a\}_f = \{\Delta a\}_a.
\end{aligned} \tag{IV.43}$$

In view of (IV.33), we recall that the eigenmodes of the film ΔU_i^I $(i=1,2;\ I=1..6)$ are written in terms of $\Delta\widetilde{A}^I$, such that $\Delta U_i^I = \Delta\mathscr{U}_i^I\cdot\Delta\widetilde{A}^I$. In view of (IV.37), the substrate eigenmodes ΔV_2^J $(J=1,2)$

are written in terms of ΔV_1^J, i.e., $\Delta V_2^J = \Delta \mathscr{V}_2^J \cdot \Delta V_1^J$. Substituting the eigenmode expressions of each layer, according to (IV.29), (IV.35) and (IV.40), into the interface/boundary conditions (IV.42) and (IV.43), we recover a 10×10 linear system, written in implicit form

$$\sum_{q=1}^{10} \mathscr{D}_{pq}(\Lambda, \omega H)\mathscr{H}_q = 0, \quad 1 \leq p \leq 10 \tag{IV.44}$$

with $\mathscr{H}_q$ the total vector of unknowns

$$\mathscr{H}_q = \{\mathscr{H}_q^f, \mathscr{H}_q^s, \mathscr{H}_q^a, \} = \left\{\Delta\widetilde{A}^I, \Delta V_1^J, \Delta\widetilde{A}_s, \Delta\widetilde{A}_a\right\}, \quad 1 \leq I \leq 6; \quad 1 \leq J \leq 2. \tag{IV.45}$$

and $\mathscr{D}_{pq}$ $(p,q = 1..10)$ the Jacobian matrix coefficients, such that

$$\mathscr{D}_{1q} = \left\{J_I \mathscr{L}^{uu}_{1212}\Delta\mathscr{U}_1^I + i\mathscr{L}^{uu}_{2112}\Delta\mathscr{U}_2^I + J_I\mathscr{L}^{\widetilde{bu}}_{112}\right\}_f, \quad q = 1,..,6$$
$$\mathscr{D}_{1q} = -\left\{\xi_I \mathscr{L}^{uu}_{1212} + i\mathscr{L}^{uu}_{2112}\Delta\mathscr{V}_2^I\right\}_s, \quad q = 7,8, \quad \mathscr{D}_{1q} = 0, \quad q = 9,10$$

$$\mathscr{D}_{2q} = \left\{i\mathscr{L}^{uu}_{1122}\Delta\mathscr{U}_1^I + J_I\mathscr{L}^{uu}_{2222}\Delta\mathscr{U}_2^I - i\mathscr{L}^{\widetilde{bu}}_{222}\right\}_f, \quad I = 1,..,6, \quad q = I$$
$$\mathscr{D}_{2q} = -\left\{i\mathscr{L}^{uu}_{1122} + \xi_I\mathscr{L}^{uu}_{2222}\Delta\mathscr{U}_2^I\right\}_s, \quad q = 7,8, \quad \mathscr{D}_{2q} = 0, \quad q = 9,10$$

$$\mathscr{D}_{3q} = \left\{J_I\mathscr{L}^{\widetilde{ub}}_{121}\Delta\mathscr{U}_1^I + i\mathscr{L}^{\widetilde{ub}}_{211}\Delta\mathscr{U}_2^I + J_I\mathscr{L}^{\widetilde{bb}}_{11}\right\}_f, \quad I = 1,..,6, \quad q = I$$
$$\mathscr{D}_{39} = -\left\{\theta_s\mathscr{L}^{\widetilde{bb}}_{11}\right\}_s, \quad \mathscr{D}_{3q} = 0, \quad q = 7,8,10$$

$$\mathscr{D}_{4q} = \left\{\Delta\mathscr{U}_1^I\right\}_f, \quad I = 1,..,6, \quad q = I$$
$$\mathscr{D}_{4q} = 1, \quad q = 7,8, \quad \mathscr{D}_{4q} = 0, \quad q = 9,10$$

$$\mathscr{D}_{5q} = \left\{\Delta\mathscr{U}_2^I\right\}_f, \quad I = 1,..,6, \quad q = I$$
$$\mathscr{D}_{5q} = -\left\{\Delta\mathscr{V}_2^I\right\}_f, \quad q = 7,8, \quad \mathscr{D}_{5q} = 0, \quad q = 9,10$$

$$\mathscr{D}_{6q} = 1, \quad I = 1,..,6, \quad q = I$$
$$\mathscr{D}_{69} = 1, \quad \mathscr{D}_{6q} = 0, \quad q = 7,8,10$$

$$\mathscr{D}_{7q} = \left\{\left[J_I\mathscr{L}^{uu}_{1212}\Delta\mathscr{U}_1^I + i\mathscr{L}^{uu}_{2112}\Delta\mathscr{U}_2^I + J_I\mathscr{L}^{\widetilde{bu}}_{112}\right]e^{J_I\omega h}\right\}_f, \quad I = 1,..,6, \quad q = I$$
$$\mathscr{D}_{7q} = 0, \quad I = 1,..,4, \quad q = I+6$$

$$\mathscr{D}_{8q} = \left\{\left[i\mathscr{L}^{uu}_{1122}\Delta\mathscr{U}_1^I + J_I\mathscr{L}^{uu}_{2222}\Delta\mathscr{U}_2^I - i\mathscr{L}^{\widetilde{bu}}_{222}\right]e^{J_I\omega h}\right\}_f, \quad I = 1,..,6, \quad q = I$$

$$\mathscr{D}_{8q} = 0, \quad I = 1,..,4, \quad q = I+6$$

$$\mathscr{D}_{9q} = \left\{ \left[J_I \mathscr{L}^{\widetilde{ub}}_{121} \Delta \mathscr{U}^I_1 + i \mathscr{L}^{\widetilde{ub}}_{211} \Delta \mathscr{U}^I_2 + J_I \mathscr{L}^{\widetilde{\widetilde{bb}}}_{11} \right] e^{J_I \omega h} \right\}_f, \quad I = 1,..,6, \quad q = I$$
$$\mathscr{D}_{910} = -\left\{ \left[\theta_a \mathscr{L}^{\widetilde{\widetilde{bb}}}_{11} \right] e^{\theta_a \omega h} \right\}_a, \quad \mathscr{D}_{9q} = 0, \quad I = 1,2,3 \quad q = I+6$$

$$\mathscr{D}_{10q} = \left\{ e^{J_I \omega h} \right\}_f, \quad I = 1,..,6, \quad q = I$$
$$\mathscr{D}_{1010} = -\left\{ e^{\theta_a \omega h} \right\}_a, \quad \mathscr{D}_{10q} = 0, \quad I = 1,2,3 \quad q = I+6$$

In the eigenvalue bifurcation problem, we search for the loads Λ that lead the model stiffness matrix to become singular, so that the problem $\mathscr{D}\mathscr{H} = 0$ has nontrivial solutions. The critical load $\Lambda = \{\lambda_1, b_0^c\}$ is found from the vanishing of the determinant of the 10×10 matrix in order to have a non-trivial solution, i.e., $\det \mathscr{D}((\lambda_1, b_0^c), \omega h) = 0$. The critical values $\{\lambda_1, b_0^c\}$ are those that minimize $1 - \lambda_1 \geq 0$ and $b_0^c \geq 0$, over all non-dimensional wavenumbers $\omega h \in \mathbb{R}$ along the chosen loading path. Note that the stability criterion is based on the incremental positive definitess of the tangent (Jacobian $\mathscr{D}$) stiffness matrix, i.e., the second derivatives of the potential energy with respect to the independent variables. Such an approach is called the "bloch-wave" problem.

IV.4 Theoretical results

To summarize the bifurcation method, an infinitely long plane-strain system made of a magnetoelastic film bonded on a infinitely deep elastic substrate is subjected to a magnetomechanical loading. The loading consists of applying compression along the X_1 direction, keeping $\lambda_1 (< 1)$ constant and subsequently increasing magnetic field b_2^0 along the X_2 direction. Given the applied pre-stretch $\lambda_1 \equiv \lambda_0$, one subsequently solves for the out-of-plane stretch λ_2 for zero out-of-plane traction ($t_2 = 0$) along the film top boundary ($(X_1, X_2) \in \mathbb{R}^2 \times \{h\}$) and the film/substrate interface ($(X_1, X_2) \in \mathbb{R}^2 \times \{0\}$). The stability of the principal solution is satisfied by incremental verification of the positive definitess of the stiffness matrix, which includes the second derivatives of the potential energy with respect to the admissible displacement field $\mathbf{u}$ and the magnetic vector potential $\mathbf{A}$. The film is made of a nonlinear elastic, slightly compressible and very soft material that magnetostrictively responds to magnetic fields. This material is fairly approximated by a neo-Hookean model combined with either a Langevin saturation magnetization (IV.7) or with a linear magnetoelastic model (IV.8) (i.e., the first order term of the Langevin function expansion about small magnetic fields, $\mathbf{B} \to 0$, see Section IV.2). The nonlinear elastic substrate is also modeled as a neo-Hookean solid. The present development pertains to the onset of the bifurcation in the bilayer system and does not deal with the stability of the bifurcated branches.

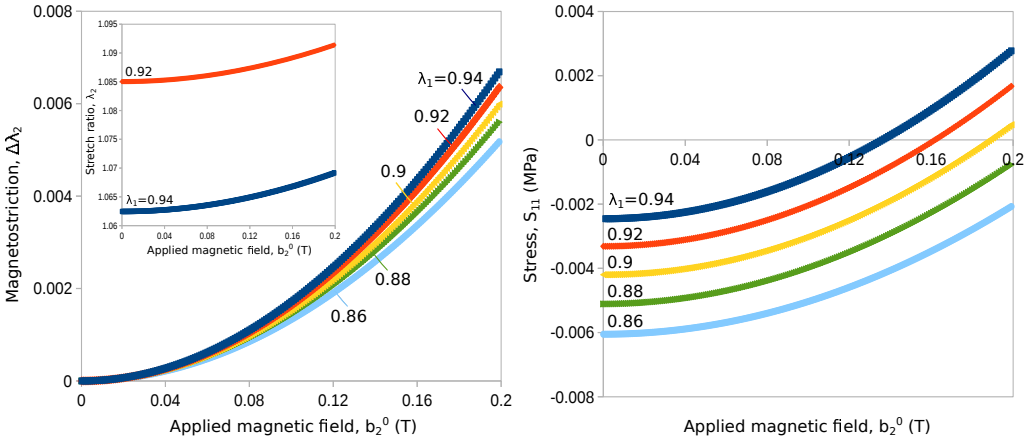

Figure IV.2: **a**, Magnetostriction $\Delta\lambda_2$ and stretch ratio λ_2 (in inset) versus the applied magnetic field b_2^0 for different applied pre-stretches λ_1. The measures are in the direction of the external field, X_2. The magnetostriction $\Delta\lambda_2$ is defined as the difference of the incremental out-of-plane stretch ratio, $\lambda_2(b_2^0)$, from the initial stretch ratio for zero magnetic field, $\lambda_2(b_2^0 = 0)$. The response is indistinguishable for very small fields, while the effect of pre-compression is notable above $b_2^0 = 0.04$T. **b**, First Piola-Kircoff in-plane stress S_{11} versus the applied magnetic field b_2^0 for different applied pre-stretches λ_1. The monotonically increasing stress remains compressive throughout the entire magnetic loading path for large pre-compressions $\lambda_1 < 0.9$, while changes sign in large magnetic fields for smaller pre-compressions, $\lambda_1 \geq 0.9$. The costitutive law used in all plots: $\rho_0^i \Phi_i(\mathbf{F},\mathbf{B}) = \frac{G^i}{2}(I_1 - 3 - 2\ln I_3) + \frac{G'^i}{2}(I_3 - 1)^2 + I_3 \frac{\mu_0 (m_s^i)^2}{3\chi^i}\left[\ln\left(\frac{3\chi^i}{I_3\mu_0 m_s^i}\sqrt{I_5}\right) - \ln\left(\sinh\left(\frac{3\chi^i}{I_3\mu_0 m_s^i}\sqrt{I_5}\right)\right)\right]$ represents a slightly compressible and very soft magnetoelastic bilayer, with material properties given in Table IV.1.

IV.4.1 Principal solution

The principal solution refers to uniform strains (or constant stretches λ_1, λ_2) in each layer and uniform magnetic fields for the MRE layer. It is incrementally obtained by means of the Newton-Raphson method while solving the equation (III.10) for the two constitutive models ((IV.7) and (IV.8)), with the loading parameter being the magnetic field b_2^0 for a given pre-compression λ_1 (and vice versa). For magnetically susceptible materials, the magnetostrictive strain is an important property. It corresponds to the magnetically induced deformation when no mechanical traction is applied. Fig.IV.2a shows the effect of the pre-compression λ_1 on the magnetostrictive response of the bilayer versus the applied magnetic field b_2^0. Here, the magnetostriction $\Delta\lambda_2$ is defined as the difference of the incremental stretch ratio in the direction of the external field, $\lambda_2(b_2^0)$, from the initial stretch ratio for zero magnetic field, $\lambda_2(b_2^0 = 0)$. The response is indistinguishable for very small fields, while the effect of pre-compression is notable above $b_2^0 = 0.04$T. The magnetostriction $\Delta\lambda_2$ monotonically increases with increasing applied magnetic field, however with a decreasing rate with increasing pre-compression λ_1. The expansive stretch ratio λ_2 increases with increasing applied magnetic field and increasing pre-compression, see the inset of Fig.IV.2a and Fig.IV.3a. The magnetostriction monotonically decreases as a function of the applied pre-compression for a fixed magnetic field, with an increasing rate as higher fields are approached. The stretch λ_2 exhibits the opposite behavior, as seen in Fig.IV.3a.

Similarly in Fig.IV.2b, the in-plane component of the Piola-Kircoff stress S_{11} is plotted versus

the magnetic field b_2^0 for different pre-compressions λ_1. The monotonically increasing stress remains compressive throughout the entire magnetic loading path for large pre-compressions $\lambda_1 < 0.9$. However, it becomes extensive in high magnetic fields for smaller pre-compressions, $\lambda_1 \geq 0.9$. The stress decreases as a function of the applied pre-compression for a fixed magnetic field with an increasing rate as the magnetic fields become higher, Fig.IV.3b. The in-plane decreasing stress S_{11} remains compressive throughout the entire mechanical loading path for small magnetic fields $b_2^0 \leq 0.1$T, while it becomes extensive along the mechanical loading path for increasing magnetic fields higher than 0.1T. For stretch values greater than 0.95, the code does not converge. This is because the initial $S_{11}(b_2^0 = 0)$ stress (in the direction of compression) is extensive (and monotonically increasing) under compression. In all plots, the constitutive model considered is that of Langevin (IV.7) with saturation in magnetization.

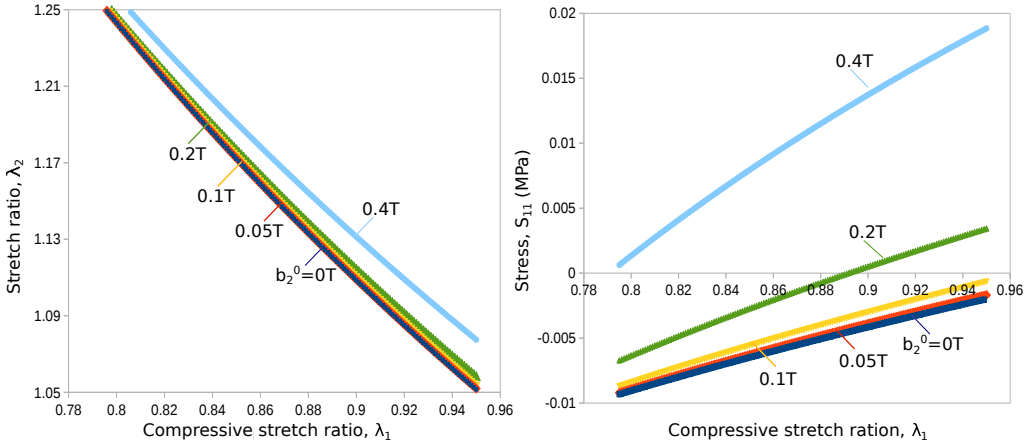

Figure IV.3: **a**, Stretch ratio λ_2; **b**, First Piola-Kircoff stress S_{11} versus the applied stretch ratio λ_1 for different values of the externally applied magnetic field b_2^0. The monotonically increasing out-of-plane stretch λ_2 versus pre-compression λ_1 is notably affected by the presence of relatively high magnetic fields, e.g., $b_2^0 = 0.4$T. The in-plane decreasing stress S_{11} versus the pre-stretch λ_1 remains compressive throughout the entire mechanical loading path for small magnetic fields $b_2^0 \leq 0.1$T, while progressively changes sign along the mechanical loading path for increasing magnetic fields higher than 0.1T. The costitutive law used in all plots: $\rho_0^i \Phi_i(\mathbf{F},\mathbf{B}) = \frac{G^i}{2}(I_1 - 3 - 2\ln I_3) + \frac{G'^i}{2}(I_3 - 1)^2 + I_3 \frac{\mu_0 (m_s^i)^2}{3\chi^i}\left[\ln\left(\frac{3\chi^i}{I_3 \mu_0 m_s^i}\sqrt{I_5}\right) - \ln\left(\sinh\left(\frac{3\chi^i}{I_3 \mu_0 m_s^i}\sqrt{I_5}\right)\right)\right]$ represents a slightly compressible and very soft magnetoelastic bilayer, with material properties given in Table IV.1.

IV.4.2 Mechanical critical behavior

An exact bifurcation analysis is employed to reveal the critical applied strain at the onset of wrinkling when $b_2^0 = 0$ (absence of magnetic field). We consider a neo-Hookean film bonded on an infinitely deep (softer) neo-Hookean substrate with the entire plane-strain system undergoing axial compression. Both layers are infinitely long in the direction of the interface. Let $\lambda_1 (< 1)$ be the applied stretch ratio. When λ_1 is relatively small, the bilayer is uniformly compressed and the surface is flat. When the stretch ratio exceeds a critical value λ_1^c, the film undergoes wrinkling for a given critical wavenumber that minimizes $1 - \lambda_1^c \geq 0$.

The potential energy $\mathscr{P}$ of the system is written with respect to the admissible displacement field $\mathscr{P} = \mathscr{P}(\mathbf{u})$ and all magnetic contributions are neglected. One needs then to apply a sinusoidal mode as the form of the expected solution. It is noted that interfacial debonding is not considered in this model. The eigenvalue problem for the two solid phases is that of equation (IV.36), i.e., only $\mathscr{L}^{uu}$ terms survive. For the film, the bi-quadratic characteristic equation gives four roots. For the substrate, the two positive roots are regarded to satisfy the decay condition, see Section IV.3. The natural and essential boundary conditions (IV.42),(IV.43) regard only the purely mechanical contributions, given in terms of the admissible displacements $\mathbf{u}$. Note that no jump condition is now applied at the film/air boundary, i.e., mechanical traction $\mathbf{t} = \boldsymbol{\sigma} \cdot \mathbf{n}$. As a result, the boundary conditions in total (=6) are as many as the unknowns $\left\{\Delta U_2^I, \Delta V_2^J\right\}$, $I = 1,..4$, $J = 1,2$. Thus, the final algebraic system is a 6×6 linear system, where the components of $\mathscr{D}_{pq}$, $p = 1,..,6, q = 1,..,6$, do not include any information about the air. Checking for changes in the sign of the imaginary part of the jacobian matrix components (real part is always zero) yields the critical $\{\lambda^c, \omega h^c\}$ values, see e.g. Fig.IV.5. In Fig.IV.4, the absolute values of the stretch ratio λ_1 are plotted versus the corresponding wavenumber ωh that satisfy a negative jacobian eigenvalue. The critical values are those corresponding to the lowest strain (or highest stretch ratio $\lambda_1 = 1 - \varepsilon_{11}$).

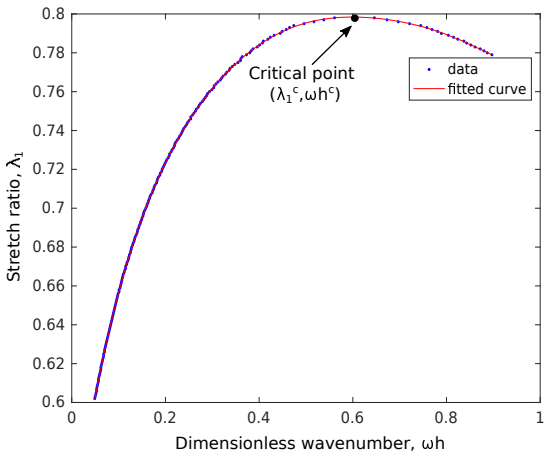

Figure IV.4: Critical applied stretch ratio λ_1 versus the corresponding dimensionless wavenumber ωh that satisfy a negative jacobian eigenvalue. An incremental bifurcation analysis in the absence of magnetic field, i.e., $b_2^0 = 0$ and $\lambda_1 (< 1)$, provides the critical mechanical load $\lambda_1^c = 0.7984$ for the onset of wrinkling and the associated wavenumber $\omega h^c = 0.6227$, for shear moduli ratio $G_s/G_f = 0.3$ and Lamé compressibility constant $G_i' = 100 G_i$, $i = f, s$ for the film and the substrate, respectively.

The mechanical bifurcation analysis provides the critical mechanical load $\lambda_1^c = 0.7984$ for the onset of wrinkling and the associated wavenumber $\omega h^c = 0.6227$ for a moderate shear moduli ratio $G_s/G_f = 0.3$ and Lamé compressibility constant $G_i' = 100 G_i$, $i = f, s$ for the film and the substrate, respectively. Since incompressibility is satisfied, the critical values depend only on the mechanical interlayer contrast G_s/G_f.

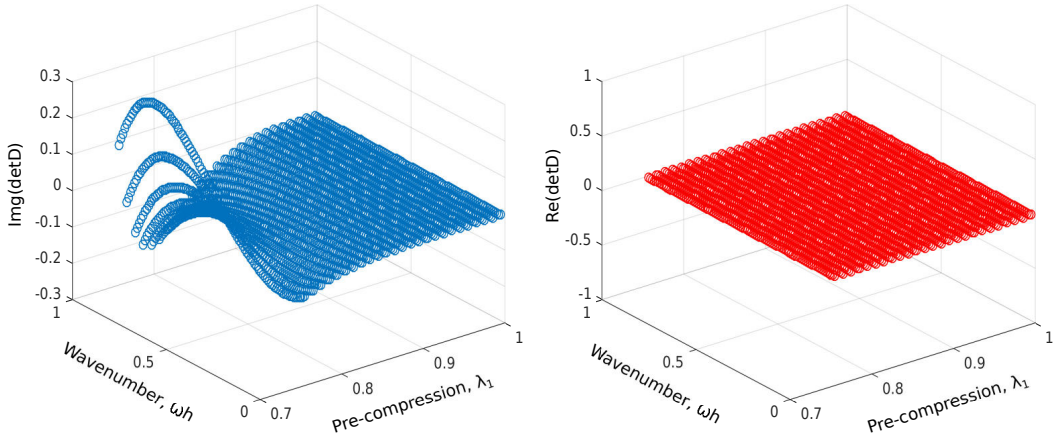

Figure IV.5: **a**, Imaginary; **b**, Real part of the stiffness matrix determinant plotted along a mechanical loading path $0.75 \leq \lambda_1 \leq 1$ over all non-dimensional wavenumbers $\omega h \in (0,1]$, for a fixed value of the applied magnetic field $b_2^0 (= 0.03\text{T})$. When the stretch ratio λ_1 is within the range $0.8 \lesssim \lambda_1 \leq 1$, the determinant is positive, $\det(\mathscr{D}) = 0 + 0.01i$, for the entire range of the scanned wavenumbers ωh. Upon further pre-compression $\lambda_1 \lesssim 0.8$, the imaginary part of the determinant exhibits changes in its sign (from positive to negative and vice versa) along the wavenumber ωh scanning path and for any sequential λ_1. The critical pair value $(\lambda_1, \omega h^c)$ selected is that of the wavenumber ωh^c minimizing the strain $1 - \lambda_1 \geq 0$ for the given external field b_2^c.

IV.4.3 Magnetomechanical critical behavior

In this section, we show the results obtained from the magnetomechanical bifurcation analysis for the MRE film/substrate assembly. The critical buckling fields $\{\lambda_1, b_2^c\}$ and the corresponding wavenumber ωh^c are found similarly to the mechanical solution: for a given applied magnetic field $b_2^0 \neq 0$, one searches for changes in the sign of the tangent stiffness matrix determinant in (IV.44), given the real part is zero, e.g., see Fig.IV.5b. More specifically, Fig.IV.5a presents the imaginary part of the stiffness matrix determinant $\det(\mathscr{D})$ plotted along a chosen mechanical loading path $0.75 \leq \lambda_1 \leq 1$ over all non-dimensional wavenumbers $\omega h \in (0,1]$, for a fixed applied magnetic field $b_2^0 (= 0.03\text{T})$. When the stretch ratio λ_1 is within the range $0.8 \lesssim \lambda_1 \leq 1$, the determinant is positive, $\det(\mathscr{D}) = 0 + 0.01i$, for the entire range of the wavenumbers ωh. Upon further increase of the pre-compression $\lambda_1 \lesssim 0.8$, the imaginary part exhibits changes in its sign (from positive to negative and vice versa) along the wavenumber ωh scanning path and for any sequential λ_1. The critical pair $(\lambda_1, \omega h^c)$ corresponds to the wavenumber ωh^c of the smallest critical strain $1 - \lambda_1 \geq 0$ for the given external field b_2^c. In each case, the lowest critical field occurs for an eigenmode with the lowest wavenumber. The critical two-field loading parameters $\{\lambda_1, b_2^c\}$ are plotted in Fig.IV.6a for the material properties given in Table IV.1 corresponding to the experimental values of our soft silicones (see Section II.1). For validation purposes, the critical buckling fields $\{\lambda_1, b_2^c\}$ are presented for three different models. The first is the finite element method (FEM) on a finite size specimen and Dirichlet boundary conditions, presented in Sections III.3 and III.4. This model resorts to a full numerical analysis, solving numerically the bifurcation equations of the augmented variational formulation

$\mathscr{P}(\mathbf{F},\mathbf{B})$ (see Section III.1) for the boundary value problem of a finite MRE film/substrate block surrounded by air.

The second model ("FB theory") is the present bifurcation analysis on an infinitely long material system of a finite thickness film bonded on an infinitely deep substrate. Unlike the FEM boundary value analysis considering the total Lagrangian magnetic field $\mathbf{B}$ as an independent variable, the theoretical infinite problem is solved in terms of the perturbed magnetic field $\widetilde{\mathbf{B}}$ (for more information see Section IV.1 and IV.3).

The third model ("FM theory") is that of Danas and Triantafyllidis (2014), considering the same infinite medium and a continuum formulation equivalent to FB. In the FM formulation, the deformation gradient tensor $\mathbf{F}$ and the magnetization $\mathbf{M}$ are the independent variables of the potential energy.[8] Each model considers an isotropic energy density function representing a slightly compressible, magnetoelastic elastomer for plane-strain deformations and magnetic field effects. Therefore, we make use of neo-Hookean solids combined with the magnetoelastic Langevin law (IV.7) for the FEM and the FB theory model versus a non-saturating law for the FM model. In the latter case, the non-saturating FM energy density of (III.48) is equivalent to that of the linear FB (IV.8), obtained by use of Legendre transform as already shown in Section III.2.2.

In the present plot, we make use of $I_1(\mathbf{F}), I_3(\mathbf{F})$ and $I_5(\mathbf{F},\mathbf{B})$ invariants for the saturating FB model. The non-saturating FM model employs $I_1(\mathbf{F}), I_3(\mathbf{F})$ and $I_6(\mathbf{F},\mathbf{M}) = \mathbf{M}\cdot\mathbf{M}$ invariants, with a supplementary small dependence in $I_7(\mathbf{F},\mathbf{M}) = \mathbf{M}\cdot\mathbf{F}^2\cdot\mathbf{M}$ to discard jacobian singularities. The stress contribution arising from $I_7(\mathbf{F},\mathbf{M})$ dependence in relatively high fields and small compressions occurs slight differences in the critical buckling values between the two theoretical models, see also Fig.IV.9 in the Appendix of the Chapter.

The critical magnetic field b_2^c decreases monotonically with increasing pre-compression λ_1 until the mechanical buckling load, $\lambda_1^c(b_2^0 = 0)$, is reached. This decreasing trend drives motivation for the design of actively controlled material-structures. Such systems can be led near (but not exactly at) a critical state by applying in-plane strain and, subsequently, undergo bifurcation with a small magnetic field. The system at hand buckles before magnetization saturation of the film is reached (set for the FEM and the FB theoretical model at $\mu_0 m_f^s = 0.5\text{T}$). Each critical curve divides the phase diagram into a stable (right to the curve) and an unstable (left) regime. The equilibrium of the flat film surface is maintained in the stable regime. A wrinkled equilibrium is obtained in the unstable regime. The differences in the critical values observed between the numerical and the theoretical models are attributed to the finite structure of the first. The boundary conditions and the existence of corners (regions of magnetic quantities concentration) inevitably affect the solution.

Fig.IV.6b shows the influence of the mechanical interlayer contrast G_s/G_f on the magnetomechanical instability, for nearly incompressible material layers ($G'_{f,s} = 100G_{f,s}$). Here, the critical values of the external magnetic field b_2^c are plotted as a function of the applied compressive stretch λ_1, for fixed film parameters $\chi_f = 0.4$, $\mu_0 m_f^s = 0.5\text{T}$ and $G_f = 10\text{kPa}$ and three different ratios

[8] Such an analysis inevitably considers the $\mathbf{B}$ as a second independent magnetic variable, since there are no boundary conditions for the magnetization $\mathbf{M}$.

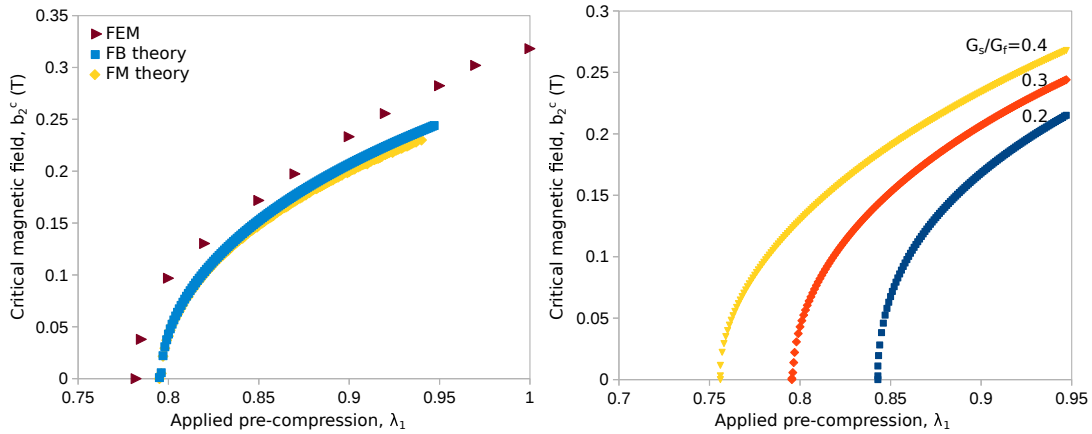

Figure IV.6: Phase diagrams in the parameter space of the applied magnetic field b_2^c and the compressive stretch ratio λ_1. Critical values of the applied magnetic field b_2^c versus the interface stretch ratio λ_1 for **a**, a fixed substrate-to-film shear moduli ratio $G_s/G_f = 0.3$ and three different models: the FEM FEAP with finite size specimen and Dirichlet boundary conditions, the FB bifurcation and the FM bifurcation model. For test purposes presented in Section III.2.2, we use the neo-Hookean law combined with the magnetoelastic Langevin law for the FEM and the FB theory model: $\rho_0^i\Phi_i(\mathbf{F},\mathbf{B}) = \frac{G^i}{2}(I_1 - 3 - 2\ln I_3) + \frac{G'^i}{2}(I_3-1)^2 + I_3\frac{\mu_0(m_s^i)^2}{3\chi^i}\left[\ln\left(\frac{3\chi^i}{I_3\mu_0 m_s^i}\sqrt{I_5}\right) - \ln\left(\sinh\left(\frac{3\chi^i}{I_3\mu_0 m_s^i}\sqrt{I_5}\right)\right)\right]$ versus a non-saturating law for the FM model: $\rho_0^i\Phi_i^{mec}(\mathbf{F},\mathbf{M}) = \frac{G^i}{2}\left(\mathbf{F}^T:\mathbf{F} - 3 - 2\ln J\right) + \frac{G'^i}{2}(J-1)^2 + \frac{(\rho_0^i)^2\ \mu_0(1-\chi^i)}{2J\chi^i}\mathbf{M}\cdot\mathbf{M}$. **b**, the FB bifurcation model and three different shear moduli ratios $G_s/G_f = 0.2, 0.3, 0.4$. The material parameters used in the plots correspond to soft silicones, with $G_{f,s} = 100\,G_{f,s}$ a large Lamé constant for both layers, $G_f = 10$kPa the shear modulus, $\chi_f = 0.4$ the magnetic susceptibility and $\mu_0 m_f^s = 0.5$T the saturation magnetization of the film.

$G_s/G_f = 0.2, 0.3, 0.4$ that practically affect the stiffness of the substrate. When $b_2^c = 0$, each curve attains the purely mechanical critical stretch corresponding to a given G_s/G_f, i.e., buckling of the film/substrate under uniaxial compression. The mechanical buckling strain $\varepsilon_{11}^c (= \lambda_1^c(b_2^c = 0) - 1)$ increases with increasing interlayer stiffness contrast G_s/G_f, see also Fig.V.4a. In the limit of $G_s/G_f \to 0$, the critical load $\lambda_1^c(b_2^c = 0) \to 1$ (and the corresponding wavenumber $\omega h^c \to 0$). This is because such a limit corresponds to the zero compressive axial load of an infinitely long and unsupported Euler beam (Danas and Triantafyllidis, 2014). Upon a threshold $G_s/G_f \approx 0.6$, non-periodic primary instability modes arise (see e.g., Hutchinson, 2013) that are beyond the scope of the present model. In that case, one needs to employ FEM calculations (see Section V.1.1). Moderate shear moduli ratios within the range $G_s/G_f \in (0, 0.6)$ yield wrinkling and thus, are reasonable to be considered. As seen in Fig.IV.6b, the lower the ratio G_s/G_f (for material parameters of the same magnitude of order), the more unstable under a given pre-compression the system at hand gets. Apart from shifting the critical curves on the purely mechanical axis, the smaller the interlayer mechanical constrast, the faster the system destabilizes until mechanical buckling is reached.

Next, we present a study on the influence of the magnetomechanical properties on the coupled critical buckling loads. The magnetoelastic law used is that of (IV.8) for non-saturating media (i.e., linear in I_5). Neglecting the saturation magnetization permits to explore the interplay between the magnetic and the mechanical properties in terms of simpler magnetomechanical ratios. Such ratios

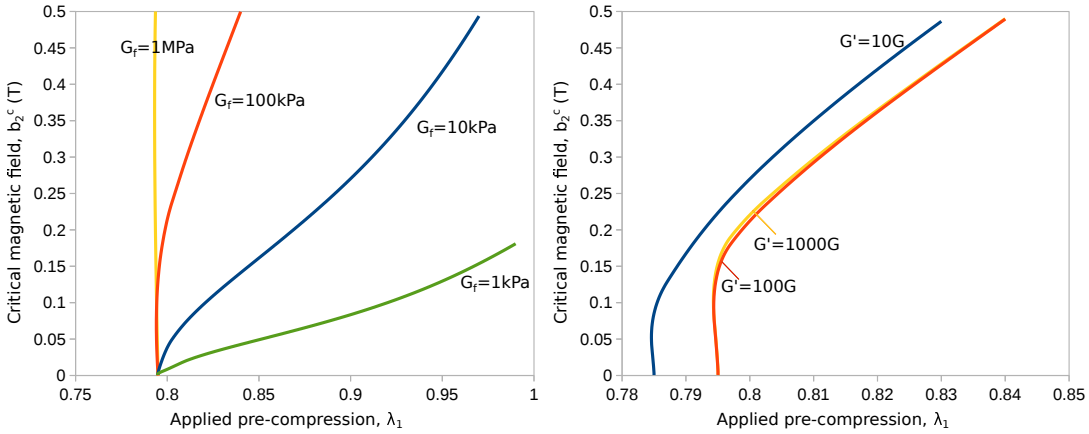

Figure IV.7: Critical values of the applied magnetic field b_2^c versus the interface stretch ratio λ_1 for fixed shear moduli ratio $G_s/G_f = 0.3$, film susceptibility $\chi_f = 0.4$ (non-saturating film) and **a**, different film shear moduli $G_f = 1, 10, 100, 1000$ kPa under a given compressibility state $G' = 100\,G$ **b**, different Lamé compressibility constants $G' = 10\,G, 100\,G, 1000\,G$ for a given film shear modulus $G_f = 100$kPa.

regard the shear modulus G_i and the susceptibility χ_i between the two solid phases, $i = f, s$ for the film and the substrate, respectively. The motivation here is to examine the possible control of the bifurcation with the perspective of designing an efficient haptic device. The energy density function contains a small dependence on an additional invariant $I_6(\mathbf{F}, \mathbf{B}) = \mathbf{B} \cdot \mathbf{C}^2 \cdot \mathbf{B}$ when the film is non-saturating. This is needed to discard the jacobian singularities, otherwise the magnetomechanical coupling coming solely from $I_5(\mathbf{F}, \mathbf{B}) = (\mathbf{F} \cdot \mathbf{B}) \cdot (\mathbf{F} \cdot \mathbf{B})$ is minor.

The influence of the absolute value of the film shear modulus G_f is shown in Fig.IV.7 for fixed shear moduli ratio $G_s/G_f = 0.3$, film susceptibility $\chi_f = 0.4$ and Lamé constants $G'_{f,s} = 100 G_{f,s}$. The critical magnetic field b_2^c reaches a very sharp asymptote when the polymeric film is very stiff, e.g., $G_f = 1$MPa. Such high modulus leads the film to bifurcate in the presence of very high fields and within a very small range of pre-compressions that is practically beyond the sensitivity of realistic setups. This behavior comes from the restriction of the MRE layer magnetization, despite the increase of the applied magnetic field. Increasing the material softness permits to trigger bifurcation with notably lower magnetic fields and within a realistic range of pre-compressions. This is because the softer the layers, the more compliant they are to deform under the same magnetization state. As a result, the critical magnetic field decreases with decreasing modulus for a given pre-compression. Overall, a way to induce bifurcation with low magnetic fields and within a wide range of applied strains is to use materials as soft as possible, e.g., polymeric gels of 1kPa shear modulus.

The influence of the compressibility factor on the critical fields $\{\lambda_1, b_2^c\}$ is studied in Fig.IV.7b, for fixed shear moduli ratio $G_s/G_f = 0.3$, film shear modulus $G_f = 100$kPa and film susceptibility $\chi_f = 0.4$. The critical external magnetic field b_2^c is plotted versus the applied pre-compression λ_1 for three different Lamé constants $G' = 10G, 100G, 1000G$. The compressibility of the two layers is taken always the same. The $G'/G = 1000$ value is considered a fair approximation of incompressibility. Thus, converging with $G'/G = 1000$ apart from a small area $0.15 < b_2^c < 0.25$ T, the ratio $G'/G = 100$ satisfies slight compressibility conditions.

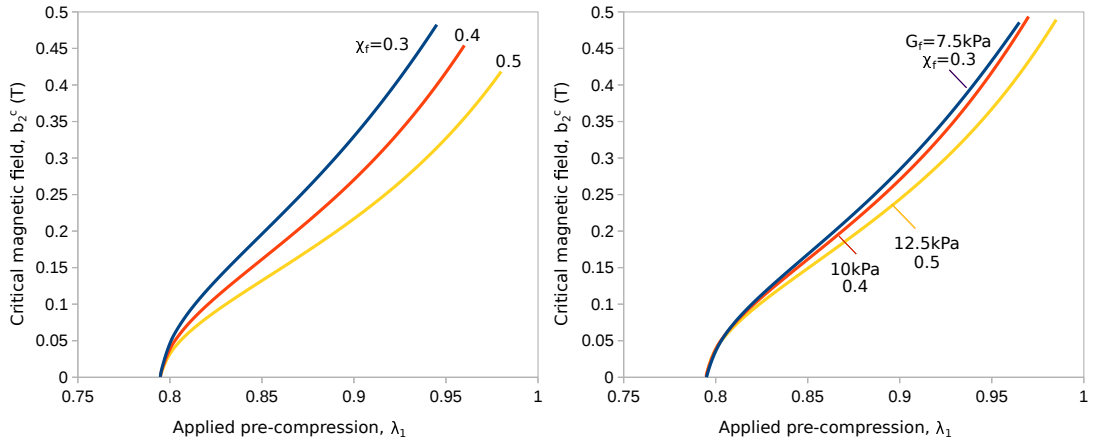

Figure IV.8: Critical values of the applied magnetic field b_2^c versus the interface stretch ratio λ_1 for fixed shear moduli ratio $G_s/G_f = 0.3$, Lamé compressibility constant $G'_{f,s} = 100\,G_{f,s}$ and three different film susceptibility values $\chi_f = 0.3, 0.4, 0.5$ for **a**, film shear modulus $G_f = 10$kPa **b**, fixed magnetomechanical ratio $G_s/(\chi_f\,\mu_0\,m_f^s) = 0.0058$.

Keeping constant the mechanical properties of the system at hand, i.e., shear moduli ratio $G_s/G_f = 0.3$, film shear modulus $G_f = 10$kPa and Lamé compressibility constants $G'_{f,s} = 100\,G_{f,s}$ for both layers, one can explore the effect of film susceptibility on the critical buckling fields. Fig.IV.8a shows the critical external magnetic field b_2^c plotted versus the applied pre-compression λ_1 for three different values of the film susceptibility $\chi_f = 0.3, 0.4, 0.5$. As expected, the more susceptible the film, the more unstable the system at hand for a given pre-compression. A more interesting feature of the magnetomechanical coupling is outlined by another ratio of combined parameters, i.e., $G_s/(\chi_f\ \mu_0\,m_f^{s\,2})$. It can be easily shown that this ratio arises from the linear (in magnetoelastic invariants I_5, I_6) energy of (IV.8). For reasons of dimensional consistency ($\mathrm{Pa} = \mathrm{T}^2 \cdot \mathrm{N}^{-1}\mathrm{A}^2$), the saturation magnetization m_f^s has to be included into the ratio. However, since the MRE film is selected to be non-saturating, the saturation magnetization can take the form of an arbitrary constant without affecting the solution, e.g., $m_f^s = 1$ $(\mathrm{A\,m^{-1}})$. Now, the system at hand, defined by the same susceptibilities $\chi_f = 0.3, 0.4, 0.5$ and a purely mechanical ratio $G_s/G_f = 0.3$, can be re-designed upon control of the magnetomechanical ratio $G_s/(\chi_f\ \mu_0\,m_f^{s\,2})$. Adjusting the shear moduli G_s and G_f to satisfy $G_s/(\chi_f\ \mu_0\,m_f^{s\,2}) = 5.8 \cdot 10^{-3}$ for the given susceptibilities, the critical magnetic field b_2^c is plotted versus pre-compression λ_1 in Fig.IV.8b. Here, one observes that the initial slopes of the critical curves now overlap for small magnetic fields, $b_2^c \lesssim 0.1$ T.

IV.5 Concluding remarks

The "bloch-wave" approach considers for stability criterion the incremental positive definitess of the tangent (Jacobian $\mathscr{D}$) stiffness matrix, i.e., the second derivatives of the potential energy with respect to the independent variables. The linearization of the problem derives from the compressibility condition, where $\lambda_2 \simeq 1/\lambda_1$ up to $O(\delta^2)$. This approach is an incremental bifurcation analysis that does not incorporate the effects of a boundary value system. The model aims at determining the

critical load for the onset of wrinkling and the associated wavelengths. The problem results in a highly nonlinear eigenvalue problem, where the characteristic equation provides the critical fields. The amplitude sharing between the eigenstates is decided by the film/air and film/substrate interface conditions in compatibility with the deformation of the surface layer. The interface compatibility conditions provide the bifurcation eigenvalue problem for the wavenumber ωh of the sinusoidal magnetomechanical buckling. The magnetic nonlinearity is found to have an impact on the critical fields for low pre-compressions.

The theoretical bifurcation (but not the post-bifurcation) analysis has already been presented in Danas and Triantafyllidis (2014) and is repeated here using the equivalent continuum formulation of Dorfmann and Ogden (2004). Nonetheless, some non-negligible differences with respect to this idealized theoretical model have been observed in our experiments. Such differences have been partially related to frictional boundary effects. To that end, the non-trivial boundary value problem is considered essential to be solved, in order to examine the coupling between the magnetic and mechanical effects in a more realistic higher-order surface patterning.

IV.6 Appendix I. F-M bifurcation model

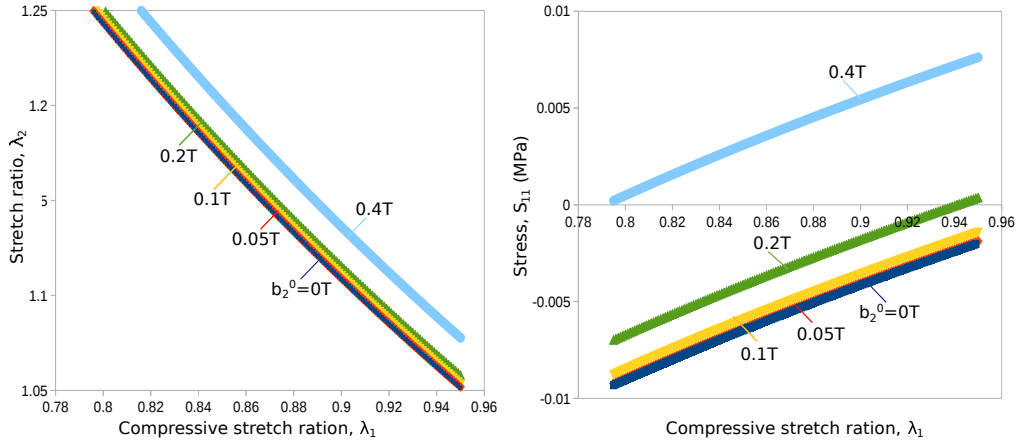

Figure IV.9: **a**, Stretch ratio λ_2; **b**, First Piola-Kircoff stress S_{11} versus the applied stretch ratio λ_1 for different values of the externally applied magnetic field b_2^0. The monotonically increasing out-of-plane stretch λ_2 versus pre-compression λ_1 is notably affected by the presence of relatively high magnetic fields, e.g., $b_2^0 = 0.4$T. The in-plane decreasing stress S_{11} versus the pre-stretch λ_1 remains compressive throughout the entire mechanical loading path for small magnetic fields $b_2^0 \leq 0.1$T, while progressively changes sign along the mechanical loading path for increasing magnetic fields higher than 0.13T. The costitutive law used in all plots: $\rho_0^i \Phi_i(\mathbf{F},\mathbf{M}) = \frac{G^i}{2}\left(\mathbf{F}^T:\mathbf{F}-3-2\ln J\right) + \frac{G'^i}{2}(J-1)^2 + \frac{(\rho_0^i)^2\ \mu_0(1-\chi^i)}{2J\chi^i}\mathbf{M}\cdot\mathbf{M}$ represents a slightly compressible and very soft magnetoelastic bilayer, with material properties given in Table IV.1.

CHAPTER V

RESULTS I: MRE FILM/PASSIVE SUBSTRATE

Summary of the Chapter. In this chapter, we initially present a stiffness sensitivity study on the primary and secondary bifurcation modes of a MRE film/passive substrate block under a) a purely mechanical, b) a purely magnetic and c) a combined magnetomechanical loading. Subsequently, we properly probe the experimental findings of Chapter II with full-field finite element simulations at large strains and magnetic fields. The influence of friction on the experimental setting needs to be taken into account. Thus, it is investigated by applying variable shear forces at the lateral edges of the virtual specimen. The full-field numerical analysis reveals the complexity of the coupled fields within the film in the post-bifurcation and thus, justifies the need of numerical treatment of the problem at hand. In the last part, we investigate the influence of the film slenderness on the critical loads and modes. The results correspond to two chosen film thicknesses: $\mathrm{H}_f = 0.2$ and 0.8mm in a 40×40 (mm^2) bilayer block. The geometry with the thicker film is used to fit the experimental data. The geometry with the thinner film is used for connection with the theoretical problem in Chapter IV considering an infinitesimally thick MRE layer.

Contents

An isotropic MRE film layer on a soft and passive substrate may produce multimodal wrinkles (or localizations) as the primary wrinkling amplitudes grow large, Figs.II.18a-p,V.10b-d. While the bifurcation of wavelengths at the first buckling point could be captured with the theoretical analysis described in Chapter IV, we further analyze highly nonlinear large-amplitude wrinkles evolving into localized patterns via a finite element (FE) method. Bifurcation is a nonlinear deformation process and hence, the prediction of the post-buckling wavelength by first-order perturbation analysis have limited accuracy beyond the primary bifurcation point. The post-bifurcation regime is defined by large amplitudes that often lead to folding (Sun et al., 2012). This or other (e.g., creases, ridges, crinkles) higher-order patterns manifest finite strains around localizations. As a result, high-order perturbation analysis are expected to improve the accuracy of the evaluation of the post-bifurcation wavelengths. Especially since the substrate becomes highly nonlinear under finite deformations and induces elastic anisotropy under incremental deformation. To that end, the present chapter numerically investigates the evolution of the post-buckling large-amplitude wrinkling towards localizations.

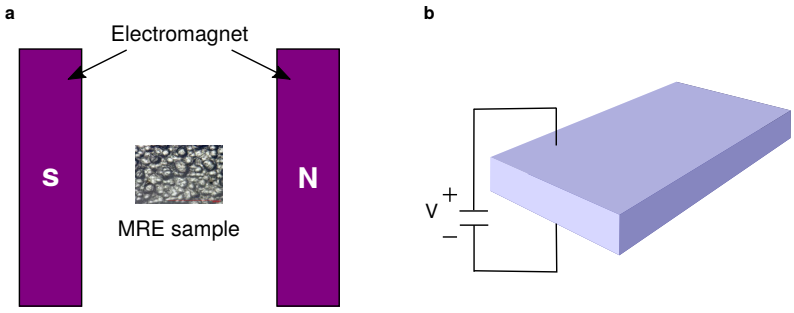

Figure V.1: Standard experimental setups for the study of **a**, magnetorheological elastomers and **b**, electroactive polymers.

In the post-buckling regime, the magnetic Maxwell stresses and fields become highly heterogeneous inside and outside the film, since there are magnetic fields in the surrounding air (see e.g., Keip and Rambausek, 2017, Lefèvre et al., 2017). The reason lies in the applied magnetic boundary conditions, which are set (relatively) far from the specimen in magnetoelasticity and are of Eulerian form (Danas, 2017). Thus, a substantial difference exists between magnetoelastic and electroelastic wrinkling, see Fig.V.1. In the context of electroelasticity, the electrodes are attached on the surfaces of the specimen and the (Maxwell) electrically induced stress fields follow the deformation of the specimen even in the post-bifurcation regime. In that case, the (Maxwell) stresses outside the specimen are zero, while the applied electric field is of Lagrangian nature, following the material deformation.

In addition to this particularity, the present experiment is determined by strong frictional effects acting on the lateral faces of the specimen. In Figs.II.18j,m corresponding to large pre-compressions ($\lambda_0 \leq 0.8$), one can easily observe a non-negligible curvature at the lateral faces of the film/substrate block in contact with the compression setup. This curvature at the corners is a direct result of friction (see Section V.3) affecting the pre- and post-bifurcation response. Thus, it needs to be taken into

account in the present analysis. To that end, we resort to a full numerical analysis of the boundary value problem at hand, so as to properly fit the experimental findings.

For such reasons, we have employed a full numerical analysis, which is proven adequate to capture even quantitatively the bifurcation amplitudes. The model allows for the full post-bifurcation response, revealing very complex strain and magnetization fields in the wrinkled state. By observation of Figs.V.12c-f, it is difficult to think of a simple analytical treatment of the edge effects and the magnetic domains of the film.

V.1 Primary and secondary bifurcations

Wrinkling modes are determined within a specific range of mechanical interlayer contrasts (e.g., G_s/G_f) for a two-layered 2D system comprised of a neo-Hookean film bonded to a neo-Hookean substrate, with the entire structure undergoing compression and/or magnetic effects. As theoretically shown in Section IV.4 (Fig.IV.6,IV.7 and IV.8), this range is determined by the absolute values of the material properties. However, in real structures, it is also conjugated with geometric features/ constrains. Therefore, the effect of the substrate-to-film shear moduli ratio G_s/G_f on the critical response is numerically studied in Sections V.1.1, V.1.2, V.1.3 on a virtual finite specimen. In the first section ($\lambda_0 \neq 1$, $b_2^0 = 0$), we compute the stretch ratio λ_0^c needed to buckle the structure as a function of the shear moduli ratio G_s/G_f. The effect of the mechanical compression is further explored by accounting for the critical wavenumber $(\omega H)^c$ as a function of the relative moduli contrast. In the second section ($\lambda_0 = 1$, $b_2^0 \neq 0$), we compute the critical magnetic field b_2^c as a function of G_s/G_f under zero applied strain. In the third section ($\lambda_0 \neq 1$, $b_2^0 \neq 0$), we present the effect of combining the independent loadings on the critical response and post-buckling regime.

Within a finite element (FE) framework, the plane-strain numerical simulations can also uncover advanced post-bifurcation modes. On the contrary, the previous theoretical analysis is restrained in the stability of the principal solution for a preferable (i.e., wrinkling) mode (see Section IV.3). The secondary modes include period-doubling, creasing and the newly identified "crinkling" mode, presented in Sections V.2, V.3, V.5 and VI.1. The results correspond to two chosen film thicknesses: $\mathrm{H}_f = 0.2$ and 0.8mm in a 40×40 (mm^2) bilayer block. The geometry of thicker film is used to fit the experimental data. The thinner film geometry is used for connection with the theoretical problem in Section IV.4 (Fig.IV.6a) considering an infinitesimally thick MRE layer. In the present calculations, the magnetic field b_2^0 is always applied in the direction of the film thickness, while the stretch λ_0 is applied along the interface direction.

V.1.1 Purely mechanical loading

Let $\lambda_0 (\equiv \lambda_1)$ be the stretch ratio. When λ_0 is relatively small, the film/substrate bilayer is uniformly compressed and the surface is flat. Upon further increase, the stretch ratio λ_0 exceeds a critical value λ_0^c and the film buckles with the substrate deforming coherently, forming surface wrinkles. Typically

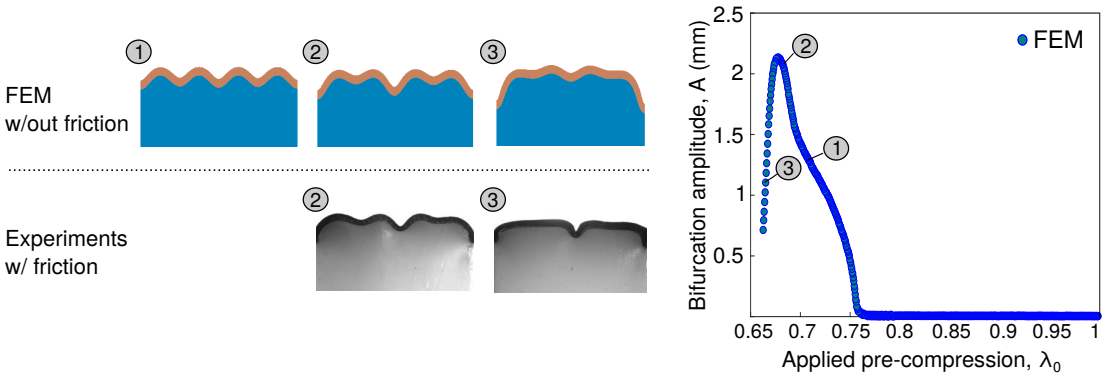

Figure V.2: Stability and (post-)bifurcation of a two-layer 2D system comprised of a neo-Hookean film bonded to a finite neo-Hookean substrate with the entire bilayer undergoing compression, denoted by the stretch ratio λ_0. The bifurcation amplitude A (in mm) is plotted versus the applied stretch ratio. The amplitude is measured as the incremental average distance of the two central peaks from the central valley. As the compressive strain $\varepsilon_{11}(=\lambda_0-1)$ increases, the flat film surface becomes unstable forming surface wrinkles at $\lambda_0^{c1}=0.763$, which subsequently evolve into a double-period pair at $\lambda_0^{c2}=0.7$. The secondary mode gets unloaded at even higher strains, $\lambda_0<0.68$. The surface modes are presented for both numerical simulations and experimental findings, apart from wrinkling for the latter. Wrinkling modes cannot be experimentally evidenced due to high frictional effects acting on the lateral faces of the specimen (modeled in Section V.3). Following the experimental process, the numerical system is described as a 40×40 (mm^2) bilayer block, with film thickness $\mathrm{H}_f=0.8$ mm, shear modulus $G_f=10$ kPa, mechanical interlayer contrast $G_s/G_f=0.3$ and no user-defined geometrical nonlinearities. Both layers are slightly compressible, a condition satisfied via a large Lamé constant $G_i'=100\,G_i$, $i=f,s$, for the film and the substrate, respectively.

when $\lambda_0<\lambda_0^c$, a linear theory (in Abaqus e.g.) is out of use and one must consider the geometrically nonlinear behavior of the wrinkles. This opens up various generalizations to include the effects of anisotropy coming from the substrate fabrication (not studied in the present work), different types of nonlinear behaviors[1] etc. The wrinkles result from the compromise between the bending and the stretching film energy, subjected to the geometric constraints imposed to the system. As a result, the critical response depends on the mechanical properties of the film and the substrate (e.g., shear moduli, compressibility factors), the boundary conditions, as well as the geometrical features of the system (e.g., substrate-to-film thickness ratio, $\mathrm{H}_s/\mathrm{H}_f$, for mimicking an infinitely deep substrate).

The present 2D system is described as a 40×40 (mm^2) bilayer block of mechanical interlayer contrast G_s/G_f. The dimensions of the block are those of the experimental specimen. The system considers a rubber-like $G_f=1$ MPa film, with thickness $\mathrm{H}_f=0.8$mm and no user-defined geometrical nonlinearities. Following the experimental process, the isotropic free energy complies with a film polymerized in the absence of a magnetic field. Both layers are taken to be nearly incompressible, i.e., second Lamé constant $G_i'=100\,G_i$, $i=f$ (for the film) and s (for the substrate). The interface is assumed to be perfect, i.e., absence of interfacial delamination in agreement with the experimental

[1]For instance, folding of the wrinkles requires multiple symmetry-breaking nonlinear material characteristics of both the substrate and the surface layer (asymmetric bending conditions). A neo-Hookean substrate is not able to fold the wrinkles regardless of the elastic surface-layer nonlinearity. In that case, an Ogden substrate combined with asymmetric bending stiffness film should be selected to reproduce folds (Sun et al., 2012).

findings. The displacements and the tractions are continuous across the interface, satisfied by use of nodal elements. A constant mesh is designed in Abaqus and consists of 10865 elements for the air, 6084 elements for the substrate and 1325 elements for the film (8 elements across its thickness). The compressive stretch ratio λ_0 is linearly decreased from 1 to 0.5 in 1000 time increments. For numerical reasons, the magnetic field b_2^0 is assigned with a tiny positive value at 10^{-6}T. The primary critical load corresponds to the first non-positive eigenvalue of the stiffness matrix. More particularly, the smallest eigenvalue of the system incrementally decreases until it reaches a first minimum close to zero. That point is defined as the primary instability point. Subsequently, the smallest eigenvalue increases but then decreases again towards a second minimum. This is then defined as a secondary instability point. Supplementary case studies have been carried out on the effect of the penalty function method applied on the air region (see Section III.4). A converged (post-)bifurcation response was obtained for penalty value ε =1e-10. An alternative to the penalty method would be to assign the air a low shear modulus.

As illustrated in Fig.V.2, a FE (post-)bifurcation analysis in the absence of magnetic field, i.e., $\lambda_0 \neq 1$, $b_2^0 = 0$, provides the critical mechanical stretch $\lambda_0^c = 0.76$ at the onset of wrinkling and the associated wavenumber $\omega = 4$ (macroscopic length scale). Upon further increase of the applied strain ($\varepsilon_{11} = \lambda_0 - 1$), the plane-strain simulations reveal a period-doubling configuration at $\lambda_0^{c2} = 0.7$. That, in turn, becomes unstable and gets unloaded at larger compressive values, $\lambda_0 < 0.68$. This response corresponds to a mechanical interlayer contrast $G_s/G_f = 0.3$, in agreement with the characterization of our material layers [2]. Although our experimental materials are softer (silicones) than the rubber-like ones used in the simulations, this is of no importance for the purely mechanical buckling under incompressibility, where only the relative ratio G_s/G_f (and not the absolute values) drives the response.[3] The double-period pair bifurcates from wrinkling by varying the amplitude of the middle valley, leading to a period twice that of the wrinkles aside. However, the experimental observations are biased by strong frictional boundary effects suppressing wrinkling, see Fig.V.3. The experimental result bypasses the point of primary wrinkling without undergoing bifurcation, see Fig.V.3. That suggests that an appropriate choice of boundary conditions could tune the surface patterns by suppressing or bypassing modes and driving the solution directly to later bifurcations.

In Fig.V.3, we probe the experimental behavior upon numerical prescription of shear forces at the lateral edges of the system, $f_2 = 75\mu$N. In the presence of friction, wrinkling tends to be suppressed. In that case, it is not easy to capture secondary modes without the prescription of numerical imperfections. However, the numerics in the absence of user-defined imperfections and the experiments are in a quite good agreement.

To give a first indication whether the experimental geometry corresponds to the case of a deep substrate (one that theoretically can be considered as infinite), we include in Fig.V.4 the purely mechanical bifurcation analysis for an infinite system of Danas and Triantafyllidis (2014) and compare

[2]The mechanical properties of the film are found by direct fitting of the magnetomechanical experiment, as described in detail in Section V.2.

[3]When the loading is magnetomechanically coupled, buckling does not depend only on the ratio G_s/G_f, but also on the absolute G_s and G_f shear moduli values, see Fig.IV.7a.

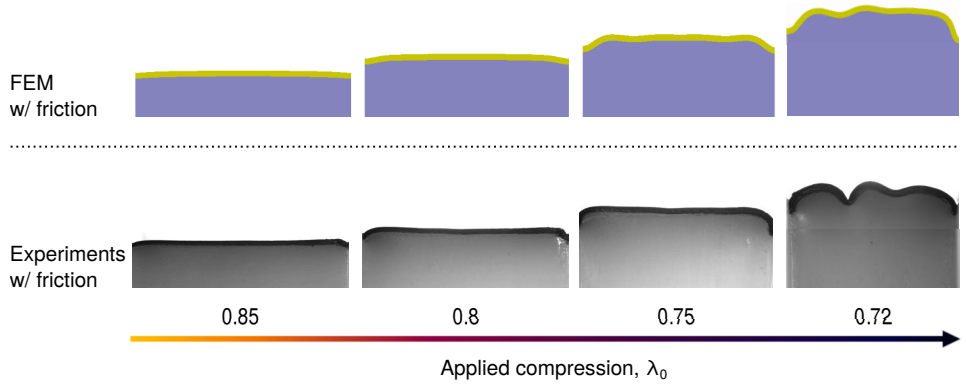

Figure V.3: Numerical versus experimental morphological response of the film/substrate system under uniaxial mechanical compression λ_0 and friction acting on the lateral faces of the system. Friction tends to suppress wrinkling and to lead directly to localizations. The simulations are in the absence of a user-defined imperfection and thus, it is not easy to capture the secondary mode. Interlayer stiffness contrast, $G_s/G_f = 0.2$. Value of friction in the numerical simulations, $f_2 = 75\mu$N.

it with the present finite (numerical) geometry. The full range of the film/substrate moduli ratio G_s/G_f is considered from the limit of a traction-free homogeneous substrate (Hutchinson, 2013) ($G_s/G_f \to 1$) to very stiff films on compliant substrates ($G_s/G_f \to 0$). Fig.V.4a presents the critical value of the stretch ratio λ_0^c versus the substrate-to-film shear ratio G_s/G_f. The numerical and theoretically predicted by Danas and Triantafyllidis (2014) buckling loads λ_0^c are in quite good agreement. We note that the theoretical study is carried out for infinite boundary conditions, whereas the numerical study is on a finite structure mimicking the experimental one. The critical buckling strain $\varepsilon_{11}^c (= \lambda_0^c - 1)$ increases with increasing interlayer contrast G_s/G_f. That implies that the stiffer the substrate, the more elastic energy needs to be stored in order for the system to buckle. In the limit of $G_s/G_f \to 0$, the critical load $\lambda_0^c (b_2^c = 0) \to 1$ (as well as the corresponding wavenumber $(\omega \mathrm{H})^c \to 0$). That is the case of zero compressive axial load of an infinitely long and unsupported Euler beam (Danas and Triantafyllidis, 2014). A unique wavelength wrinkling is observed for $G_s/G_f \in (0, 0.6]$, validating our theoretical bifurcation model in Chapter IV.

When $G_s/G_f \in (0.6, 1)$, the post-bifurcated configuration becomes non-periodic, indicating possible initiation of creases in accordance with literature (e.g., see Cao and Hutchinson, 2012a, Hutchinson, 2013, Wang and Zhao, 2013b). In this latter case, the instability is generated before the so-called "surface bifurcation" of Biot (1965) ($G_s/G_f = 1$). In finite strains, geometry and material properties are coupled. The surface bifurcation is attributed to the stiff substrate ($G_s/G_f > 0.6$), in combination with the divergence from Euler buckling geometry[4] due to high strains ($\varepsilon_{11}^c \geq 35\%$) that set H_f comparable to the length l. The maximum value of critical stretch is $\lambda_0^c = 0.54$ (or critical strain $\varepsilon^c = 0.46$) for $G_s/G_f = 1$, in consistence with Cao and Hutchinson (2012a), Wang and Zhao (2013b). Biot's result, $\varepsilon^w = 0.456$, corresponds to surface wrinkling of a homogeneous ($G_s/G_f = 1$) neo-Hookean half space[5] under plane-strain compression. Since there is no length scale associated

[4] i.e., Euler beam requires: $\mathrm{H}_f \gg l$, where H_f the thickness and l the length of the film
[5] half space: $-\infty < X_1 < \infty$ (in-plane direction) and $-\infty < X_2 < 0$ (thickness direction)

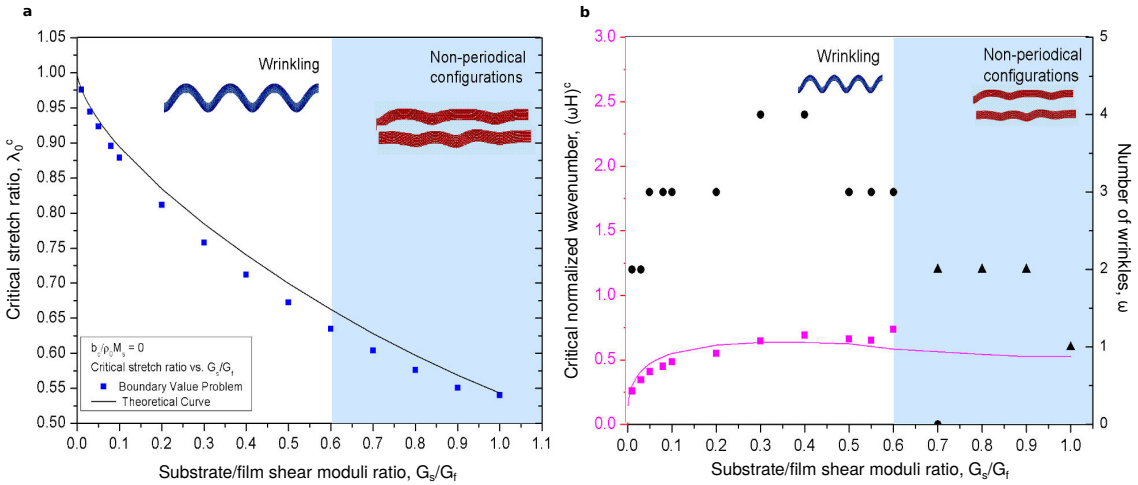

Figure V.4: **a**, Critical mechanical stretch; **b**, normalized wavenumber (left axis) for an infinite (pink curve) and a finite film/substrate system (pink symbols) and number of finite wrinkles (right axis) for the structure (black symbols) versus the substrate-to-film shear moduli ratio G_s/G_f. The infinite system is described as an infinitely long two-dimensional bilayer with the film bonded on an infinitely deep substrate. The finite system is described as a 40×40 (mm^2) bilayer block, with film thickness $\mathrm{H}_f = 0.8$ mm and none user-defined geometrical nonlinearity. The shear modulus of the film is fixed at $(G_f =)1$ MPa. Both layers are slightly compressible, a condition satisfied via a large Lamé constant $G_i' = 100\,G_i$, $i = f,s$, for the film and the substrate respectively. For $G_s/G_f = 0.3$, the number of wrinkles is $\omega = 4$. That is the value also found in the magnetomechanical experiment while approaching the mechanical bifurcation point at $\lambda_0^c \approx 0.76$ (see Figs.II.16, II.17, II.18a-p).

with the homogeneous half-space, the bifurcation mode in this limit can have any wavelength (Cao and Hutchinson, 2012a). However, it has been shown that surface wrinkling of a homogeneous half-space is highly unstable and imperfection-sensitive, such that imperfections will trigger surface creases before wrinkling is attained (Cao and Hutchinson, 2012a).

In the present study, a reasonable question is how the film bifurcates to advanced patterns (creases) in the absence of user-defined geometrical imperfections. First, it should be stated that it is the size (i.e., magnitude of order) and not the type (e.g., linear, sinusoidal, Gaussian bump function etc) of the imperfection that affects the critical modes. In our case, the tiny magnetic field $b_2^0 = 10^{-6}$ T (applied for numerical reasons) acts as a slight imperfection in the corners of the film, where the concentration of magnetic quantities has been observed (see Fig.V.7). As a result, the non-uniformity of the magnetic field due to the presence of sharp changes in geometry, as well as the presence of the (unstructured) air mesh act as sufficient imperfections to trigger mechanical buckling.

In Fig.V.4b, the wavenumber corresponding to the critical buckling load is plotted as an integer ω and as a normalized value $(\omega H)^c$ versus the shear moduli ratio G_s/G_f. The normalized wavenumber of the boundary value system reads $(\omega H)^c = 2\pi/L$, with ω the number of wrinkles, H the thickness of the film and L the wrinkling wavelength at the onset of buckling. The numerical values are in accordance with the theoretical solution of Danas and Triantafyllidis (2014), giving direct access to the number of wrinkles for a given film thickness. This is an indication that the present geometry

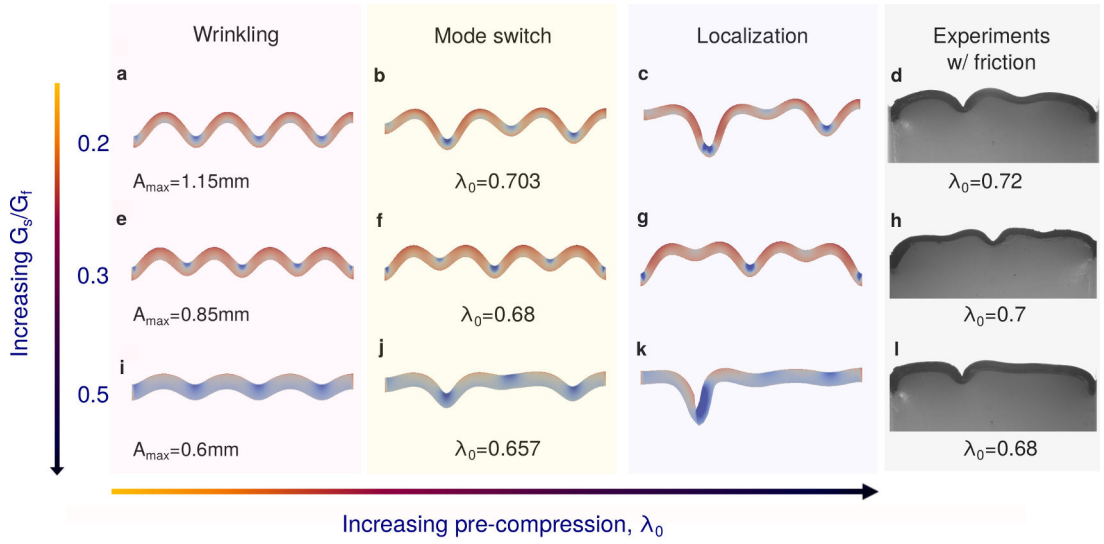

Figure V.5: Morphological response of the film under compression in the parameter space of the stretch ratio λ_0, for three different values of the substrate-to-film shear modudi ratio: $G_s/G_f = 0.2, 0.3, 0.5$. Depending on the mechanical properties of the phases, the equilibrium points vary. In the post-bifurcation regime, the wrinkles evolve into localized modes versus the moduli contrast G_s/G_f. Beyond the secondary bifurcation, the depth of the localizations grows upon further compression. The secondary surface modes are presented for both numerical and experimental findings. The numerical two-dimensional system is described as a 40×40 (mm^2) bilayer block, with film thickness $\text{H}_f = 0.8$ mm, shear modulus $G_f = 1$ MPa and none geometrical nonlinearity. Both layers are slightly compressible, a condition satisfied via a large Lamé constant $G_i' = 100\,G_i$, $i = f, s$, for the film and the substrate respectively. The incremental ratio of the film thickness-to-length H/l increases with increasing shear moduli contrast G_s/G_f. As a result, the amplitude of the primary wrinkling mode decreases with increasing G_s/G_f ratio.

is indeed representative of a film/substrate system. The maximum number of wrinkles in the finite stucture is four within the range $0.3 \leq G_s/G_f \leq 0.4$. This is also in agreement with our experimental findings, shown in the magnetomechanical morphological map of Figs.II.18a-p. The critical stretch ratio corresponding to this range is $0.76 \geq \lambda_1^c \geq 0.71$.

The critical wavenumber $(\omega H)^c$ initially shows a sharp increase as it increases from zero, while it becomes less sensitive to the interlayer shear moduli ratio for $G_s/G_f > 0.2$. Contrary to small-to-moderate moduli ratios, the surface instabilities do not display wrinkling but creasing. Although the bifurcation theory on the infinite system of Danas and Triantafyllidis (2014) considers wrinkling for $G_s/G_f > 0.6$, the boundary value system would buckle under a creasing mode in this regime of material properties. A representative morphology of the non-periodic modes[6] is shown in Fig.V.4a,b (red inset figures). Fig.V.4 can be of use for designing different surface patterns on film/substrate systems made of different materials, under mechanical compression.

Next, the morphological instabilities and the post-instability evolution of the system are considered in Fig.V.5. The system exhibits a rich behavior and thus, a map of three indicative evolution paths is developed in the parameter space of the mechanical loading λ_0 and the relative stiffness

[6]Such modes are a direct consequence of the finite size boundary-value problem we analyze.

properties of the layers G_s/G_f. The system undergoes secondary bifurcations, following patterns that are sensitive to the interlayer stiffness contrast. We classify the configuration space for three substrate/film shear ratios: $G_s/G_f = 0.2, 0.3, 0.5$. The advanced bifurcation modes are triggered in the absence of user-defined imperfections and thus, they approximately occur as secondary instabilities on a perfect system. For each material contrast, we show the shape configuration in the primary post-bifurcated regime (pink), immediately after the secondary bifurcation (yellow), as well as deep in the secondary post-bifurcated regime (purple and grey). It is recalled that the primary bifurcation corresponds to the first non-positive eigenvalue of the stiffness matrix. More particularly, the smallest eigenvalue of the system incrementally decreases until it reaches a first minimum close to zero. That point is defined as the primary instability point. Subsequently, the smallest eigenvalue increases but then decreases again towards a second minimum, which is then defined as a secondary instability point.

Once the compressive strain reaches the first critical instability point, the layer forms wrinkles under a sinusoidal pattern ($G_s/G_f < 0.6$), Figs.V.5a,e,i (pink regime). The amplitude of the wrinkles under a given stretch λ_0 decreases with increasing stiffness contrast G_s/G_f. For $G_s/G_f = 0.2$, the maximum amplitude is at 1.15mm (well-touchable pattern), while for $G_s/G_f = 0.5$, it gets less than the half at 0.6mm. Further increase of the loading triggers symmetry breaking into non-symmetric modes of growing and decaying valleys with, respectively, progressively increasing and decreasing amplitudes, Figs.V.5b,f,j (yellow regime). As loading increases beyond the secondary instability point, advanced localizations emerge, Figs.V.5c,d, g,h,k,l (purple and grey regime). The secondary critical modes are sensitive to G_s/G_f contrast: a ratio of $G_s/G_f = 0.2$ favors a double localization of different amplitudes (Figs.V.5b), a ratio of $G_s/G_f = 0.3$ favors a double-period pair (Figs.V.5f), a ratio of $G_s/G_f = 0.5$ favors a crease (Figs.V.5j). The depth (amplitude) of localizations grows upon the increase of compression, while the decaying valleys get unloaded, i.e., they morphologically flatten-out followed by stress decrease. As the contour plots in Figs.V.5c,g,k illustrate, the localization of the amplitude is respectively followed by stress concentration. The local strains around the creases are large ($\sim 40\%$) (see also Zhao and Suo, 2009) and thus, only finite element methods under finite strains are able to capture these modes. A linear (small deformation) stability analysis is not adequate to analyze the critical strains of creasing instability.

Experimental evidence of the well-formed secondary modes accompany the numerical simulations at Figs.V.5c,d,g,h,k,l (purple and grey regime). Although it is difficult to measure the exact shear moduli of our experimental materials (see discussion in Section II.5.3), changing the quantity of the hardener in the polymeric mixture creates different material behaviors. More precisely, the hardener affects the number of cross-links in the polymeric chains and as a result, the macroscopic stiffness of the material. In that way, for fixed film material properties, two substrates of 0.85:1 and 1.3:1 hardener:polymer mass ratios are fabricated, corresponding to mechanical contrasts $G_s/G_f < 0.3$ and $G_s/G_f > 0.4$, respectively. As seen in Fig.V.5, the surface patterns under experimental compressions, $\lambda_0 < 0.73$, are in agreement with the secondary numerical modes. The critical loads are also sensitive to the material contrast; the greater the ratio G_s/G_f, the greater the

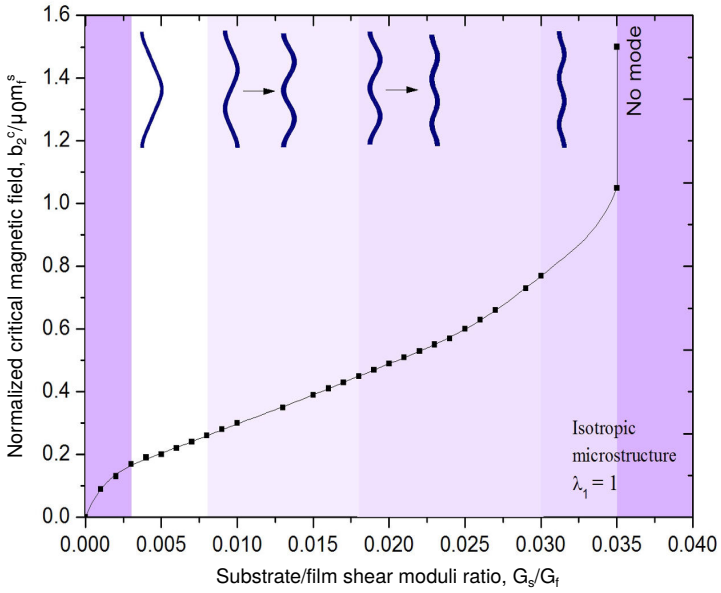

Figure V.6: Numerical study on the critical value of the dimensionless applied magnetic field $b_2^c/\mu_0 m_f^s$ versus the substrate/film shear moduli ratio G_s/G_f, in the absence of stretching $\lambda_0 = 1$. The buckling and post-buckling configurations are also shown for different mechanical interlayer contrast G_s/G_f regimes.

compressive strain needed to trigger a secondary bifurcation, Figs.V.5b,f,j.

V.1.2 Purely magnetic loading

In this section, we examine the critical magnetic field b_2^c needed to trigger the instability in the absence of a pre-stretch ($\lambda_0 = 1$). The magnetic field b_2^0 is applied perpendicular to the film. The mechanism of the magnetic buckling can be intuitively understood by considering the interaction of magnetized particles dispersed in a soft matrix with the external magnetic field. The applied magnetic field first magnetizes the particles, which in turn interact one with another, trying to be realigned into the minimal magnetic energy configuration. The compliance of the soft medium allows the magnetized particles to induce small deformations, producing internal stresses. If the matrix is soft enough, the external magnetic field can induce significant changes in the geometrical shape, as well as in the mechanical properties of the composite (e.g., see Ginder et al., 2000, Kankanala and Triantafyllidis, 2004). At the macroscopic level, the magnetized film exhibits the compass effect (it rotates to align with the field direction). Instabilities arise from the compromise between competitive effects. The presence of the substrate penalizes the elastic bending energy of the film while trying to align with the external field. The competition between the magnetic and the elastic energy leads to buckling at some critical magnetic field value.

The bilayer specimen is that used in the previous purely mechanical loading case. It consists of a 40×40 (mm^2) block of $H_f = 0.8$mm film thickness. The constant mesh does not include any geometrical imperfection, apart from the unstructured air regime and the corners of the block. Following convergence studies (not shown here), the air penalty value is set at ε =1e-10. The

isotropic magnetoelastic film is modeled as a rubber, with shear modulus $G_f = 1$MPa. The magnetic properties of the film are found from experimental measurements and theoretical estimates (see Section II.6), presented in Table IV.1 and plugged into the Langevin law (see Section III.2). The model accounts for the susceptibility of the film $\chi_f = 0.4$ and the saturation magnetization $\mu_0 m_f^s = 0.5$T. The vacuum permeability μ_0 is set equal to $4\pi\,10^{-1}$NA^{-1} for unit compatibility with the shear moduli given in MPa. The two neo-Hookean layers are set nearly incompressible via a large Lamé constant $G_i' = 100\,G_i$, $i = f, s$ for the film and the substrate, respectively. Zero susceptibility and saturation magnetization are assigned to the substrate and the air. For pre-stretch $\lambda_0 = 1$, the external magnetic field is linearly applied at the boundaries of the free space from 0 to 3T in 1000 steps. More precisely, the magnetic loading is applied in form of displacement via the magnetic vector potential $a = -B_2^0 X_1$, with $B_2^0 = \lambda_0 b_2^0$ the magnetic field and X_1 the coordinate component in the reference configuration, respectively.

Fig.V.6 shows the critical value of the normalized applied magnetic field $b_2^c/\mu_0 m_f^s$ as a function of the substrate-to-film shear moduli ratio G_s/G_f. At the top of the graph, the (post-)buckling configurations are also shown. The modes evolve in a different manner than those under a purely mechanical loading. Here, a given shape configuration defines a range of G_s/G_f ratios and not just a single value. The critical magnetic field monotonically increases as a function of G_s/G_f, attaining an asymptote due to saturation of magnetization at $G_s/G_f = 0.035$. To give a possible explanation for this phenomenon: when the substrate is relatively stiff compared to the film, the magnetic energy (the work done by magnetic body forces if it helps to visualize it as such) is highly penalized under a given magnetization saturation state, despite the increase of the applied magnetic field. This result is also found by Danas and Triantafyllidis (2014), while working with an equivalent continuum formulation. The $G_s/G_f = 0.035$ value (with $G_f = 1$ MPa) denotes an upper limit for the substrate stiffness, beyond which the onset of instability is prevented. In the view of applications for surface patterning triggered by magnetic fields, softer materials would be recommended so as to widen the range of G_s/G_f. In that way, the layers would be more compliant to deform under the same state of magnetization (see also the effect of material properties on the critical response, obtained by the theoretical bifurcation analysis in Fig.IV.7a and Fig.IV.8a).

A classical bending mode is obtained for $0.003 \leq G_s/G_f < 0.008$, while a long-wavelength configuration describes the initial post-bifurcated regime for $0.008 \leq G_s/G_f \leq 0.018$. A primary well-defined wrinkling is then attributed to $0.018 < G_s/G_f \leq 0.035$. Note that the operational range $0 < G_s/G_f \leq 0.035$ for the onset of wrinkling under a purely magnetic loading is essentially lower than that of the purely mechanical loading, $0 < G_s/G_f \leq 0.6$. To expand the validity of this range and to increase the wrinkling wavenumber, a combined magnetomechanical loading is proposed in Section V.1.3.

The distribution of the magnetic field throughout the film and the surrounding space in the pre- and post-bifurcated regime is considered in Fig.V.7a and V.7b, respectively. The magnetic flux $b_2 (= b||e_2)$ is plotted along a horizontal line located in the middle of the film ($X_2 = +19.6$ mm) for applied magnetic field $b_2^0 = 0.28$T and $b_2^0 = 0.5$T, respectively. The magnitude of the field is

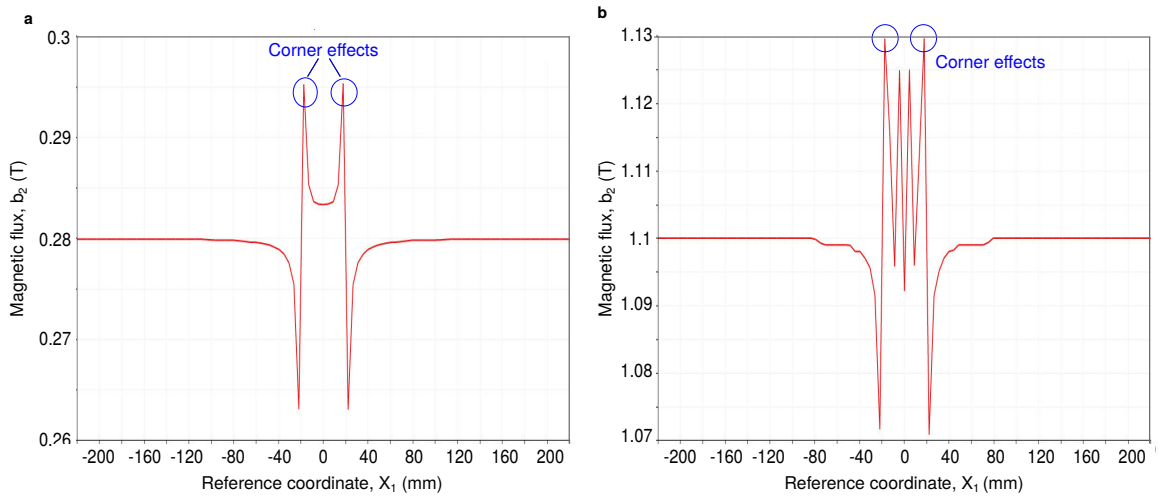

Figure V.7: Variation of the magnetic flux $b_2(=b||e_2)$ along a horizontal line throughout the film and the surrounding air ($X_2 = +19.6$ mm) for applied magnetic field **a**, $b_2^0 = 0.28$T corresponding to pre-bifurcation and **b**, $b_2^0 = 0.5$T corresponding to post-bifurcation.

symmetric about the direction e_2. The magnetic flux sharply increases when it approaches the boundaries ($X_1 \to \pm 20$ mm), where it reaches its maximum value for both pre- and post-bifurcation configurations. In the pre-bifurcated regime (Fig.V.7a), the flux is uniform within the film apart from the boundary. That uncovers the effect of the corners on the concentration of magnetic quantities (e.g., magnetization is affected in the same way, see Fig.V.12f). In the post-bifurcation regime (Fig.V.7b), the flux also varies within the film as the system wrinkles. To conclude, the existence of the corners alters the uniformity of the magnetic flux b_2, since the sharp changes in geometry constitute concentration areas. This acts as an unavoidable imperfection in the magnetoelastic system (plus the unstructured mesh of the air) and thus, is sufficient to trigger the bifurcation in the absence of an additional user-defined geometrical imperfection.

V.1.3 Coupled magnetomechanical loading

Instabilities on MRE film/substrate bilayers are triggered for a wider range of systems by a combined magnetomechanical loading, rather than by the independent loads (e.g., see Danas and Triantafyllidis, 2014). A prior step to the experimental verification of this concept is a numerical study that aids to design our materials and loading setups. Here, the effect of the coupled loading versus the independent loadings is studied in the parameter space of the mechanical properties G_s/G_f of the bilayer system, for a fixed film modulus $G_f = 1$ MPa. It should be noted that the magnetomechanical bifurcation is a rich problem that does not depend only on the applied magnetic field b_2^0, the applied stretch ratio λ_0 and the substrate-to-film shear modulus G_s/G_f. Other parameters affecting the critical response have been discussed in Section IV.4. In this section, the loading case consists of applying a pre-stretch λ_0 close to (but not at) the mechanical instability and then increasing the magnetic field b_2^0 beyond the instability point to obtain surface wrinkles. Illustrating that this process is feasible, one comes a step closer to verify the initial concept of Danas and Triantafyllidis

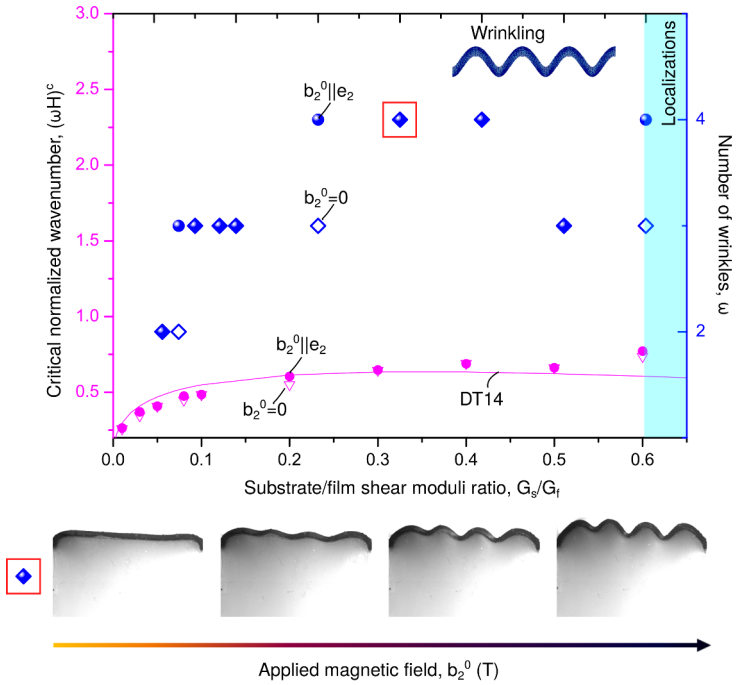

Figure V.8: Numerical study on the critical value of the normalized wavenumber $(\omega H)^c$ and the number of wrinkles ω formed on the finite film/substrate sytem versus the substrate-to-film shear ratio G_s/G_f for the purely mechanical ($b_2^0 = 0$) and the magnetomechanical ($b_2^0||e_2$) loading case. The continuous curve corresponds to the results of Danas and Triantafyllidis (2014) on an infinite bilayer, as described in Section IV.2. The discrete values correspond to the numerical boundary value problem, also described in Section III. The loading case consists of applying a pre-stretch λ_0 close to (but not at) the mechanical instability and then increasing the magnetic field b_2^0 beyond the instability point to obtain surface patterns. For $G_s/G_f = 0.3$, we show the experimental pattern that is magnetically-triggered at $b_2^c = 0.2$T. The applied pre-stretch is $\lambda_0 = 0.78$, which is not far from the mechanical instability point $\lambda_0^c \approx 0.76$. The experimental wavenumber, $\omega = 4$, is in agreement with the theoretical and numerical results.

(2014) applied on a non-trivial boundary value system and to get a better insight into the design of the experiment system.

The phenomenological approach used needs to account for nonlinear effects associated with finite strains and magnetic saturation of the particles at sufficiently high magnetic fields. For the definition of the free energy, it suffices in the present study (see discussion in Section II.5.2 and III.2) to propose a simple combination of a Neo-Hookean elastic energy and a Langevin (without hysteresis) magnetic energy. The input values of the problem are set as follows: the magnetic properties of the film are found from experimental measurements and theoretical estimates (see Section II.6), presented in Table IV.1 and plugged into the Langevin law. The model accounts for the susceptibility of the film $\chi_f = 0.4$ and the saturation magnetization $\mu_0 m_f^s = 0.5$T. The vacuum permeability μ_0 is set equal to $4\pi\, 10^{-1}$NA^{-1} for unit compatibility with the shear moduli expressed in MPa. The hyperelastic layers are set nearly incompressible via a large Lamé constant $G_i' = 100\, G_i$, $i = f, s$ for the film and the substrate, respectively. Zero susceptibility and saturation magnetization are assigned to the substrate and the air. The bilayer specimen is that used in the previous purely mechanical and purely magnetic loading cases. It consists of a 40×40 (mm^2) block of $H_f = 0.8$mm film thickness.

The constant mesh does not include any geometrical imperfection, apart from the unstructured air region and the corners of the block (see Fig.V.7). Following convergence studies, the air penalty is set at ε =1e-10. For a given G_s/G_f value, the applied pre-stretch λ_0 is linearly decreased from 1 close to the critical pre-stretch $\lambda_0^c + 0.1$ over 100 time increments. Then, the applied magnetic field b_2^0 is linearly increased from 0 to 3T over 1900 increments.

The most direct comparison between the magnetomechanical and the independent loadings in the parameter space of the mechanical contrast G_s/G_f, can be done in terms of the wavenumber at the onset of wrinkling. In Fig.V.8, we plot the critical value of the normalized wavenumber $(\omega H)^c$ and the number of wrinkles ω formed on the finite film/substrate system under a purely mechanical $(b_2^0 = 0)$ and a magnetomechanical $(b_2^0 || e_2)$ loading as a function of the substrate-to-film shear moduli ratio G_s/G_f. The normalized wavenumber $(\omega H)^c$ is plotted for the infinite problem of Danas and Triantafyllidis (2014) bifurcation analysis, as well as the numerical finite structure. A very good agreement is found between the theoretical analysis and the numerical simulations, carried-out in two different but equivalent variational frameworks.

A first feature observed in Fig.V.8 is that the number of the wrinkles in the block increases by one upon application of the coupled loading, for $G_s/G_f = 0.03$, 0.2 and 0.6. In comparison with the purely magnetic loading case, the long wavelength configurations give rise to finite-wavelength wrinkling. Moreover, the range of the film/substrate stiffness contrast is that of the purely mechanical loading case, i.e., $G_s/G_f \in (0, 0.6]$. In virtue of the magnetomechanical loading coupling, the G_s/G_f range is now expanded to impressively higher values that can be experimentally applied, unlike the purely magnetic loading case (where $0 < G_s/G_f \leq 0.035$). The bifurcation is found to be triggered by magnetic fields decreased by 200% with respect to the purely magnetic loading case (not shown here). We note that the critical magnetic field follows an increasing trend with increasing G_s/G_f ratio.

For $G_s/G_f = 0.3$, the relevant response of the experimental MRE film/substrate specimen is presented. Surface wrinkling is magnetically-triggered at $b_2^c = 0.2$T, under a pre-compression $\lambda_0 = 0.78$ that is close to the mechanical instability point $\lambda_0^c \approx 0.76$. The experimental wavenumber, $\omega = 4$, is in agreement with the theoretical and numerical results. To conclude, Fig.V.8 can be used to design the response of MRE film/substrate blocks for different mechanical ratios (fixed $G_f = 1$MPa), under given magnetic properties for the film (i.e., susceptibility $\chi_f = 0.4$, saturation magnetization $\mu_0 m_f^s = 0.5$T). These magnetic properties correspond to the film we experimentally fabricate. As a result, a next step is to fit the experimental magnetomechanical findings on soft silicones with moderate $G_s/G_f \approx 0.3$, performed within a wide range of applied pre-compressions.

V.2 Experiments versus numerical simulations

A combined method of experiments and FE implementations is employed to evaluate the stiffness of the material-layers by numerically fitting the amplitudes of the experimental surface patterns. This is attributed to the difficulties in characterization of composite films under compression, see Section

II.5.3. The experimental (post-)bifurcation amplitudes are successfully probed with the full-field finite element calculations. For clarity, we show in Fig. V.9a such comparisons for three values of pre-compression. We note that the amplitude curves corresponding to a pre-compression $\lambda_0 = 0.8, 0.85$ have been used to identify the shear moduli of the MRE film ($G_f = 10$KPa) and the substrate ($G_s = 3$kPa), thus leading to a substrate-to-film shear moduli ratio $G_s/G_f = 0.3$. Considering an almost incompressible response and small magnetomechanical coupling, the total number of material parameters used in the modeling is four. An additional parameter related to the applied shear force is used to model the lateral friction between the specimen and the compression device (see Section V.3). These assumptions have been found sufficient to extract all (twelve) experimental curves. Nevertheless, this does not necessarily mean that the obtained model is unique, due to the strong nonlinearities. The strategy to fit the model with the minimum set of experiments will be summarized as following:

1) The magnetic susceptibility of the MRE material is obtained by fabricating and measuring the susceptibility χ_f of an independent cylindrical sample.

2) For the magnetic saturation m_f^s of the film, previous experimental and theoretical results state that the magnetic saturation of a two-phase composite, with one phase being non-magnetic, is only a function of the volume fraction and the magnetic saturation of the magnetic phase itself (see Danas, 2017, Danas et al., 2012).

3) For the shear moduli of the substrate and the film, the curing processes of the 40mm edge cube and the thin-section dogbone sample lead to different polymerization times/processes, see Section II.5.3. In addition, the film/substrate system is pre-compressed in a fixed setup under a fully relaxed state, while a tension experiment has intrinsic rate effects. The incremental moduli of neo-Hookean solids also exhibit tension-compression asymmetric response. Thus, the tensile stress-strain curve cannot accurately recover the response under compression. For the MRE material characterization, it is not straightforward to have direct access to the properties when deposited as a film. The response of a film is possibly not identical to that of a dogbone specimen, due to fabrication uncertainties and possible particle clustering while depositing the film. As a result, we use two bifurcation curves obtained experimentally, corresponding to pre-compressions $\lambda_0 = 0.8$ and $\lambda_0 = 0.85$. For further validation of the substrate shear modulus and the neo-Hookean constitutive law, we carried out independent uniaxial tension tests at a very low rate ($\dot{\varepsilon} = 5 \cdot 10^{-6}\, s^{-1}$) in a standard dogbone sample and obtained a neo-Hookean response up to 10% straining with shear modulus $G_s = 3.5$kPa. From the fitting of the bifurcation curves, we obtain $G_s = 3$kPa for the substrate and $G_f = 10$kPa for the MRE film, such that $G_s/G_f = 0.3$. These values are then sufficient to fit the rest of the nine experimental curves accurately.

5) Acting on the lateral faces of the film/substrate block to simulate friction, the maximum applied shear force is obtained by fitting (to the best possible accuracy) the bifurcation curve for $\lambda_0 = 0.75$ (see Fig. V.10). Table V.1 summarizes the material parameters corresponding to the experimental and numerical MRE film/passive substrate. Given the very good agreement between the numerical and experimental results for a very large range of pre-compressions and magnetic

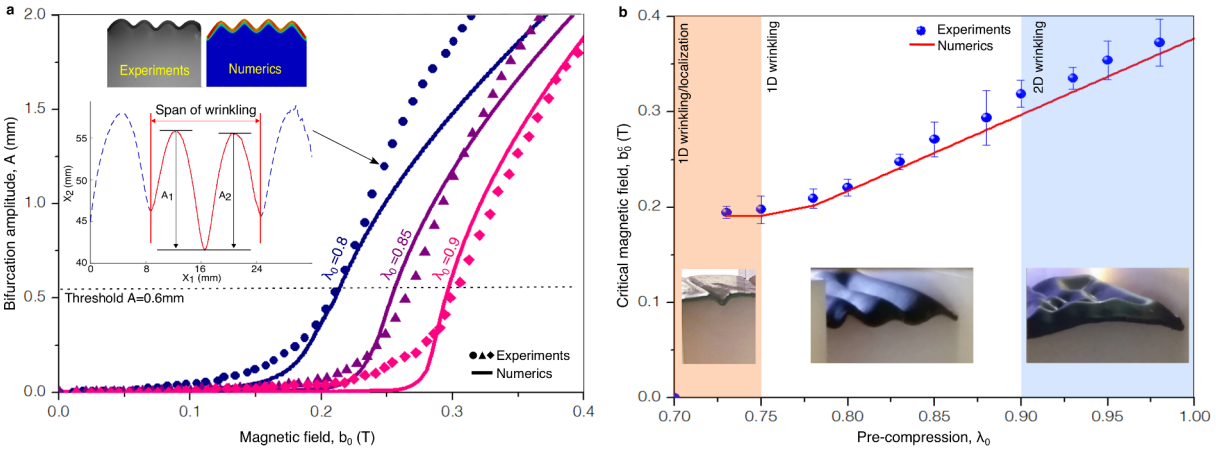

Figure V.9: Identification of bifurcation in the two-field parameter space: mechanical pre-compression λ_0 and magnetic field b_0. A decreasing trend of the critical magnetic field b_0^c as a function of the applied pre-stretch λ_0 is observed in: **a**, Supercritical bifurcation curves for $\lambda_0 = 0.8, 0.85, 0.9$. Continuous lines correspond to numerical predictions, while symbols correspond to experimental data reported in Fig.II.18q. The insets present, at $\lambda_0 = 0.8$ and $b_0 = 0.25$T, comparisons between experimental and numerical profiles, as well as the experimental film profile used to obtain the amplitude curves. **b**, A two-field stability phase diagram of morphological patterns. Experimental and numerical (λ_0, b_0^c) critical points for 2D wrinkling (blue), 1D wrinkling (white) and wrinkling followed by curvature localization patterns (orange) are defined from the bifurcation curves (in Figs.II.18q, V.9a and V.10a) by considering a threshold of macroscopically observed bifurcation amplitude $A = 0.6$mm. Standard deviation of measurements among three specimens is included in the experimental data points.

fields, the proposed simple-material model is indeed sufficient to probe the problem at hand.

H_f (mm)	H_s/H_f	G_s (kPa)	G_s/G_f	χ_f	$\mu_0 m_f^s$ (T)	f_{max} (μN)
0.8	49	3	0.3	0.4	0.5	72

Table V.1: Geometry and material properties of the film/substrate block, used in the experimental and numerical analysis.

The rest of the numerical estimates are then found to be in good agreement with the experimental measurements for the aforementioned loading parameters. The numerical simulations are capable to reproduce the decrease of the critical magnetic field b_0^c with increasing pre-compression λ_0. Agreement between the numerics and the experiments is also obtained in terms of the surface patterns, as shown in the inset of Fig.V.9a. The numerical results predict exactly four wrinkles along the film length. This fair comparison allows us to use the FEM results in the following section, so as to investigate the resulting magnetic fields in the post-bifurcation. Fig.V.9a illustrates the evolution of the bifurcation amplitude A versus the applied magnetic field b_0 for three different pre-stretches λ_0. When the applied field b_0 is relatively low, the flat state of film/substrate system gives zero wrinkling amplitude. As the applied field approaches a critical value b_0^c, the potential energy of a new state becomes equal to that of the flat state and the system transits into wrinkling, i.e., non-zero amplitude. The transition is, however, smooth due to imperfections coming from the

applied boundary conditions. It is noted that we define the wrinkling state switched from the flat state as the initial instability mode.

Using next the experimental and numerical curves together with the threshold value $A(=0.6\text{mm})$, we propose a comprehensive two-field stability phase diagram in Fig.V.9b. The stability map shows that pattern switching can be achieved by proper control and cooperation of the magnetic and mechanical fields. In addition, the reduction of the critical magnetic field b_0^c with increasing pre-compression is experimentally quantified and numerically probed. For instance, when the block is under significant pre-compression (e.g., $\lambda_0 = 0.8$), the critical magnetic field $b_0^c(=0.2\text{T})$ reduces to half of that for small mechanical pre-compression (e.g., $\lambda_0 = 0.98$, $b_0^c = 0.38\text{T}$).

Based on pattern distinction, this diagram can be qualitatively divided into three representative domains: 2D wrinkling (blue), 1D wrinkling (white) and a 1D period-doubling (orange, see Fig.II.18o) regime that is followed by a mechanical crease at $\lambda_0 = 0.7$, see inset picture. At smaller pre-compressions (blue region), one observes 2D wrinkling as a result of high biaxial in-plane symmetry of the system and no particular bias to plane-strain modes. In this regime, the numerical and experimental results exhibit a slight deviation. This can be explained by noting that the numerical calculations assume plane-strain conditions, while the experimental camera-setup does not have access to the middle of the film surface, where the maximum amplitudes occur, see inset Fig.V.9b in blue regime. In turn, under moderate-to-high pre-compressions (especially for $\lambda_0 < 0.85$), the experimental and numerical bifurcation points (λ_0, b_0^c) are in excellent agreement. This is a result of the uniquely prescribed plane-strain conditions. Such a response validates qualitatively the simplified bifurcation analysis carried out in Chapter IV.

Interestingly, the critical b_0^c field decreases linearly with increasing pre-compression $\varepsilon_{11}(=\lambda_0 - 1)$ up to the theoretical mechanical bifurcation point, $\lambda_0^c \simeq 0.76$. Beyond that point, an asymptotic response is observed with no further reduction of b_0^c (orange regime in Fig.V.9b). The asymptotic saturation of the critical magnetic field at large pre-compressions is a direct consequence of friction and curvature effects at the lateral faces of the film, see context of Fig.II.18m-p. As a result of such frictional effects, the mechanical (i.e., localized) and the magnetic (i.e., wrinkled) bifurcation modes become different and thus, non-cooperating. In turn, this incompatibility prevents further decrease of the critical magnetic field b_0^c, despite the increase of pre-compression. One could improve this effect with a thinner film, see Section V.5. Then, the number of wrinkles increases and the boundary effects become less important. Nevertheless, the influence of friction upon the observed bifurcation mode is by itself an interesting result that requires further investigation, see Section V.3 .

To conclude Fig.V.9b, the critical field reduction is clearly demonstrated for the first time. Such a result is a direct consequence of the magnetomechanical coupling and the proper cooperation of the resulting mechanical and magnetic instabilities. The qualitative explanation behind it is the following: the elastic energy stored by pre-compression λ_0 brings the system near (but not exactly to) a mechanically critically stable state. Such a state aids in turn to trigger a cooperative magnetic instability at a lower magnetic field b_0^c. The low magnetic fields at play and the simplicity of the proposed MRE film/substrate geometry (e.g., one can easily touch the film surface during the

experiment and feel the roughness at a mm scale) makes the present system a potential candidate for an actual magnetomechanical device that allows for dynamic active control of surface patterns. The critical magnetic field can be further reduced by more unstable microstructures, such as particle-chain ones (e.g., see Danas and Triantafyllidis, 2014). Such a work is under way and will be presented in the future.

V.3 Friction effects at large pre-compressions

In this section, we numerically investigate the response of the MRE film/substrate system under large pre-compressions $\lambda_0 \in [0.7, 0.78]$ and we probe the relevant experimental findings. This study aims to give an insight on the experimental absence of wrinkling under compression ($b_0 = 0$), even beyond the purely mechanical bifurcation point $\lambda_0^c = 0.76$. We note that the mechanical bifurcation point is obtained numerically for interlayer stiffness contrast $G_s/G_f = 0.3$.

We begin the analysis after observing a noticeable curvature at the corners of the film in Figs.II.18 e,f,i,j,m,n. Such a curvature grows with increasing pre-compression and is related to frictional effects at the boundary of the specimen in contact with the compression device[7]. Under finite pre-strains, the curvature is no further negligible when compared to the thickness of the film and the size of the specimen, Figs.II.18,m,n. As numerically verified in Figs.V.3,V.9b, the frictional effect inhibits a clean mechanical wrinkling and leads to a localized pattern. Albeit experimentally not observed, the primary mechanical buckling is numerically found at $\lambda^c \simeq 0.76$, see Fig.V.2. About that compressive stretch, the incremental modulus of the neo-Hookean substrate is possibly different from the ground state and becomes anisotropic. Such an indication can be retrieved from the tensile stress-strain response of the soft silicone substrate, following the neo-Hookean law within the range $1 \leq \lambda \leq 1.25$. We note that compression and tension are not necessarily anti-symmetric about the nominal stress axis; the incremental modulus of neo-Hookean solids undergoes different slopes in the tensile and compressive direction. As a result, a tensile stress-strain curve cannot accurately recover the response under compression[8]. In turn, a higher interlayer stiffness contrast is possibly formed, $G_s/G_f \geq 0.6$, known to yield mechanically localized instabilities, e.g., creases.

Considering the complexity of the air modeling and the partial continuity of the magnetic fields, we employ an approximate procedure to model friction that does not necessitate the direct modeling of contact. Specifically, one can bypass the contact problem by adding an empirical tangential force f_2 (in the X_2 direction) at the lateral edges of the block to mimic contact, see Fig.III.1. This force is a function of the applied pre-compression λ_0 and reads

$$f_2 = f_{max}\,\frac{1-\lambda_0}{1-\lambda_0^{max}}, \qquad f_{max} = 72\mu N, \quad \lambda_0^{max} = 0.73. \tag{V.1}$$

The quantity λ_0^{max} corresponds to the maximum compressive pre-stretch experimentally achieved. This law is related to a nonlinear friction relation, in the sense that the applied stretch in direction

[7] even after silicone oil is applied onto the lateral faces that are in contact

[8] e.g., PDMS exhibits uniaxial neo-Hookean behavior within the range $0.7 \leq \lambda \leq 1.5$ (see Sun et al., 2012).

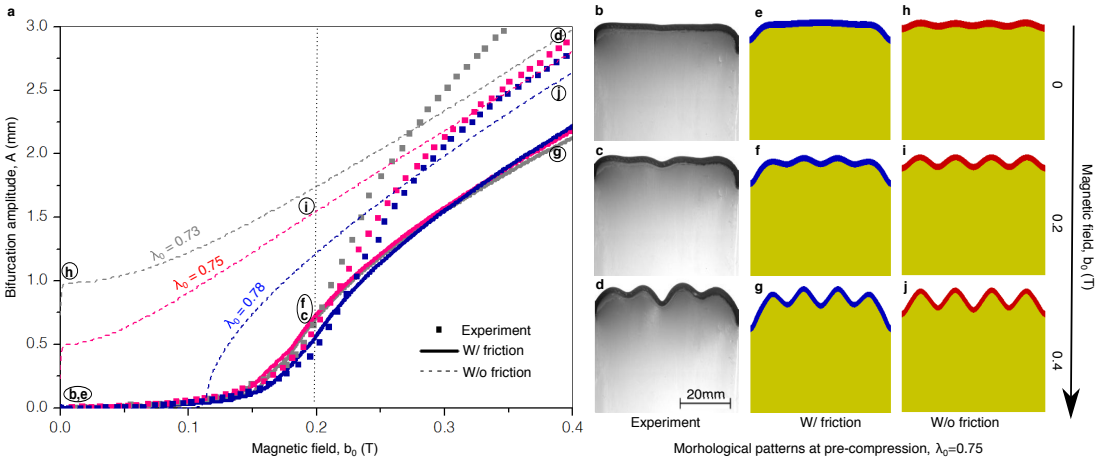

Figure V.10: Role of lateral friction on critical loads and patterns for high pre–compressions λ_0. Friction is modeled by applying a tangential force $f_2 = 72\mu$N along X_2 direction at the lateral edges of the two-dimensional solid. **a**) Comparison between the experimental bifurcation curves (symbols) and numerical curves with and without friction (continuous and dashed lines respectively) for $\lambda_0 = 0.73, 0.75, 0.78$; (**b-d**) Experimental and (**e-j**) numerical morphological modes with friction (film in blue) and without friction (film in red), respectively. At high pre-compression $\lambda_0 = 0.75 < \lambda_0^c$ and in the presence of friction (**e**), the mechanical wrinkling mode vanishes but not in the case without friction (**h**); The numerical pattern with friction turns into a more localized configuration (**g**), which fits better the experimental period-doubling and localized morphology (**d**) than the numerical pattern without friction (**j**).

X_1, i.e., $\lambda_0 \equiv \lambda_1$, is related in a nonlinear fashion to the normal force f_1 applied on the lateral face. The maximum force f_{max} is then a simple fitting parameter, which is obtained by fitting the early stage of the post-bifurcation response at $\lambda_0 = 0.73$.

In Fig.V.10a, we examine quantitatively the effect of friction on the bifurcation amplitude under three pre-stretches, $\lambda_0 = 0.73, 0.75, 0.78$. The main observation is that the bifurcation stagnates with increasing pre-compression when friction is applied (continuous curves denoted with "W/ friction"). By contrast, when the numerical calculations are frictionless, the curves exhibit a strong dependence on pre-stretch λ_0. For sufficiently small $\lambda_0 (= 0.73)$, the numerical wrinkles develop a non-zero amplitude well before the application of the magnetic field b_0. There is of course a transition point, which is directly linked to the purely mechanical critical wrinkling load, $\lambda_0^c = 0.76$. In this case, the bifurcation curve would start exactly at the origin in Fig.V.10a. This observation implies that by reducing the friction and hence the boundary effects, one can achieve wrinkling via a critical magnetic field that is very close to zero, $b_0^c \sim 0$T, as theoretically suggested by Danas and Triantafyllidis (2014). That is a significant point that deserves further investigation and will be addressed in a future work.

The influence of friction on the critical modes is depicted in Figs.V.10b-j for pre-stretch $\lambda_0 = 0.75$. Here, we compare qualitatively the experimental morphological patterns (Figs.V.10b-d) versus the numerical configurations with (Fig.V.10e-g) and without (Fig.V.10h-j) friction. In the absence of friction, the numerical simulations illustrate well-formed wrinkles of uniform amplitude, Figs.V.10h-j. Upon prescription of friction however, the numerical wrinkles vanish (Fig.V.10e), whereby a

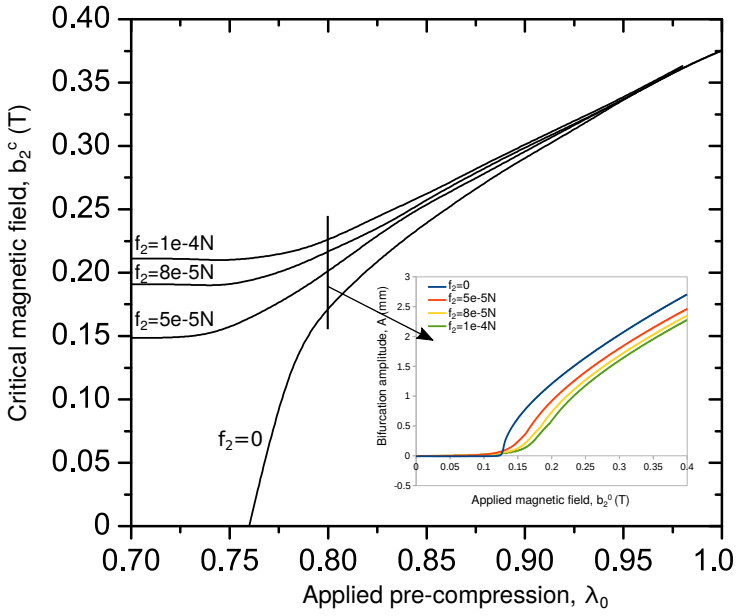

Figure V.11: Critical magnetic field b_2^c as a function of the applied pre-compression λ_0 under different values of shear force f_2 mimicking lateral friction. The value $f_2 = 8e-5$N is selected to fit the experimental findings. At pre-compression $\lambda_0 = 0.8$, the bifurcation amplitude is plotted versus the applied magnetic field b_2^0 for the corresponding shear forces f_2 (inset).

non-zero curvature appears at the film boundaries (Figs.V.10b,e). Upon further increase of the magnetic field, a slight localization at the center of the wrinkled film develops, Fig.V.10g. Such a morphological configuration resembles qualitatively the experiments, Figs.V.10c-d,f-g.

To conclude, the frictional FEM calculations under large pre-compressions result in: a) the saturation of the magnetic field beyond the critical mechanical point λ_0^c (Figs.II.19, V.9b); b) a pronounced curvature at the edges of the film that increases monotonically with pre-compression (Figs.II.18a,e,i,m for experiments and Fig.V.10 b-j for numerics); and c) the inhibition of mechanical buckling and appearance of a magnetomechanically-triggered localized pattern instead (Fig.V.9m-p for experiments and Fig.V.10b-j for numerics). This new configuration arises from the coexistence of magnetically-induced wrinkling and mechanical creasing. The latter is due to the boundary conditions, i.e., restricted extensive out-of-plane displacement upon compressive friction at the edges of the film. The magnetic and mechanical instabilities are not cooperative and as a consequence, no further decrease of the critical magnetic field b_0^c can be achieved. However, further investigations should be carried out to better understand the coexistence of mechanical localized modes and magnetic wrinkles.

The influence of friction on the critical response can be further illustrated in Fig.V.11, where the critical magnetic field b_2^c is plotted versus the applied pre-compression λ_0 under four different values of shear force $f_2 = 0, 5e-5, 8e-5, 1e-4$N. The greater the shear force mimicking friction, the greater the value of the critical magnetic field b_0^c under a given pre-compression. When $f_2 = 0$, the critical curve attains zero magnetic field at the purely mechanical buckling point. For non-zero forces, $f_2 \neq 0$, the saturation of the critical field is unavoidable. The value $f_2 = 8e-5$N is selected to fit the

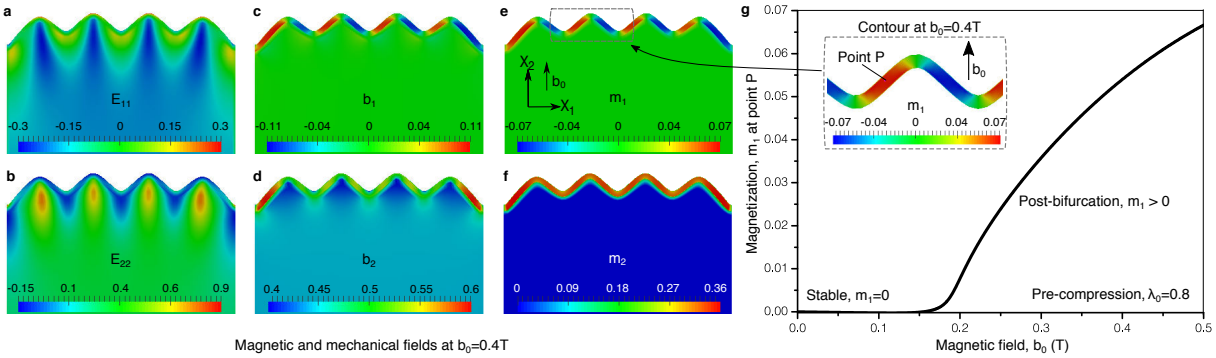

Figure V.12: Numerical post-bifurcation results for the MRE film/substrate system at applied pre-compression $\lambda_0 = 0.8$ and magnetic field $b_0 = 0.4$T. Simulation parameters: $H_f = 0.8$mm, $H_s = 39.2$mm, $G_f = 10$KPa, $G_s = 3$KPa, $\chi_f = 0.4$, $\mu_0 m_f^s = 0.5$T. **a-f**, Deformed configurations and contour plots of the spatial distribution of the Green-Lagrange strains, magnetic fields and magnetization along X_1 and X_2 directions. For clarity: bottom part of the substrate is not shown. **g**, Supercritical bifurcation curve of magnetization m_1 as a function of the applied magnetic field b_0, at a fixed point P within the film.

experimental critical curve. In the inset of the figure, the bifurcation amplitude A is plotted versus the applied magnetic field b_2^0 for the corresponding shear forces f_2 and pre-stretch $\lambda_0 = 0.8$. There, one can observe that the application of friction delays the occurence of the magnetically-triggered bifurcation. Moreover, only the frictionless system undergoes a sharp bifurcation transition. The rest curves bifurcate gradually as a result of the friction that acts as imperfection of the system.

V.4 Full-field numerical analysis

To understand better the magnetomechanical bifurcation, we show representative contour plots from the full-field simulations in Fig.V.12a-f, omitting the surrounding air. The MRE film/substrate system is at a post-bifurcated state at $b_0 = 0.4$T, exhibiting wrinkling for $\lambda_0 = 0.8$ (white regime in Fig.V.9b). The spatial distribution of the Green-Lagrange strains $\mathbf{E}$ is shown in Fig.V.12a,b. The corresponding magnetic field $\mathbf{b}$ and the magnetization $\mathbf{m}$ are depicted in Fig.V.12c,d and Fig.V.12e,f, respectively. The strain fields are classical for such problems, i.e., bending deformation state within the film that gradually becomes uniform within the substrate, upon increasing distance from the film/substrate interface.

In turn, the magnetic fields display an interesting distribution pattern. The components b_2 and m_2, which are in the direction of the applied magnetic field b_0, are more pronounced near the corners and remain positive in the entire film and substrate. However, the perpendicular to the applied field b_0 components b_1 and m_1 exhibit symmetrical alternating patterns, ranging from negative to positive values. While b_1 and m_1 fields are locally heterogeneous, on average they can be thought as magnetic phase domains with interchanging magnetization direction. Such a polarization further enhances the wrinkling amplitude and, in turn, the overall deformation of the system upon increase of the applied magnetic field b_0, until magnetic saturation is reached.

For completeness, in Fig.V.12g, we show the magnetization component m_1 at a representative

point P located within the MRE film with positive values of m_1 (see inset). At this point P, the magnetization displays a supercritical pitchfork post-bifurcation response versus the applied magnetic field b_0. Such a magnetization curve exhibits a similar trend to the bifurcation amplitude curves shown in Fig.V.9, although it can only be currently accessed via full-field numerical simulations.

In the magnetoelastic problem, the stresses are magnetomechanically coupled and the stress state induced by the applied magnetic field is not straightforward to be explained. This is due to the tremendous effect of the magnetic boundary conditions on the local fields within the material and the surrounding space. Specifically, the magnetic field is decomposed into an applied and a perturbed component, the latter caused by the existence of the magnetic material within the applied magnetic field, see Section IV.1. However, the out-of-plane first Piola-Kircoff stress component S_2 is extensive everywhere within the film at pre- and post- bifurcation and thus, the response is probably not stress-driven. This is in contrast with the electroactive problem, where the out-of-plane attraction of the electrodes and the produced voltage create an in-plane biaxial compressive stress state that leads to film buckling, upon the imposition of in-plane boundary conditions. Instead, we argue that the creation of alternating (+ and -) magnetization patterns within the post-bifurcated film plays the predominant role in the magnetic instability.

The components b_1 and b_2 of the magnetic field, as well as the corresponding Maxwell stresses, are highly heterogeneous and non-zero outside the film. That is a direct consequence of the Eulerian applied magnetic field far from the specimen (e.g., see Danas, 2017, Keip and Rambausek, 2017, Lefèvre et al., 2017). As a result, the analytical treatment of the post-bifurcation problem becomes difficult or even it can be accessed only via numerical analysis. Such an analysis requires a better discussion, since the stress field in magnetoelastic problems can be substantially different than that in the electroactive problems. The magnetic Maxwell stresses are highly non-uniform inside and outside of the film, since there exist magnetic fields in the surrounding air. The background energy sits everywhere within the entire space and causes the stress to be non-zero outside the material. The Maxwell-Cauchy stress $\boldsymbol{\sigma}$ is in the order of $(\mathbf{F}\cdot\mathbf{B})\cdot(\mathbf{F}\cdot\mathbf{B}) \approx \mathbf{b}^2 \approx (\mu_0 m)^2$, with $\mathbf{F}$ the deformation gradient tensor, $\mathbf{B}$ the Lagrangian magnetic field, $\mathbf{b}$ the eulerian magnetic field and $\mu_0 m$ the magnetization. By contrast, when electrodes are attached on the specimen surfaces, the (Maxwell) electrically induced stress fields follow the deformation of the specimen even in the post-bifurcation regime. Therefore, the stress outside the material is zero and within the material is uniform at the pre- and post-bifurcation. Some recent papers of Danas (2017), Lefèvre et al. (2017) and Keip and Rambausek (2015) are trying to address that question. On the contrary, the bifurcation problem is analytically tractable (except when friction effects are present) and it has been presented in Section IV.3.

To conclude, the present numerical model has been carried-out to understand better the experimental response of the given MRE film/substrate system. The fact that it has also proven to be quantitatively accurate allows us to use it in further studies, so as to explore MRE film/substrate systems in an extended geometrical and material parameter space. Such a work considering a thinner film is presented in the subsequent Section.

V.5 Film slenderness effects on the (post-)bifurcation response

In this section, we discuss how a thinner film affects the magnetoelastic critical response of a finite MRE film/substrate block. The numerical model has been found quantitatively accurate to probe the experimental findings (see Sections V.2,V.3) and thus, provides confidence to be employed in further parametric studies. Modeling the experimental structure in Section V.2 aims at having one to one correspondence between the experimental observations and the numerical implementations. However, one could further study the effect of various geometrical parameters on the critical response of the structure, e.g., the length l and thickness H of the specimen would certainly affect the critical fields and the corresponding patterns.

To mimic an infinitely deep substrate, the thickness of the specimen should be significantly larger than the expected wavelength, $H \gg \mathcal{L}$. For a given film thickness H_f, a large (domain) length with respect to the wavelength, $l \gg \mathcal{L}$, is favorable to induce large wavenumbers ω. We recall that the experimental geometry is a cube of 40mm edge, with film thickness ($H_f =$)0.8mm. To show whether such geometry corresponds to the case of a deep substrate (one that theoretically can be considered as infinite), we design a 40×40 plane-strain bilayer geometry of film thickness ($H_f =$)0.2mm and we subject it to the magnetomechanical loading of the experimental process. The loading consists of applying a pre-compression within the range $\lambda_0 \in (0.71, 1)$ and then linearly increasing the magnetic field b_0 beyond bifurcation.[9] Slightly compressible neo-Hookean and magnetically saturating materials are once more employed for both layers. The material parameters are those of the previous studies (experimental, theoretical and numerical), so as to have a comparison between all the different analyses (all having the material properties of Table V.1).

Fig.V.13a presents the post-bifurcated morphological response of the bilayer-system considering a thinner film ($H_f = 0.2$mm over $H = 40$mm specimen thickness). At this point, the numerical simulations neglect the effect of friction acting at the lateral sides of the specimen. This is fairly attributed to the slenderness (effective length-to-thickness) ratio[10] $l(=40\,\lambda_0)/H_f(=0.2)$ that prevents pronounced boundary effects (curvature due to friction). The wrinkled patterns correspond to a fixed magnetic field $b_0 = 0.3$T under four different compressive pre-stretches $\lambda_0 = 0.8, 0.85, 0.9, 0.95$. The applied pre-strains are lower than the mechanical instability load and thus, the morphological instability is triggered by the magnetic field b_0. When the magnetic field reaches a critical value, the initially flat top layer deforms into a pattern of wrinkles. Once wrinkling occurs, the response is representative with respect to the minimum wavelength; this is a standard theory of bifurcation (see Section IV.4.3). The critical wavenumber ($H_f = 0.2$mm, 16-19 wrinkles) is now notably higher than that in the experiments/simulations considering a thicker film ($H_f = 0.8$mm, 4 wrinkles). The wrinkling wavelength $\mathcal{L}$ is inversely proportional to the wavenumber, $\mathcal{L} = l/\omega$, and a monotonic function of film thickness, $\mathcal{L} = f(H_f)$, for fixed length $l = 40\,\lambda_0$. As a result, increasing the slenderness ratio l/H_f, drives the numerical solution into higher wavenumbers (under increasing stretch

[9] The geometry is designed in Abaqus and the numerical implementations take place in FEAP, see Section III.4. The ratio of the wavelength to the element size is found to be approximately 20.

[10] Slenderness ratio is a measure of how long a beam-column is compared to its cross-section's effective thickness (resistance to bending or buckling).

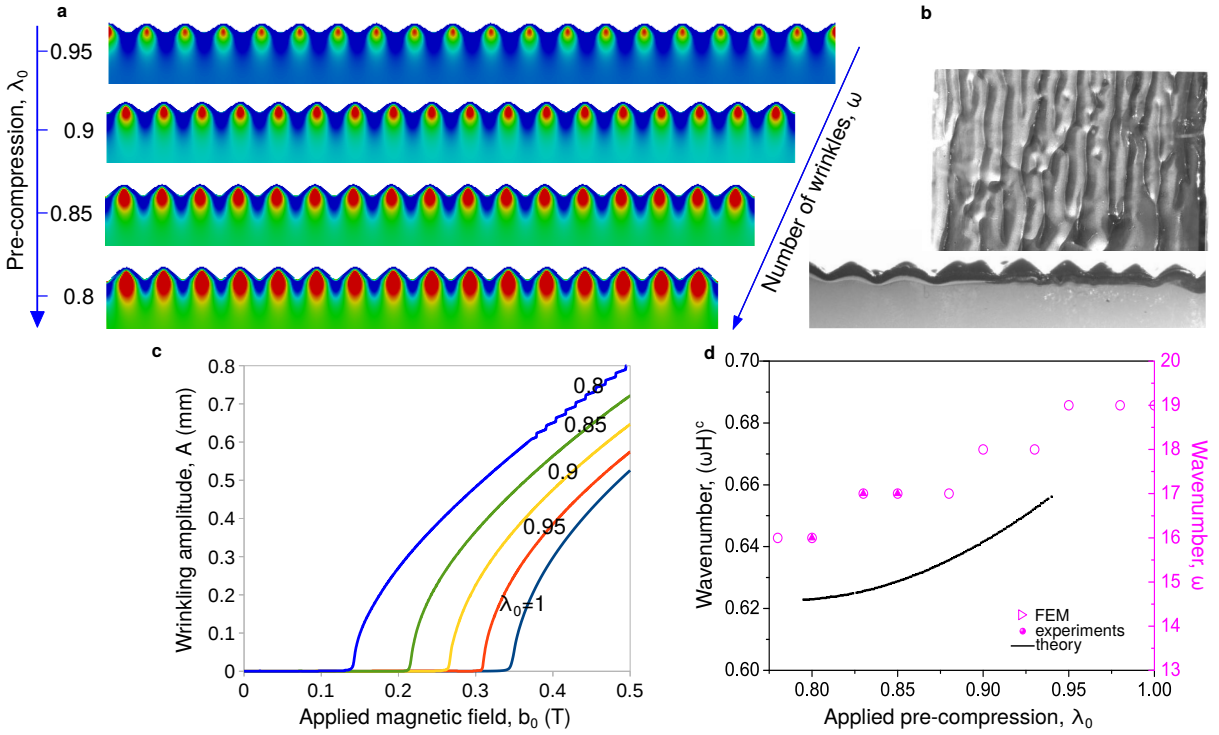

Figure V.13: Geometrical and material parameters for numerical simulations and experimental observations: $H_f = 0.2$mm, $H_s = 39.8$mm, $G_f = 10$kPa, $G_s = 3$KPa, $\chi_f = 0.4$, $\mu_0 m_f^s = 0.5$T. **a**, Numerical post-bifurcated pattern of the MRE film/substrate system corresponding to a fixed magnetic field $b_0 = 0.3$T under four different compressive pre-stretches $\lambda_0 = 0.8, 0.85, 0.9, 0.95$. Bottom part of the substrate is not shown. **b**, Experimental wrinkling at $\lambda_0 = 0.8$ and $b_0 = 0.3$T. Two views: From the top of the film and from the side of the bilayer (profile plane) - only half plane is depicted. **c**, Numerical wrinkling amplitude A versus the applied magnetic field b_0. The supercritical bifurcation curves correspond to five pre-stretches $\lambda_0 = 0.8, 0.85, 0.9, 0.95, 1$. The bifurcation point is defined at the point of divergence (sharp change due to absence of geometrical imperfections). A decreasing trend of the critical magnetic field with increasing pre-compression is evidenced. **d**, Critical wavenumber $(\omega H)^c = 2\pi/L$, with L the wavelength) and (integer) number of wrinkles ω versus the applied pre-compression λ_0. The continuous curve results from the theoretical analysis on an infinite system, while the discrete points correspond to the numerical and experimental boundary value problem.

ratio $\lambda_0 (= \varepsilon + 1)$).

In Figs.V.13a,d, the evolution of the wavenumber in the parameter space of pre-compression is evidenced in agreement with the theoretical predictions. We recall that the theoretical analysis considers idealized boundary conditions of an infinitesimally thick film bonded on a semi-infinite substrate (plus the semi-infinite air, see Section IV.3). In Fig.V.13d, we plot the wavenumber (number of wrinkles) as a normalized real number, as well as the integer appeared on the surface layer of the finite structure, versus the applied pre-compression λ_0. Although this feature is absent from the initial experiment (see Fig.II.18a) due to a small slenderness l/H_f ratio, it has been now numerically and theoretically shown that the wavenumber follows a decreasing trend with increasing pre-compression. To validate this trend, a set of experiments is conducted on samples of MRE Ecoflex bilayers for the present thickness ratio, $H_s (= 39.8)/H_f (= 0.2)$. As seen in Fig.V.13d, the experimental and numerical critical wavenumber are in agreement within the range of the pre-

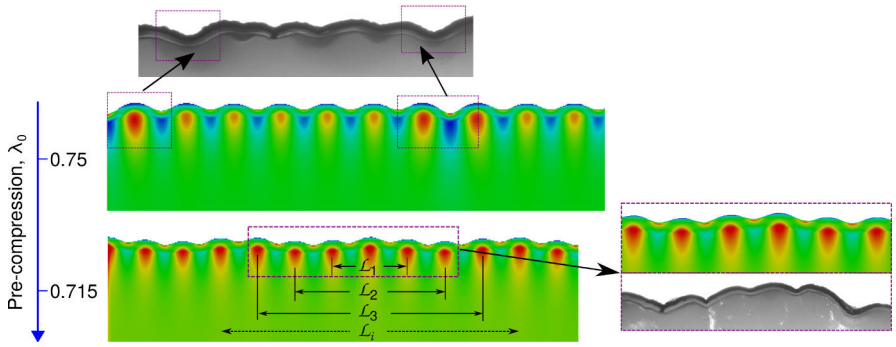

Figure V.14: Geometrical and material parameters for numerical simulations and experimental observations: $H_f = 0.2$mm, $H_s = 39.8$mm, $G_f = 10$kPa, $G_s = 3$KPa, $\chi_f = 0.4$, $\mu_0 m_f^s = 0.5$T. Post-bifurcated pattern of the MRE film/substrate system corresponding to a fixed magnetic field $b_0 = 0.1$T under two different compressive pre-stretches $\lambda_0 = 0.715, 0.75$. Once the pre-compression increases beyond the purely mechanical instability point, the mechanically-triggered wrinkling switches to a new behavior upon activation of the magnetic field. The bottom part of the substrate is not shown.

stretches λ_0 tested. The corresponding theoretical critical wavenumbers are obtained as $(\omega H)^c = 2\pi/\mathcal{L}$ (with $\mathcal{L}$ the wavelength), defining directly the number of the wrinkles in the finite structure. The critical wavenumbers approximately match the theoretical predictions. Therefore, one can conclude that the present geometry is indeed representative of a film/substrate system.

In Fig.V.13c, the amplitude of the wrinkles A in mm is plotted versus the applied magnetic field b_0 (T). The bifurcation curves are supercritical following the previous results on the thicker film, see Figs.V.9a,V.10a. However, the wrinkling amplitudes on the present film (0.2mm) are notably lower than that of the thicker (0.8mm), i.e., amplitude is a monotonic function of the film thickness. Due to lack of geometrical imperfections (or friction that acts as a source of imperfection), the curves diverge in a sharp manner from the principal solution. In view of that, the critical magnetic field needed to trigger the instability is determined directly from the divergence point and no thresholds over amplitude (for smooth curves) are needed (see Section V.2). A decreasing trend of the critical magnetic field with increasing pre-compression is also manifested, as shown in Fig.V.16. The numerical simulations are followed by experimental evidences of the wrinkled pattern for $\lambda_0 = 0.8$ and $b_0 = 0.3$T. In Fig.V.13b, two views of the pattern are considered: From the top of the film and from the side of the bilayer (profile plane). Once the magnetic field is removed, the pattern spontaneously disappears and the surface of the film returns to the flat state. Structural imperfections lead to variations in film stiffness and non-uniformity of wrinkling; the thinner the film, the higher the defect-sensitivity.

Once the pre-compression increases beyond the mechanical instability point, new patterns with multiple wavelengths emerge. Such modes of superimposed wavelengths are triggered by the magnetic field and are sensitive to the film slenderness l/H_f ratio: a thinner film (for a given length) favors their appearance. That is possibly attributed to the sufficiently high slenderness ratio that allows for the appearance of large wavelengths. Such wavelengths might be larger than the characteristic size of the specimen under a lower slenderness and thus, cannot develop. Instead, smaller-wavelength

(than the size of the specimen) wrinkles are only able to appear, such as in the case of $H_f = 0.8$mm film.

Fig.V.14 presents numerical simulations and experimental observations of the post-critical multi-period patterns under two pre-compressions $\lambda_0 = 0.715, 0.75$ and applied magnetic field $b_0 = 0.1$T. When $\lambda_0 = 0.75$, the mechanically-triggered wrinkling switches to a new behavior with twice the period, upon activation of the magnetic field. Once the magnetic field reaches a critical value $b_0 \approx 0.1$T, the sinusoidal surface of the MRE film folds against itself to form a double-period pattern. More specifically, the critical magnetic field triggers symmetry breaking into a wrinkling mode with periodically deeper valleys. Once the pre-compression is further increased, $\lambda_0 = 0.715$, a period-hextupling pattern occurs for $b_0 < 0.1$T. This secondary pattern alternates between growing and decaying valleys with progressively increasing and decreasing amplitudes. The pattern displays six distinct wavelengths $\mathcal{L}_i\,(i = 1, .., 6)$, without any localization emerging. The numerical simulations stop, however, before $b_0 = 0.15$T is reached, probably due to absence of user-defined geometrical imperfections. Preliminary experimental findings in such thin film ($H_f = 0.2$mm) under such high strains accompany the numerical patterns.

Subsequently, a full-field numerical analysis of the thin film is presented in Fig.V.15. This analysis serves for later comparison with the fields formed when the substrate is magnetic. In Figs.V.15a,b,c, the transverse component of the displacement u_2 and Green-Lagrange strain E_{22}, as well as the in-plane component of film magnetization m_1, are plotted along the reference (undeformed) length (at 40 mm) of the magnetic layer, under pre-stretch $\lambda_0 = 0.78$ and different magnetic field values, $b_0 = 0.026, 0.08, 0.18, 0.24, 0.34, 0.4, 0.5$T. The smallest magnetic field $b_0 = 0.026$T corresponds to the pre-bifurcation regime, i.e., uniform fields - flat film surface. The subsequently applied fields correspond to a wrinkled pattern of 16 wrinkles with increasing amplitude versus increasing magnetic load. The depicted fields are symmetric about the out-of-plane e_2 direction. The strain u_2 and magnetization m_1 are also symmetric about e_1 direction, altrernating from positive to negative values.

At high magnetic fields, $b_0 = 0.5$T, a new pattern starts growing on the single-period wrinkles, manifested in terms of displacement u_2 and strain E_{22}. This secondary pattern seems to be altered at the boundaries of the film. As seen in Figs.V.15a,b and contour plot in Fig.V.15d, the wrinkles at the boundary are pulled towards the substrate, even though no lateral shear forces (friction) have been added. Fig.V.15d presents the magnetization m_1 of two fixed points (pink and blue dots) within the film versus the applied magnetic field b_0 (pink and blue curves, respectively). The magnetization m_1 exhibits a supercritical pitchfork bifurcation of short stable regime. This is due to the high pre-compression ($\lambda_0 = 0.78$), close to the mechanical instability point. Following the morphological response, the magnetic instability occurs under a tiny magnetic field $b_0 < 0.05$T; the same value of the wrinkling amplitude divergence. The blue fixed point sitting on the peak of a central wrinkle corresponds to the transition from positive to negative magnetization and is the lower magnetization curve with amplitudes about zero. This curve attains zero in high magnetic fields, which is a possible indication of change in the wavenumber. Nevertheless, the finite geometry

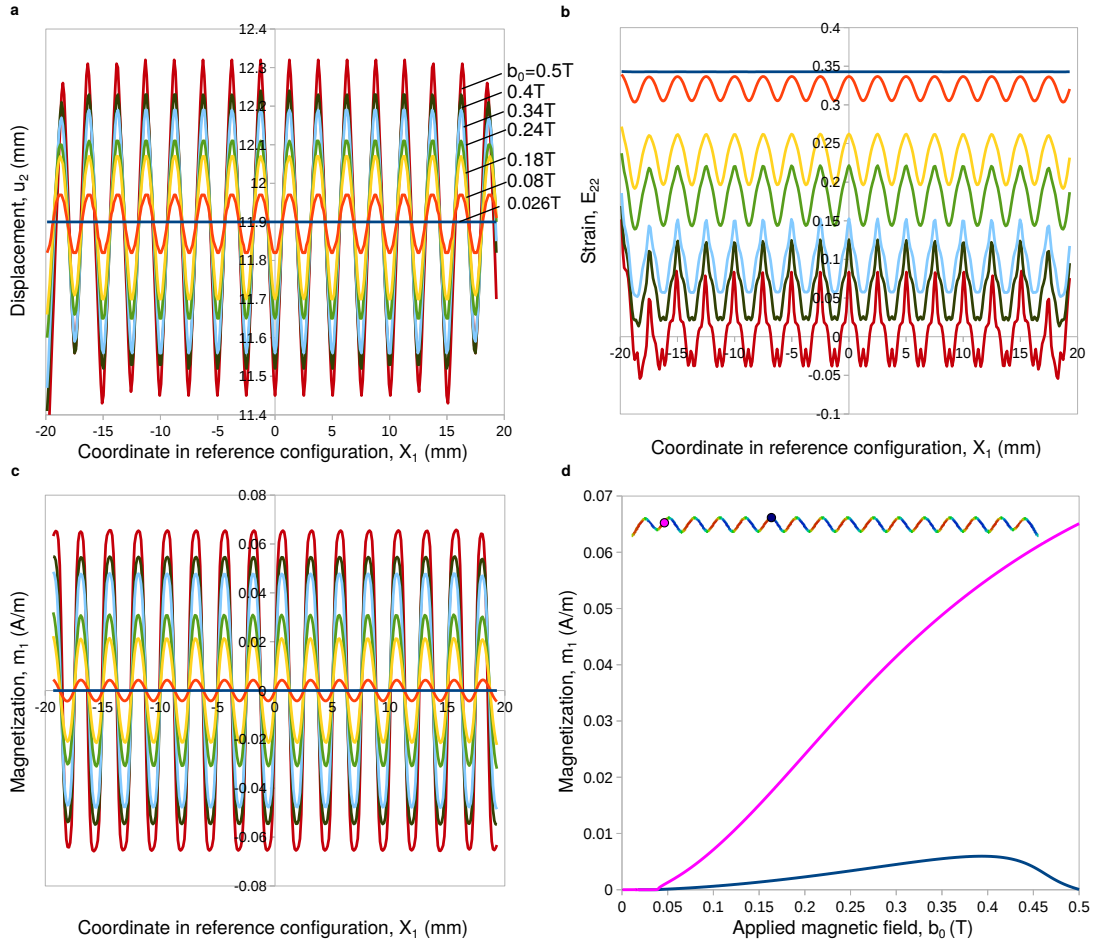

Figure V.15: Numerical pre- and post-bifurcation results for the MRE film/passive substrate system under fixed pre-stretch $\lambda_0 = 0.78$ and several applied magnetic fields $b_0 = 0.026, 0.08, 0.18, 0.24, 0.34, 0.4, 0.5$T. Simulation parameters: $H_f = 0.2$mm, $H_s = 39.8$mm, $G_f = 10$KPa, $G_s = 3$KPa, $\chi_f = 0.4$, $\mu_0 m_f^s = 0.5$T. Spatial distribution of the **a**, transverse displacement u_2; **b**, transverse Green-Lagrange strain E_{22}; **c**, in-plane magnetization m_1 along the reference coordinate X_1 (undeformed length). **d**, Supercritical bifurcation curves of magnetization m_1 versus the applied magnetic field b_0 of two fixed points (blue and pink dots) within the film. Each colored curve corresponds to the material point of the same color.

does not allow to visualize such changes and an infinitesimally thick film should be employed.

In Fig.V.16a, we summarize the magnetomechanical critical response of the MRE film/passive substrate obtained by several analysis: the boundary value system of (H_f =)0.8mm film thickness with friction to fit the experiment (blue), the boundary value system of $H_f = 0.8$mm without friction (red continuous), the boundary value system of thinner film $H_f = 0.2$mm without friction (red dotted), as well as the theoretical infinite problem of an infinitesimally small film thickness (green). The phase diagrams for a MRE film/passive substrate are separated by the curve of the decreasing critical magnetic field b^c with increasing applied pre-compression λ_0. The regime right to the curve is stable (flat film surface), while the regime at left is unstable (formation of surface patterns). Experimental and numerical wrinkled patterns for $\lambda_0 = 0.78$ are shown for the two film thicknesses. When $H_f = 0.8$mm, four wrinkles emerge along the film surface, numerically probed considering lateral shear forces (blue film configuration). As a result of the unfavorable film slenderness ratio, the

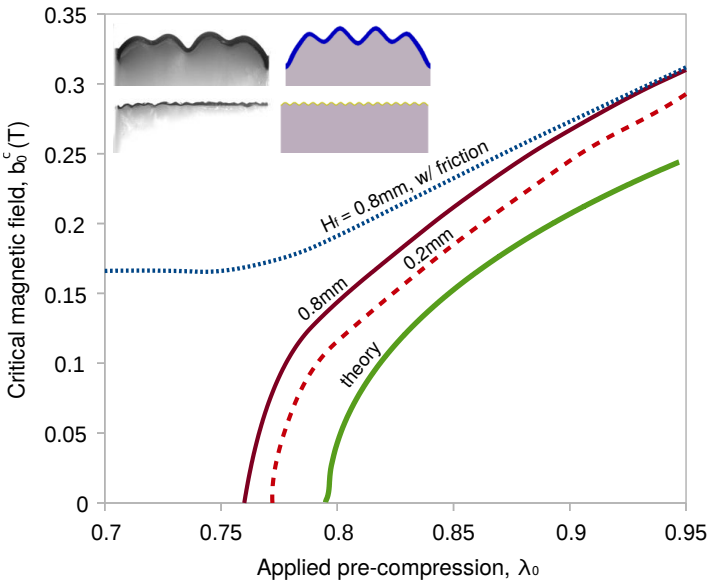

Figure V.16: Phase diagram in the parameter space of applied pre-compression λ_0 and critical magnetic field b_0^c needed to trigger the instability. Material parameters: $G_f = 10$KPa, $G_s = 3$KPa, $\chi_f = 0.4$, $\mu_0 m_f^s = 0.5$T. The magnetomechanical critical response of the MRE film/passive substrate is summarized for several analyses: the boundary value system of $H_f = 0.8$mm film thickness with friction fitting the experiment (blue), the boundary value system of $H_f = 0.8$mm without friction (red continuous), the boundary value system of $H_f = 0.2$mm without friction (red dotted), as well as the theoretical infinite problem (green). Experimental and numerical patterns for $\lambda_0 = 0.78$ are shown for both film thicknesses. When $H_f = 0.8$mm, four wrinkles emerge along the film surface, numerically probed considering lateral friction (blue film configuration). When $H_f = 0.2$mm, sixteen wrinkles of notably lower amplitude are formed (yellow film configuration) and experimentally evidenced given the fabrication imperfections.

pattern is subjected to pronounced frictional effects. Under such high pre-compression $\lambda_0 = 0.78$, the corners of the film are pulled towards the substrate and a double-period pair emerges. It is interesting to note that the system without friction is led to single-period wrinkling instead of period-doubling (see Figs.V.10b-j). When $H_f = 0.2$mm, sixteen wrinkles of small amplitude are formed (yellow film configuration) and experimentally evidenced given the fabrication imperfections. The number of wrinkles is hence a decreasing function of increasing film thickness. The thinner film ($H_f = 0.2$mm) leads to higher wavenumbers and thus, prevents the observations far from the boundaries to be affected by frictional effects. Nevertheless, only preliminary experiments are included at this stage.

The numerical curves of $H_f = 0.8$mm with and without friction undergo the same trend in small pre-compressions; however, the influence of friction becomes very soon non-negligible (see for better understanding Fig.V.11). Under high pre-compressions, the numerical curve with friction manifests saturation in the critical magnetic field b^c, while the perfect system attains the mechanical buckling point for zero magnetic field. In Figs.V.4,V.8, we show that the experimental system of $H_f = 0.8$mm recovers the (magneto)mechanical infinite film/substrate bifurcation for stiffness contrast $G_s/G_f = 0.3$. Such an analysis is used to have one to one correspondence with the initial experiments. When $H_f = 0.2$mm, the critical curve is shifted towards the theoretical response along the mechanical loading axis. However, there is indeed the difference that the film/substrate block

is a finite structure, while the theoretical problem considers a semi-infinite size specimen. A larger slenderness ratio leads to higher wavenumbers of notably lower amplitude, see also Fig.V.16. To that end, the selection of the geometrical parameters of a MRE film/substrate block is application-oriented, e.g., in haptic systems, thicker films would probably be preferable when user-accessibility is required.

V.6 Concluding remarks

A FE (post-)bifurcation analysis in the absence of magnetic field, i.e., $\lambda_0 \neq 1$, $b_2^0 = 0$, provides the critical mechanical stretch $\lambda_0^c = 0.76$ at the onset of wrinkling and the associated wavenumber $\omega = 4$ (macroscopic length scale). Upon further increase of the applied strain ($\varepsilon_{11} = \lambda_0 - 1$), the plane-strain simulations reveal a period-doubling configuration at $\lambda_0^{c2} = 0.7$, which becomes unstable and gets unloaded at larger compressive values, $\lambda_0 < 0.68$. This response corresponds to a mechanical interlayer contrast at $G_s/G_f = 0.3$, in agreement with the material characterization of our material layers. However, the experimental findings are biased by strong frictional boundary effects that suppress the primary wrinkling. To fit the experiment, the numerical solution is able to bypass the point of primary wrinkling without undergoing bifurcation when lateral boundary friction is added. Thus, an appropriate choice of boundary conditions could tune the surface patterns by suppressing or bypassing modes and driving the solution directly to later instabilities.

The film/substrate system subjected to a purely mechanical loading exhibits a rich behavior in the parameter space of the interlayer mechanical contrast, considered from the limit of a traction-free homogeneous substrate ($G_s/G_f \to 1$) to very stiff films on compliant substrates ($G_s/G_f \to 0$). The corresponding patterns vary from wrinkling for small ratios ($G_s/G_f \leq 0.6$) to localizations when higher ratios ($G_s/G_f > 0.6$) are reached. On the top of the primary instabilities, the system undergoes secondary localized patterns that are also sensitive to the interlayer stiffness ratio.

The numerical estimates of the MRE film/passive substrate block simulating the experiment (with film thickness $H_f = 0.8$mm) are found in good agreement with the experimental measurements for the aforementioned loading parameters. The simulations are able to reproduce extremely well the decrease of the critical magnetic field with increasing pre-compression, as well as the obtained morphological patterns. Well-defined wavelengths that are close to those predicted by the infinite film/substrate bifurcation analysis are recovered and thus, the results are representative of infinitely deep geometries. Such fair comparisons allows us to use the FEM in order to investigate the resulting magnetic fields in the post-bifurcation regime.

In turn, the magnetic quantities display an interesting distribution pattern. Concentration of the magnetic field and the magnetization is observed at the corners of the specimen (edge effects). The in-plane components of these magnetic quantities exhibit symmetrical alternating patterns ranging from negative to positive values. While these fields are locally heterogeneous, on average they can be conceived as magnetic phase domains with interchanging magnetization direction. This further enhances the bifurcation amplitude and in turn, the overall deformation of the system upon

increase of the applied magnetic field (until magnetic saturation is reached). In addition, the in-plane magnetization component at a material point, located within the MRE film, displays a supercritical pitchfork post-bifurcation response versus the applied magnetic field. Such a magnetization curve has a similar trend to the bifurcation amplitude curves, although it can only be currently accessed via full-field numerical simulations.

The numerical simulations of $H_f = 0.8$mm geometry is used to have one to one correspondence with the initial experiments. The numerical FEM model is further employed in parametric studies, so as to investigate the effect of film slenderness on the critical and post-critical system behavior. Increasing the slenderness ratio leads to a slightly more unstable response of higher wavenumbers and notably lower amplitudes. Therefore, the selection of the geometrical parameters of a MRE film/-substrate system can be application-oriented, e.g., in haptic systems, thicker films would probably be preferable when user-accessibility is required.

CHAPTER VI

RESULTS II: FROM WRINKLES TO CRINKLES

Summary of the Chapter. In this chapter, we present a study on post-bifurcation crinkling patterns emerged from harmonic (wrinkling) modes. Such patterns are obtained by further exploiting the magnetoelastic coupling of the film/substrate structure. First, we carry out a curvature localization analysis at the post-bifurcation regime of the experimental and numerical MRE film/passive substrate system. Such an analysis reveals that curvature localization is an intrinsic feature of MRE instabilities that leads to crinkling under the given boundary conditions. Next, we investigate the formation and post-stability evolution of crinkles on MRE films bonded on MRE substrates. The underlying idea is to create different interlayer contrasts of magnetic/mechanical properties and thus, trigger a richer range of surface modes than that already obtained when using a MRE film on a passive (magnetically insensitive) foundation. Subsequently, the study is expanded to higher slenderness ratios. We vary the magnetic properties of the substrate and we obtain an extremely large range of unique crinkled (secondary) surface patterns tuned by the magnetomechanical loading. A full-field numerical analysis of the fields is presented and accompanied by preliminary experiments. The curvature localization analysis on a MRE film/MRE substrate is followed by an insight on the magnetization spatial distribution and how that contributes to the evolution of crinkling.

Contents

A surface pattern manifesting curvature-localization has been experimentally observed on the (H_f =)0.8mm film thickness geometry of the MRE film/passive substrates in Section II.7 (see Figs.II.18m-p) and numerically probed after considering frictional boundary effects in Section V.3 (see Fig.V.11). In the prior magnetomechanical findings, this localized pattern gradually evolves from harmonic (wrinkling) modes, manifesting symmetry-breaking deformations under large amplitudes and resulting in a sawtooth mode of straight segments, see Fig.II.18p. Kothari et al. (2018) and Li et al. (2018) recently reported the existence of such a surface pattern on graphene sandwich nanostructures triggered by (electro-)mechanical loading mechanisms. This newly evidenced shape configuration was called "crinkling", after the theoretical work of Pipkin (1986) on functions that exhibit sawtooth-type response (i.e., functions with a weakly convergent average value, but highly oscillating first derivative). In the study of Kothari et al. (2018), crinkling was found to result either from a secondary supercritical interlayer-shear (snake) mode evolving from a sinusoidal profile (wrinkles) under mechanical buckling[1] or as a primary subcritical hinge (or sawtooth) mode emerged when flexoelectric interactions are taken into account. The coupling between (atomic-)layer curvature and electric-charge polarization, i.e., quantum flexoelectricity, was found to lead to the emergence of a boundary layer (band width) in which curvature is highly concentrated.

In this chapter, we analyze the experimentally observed curvature localization in MRE films bonded on a passive substrate. The analysis is also extended to magnetic (MRE) substrates. Competing mechanisms that cause curvature localization are investigated using numerical and experimental results.

VI.1 Crinkling of MRE film on passive substrate

The evolution of curvature localization was initially observed while analyzing the amplitude of wrinkled patterns under high applied pre-compressions. In Fig.II.17 for instance, we plotted the bifurcation amplitude A versus the applied magnetic field b_0 for two neighboring undulations of the wrinkled pattern at pre-stretch $\lambda_0 = 0.78$. As the applied field reaches a critical value $b_0^c \simeq 0.1$T, the system transits from the non-diverging (flat) state into a uniform wrinkling state; all wrinkles have the same amplitude. Upon further increase of the magnetic field $b_0 \simeq 0.32$T however, the translational symmetry of the surface layer breaks, with the undulation around the center diverging from the primary bifurcated branch. For $b_0 > 0.35$T, the amplitude (depth) of the central valley grows much larger than those at its sides, resulting in the formation of a double-period wrinkling pair, also illustrated by the shape configuration in Fig.VI.1e for $\lambda_0 = 0.75$ and $b_0 = 0.4$T. As the magnetic field reaches higher values $b_0 \simeq 0.5$T, the central undulation becomes dominant, forming a symmetric kink-type localization with flat-zone segments. This localization manifests the maximum deflection in the neighborhood, relaxing the amplitude of the surrounding wrinkles

[1] Under a purely mechanical buckling, the predominance of the interlayer-shear (snake) mode of deformation over the overall-bending mode (Euler long-wavelength) depends on the slenderness of the surface layer. If the film is extremely slender, i.e., the length is beyond a critical value for a given number of atomic layers, the structure develops wrinkles in the overall-bending mode under axial compression. Otherwise, the structure develops crinkles.

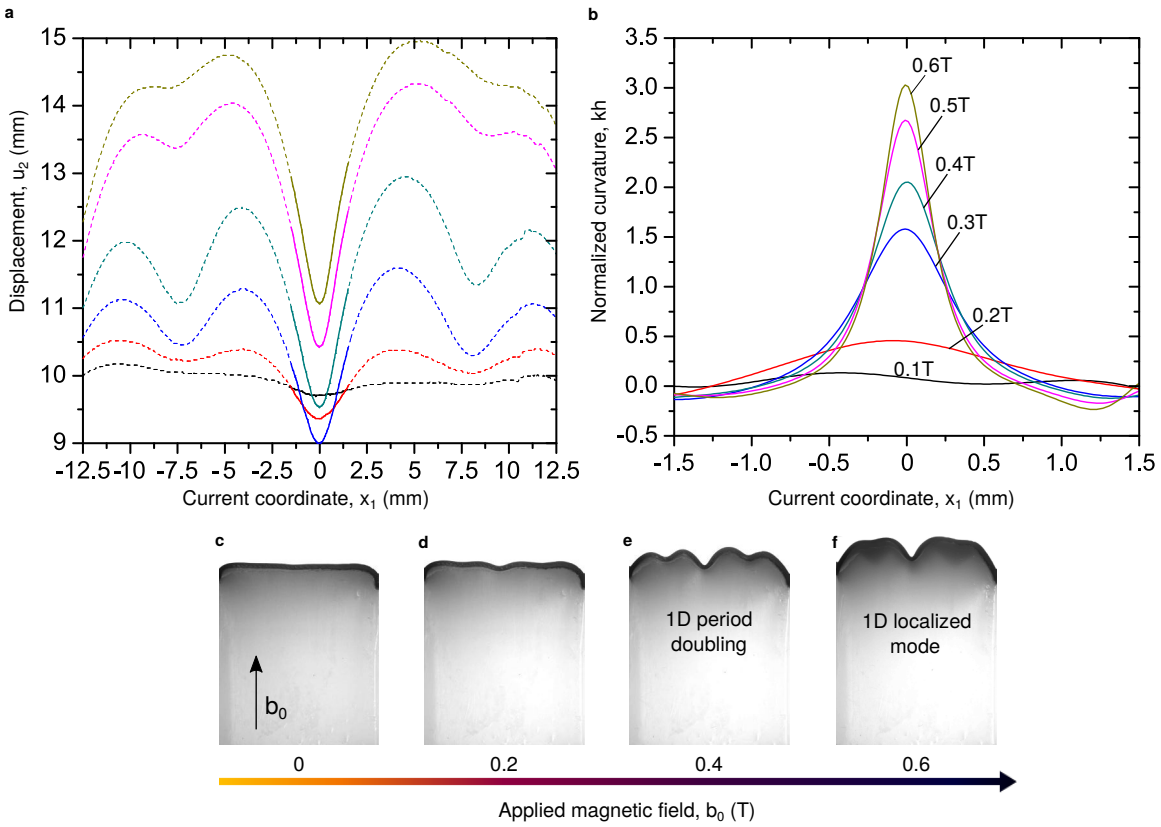

Figure VI.1: **a**, Profile evolution of the displacement u_2 on the top surface of the MRE film at $\lambda_0 = 0.75$ and various applied magnetic fields b_0 as a function of the current coordinate x_1. **b**, Normalized curvature kh (h the film thickness) of the central wrinkle/crinkle at the same applied magnetic fields b_0 as a function of the current coordinate x_1. Upon increase of the magnetic field, the post-bifurcation mode evolves from a quasi-smooth wrinkled pattern (initiation of period-doubling) to a crinkled shape configuration, focusing its curvature within a decreasing width band. The regime within the curvature localization analysis is focused corresponds to the displacement span of continuous line. **c-f**, Optical images of the experimental pattern, illustrating the morphological evolution of curvature localization from the flat to the crinkled state versus increasing magnetic field b_0.

into an energetically minimum configuration. The resulting post-bifurcated configuration will be called "crinkling" mode, Fig.VI.1f.

The magnetomechanical experimental observations in Figs.II.16b-m,II.18m-p have revealed the formation of an evolving localization around the center of the surface layer under finite pre-stretching. In such cases, the 1D wrinkled configuration subjected to strong frictional (boundary) effects is highly unstable, magnetically switched to an 1D localization under very small post-bifurcation amplitudes. To further study such peculiar pattern evolution, we carry out a curvature localization analysis considering sequential post-buckling shape configurations upon increase of the magnetic field. The direct experimental measurement of a moment-curvature relationship[2] is difficult for such a thin film. Therefore, we evaluate the bending state by considering the second derivative of the out-of-plane displacement $(k =)(\partial^2 u_2/\partial x_1^2)/(1+(\partial u_2/\partial x_1)^2)^{3/2}$, x_1 the current position. The

[2]For elastic beam bending: $k = M/EI$, M the moment, E the Young's modulus, I the area moment of inertia, EI the flexural rigidity ≡ resistance of the beam to bending for a given curvature.

displacement profile is obtained from the trajectory of the surface layer, detected from the film/air interface by means of image processing, see Fig.II.8. Subsequently, we define the span of interest in which the curvature localization evolves (continuous line regimes in Figs.VI.1b,VI.3a) and fit it with a 9^{th} degree polynomial (converged at every point). The curvature is then assessed from the second derivative of the fitted displacement profile within the span of interest.

In Fig.VI.1a, we present the out-of-plane displacement profile of the surface layer, from which the curvature is evaluated. The post-bifurcated deflection progressively evolves from a quasi-smooth pattern (initiation of a double-period sine) at $b_0 = 0.1\text{T}$ to a single crinkle configuration at $b_0 \simeq 0.5\text{T}$. For $b_0 > 0.2\text{T}$, the curvature at the valley of the central wrinkle becomes noticeably larger than that at its peaks. Simultaneously, the amplitude of this undulation grows larger upon increase of the magnetic field, while the neighboring wrinkles progressively decay in the most favorable fashion to create the minimum energetic configuration (given the imperfections). In Fig.VI.1b, we plot the curvature corresponding to the central undulation for increasing applied magnetic field b_0 and a fixed compressive pre-stretch $\lambda_0 = 0.75$. The normalized curvature kh (h the film thickness) is plotted along the current coordinate (position) x_1 attached to material points in the deformed film. As the magnetic field increases, the curvature amplitude and distribution (width) evolve progressively as a monotonic function of the decreasing kink angle, $\theta \sim \frac{\pi}{2} - \frac{\partial u_2}{\partial x_1}$, depicted in the continuous line regime of Fig.VI.1a. Starting from an infinitesimal curvature at $b_0 = 0.1\text{T}$ spread along a wide area of $\sim 3\text{mm}$, the localized regime progressively focuses its curvature within a decreasing width band of increasing amplitude. Figs.VI.1c-f show corresponding optical images of the experimental system, capturing the morphological evolution of curvature localization from the flat state to a crinkling pattern with increasing magnetic field. Starting from period-doubling (Fig.VI.1d) at the onset of buckling $b_0 \simeq 0.1\text{T}$, the post-bifurcation develops a kink mode with nearly straight ends (Fig.VI.1f) at higher fields $b_0 > 0.4\text{T}$.

As discussed in Section II.7, competitive surface patterns enhanced by nonlinear deformation features can be related to the formation of localizations. The observed curvature-localizing behavior might result from the incompatibility of the bifurcation modes triggered by the two independent fields (mechanical and magnetic) under finite strains that are coupled with the experimental boundary conditions (interpreted in Section V.3). Under large pre-compressions, the friction developed between the lateral faces of the specimens and the walls of compression device is not negligible, manifested by a noticeable curvature at the corners of the surface layer (see Figs.II.18i,m). The corresponding curvature affects, in turn, the morphology of the surface pattern by pulling the corners of the film towards the substrate. Within such finite strain regime, the incremental moduli of the neo-Hookean substrate is different from the ground state and becomes anisotropic. In turn, a higher interlayer stiffness contrast is possibly formed, known (e.g., see Cao and Hutchinson, 2012b) to yield mechanically localized instabilities when $G_s/G_f \geq 0.6$ (see Fig.V.4). By contrast, the film/substrate magnetic contrast is infinite (i.e., $\chi_s/\chi_f = 0$) and thus, the magnetic field triggers 1D single-period wrinkling. Consequently, the morphological pattern is a trade-off between the purely mechanical and purely magnetic loading contributions.

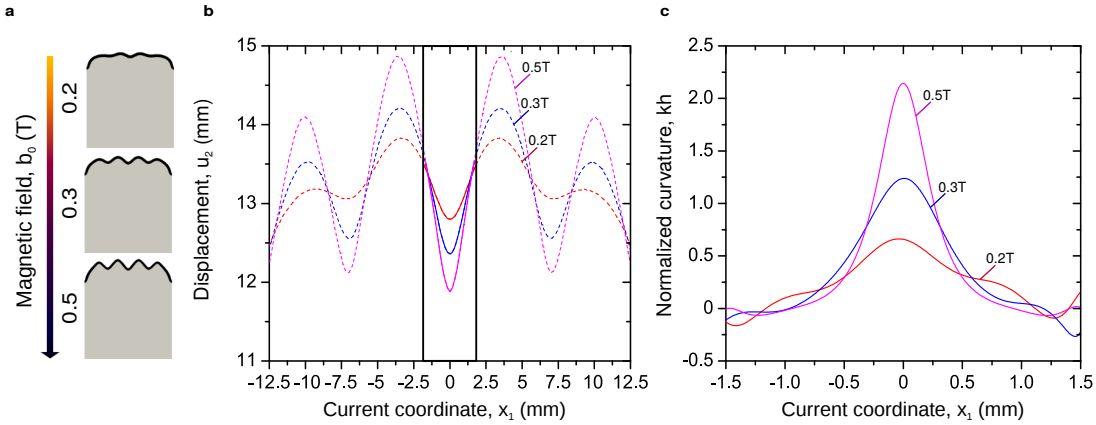

Figure VI.2: Numerical post-bifurcation curvature localization on the MRE film/substrate block ($H_f =$ 0.8mm film thickness) at $\lambda_0 = 0.75$. **a**, Morphological patterns with increasing magnetic field b_0; **b**, profile evolution of the displacement u_2 on the top surface of the MRE film at various applied magnetic fields b_0 as a function of the current coordinate x_1; **c**, normalized curvature kh (h the film thickness) of the central wrinkle/crinkle as a function of the current coordinate x_1. The bifurcation primarily emerges under a (magnetically-triggered) wrinkling mode subjected to frictional boundary effects. Upon further increase of the magnetic field, the middle undulation grows deeper than the neighboring wrinkles towards the substrate, e.g., $b_0 = 0.2$T, with the overall surface shape remaining stable as the amplitudes grow larger, e.g., $b_0 = 0.5$T. The post-bifurcation of increasing amplitudes supercritically localizes the curvature of the middle undulation in a decreasing band width < 3mm. This behavior is representative for bilayers under simulation parameters: $G_s = 3$KPa, $G_f = 10$KPa, $\chi_f = 0.4$, $\mu_0 m_f^s = 0.5$T, $H_s/H_f = 49$, $f_{max} = 8e-5$N.

In addition to the prior mechanisms, asymmetric bending stiffness[3] due to fluctuations in film thickness and/or roughness (coming from the fabrication) lead to variations in film stiffness and thus, to non-uniform wrinkles (e.g., see Lipowsky, 2014, Sun et al., 2012). Asymmetric bending stiffness owed to variations in the structural properties of the surface layer has been shown to produce bending configurations with high contrast of curvatures[4] between the valley and the peak of a wrinkle (experimentally observed in Fig.VI.1b) and that seems to promote localizations (Sun et al., 2012). In the present case, it is not erroneous to assume that the film comprises an asymmetric distribution of iron particles on the top and bottom of its surface, as a consequence of gravitational forces present during the deposition and subsequent curing of the MRE layer. Besides, optical microscopy observations of the specimens have shown that the substrate close to the film/substrate interface is weakly porous (Fig.II.4b) and thus, the local mechanical properties on the bottom surface of the film must be lower than those on the top.

To identify a possible mechanism of crinkle formation and further understand the localizing process, we carry out the same curvature localization analysis on the numerical specimen under plane-strain simulations considering lateral friction. To provide a direct comparison with the experiments under finite strains, Figs.VI.2b and c present the displacement profile u_2 and the normalized cur-

[3] Asymmetric bending stiffness occurs when the top and bottom surface of a thin layer object have different local stiffness due to different types of inhomogeneities at each side. Not to be confused with bending of asymmetrical sections.

[4] High contrast for Sun et al. (2012) implies $k_1 \gg k_2$, with k_1 and k_2 the curvature of the valley and the peak, respectively.

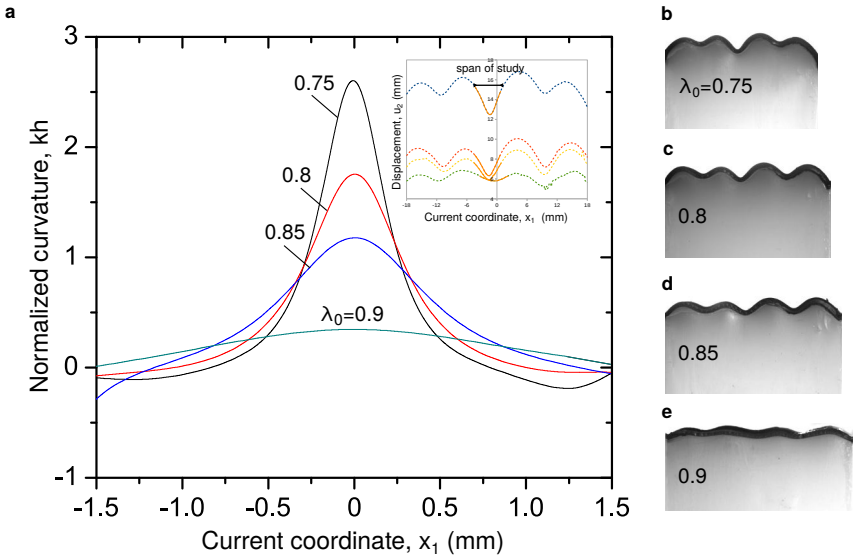

Figure VI.3: **a**, Normalized curvature kh (h the film thickness) distribution versus position x_1 attached to material points in the (current) deformed film, under four pre-stretch values $\lambda_0 = 0.75, 0.8, 0.85, 0.9$ and fixed applied magnetic field $b_0 = 0.5$T. Upon increase of the pre-compression, the post-bifurcation symmetry-breaking wrinkling pattern focuses its curvature within an increasing width band. The regime within the curvature localization analysis is concentrated corresponds to the displacement span of orange color in the inset of the figure, i.e., the central undulation. **b-e**, Optical images of shape configurations illustrating the morphological evolution of curvature localization on the experimental system for increasing pre-compression.

vature kh respectively, along the deformed film length for applied magnetic field $b_0 = 0.2, 0.3, 0.5$T and fixed applied pre-stretch $\lambda_0 = 0.75$. The surface layer primarily bifurcates into wrinkling with the particularity that the side wrinkles are subjected to friction and thus, their deflection is lower, e.g., $b_0 = 0.2$T in Fig.VI.2a,b. Upon increase of the magnetic field, the middle undulation grows deeper than the neighboring wrinkles towards the substrate, e.g., $b_0 = 0.3$T, with the overall surface shape remaining stable as the amplitudes grow, e.g., $b_0 = 0.5$T. The post-buckling evolution shows curvature localization (continuous line regime in Fig.VI.2b) that can be assessed by the second derivative of the out-of-plane displacement, $k = (\partial^2 u_2/\partial x_1^2)/(1+(\partial u_2/\partial x_1)^2)^{3/2}$, x_1 the current position. Upon increase of the magnetic field, the post-bifurcated mode of increasing amplitudes supercritically localizes the curvature of the middle undulation in a decreasing band width < 3mm. The curvature distribution evolves monotonically as a function of the kink angle $\theta(\sim \frac{\pi}{2} - \frac{\partial u_2}{\partial x_1})$.

To investigate whether the curvature-localizing process is sensitive to finite pre-compressions, we plot in Fig.VI.3a the normalized curvature kh versus the current position x_1 for four different pre-compressions $\lambda_0 = 0.75, 0.8, 0.85, 0.9$ and a fixed applied magnetic field $b_0 = 0.5$T. The post-bifurcated shapes corresponding to $b_0 = 0.5$T evolve from a smooth wrinkling profile under low pre-compressions to symmetry-breaking wrinkling (a double-period pair) as higher pre-compressions are reached. The central undulation (orange regime in the displacement profile of Fig.VI.3a inset) progressively grows large within the neighboring wrinkles upon increase of pre-compression, as shown by the optical images of the morphological evolution, Fig.VI.3b-e. Under a low pre-compression on

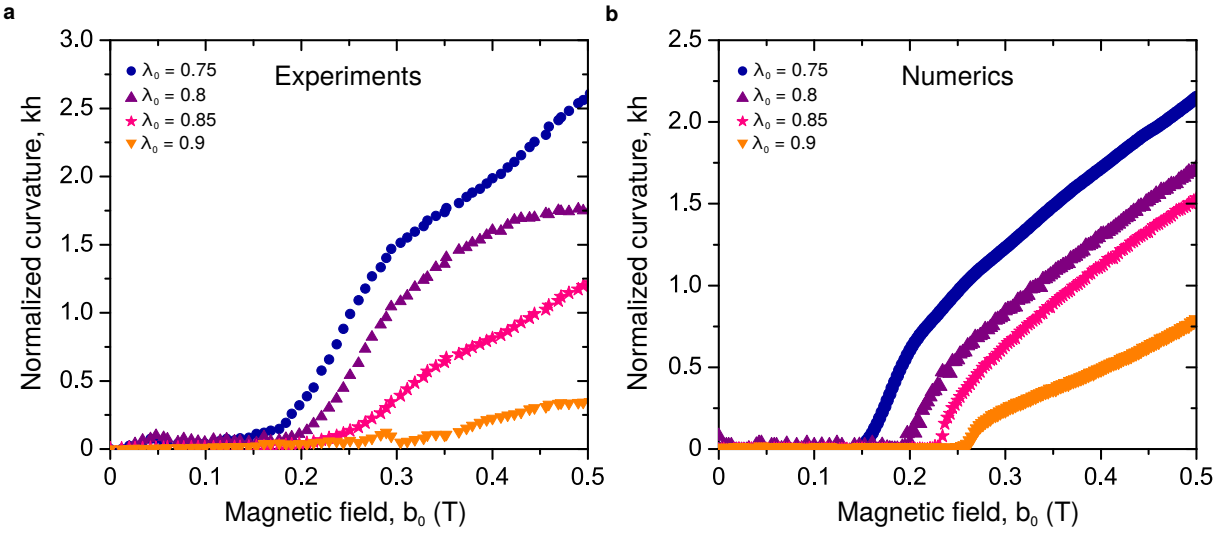

Figure VI.4: Evolution of curvature localization in the two-field parameter space of applied pre-compression $\lambda_0 = 0.75, 0.8, 0.85, 0.9$ and magnetic field $0 \leq b_0 \leq 0.5$T, corresponding to the **a**, experimental and **b**, numerical specimens. The localization does not require substantial uniaxial compression in order to be formed, i.e., it evolves within the entire range of low-to-high pre-stretches that provide 1D surface modes, $\lambda_0 \leq 0.9$. Hence, the curvature localization seems to be an intrinsic feature of the MRE instability under the existing boundary conditions.

the threshold of 2D to 1D wrinkling, $\lambda_0 = 0.9$ (see Fig.II.19a), the parabolic deflection of the central bump (Fig.VI.3e) leads to a flat plateau in Fig.VI.3a that is broadly distributed over the entire span of study (orange regime). Subsequently, the curvature distribution monotonically increases with pre-compression and the decrease of the kink angle (similar to Figs.VI.1b,VI.2c). In particular, the curvature expands within a band width (< 1mm), in which the distance between the symmetric inflection points of the curve for a given curvature value decreases with applying pre-compression. As a result, the curvature distribution is found to be dependent on the kink angle of the localization.

In Fig.VI.4a and b, we summarize the curvature-localization amplitude in the two-field parameter space of applied pre-compression $\lambda_0 = 0.75, 0.8, 0.85, 0.9$ and magnetic field $0 \leq b_0 \leq 0.5$T, corresponding to the experimental and numerical specimens, respectively. Both experimental findings and numerical simulations undergo a supercritical curvature localization versus the applied magnetic field b_0. The flat state is a local minimum of the energy for $kh = 0$. As the curvature diverges from the principal solution, its value monotonically increases as a function of the magnetic field, undergoing distinct regimes of different slope. Each such regime corresponds to a progressive morphological step in the localization process. In Fig.VI.4a, these regimes confirm the sensitivity of the onset of the bifurcation modes on the pre-compression, optically observed and reported in previous Sections (e.g., see Figs.II.18a-p). The primary (sine-wave) and secondary (double-period sine-wave) configurations become less stable with increasing pre-compression, i.e., they evolve to the subsequent configuration in lower magnetic fields. When $\lambda_0 = 0.75$, the single-period wrinkling mode is even bypassed with the primary mode being the period-doubling, as analyzed in Fig.VI.1. The same behavior will be subsequently illustrated when having a magnetic substrate in Section VI.1.

The post-buckling evolution manifests nonlinear growth of the curvature as the dominant crinkle is formed and the wrinkles in the neighborhood are flattened-out. These features are qualitatively obtained by the numerical calculations, but are less faithful in quantitative terms when compared with the corresponding experimental findings. One possible reason for such a quantitative difference could be due to the fact that capturing localizations accurately requires the use of precise imperfections that are not used in our calculations. However, the numerics confirm the monotonicity of the curvature evolution versus pre-compression, which is a novel feature. It appears that the localization does not require substantial uniaxial compression in order to be formed, i.e., it evolves within the entire range of low-to-high pre-stretches that provide 1D surface modes, $\lambda_0 \leq 0.9$. Hence, curvature localization seems to be an intrinsic feature of the MRE film/substrate instability under the given boundary conditions. In Section VI.3, it will be further shown that the mechanism of formation of crinkling is strongly related to repelling magnetoelastic interactions.

VI.2 Crinkling of MRE film on MRE substrates

In this section, we investigate the formation and post-stability evolution of crinkling modes on MRE films of ($H_f =$)0.8mm bonded on MRE substrates.

With the perspective of extending surface actuation to obtain novel magnetomechanically triggered patterns, we investigate the (post-)stability of an entirely magnetorheological bilayer block. The underlying idea is to create different interlayer contrasts of magnetic/mechanical properties and trigger a wider range of surface modes than that already obtained when using a MRE film on a passive (magnetically insensitive) foundation. To study the contribution of the magnetizable substrate to magnetically triggered localizations, the interlayer stiffness contrast remains moderate-to-low $G_s/G_f = 0.3$, so as to avoid the mechanical actuation of creases (for more information on the mechanical patterning see Fig.V.4). As shown in Figs.V.2,V.4,V.5, such stiffness ratio yields 1D smooth wrinkling when the bilayer is subjected to uniaxial in-plane buckling. However, when the magnetoelastic nature of the bilayer under a combined magnetomechanical loading is employed, the ratio G_s/G_f is no longer sufficient in determining the bifurcation modes.

In virtue of this coupling in material properties, geometry and loading, new contrasts between the mechanical G_s, G_f and magnetic $\chi_s, \chi_f, m_s^s, m_f^s$ properties of the layers take the lead in bifurcation. These contrasts can be written in form of ratios, e.g., $G_s/(\chi_f \mu_0 m_f^s)$, only if the constitutive behavior of the materials is linear, see relevant theoretical analysis in Section IV.4. In the present numerical investigation, we use the non-linear Langevin magnetoelastic law eq.(III.34) and thus, magnetomechanical property ratios are meaningless. To that end, the finite magnetic interlayer contrasts will be simply given in the form of substrate-to-film particle volume fraction c_s/c_f ratios, for fixed mechanical contrast $G_s/G_f = 0.3$. For clarity, it is emphasized that the particle concentrations are used to assign magnetic properties to the layers, as deduced by means of theoretical estimates and bounds (see Section II.8). In other words, by increasing c_s/c_f, we increase the magnetic sensitivity of the substrate with respect to that of the film.

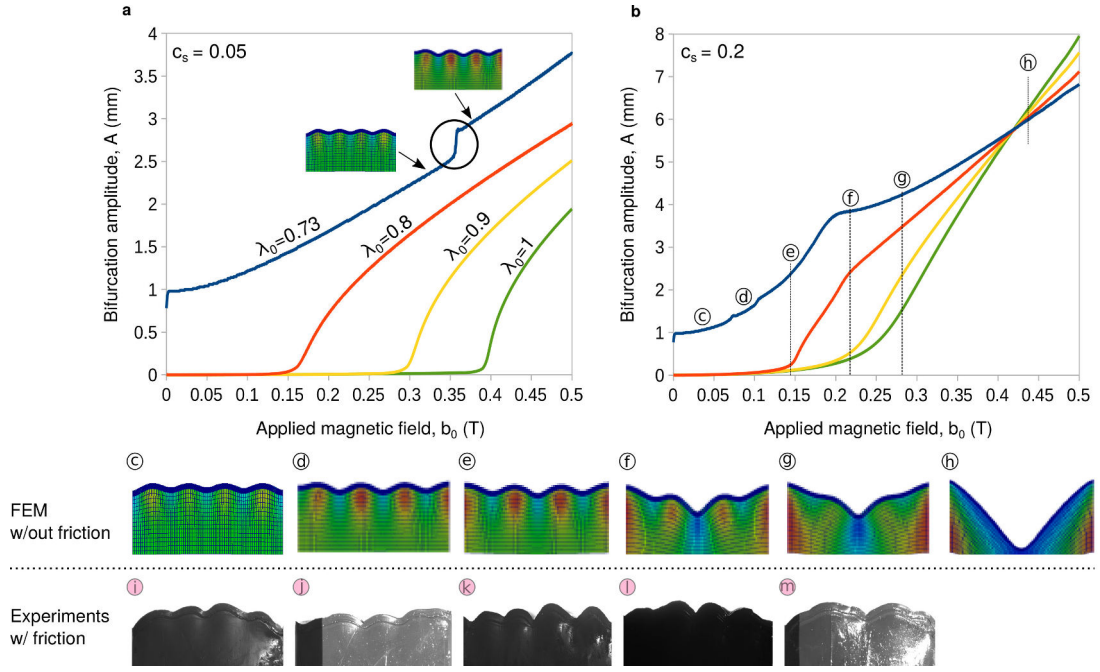

Figure VI.5: Numerical simulations of the average bifurcation amplitude A versus the applied magnetic field b_0, under four pre-compressions $\lambda_0 = 0.73, 0.8, 0.9, 1$ applied on a MRE film of shear modulus $G_f =$ 10kPa and particle volume fraction $c_f = 0.2$, bonded on a MRE substrate of shear modulus $G_s = 3$kPa and particle volume fraction **a**, $c_s = 0.05$; **b**, $c_s = 0.2$. The particle concentrations are just to assign magnetic properties to the layers, χ_s, $\mu_0 m_s^s$, under fixed mechanical properties. **c-h**, Plane-strain contours of the post-bifurcated shape configurations illustrating the evolution from wrinkling to crinkling with increasing magnetic field. Such an evolution of curvature localization retains invariant its sequential form of patterns within the entire range of applied pre-stretches. Instead, the amplitude of the patterns evolves differently as a function of the pre-stretch. **i-m**, Optical images of the MRE bilayer block under the magnetomechanical loading. Both experiments and numerics exhibit curvature localization in the middle wrinkle/crinkle. The comparison between experiments and numerics is only qualitative. This is due to strong friction observed at the lateral faces of the experimental specimen, whereas no friction is used in the numerical calculations.

The elastomeric substrate is gradually reinforced from 0 to 40% particle volume fraction. Using the Hashin-Shtrikman lower bound and the rule of mixtures (see Section II.6), we estimate the magnetic susceptibility χ_s and the saturation magnetization $\mu_0 m_s^s$ of the substrate, respectively. For the sake of keeping the number of parameters low, the shear modulus of the substrate is numerically fixed, $G_s = 3$kPa. In practice, this can be achieved by using softer/harder polymers for the two layers, since the increase of the particle volume fraction affects the mechanical properties as well. The material properties of the film are those of the prior studies, $G_f = 10$kPa, $\chi_f = 0.4$ and $\mu_0 m_f^s = 0.5$T ($c_f = 20\%$). At this stage, the numerical simulations are carried-out in the absence of friction, so as to illustrate the ideal response of the MRE block.

In Figs. VI.5a and b, we show the average bifurcation amplitude A of the surface layer as a function of the applied magnetic field b_0, for particle volume fraction $c_s = 0.05$ (or $c_s/c_f = 0.25$) and $c_s = 0.2$ (or $c_s/c_f = 1$), respectively. The instability and post-instability patterns develop in a progressive manner with increasing substrate volume fraction; range tested $c_s \in [0, 0.4]$. However, only these two

distinct but representative cases will be presented. The rest of the cases are discussed briefly since they exhibit similar responses. For low particle volume fractions $c_s \in (0, 0.05)$, the film magnetically buckles under a stable sine-wave configuration of four wrinkles within the entire range of applied pre-compressions $\lambda_0 \in (0.73, 1)$. This wavenumber is in agreement with that of the MRE film/passive substrate system, $c_s = 0$. For pre-compressions beyond the mechanical buckling point $\lambda_0^c (\simeq 0.76)$, the bifurcation amplitude is non-zero for zero applied magnetic field, i.e., $A \neq 0$ for $\{b_0 = 0$ and $\lambda_0 < \lambda_0^c\}$ (as also seen in Figs.VI.5a,b for $\lambda_0 = 0.73$). For volume fractions $c_s \in [0.05, 0.1)$, the film bifurcates into the standard wrinkling mode within the range $\lambda_0 \in (\lambda_0^c, 1)$[5]. Beyond the mechanical buckling point, the sinusoidal mode exhibits a decrease in the wavenumber (by half wrinkle) as the amplitude grows, Fig.VI.5a. Manifested by a jump in the bifurcation amplitude at $b_0 \sim 0.35$T, the change in the wavenumber is the first feature demonstrated by a magnetic substrate (slightly magnetizable).

For volume fractions $c_s \in [0.1, 0.25)$, the surface patterns progressively evolve from wrinkling to crinkling within the entire range of pre-stretches tested $\lambda_0 \in (0.73, 1)$, Figs.VI.5c-h. For compressive stretches beyond the mechanical buckling, e.g., $\lambda_0 = 0.73$, the change in the wavenumber (Fig.VI.5c-d) is now followed by a crinkle evolving around the center of the film (Fig.VI.5f-h). The middle valley of the pattern grows larger as the side wrinkles flatten-out with increasing magnetic field. This pattern gradually results in a single long-wavelength crinkle that is spread along the entire surface layer; that is an entirely new mode. Such an evolution of curvature-localization, Figs.VI.5e-h, retains invariant its sequential form of patterns within the entire range of applied pre-stretches. Instead, the amplitude of the patterns evolves differently for the various applied pre-stretches, as shown in Figs.VI.5a,b. Nevertheless, the onset of each such pattern is insensitive to the pre-stretch, depending solely on the magnetic field value for a given substrate c_s. However, we recall that the bifurcation is shifted in higher magnetic fields with decreasing pre-compression. Thus, if the system has not yet bifurcated for a given magnetic field ($b_0 < b_0^c$) under a pre-stretch value, the corresponding to that field pattern is bypassed. Eventually, the system will buckle under a following mode at $b_0 = b_0^c$. For instance, we observe in Fig.VI.5b that the sinusoidal wrinkles do not emerge for $\lambda_0 = 0.9, 1$, whereas the primary bifurcation is the localization of Fig.VI.5f. The other way round, as the particle volume fraction c_s increases under a given pre-stretch, less modes emerge versus the magnetic field [6].

Figs.VI.5i-m show optical images of preliminary experimental findings under selective loadings. Both experiments and numerics exhibit curvature localization in the middle wrinkle/crinkle. At this stage, the comparison between experiments and numerics is only qualitative. This is due to strong friction observed at the lateral faces of the experimental specimen, whereas no friction is used in the numerical calculations.

For further correlation with the experimental findings, the friction sensitivity of surface patterns for (non-)magnetic substrates can be seen in Fig.VI.6. Here, we show the pre- and post-bifurcation

[5] We note that the mechanical buckling load is found $\lambda_0^c \simeq 0.76$ for 0.8mm film thickness, see Fig.V.16 for geometrical sensitivity.

[6] To provide an example, for $\lambda_0 \in [0.8, 1)$, the last two crinkling configurations (Figs.VI.5g-h) are formed when $c_s = 0.25$, whereas only the very final long-wavelength (Fig.VI.5h) configuration is formed when $c_s = 0.4$.

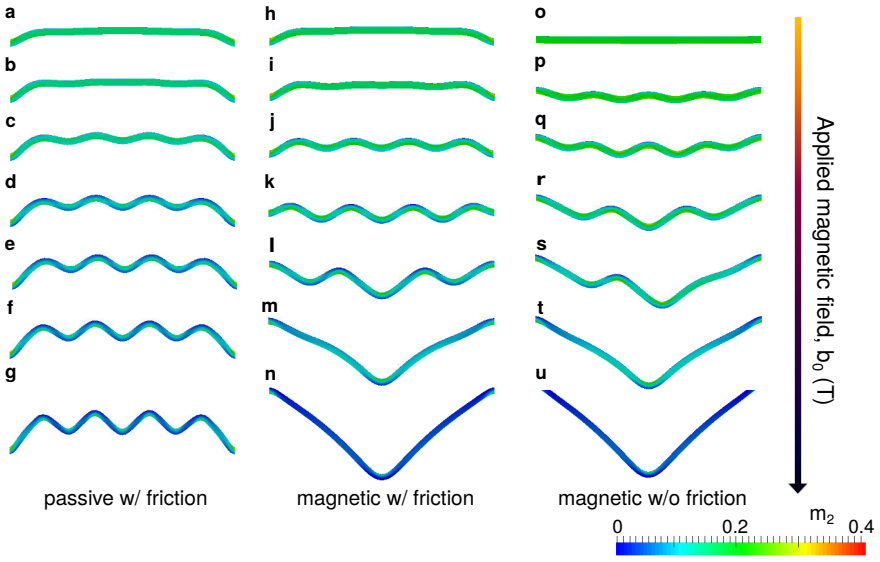

Figure VI.6: Friction sensitivity of surface patterns for passive and magnetic substrate. Pre- and post-bifurcation morphology of the film/substrate system versus the applied magnetic field under fixed pre-stretch $\lambda_0 = 0.78$. The system is defined by fixed interlayer stiffness contrast $G_s/G_f = 0.3$ and variable magnetic contrast and lateral shear forces: **a-g**, $c_s/c_f = 0$, $f_2 = 8e{-}5$N; **h-n**, $c_s/c_f = 0.75$, $f_2 = 8e{-}5$N; **o-u**, $c_s/c_f = 0.75$, $f_2 = 0$, respectively.

morphology of the film patterns versus the applied magnetic field b_0, under a fixed pre-stretch $\lambda_0 = 0.78$. The system is defined by a fixed interlayer stiffness contrast $G_s/G_f = 0.3$, but variable magnetic contrast c_s/c_f and applied lateral shear force f_2. Figs.VI.6a-g consider the evolution of the MRE film/passive substrate system, subjected to lateral forces $f_2 = 8e{-}5$N that fitted the experimental findings in Section V.2, $c_s/c_f = 0$. Prescribed to model the experimental friction, the same tangential forces are now applied on the MRE film/MRE substrate of magnetic ratio $c_s/c_f = 0.75$ in Figs.VI.6h-n. In addition, Figs.VI.6o-u include the same magnetic film and substrate $c_s/c_f = 0.75$, in the absence of friction $f_2 = 0$ (reference magnetic patterns). The lateral edges of the film are subjected to forces in the opposite to the displacement (negative) direction, creating a negative[7] curvature at the film corners (Figs.VI.6h vs. Figs.VI.6o). This curvature subsequently affects the morphology of the pattern by either vanishing wrinkling (Figs.VI.6i,p) or changing the wavenumber (Figs.VI.6k-l,r-s) on the surface layer. However, what makes a difference is that prescribing frictional forces leads the corners of the film to be pulled down (Figs.VI.6h-k) similarly to the experiments (Figs.VI.5i-m). Increasing the numerical friction value is expected to provide a better correlation with the experiments in high magnetic fields. Such a study is left for future work.

The numerical critical response of the MRE film/MRE substrate for sequentially magnetizated substrates is summarized in Fig.VI.7. The critical magnetic field b_0^c needed to trigger the primary instability is plotted versus the applied pre-compression λ_0 for different substrate particle volume fractions, $c_s = 0, 3, 5, 10, 15, 20, 25, 40\%$. A non-monotonic critical response is observed with increasing volume fraction in this three-parameter phase diagram. Starting from the passive case, $c_s = 0$, the incremental increase of the volume fraction delays the onset of bifurcation to higher

[7]Negative in the sense that the layer bends towards the interior compartment.

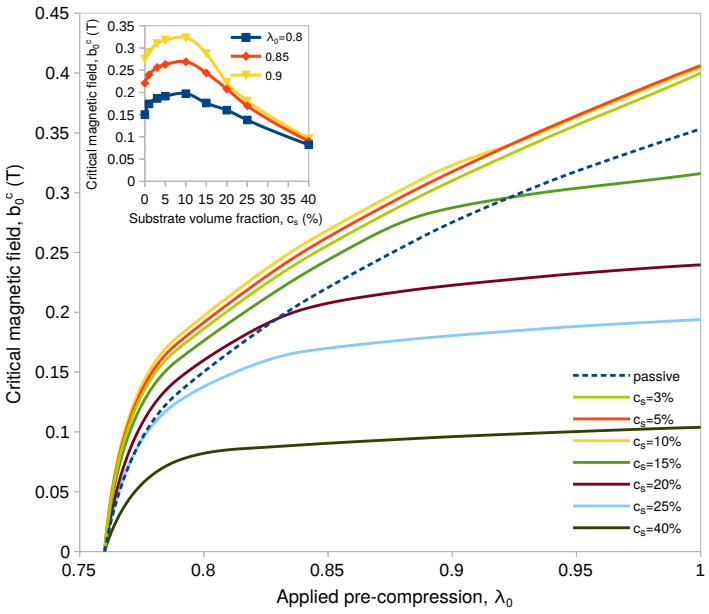

Figure VI.7: Numerical phase diagram of a MRE film bonded on a MRE substrate in a three-parameter field. The critical magnetic field needed to trigger the primary instabiliry b_0^c is plotted as a function of the applied pre-compression λ_0, for different substrate particle volume fractions $c_s = 0,3,5,10,15,20,25,40\%$. The particle concentrations are used to assign magnetic properties to the layers, $\chi_s, \mu_0 m_s^s$, under fixed mechanical properties. A non-monotonic trend of the onset of buckling as a function of the particle volume fraction is obtained, also demonstrated for three pre-stretches $\lambda_0 = 0.8.85, 0.9$ in the inset of the figure. Such a behavior is representative for magnetoelastic bilayers under simulation parameters: $H_f = 0.8$mm, $H_s/H_f = 49$, $G_s = 3$KPa, $G_f = 10$KPa, $\chi_f = 0.4$, $\mu_0 m_f^s = 0.5$T $(c_f = 20\%)$.

magnetic fields b_0 for a given pre-stretch λ_0. However, for $c_s \geq 10\%$, further increase of the particle concentration shifts down the critical point to sequentially lower magnetic fields. As the volume fraction increases, the critical magnetic field monotonically reaches saturation within a wider range of applied pre-stretches. At very large volume fractions, e.g., $c_s = 40\%$, the long-wavelength crinkle instability (exclusive mode at this c_s) is triggered by tiny magnetic fields $b_0^c \leq 0.1$T, which nearly saturates throughout the entire pre-stretch regime. This non-monotonic evolution of the onset of buckling can be also seen in the inset of Fig.VI.7, for three pre-stretches $\lambda_0 = 0.8.85, 0.9$. Moreover, the mechanical buckling point, i.e., $\lambda_0^c \simeq 0.76$ for $b_0 = 0$, is invariant to the substrate volume fraction.

To investigate the surface patterns triggered on the composite silicones that we can practically fabricate, we deduce the magnetic and mechanical material properties of the substrate from homogenization estimates and bounds, respecting the restrictions of our Ecoflex materials as discussed in Section II.8. Given the properties of the film already fabricated and used in the magnetomechanical experiment, i.e., $G_f = 1$MPa, $\chi_f = 0.4$ and $\mu_0 m_f^s = 0.5$T at volume fraction $c_f = 20\%$, the magnetic substrate can be reinforced up to $c_s = 18\%$ if mechanical creasing is not desirable[8]. The corresponding maximum magnetic contrast in terms of susceptibility ratio is then $\chi_s/\chi_f = 0.9$ from Fig.II.21a, with $G_s = 5.5$kPa and $\chi_s = 0.4$ from Fig.II.21b. Respecting these bounds, two cases of $c_s = 10\%$ and $c_s = 15\%$ were explored under a stiffness contrast $G_s/G_f = 0.38$. The numerical

[8] i.e., $G_s/G_f \in (0, 0.6]$ to prevent Biot's surface localizations (see for such localizations in Fig.V.4).

findings revealed a stable sawtooth (crinkle) response of four peaks, growing large in amplitude with increasing magnetic field and pre-compression. Such an instability mode was also found to coexist with the pre- and post-instability deformation mode of the system under a curvature that increases with increasing substrate volume fraction (see more in Section VI.3).

VI.3 Numerical study of crinkling and film thickness

Increasing the slenderness ratio (effective length-to-thickness) of the film was shown to increase the wrinkling wavenumber in Section V.5 (for an infinitely deep substrate). Here, we explore the evolution of crinkling patterns on magnetic bilayers, providing enough space (or a favorable slenderness) to the mechanisms to develop far from the side boundaries (lateral edges). Therefore, we carry out numerical simulations of a 40×40 (mm^2) MRE film/substrate block under a thinner ($H_f =$)0.2mm film, varying the magnetic interlayer contrast c_s/c_f for a fixed shear moduli ratio $G_s/G_f = 0.3$. The film is once more modeled as the experimental system, with $G_f = 10\text{kPa}$, $\chi_f = 0.4$, $\mu_0 m_f^s = 0.5\text{T}$ ($c_f = 20\%$). The simulations are followed by a post-processing curvature localization analysis to illustrate the formation and evolution of crinkling.

We start the analysis by plotting in Fig.VI.8 the bifurcation amplitude A of the patterns as a function of the applied magnetic field b_0, for two filler contrasts $c_s/c_f = 0.75, 1.25$ (or $c_s = 0.15, 0.25$) and four different pre-stretches $\lambda_0 = 0.78, 0.8, 0.83, 0.85$. The bifurcation amplitude is defined as the distance between the highest peak and the lowest valley of the evolving pattern. A feature initially observed in the thicker film specimen (e.g., Fig.VI.5 for $c_s/c_f = 1$ and $\lambda_0 = 0.9, 1$) is now illustrated in clarity: the pre-bifurcation solution exhibits non-uniform displacements versus the applied magnetic field. The primary divergence occurs upon a non-zero solution where $A \neq 0$ for $b_0 < b_0^c$. That implies that the film is not flat before bifurcation, but is pulled upwards from the corners in a quartic manner versus the external field (see Fig.VI.16 in Appendix).

Such a non-intuitive response is related to shape effects (e.g., see Diguet et al., 2010, Lefèvre et al., 2017) coming from the magnetic nature of the bulky substrate (not observed for passive foundations). The bifurcation (divergence) point is evident though, shifted in lower magnetic fields with increasing pre-compression λ_0 and magnetic ratio c_s/c_f. However, such amplitude measurements can only be seen qualitatively: they trace the trends of the critical response and illustrate the nonlocal behavior. This is because the magnetostriction of the system evolves as well throughout the post-bifurcation, until magnetization saturation is reached (see clearer pattern evolution in Figs.VI.9,VI.10). As a result, the measurements of the post-bifurcated amplitude account for this long-wavelength deflection[9].

For magnetic ratio $c_s/c_f = 0.75$ and pre-compression $\lambda_0 = 0.78$, we observe in Fig.VI.8 the sequential loss of the formed wrinkles, displayed as jumps in the bifurcation amplitude versus the applied field. This feature is in consistence with the behavior of the thicker film specimen, Fig.VI.5.

[9] e.g., in the inset configuration of Fig.VI.8 for $c_s/c_f = 1.25$, wrinkling grows upon a slope coming from the curvature of the magnetostrictive bending.

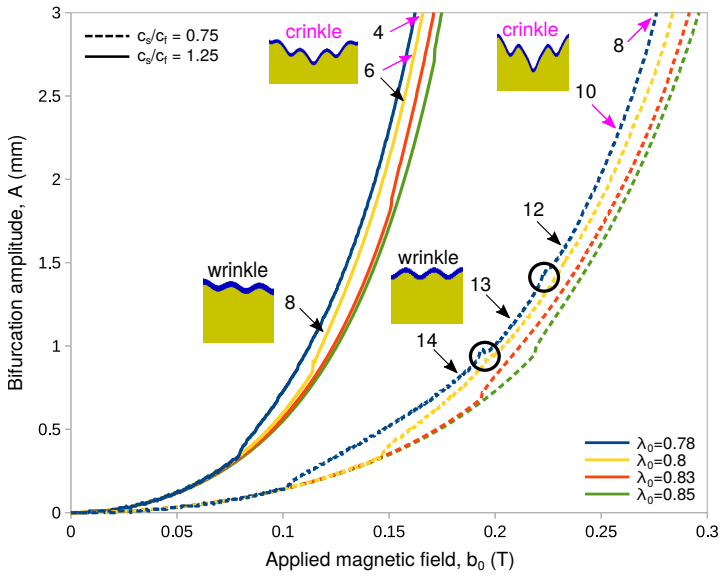

Figure VI.8: Numerical simulations and post-processing measurements of the film deflection amplitude A as a function of the applied magnetic field b_0, for two substrate/film magnetic contrasts $c_s/c_f = 0.75, 1.25$ and four different pre-stretches $\lambda_0 = 0.78, 0.8, 0.83, 0.85$. Part of the numerical morphological patterns is shown under selective loads $\{\lambda_0, b_0\}$, with the corresponding wavenumber (number of wrinkles or crinkles) noted. Simulation parameters: $H_f = 0.2$mm, $H_s/H_f = 199$, $G_s = 3$KPa, $G_f = 10$KPa, $\chi_f = 0.4$, $\mu_0 m_f^s = 0.5$T ($c_f = 0.2$).

The change in the wavenumber coexists with the gradual switch of wrinkling to sawtooth configurations (see also Figs.VI.11a,VI.15a,c). The crinkles subsequently evolve into a stable configuration upon further increase of the applied magnetic field. This process involves the relaxation of the side crinkles under the influence of increasing shape effects and magnetic fields, until the equilibrated mode upon saturation magnetization (of eight crinkles in this case) is formed.

When the substrate is more magnetizable than the film, $c_s/c_f = 1.25$, the structure in Fig.VI.8 buckles in lower magnetic fields, in agreement with the phase diagram in Fig.VI.7. The patterns now manifest lower wavenumbers than those in bilayers of lower magnetic contrasts, e.g., $c_s/c_f = 0.75$. This is also in agreement with the previous (thicker film) analysis in Section VI.2. For $\lambda_0 = 0.8$ for instance, we find that the bifurcation emerges with eight sine-waves progressively decreased to four sawteeth (see similar morphological patterns in Fig.VI.10 1m-1o for $\lambda_0 = 0.78$). The bending deflection of the film is regarded as a deformation mode (coming from magnetostrictive shape effects) and not an instability. This can be easily verified by checking the positive definitess of the jacobian matrix before primary wrinkling. When wrinkles emerge, that is the first time a non-positive eigenvalue appears. In the pre-bifurcation, the curvature seems to be insensitive to the applied pre-compression.

When the substrate is magnetic, the reponse is found to be dependent on its magnetic properties. The new features observed are a) the shape-driven curvature and b) the significantly high concentration of the magnetic field at the corners of the film. The curvature localization is related to pronounced extensive deformations ($E_{22} > 0$) at the lateral edges of the substrate that pull upwards

the corners of the film versus the magnetic field (visualized in strain contours of Fig.VI.10). These deformations and magnetic concentrations are found to be increasing functions of the magnetic interlayer contrast c_s/c_f and the applied pre-compression λ_0. The response of the MRE block is governed by such magnetostrictive shape effects [10] that are due to the uniform field applied far for the specimen. The present boundary value problem is definitely different from the theoretical bifurcation analysis that does not take into consideration such effects. Prescribing a negative[11] curvature (through lateral negative forces for instance) on the initial configuration of the numerical specimen gives insight to the sensitivity of the evolution of the modes on the shape effects, see discussion in Fig.VI.6.

VI.3.1 Morphological strain maps for different pre-compressions

In Figs.VI.9,VI.10, several cases of crinkling evolution paths are shown in the triple parameter-space of pre-compression λ_0, magnetic field b_0 and magnetic interlayer contrast c_s/c_f (for fixed stiffness ratio $G_s/G_f = 0.3$). These morphological maps illustrate when the patterns are formed and how long they stay active versus the magnetic field, under representative combinations of pre-stretches and magnetic interlayer contrasts. In Figs.VI.9 1a-1l and 2a-2l, we show contours of the transverse component of the Green-Lagrange strain E_{22} versus the applied magnetic field b_0, for magnetic contrasts $c_s/c_f = 0.75, 1$. For each magnetic ratio c_s/c_f, three representative (per case) pre-stretches are considered.

As seen in Fig.VI.9, the MRE bilayer systems display a rich variety of post-buckling patterns. The primary instability always develops on the top of the pre-bifurcated curvature. Once the primary waves appear, they start diminishing from the sides to the center of the film upon increase of the magnetic field. Simultaneously, the rest of the undulations grow their amplitude and switch into crinkles early in the post-bifurcation regime. To do so, the curvature around the extrema (peaks and valleys) of the undulations is localized, leading to the formation of sawtooth configurations (see also deformed configurations in Figs.VI.11a,VI.15a,c).

The patterns observed in VI.9 can be significantly varied from short (1h,1l) to long wavelength (1d,2d,2h,2l) modes that are sensitive to pre-stretch λ_0. Low pre-compressions (or high stretches λ_0) delay the instability to higher magnetic fields (Figs.VI.9 1b,1f,1j). The modes developed under low axial loading illustrate clearer the evolution of the magnetostrictive curvature, until the critical magnetic fields are reached (Figs.VI.9 1a-1d,2a-2d). Large pre-compressions cause the instability to emerge at lower fields, but under a higher wavenumber (Figs.VI.9 1b,1f,1j). It is easily observed that the greater the pre-compression, the faster the critical wavenumber diminishes in the post-bifurcation (Figs.VI.9 2b-2d,2f-2h,2j-2l). That implies that the uniaxial loading advances the curvature localization (also shown for the experimental specimens in Figs.VI.3,VI.4) and thus, the undulations in the surroundings of the central crinkle are faster decompressed. In view of Fig.VI.11b

[10] Such magnetostrictive effects have been also observed in the MRE film/passive substrate (zero magnetic interlayer contrast) but in a much milder manifestation, see Fig.V.7.

[11] negative in the sense that the film bends towards the interior compartment. By definition, a positive curvature is visualised by an arrow, which points from the concave side to the convex side of the curved beam.

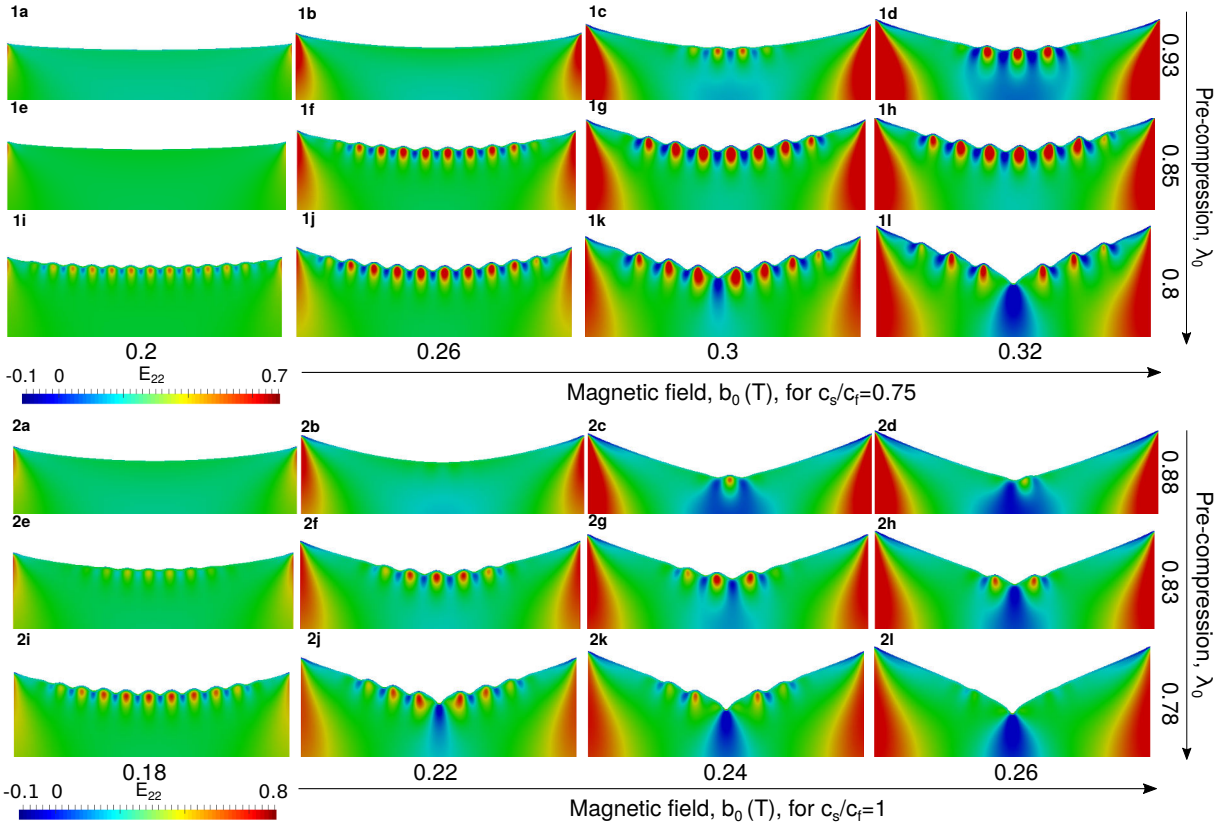

Figure VI.9: Numerical contours of the transverse component of the Green-Lagrange strain E_{22} versus the applied magnetic field b_0, for fixed mechanical interlayer contrast $G_s/G_f = 0.3$ and magnetic contrast **1a-1l**, $c_s/c_f = 0.75$; **2a-2l**, $c_s/c_f = 1$. For each interlayer contrast, three representative (per case) pre-stretches are presented. Fixed simulation parameters: $H_f = 0.2$mm, $H_s/H_f = 199$, $G_s = 3$KPa, $G_f = 10$KPa, $\chi_f = 0.4$, $\mu_0 m_f^s = 0.5$T ($c_f = 0.2$).

showing the spatial distribution of the transverse strain E_{22} along the film, the deformation at the lateral edges of the specimen increases with applied pre-compression. In turn, such extensive magnetostriction focuses more the layer curvature.

At some applied field b_0, the mode stabilizes into an equilibrated crinkled shape (Fig. VI.9 1d,1h,1l, 2d,2h, 2l). Such a shape is a multiple interfaces shape configuration of straight segments (crinkles), whose wavelength depends on the pre-compression under a given magnetic contrast c_s/c_f. For $c_s/c_f = 0.75$ and $\lambda_0 = 0.8$, a deep crinkle develops around the center of the layer (point of maximum deflection of the global mode) surrounded by smaller amplitude crinkles, Figs. VI.9 1i-1l. Such a post-buckling configuration of multiple interfaces emerges in lower magnetic ratios ($0.5 < c_s/c_f \geq 1$) and requires substantial pre-compression ($\lambda_0 \leq 0.85$).

The patterns are also sensitive to the magnetic interlayer contrast. Increasing the magnetic ratio c_s/c_f shifts the instability to lower magnetic fields b_0 but larger strains λ_0. For instance, when $c_s/c_f = 1$, the first strain at which instability occurs is $\lambda_0 = 0.88$ (Fig. VI.9 2p). In contrast, when $c_s/c_f = 0.75$, the system manifests instabilities already at $\lambda_0 = 0.93$ (Fig. VI.9 1d). When $c_s/c_f = 1$ and $\lambda_0 > 0.88$, only the magnetostrictive deformation mode appears within $b_0 \in [0,3]$T. This feature will be further illustrated in the context of Figs. VI.10.

VI.3.2 Morphological strain maps for different interlayer magnetic contrasts

In Figs.VI.10 1a-1t and 2a-2t, we present contours of the transverse component of the Green-Lagrange strain E_{22} versus the applied magnetic field, for pre-stretches $\lambda_0 = 0.78$ and $\lambda_0 = 0.83$, respectively. For each pre-stretch, five representative magnetic ratios $c_s/c_f = 0, 0.75, 1, 1.25, 2$ are considered for fixed film concentration $c_f = 0.2$. Following parametric studies, the magnetic interlayer ratio is set to be $c_s/c_f \geq 0.25$, in order for magnetostrictive shape effects and crinkles to be observed. These two features emerge together in the simulations, implying that crinkling and curvature localization are related (see also curvature localization analysis in Fig.VI.14).

When the substrate reinforcement is relatively small $c_s/c_f < 0.25$, the behavior is qualitatively similar to that of the passive substrate. The primary wavenumber is a decreasing function of the magnetic contrast c_s/c_f (Figs.VI.10a,e,i,m,q). As seen in the contours, increasing the substrate filler leads to higher deformations at the lateral edges of the substrate and that, in turn, focuses more the overall curvature of the upper surface of the specimen (see similar effects in Lefèvre et al. (2017)). That process leads to lower wavenumbers. Following this critical trend under a fixed pre-stretch, the sequential post-buckling patterns are triggered by lower magnetic fields with increasing magnetic contrast c_s/c_f. As a result, a surface configuration can be triggered by more than one combinations of magnetic loading and substrate properties, e.g., Figs.VI.10 2k-2l,2m-2n.

The crinkling post-buckling behavior changes dramatically for large substrate reinforcements. A single long-wavelength crinkle (Fig.VI.10 1p) emerges in the post-bifurcation, especially when large pre-compressions are considered, $\lambda_0 \leq 0.83$. As such crinkle forms, it relaxes the compression in the film on both sides of itself and thereby, the amplitude of the crinkles in the neighborhood is reduced. Such a configuration is equilibrated and is shifted to lower fields with increasing magnetic interlayer contrast. For instance, when $c_s/c_f \geq 1.25$, it emerges at magnetic fields that are slightly larger than the bifurcation field, Fig.VI.10 1m-1p,2m-2p. This long-wavelength localization mode is observed in all simulations performed in the range of substrate reinforcement $c_s \in [0.2, 0.25]$ (or $c_s/c_f \in [1, 1.25]$) and $\lambda_0 \leq 0.85$.

The larger the magnetic contrast c_s/c_f, the greater the pre-compression λ_0 at which the (magnetically triggered) instabilities start to emerge. Such a distinctive case is seen in the morphological map in Fig.VI.10 2q-2t for $c_s/c_f = 2$: when $\lambda_0 \geq 0.85$, the structure solely develops the magnetostrictive deformation mode, growing large upon the activation of the magnetic field. To obtain such a mode requires substantial substrate reinforcement and not large pre-compressions. However, the higher the magnetic ratio, the more insensitive it becomes to the pre-compression. This shape deformation is different from the long-wavelength crinkle mode, which requires $\lambda_0 \geq 0.78$ to be magnetically triggered (Fig.VI.10 1q-1t). The latter emerges at magnetic fields that are slightly larger than the critical field, see Figs.VI.10 1q-1t.

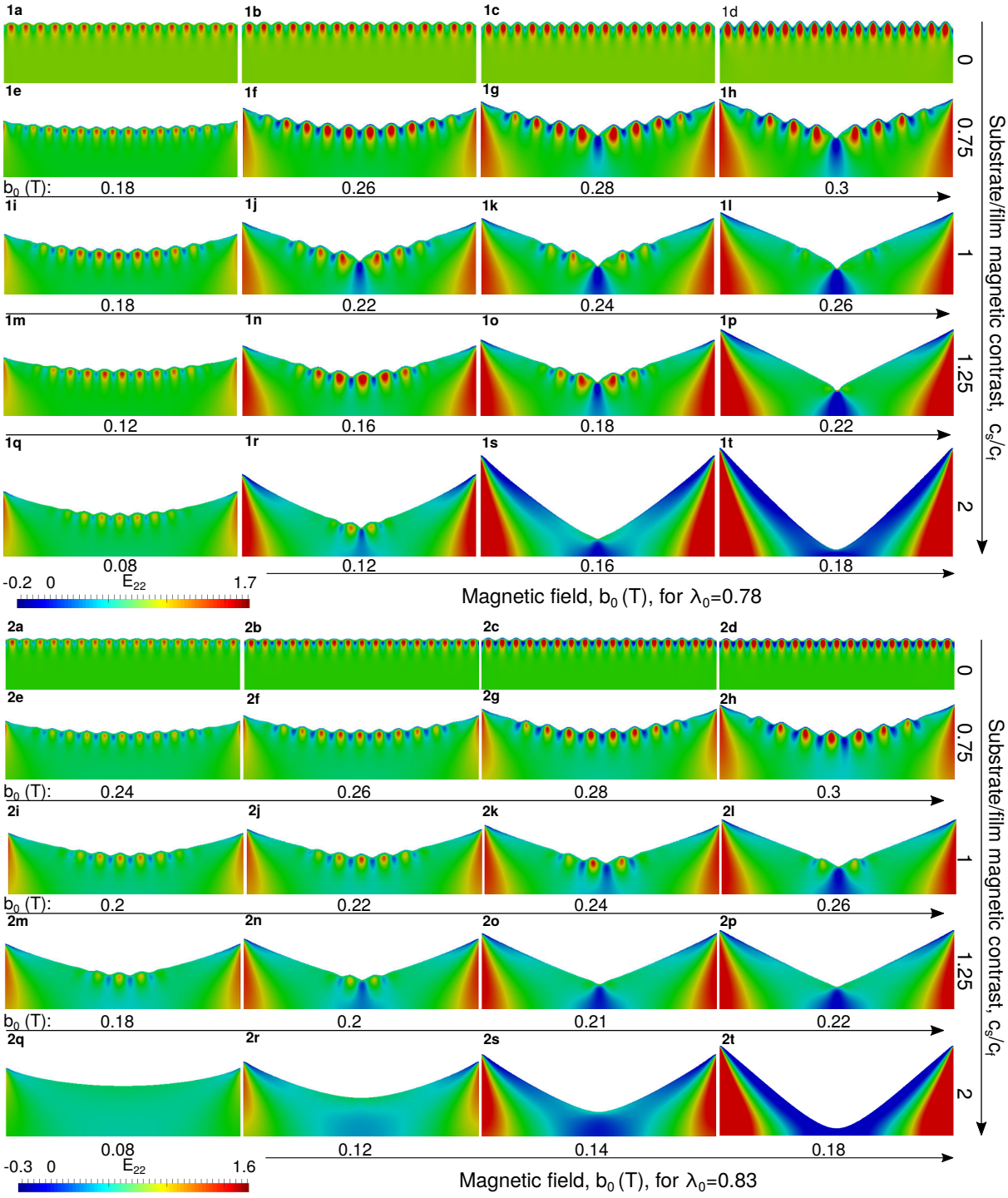

Figure VI.10: Contours of the transverse component of the Green-Lagrange strains E_{22} versus the applied magnetic field b_0, for five interlayer magnetic contrasts $c_s/c_f = 0, 0.75, 1, 1.25, 2$ (under a fixed mechanical ratio $G_s/G_f = 0.3$) and two pre-compressions: **1a-1t**, $\lambda_0 = 0.78$ and **2a-2t**, $\lambda_0 = 0.83$. Fixed simulation parameters: $H_f = 0.2$mm, $H_s/H_f = 199$, $G_s = 3$KPa, $G_f = 10$KPa, $\chi_f = 0.4$, $\mu_0 m_f^s = 0.5$T ($c_f = 0.2$).

VI.3.3 Local magnetomechanical fields

In Fig.VI.11, we present a full-field numerical analysis of the thin MRE film bonded on a MRE substrate under magnetic contrast $c_s/c_f = 0.75$. Figs.VI.11a-b report the transverse component

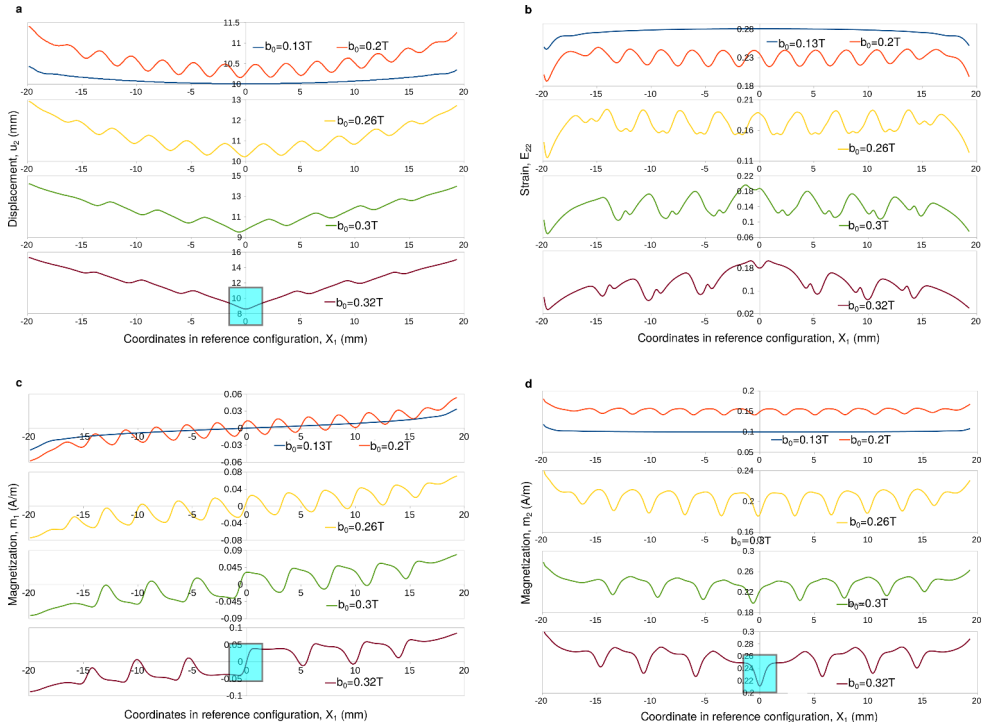

Figure VI.11: Numerical results of the spatial distribution of the **a**, transverse displacement u_2; **b**, transverse Green-Lagrange strain E_{22}; **c**, in-plane magnetization m_1; **d**, transverse magnetization m_2 along a contour line of reference coordinate X_1 within the film. The plots correspond to magnetic interlayer contrast $c_s/c_f = 0.75$ (fixed mechanical ratio $G_s/G_f = 0.3$), pre-stretch $\lambda_0 = 0.8$ and different applied magnetic fields $b_0 = 0.13, 0.2,\ 0.26, 0.3, 0.32$T. Fixed simulation parameters: $H_f = 0.2$mm, $H_s = 39.8$mm, $G_f = 10$KPa, $G_s = 3$KPa, $\chi_f = 0.4$, $\mu_0 m_f^s = 0.5$T ($c_f = 0.2$).

of the displacement u_2 and the corresponding Green-Lagrange strain E_{22} along a reference (at 40 mm) contour line within the film. Figs.VI.11c-d present the two components of the magnetization $\mathbf{m} = (m_1, m_2)$, plotted along the same reference line. The quantities are considered for pre-stretch $\lambda_0 = 0.8$ and five magnetic field values, $b_0 = 0.13, 0.2, 0.26, 0.3, 0.32$T. The depicted plots correspond to the contours in Figs.VI.9 1i-1l.

The smallest external magnetic field $b_0 = 0.13$T corresponds to the pre-bifurcation regime of the system. In Fig.VI.11a, the displacement profile u_2 illustrates the non-uniformly deformed layer at $b_0 = 0.13$T. The primary instability to emerge is wrinkling on the top of the magnetostrictive curvature ($b_0 = 0.2$T). Upon further increase of the magnetic field, the wrinkles progressively evolve into crinkles. Such a process involves the localization of the curvature around their extrema, as seen for $b_0 = 0.26$T and $b_0 = 0.3$T. The pattern experiences a decreasing wavenumber of increasing amplitudes with increasing magnetic field. The relaxation of the side crinkles is related to the increasing deformation of the lateral edges within the substrate versus the applied field (shown in Figs.VI.9,VI.10).

The evolution of wrinkling to crinkling is also outlined by variations of the strain field E_{22} in Fig.VI.11b. For relatively small magnetic fields $b_0 < 0.26$T, the strain is following a smooth and periodic (apart from the boundaries) trend. When $b_0 = 0.26$T, the regime around the peaks of the

pattern manifests a rapid spatial variation of strain, maintaining nonetheless the periodicity of the trend. Within the straight segments of the pattern (not close to the extrema), the strain is relatively smooth and varies monotonically. Between two closest peaks in u_2, E_{22} increases until the valley is attained and then decreases to the next peak. For $b_0 > 0.26\mathrm{T}$, the translational symmetry of the pattern breaks about $X_1 \simeq 0$. The central undulation manifests higher strain than the rest, while the layer localizes its curvature about the center of the layer (see also curvature localization analysis in Fig.VI.14). At $b_0 = 0.3\mathrm{T}$, a change in the wavenumber breaks the reflection symmetry (three versus four crinkles at the two opposite sides of the folded film). At $b_0 = 0.32\mathrm{T}$, a sequential change in the wavenumber restores that symmetry about $X_1 = 0$.

From the displacement u_2 and corresponding strain E_{22} plots in Figs.VI.11a,b, it is evident that the pattern is formed in two scales: i) the short-wavelength crinkles and ii) the shape-driven curvature localization of the entire film. As the magnetic field increases, the film is stretched so as the peaks approach the valleys so closely that they form very small segments of negative slope, see deformed configuration in Fig.VI.11a, $b_0 = 0.32\mathrm{T}$. These small segments concentrate rapid variations of strain with increasing magnitude versus the magnetic field. The long (straight) segments of positive slope experience a non-monotonic variation of strain that first increases and then decreases, as the next small segment is approached.

The magnetization m_1 is antisymmetric and oscillates between local minima and maxima. The system develops the m_1 component perpendicular to the applied field $b_0(\equiv b_2)$, as a result of the deformed pattern itself, which is not exactly perpendicular to the applied field (see also Fig.VI.12e). In the right half plane, m_1 alternates between positive maxima, and minima that start negative at $X_1 \simeq 0$ and switch sign as one approaches the right edge. The oscillation of the other half (left) plane is described by the antisymmetric trend. Such a feature is a direct consequence of the magnetic substrate, since m_1 is entirely symmetric for a magnetically insensitive substrate, see Fig.V.15. The antisymmetry itself implies that apart from the level of oscillatory undulations, a larger-scale magnetic pattern is formed between the two opposite sides about the point of maximum deflection, $X_1 = 0$. This will be better illustrated for higher substrate concentrations in Fig.VI.15d.

The amplitude and the period of m_1 oscillation increase with the magnetic field b_0. As the crinkling pattern evolves for $b_0 > 0.26\mathrm{T}$, m_1 tries to be constant along the (long) segments of positive slope on the crinkled pattern (the wrinkled pattern can be seen in Fig.VI.11a). In these regimes, the solution is relatively smooth far from the joint points (corners) with the neighboring (small) segments of negative slope. When the joint points are reached, the solution makes a jump to opposite sign values. At the right (left) half plane, the attained negative (positive) minima (maxima) correspond to the small negative slope segments. That implies that these regimes are alternating magnetized from the longer positive slope segments. This is not the case as one approaches the edges, where the film is under oscillatory values of the same sign. When the joint point of the two central co-axially magnetized segments is reached, the solution in m_1 alternates signs (blue window in Fig.VI.11c).

The transverse component m_2 is positive along the reference length of the layer, as it prefers to align with the direction of the applied magnetic field $b_0(\geq 0)$. However, m_2 also oscillates around

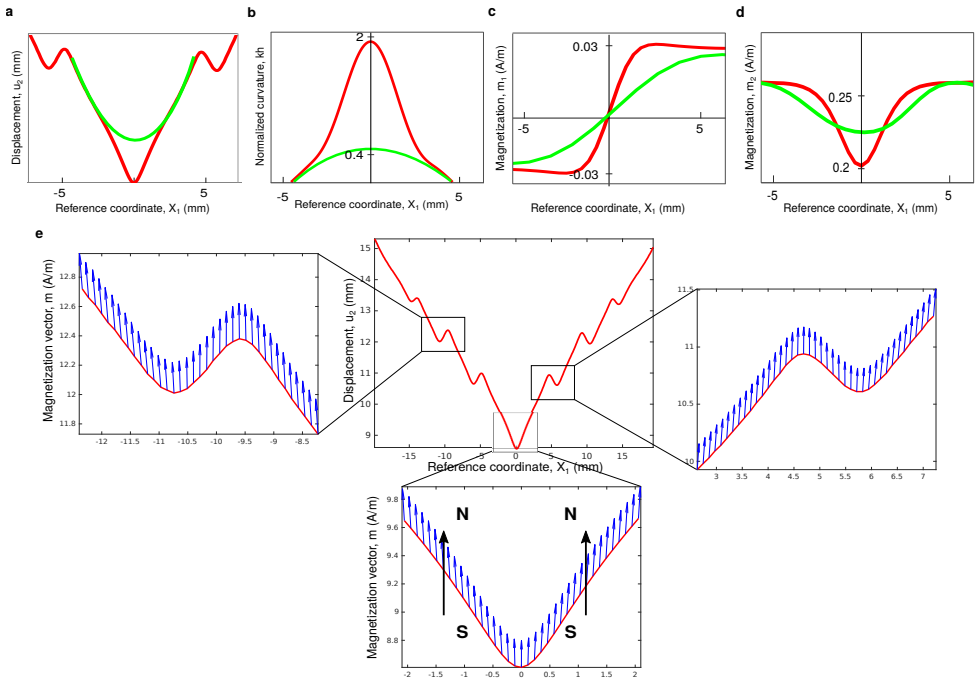

Figure VI.12: Wrinkling (green) versus crinkling (red). **a**, Transverse component of displacement u_2; **b**, in-plane component of magnetization m_1; **c**, curvature localization k; **d**, transverse component of magnetization m_2 of the middle undulation on the surface layer versus the reference position. **e**, Magnetization vector **m** plotted along a contour (reference position) line within the film and on the top of the deformed crinkled configuration.

the small linear segments of negative slope of the pattern. The highest magnitude of the field is at the edges of the film. The depicted u_2, E_{22} and m_2 fields are not necessarily reflectional symmetric about $X_1 = 0$, see $b_0 = 0.3$T. This owes to the unequal change of the wavenumber between the regimes $X_1 = [-l/2, 0)$ and $X_1 = (0, l/2]$, $l = 40$ (mm) the length of the film. When the joint point of two co-axially magnetized segments is reached, the solution in m_2 makes a jump (blue window in Fig.VI.11d). These variations in the fields leading to a crinkle are also illustrated in Fig.VI.12a-d. There, the local fields of the central crinkle are plotted versus those of a wrinkle formed under a lower magnetic field. In this way, the evolution of the fields outlines the mechanisms of the gradual pattern change, i.e., curvature localization and gradually sharper magnetic interfaces versus the applied magnetic field.

In Fig.VI.12e, we plot the magnetization vector **m** along a contour line $X_2 = 19.89$ (mm) within the film, on the top of the deformed crinkled configuration. The pattern corresponds to a MRE bilayer of magnetic contrast $c_s/c_f = 0.75$ under applied fields $\lambda_0 = 0.8$ and $b_0 = 0.33$T. Once more, the transverse component m_2 aligns with the externally applied magnetic field. The component m_1 develops perpendicular to the applied magnetic field. The magnitude of component m_2 is much larger than that of m_1[12] and thus, the vectors are all nearly pointing the out-of-plane direction. The linear segments of the pattern are found co-axially magnetized to their neighbors. As seen in the bottom figure of Fig.VI.12e, the magnetization repels the two opposite segments of the central

[12]The difference between $m_1 \sim 0.03$ and $m_2 \sim 0.25$ (A/m) in Figs.VI.12a,b is significant.

crinkle and contracts them with the smaller segments (of negative slope) of the neighboring crinkles.

The mechanism of crinkling formation is not straightforward to be explained from the numerical solutions. The local fields are structured in such a way to minimize the total energy. That permits the creation of magnetic walls, where the magnetization jumps accross their interface. These walls correspond to the joint points (local extrema) between neighboring segments of the pattern and tend to form sharp interfaces (regimes where the rapid spatial variations occur, Figs.VI.11,VI.15). In such regimes, the continuity is possibly not satisfied and charges are accumulated (not divergence-free points). However, the closer one gets to the edges of the film, the smaller the difference between the (opposite sign) oscillatory values of neighboring domains becomes, until the smaller (absolute) value switches sign. Then, the charges in the neighborhood relax and thus, the crinkles flatten-out (Figs.VI.15b,d). This process spreads from the edges to the center of the film versus the applied magnetic field. This implies that the magnetization and the morphological crinkling are closely related. The solution far from the walls is relatively smooth, as also seen in Figs.VI.11c,VI.15b,d.

VI.3.4 Wrinkling to crinkling as a cascade of bifurcations

The evolution of the post-buckling behavior is defined by sequential patterns of reducing wavenumber and curvature localization. To better understand the post-bifurcated response, we present in Fig.VI.13 the magnetization component m_1 at several points located within the film. The magnetization m_1 is traced versus the applied magnetic field b_0 under a pre-stretch $\lambda_0 = 0.8$, for magnetic interlayer contrast $c_s/c_f = 0.75$ and mechanical shear moduli ratio $G_s/G_f = 0.3$. Each curve correponds to a given nodal (material) position, depicted by the same color on the deformed film contours

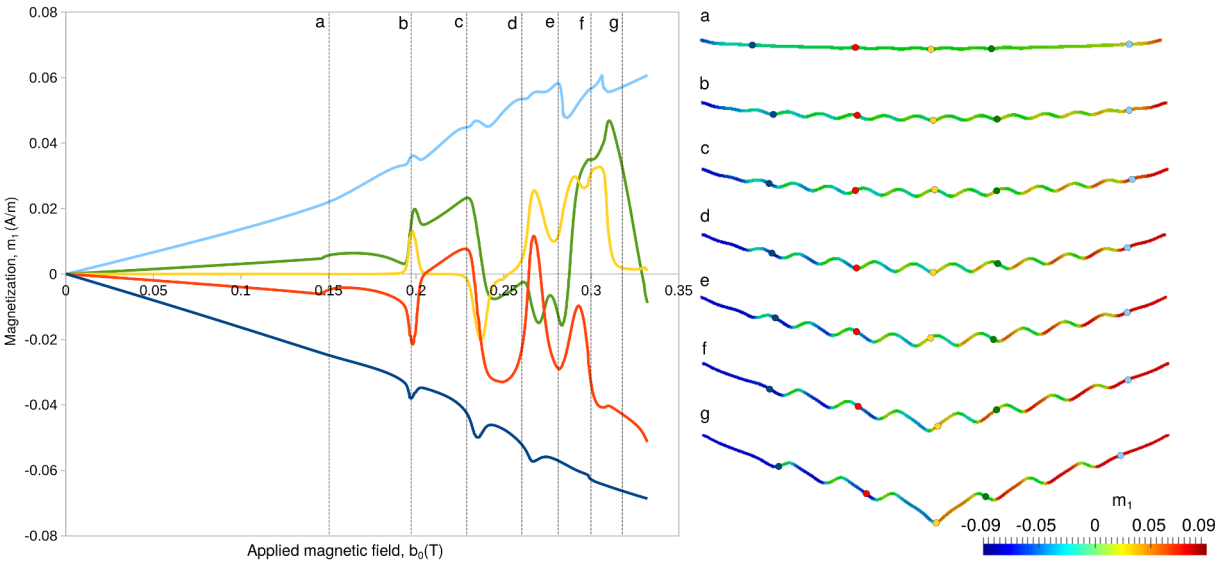

Figure VI.13: Magnetization component m_1 at five material points located within the film. The curves are plotted for a MRE bilayer of magnetic interlayer contrast $c_s/c_f = 0.75$ at pre-stretch $\lambda_0 = 0.8$. Each magnetization curve correponds to a given nodal (material) position, depicted with the same color on the deformed film contour of magnetization m_1.

of magnetization m_1 in Figs.VI.13a-g. Each contour corresponds to a given applied magnetic field b_0, marked in the magnetization plot.

The magnetization m_1 increases linearly with the magnetic field along the pre-bifurcation regime, $b_0 < 0.15$T. When $b_0 = 0.15$T, the primary bifurcation (wrinkling in Fig.VI.13a) causes a first change in the slope of the nodal magnetization m_1 curves. For $b_0 > 0.15$T, the curves undergo sequential and abrupt changes of slope. At each magnetic field for which such a change occurs, the wavelength of the wrinkles (or subsequently the crinkles for higher fields) increases, Figs.VI.13a-g. Considering the positive definitess of the jacobian matrix, these sudden changes of slope correspond to a new zero eigenvalue. That implies that the system undergoes multiple sequential bifurcations from the primary wrinkles to the crinkles.

The primary instability corresponds to the first non-positive eigenvalue of the stiffness matrix at $b_0 = 0.15$T. To do so, the smallest eigenvalue of the system incrementally decreases, until it reaches a first minimum close to zero. Subsequently, this eigenvalue increases and another one (corresponding to a new nodal point) decreases again towards a second minimum. Then, that is defined as a secondary instability point at $b_0 = 0.23$T. This process of sequentially new minima is followed until the equilibrated mode is reached at $b_0 = 0.32$T. To obtain such clear variation of eigenvalues corresponding to unique paths (one eigenmode per time), one needs to run saturatedly converged simulations of very large number of time steps (~ 4000). The material points that are close to the edges display magnetic bifurcations of increasing magnitude. The points closer to the middle of the film display bifurcations of alternating signs. Such an oscillating (+ and -) magnetization within

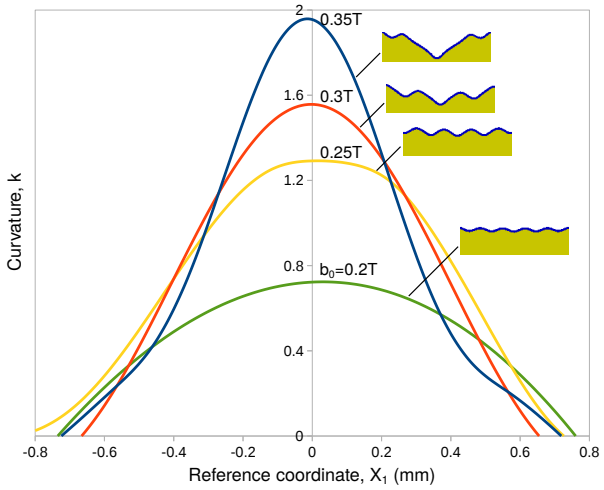

Figure VI.14: Numerical post-bifurcation curvature localization of the MRE film/MRE substrate block ($H_f = 0.2$mm film thickness). Curvature k is plotted versus position X_1 attached to material points in the (reference) undeformed film, under four magnetic field values $b_0 = 0.2, 0.25, 0.3, 0.35$T and a pre-stretch $\lambda_0 = 0.8$. The bifurcation primarily emerges under a wrinkling mode. Upon further increase of the magnetic field, $b_0 \simeq 0.3$T, the middle undulation grows deeper than the neighboring wrinkles and gradually evolves into a stable crinkle for $b_0 = 0.35$T. The curvature of the middle undulation is localized within a decreasing band width. Fixed simulation parameters: $H_f = 0.2$mm, $H_s = 39.8$mm, $G_f = 10$KPa, $G_s = 3$KPa, $\chi_f = 0.4$, $\mu_0 m_f^s = 0.5$T ($c_f = 0.2$).

the post-bifurcated film illustrates the formation of magnetic walls that decay as one approaches the edges.

To provide a direct relation with the magnetization patterns analyzed under pre-compression $\lambda_0 = 0.8$ in Figs.VI.12,VI.13, we carry out a curvature localization analysis on the numerical specimen under the same loading. In Fig.VI.14, we plot the spatial distribution of the curvature k corresponding to a central valley of the film. The curvature is plotted along the reference coordinate (position) X_1 (attached to material points in the undeformed film configuration) and for increasing applied magnetic fields b_0. As expected, the primary wrinkles focus their curvature into a decreasing band width, as a central crinkle grows large upon increase of the magnetic field. The deformed configurations of the MRE film/MRE substrate are also shown in Fig.VI.14.

VI.3.5 Numerical local fields: pre-compression and magnetic contrast sensitivity

In Fig.VI.15a,b, the displacement u_2 and the magnetization m_1 are reported for the same magnetic contrast $c_s/c_f = 0.75$ as in Fig.VI.11a,c, but lower applied pre-compression $\lambda_0 = 0.93$. Under the same applied field values b_0, the sensitivity of the fields on pre-compression can be better illustrated. In the pre-bifurcation regime, the evolution of the magnetostrictive curvature can be seen from the displacement profile u_2 for $b_0 = 0.2$T and 0.26T. The displacements are significantly lower with respect to Fig.VI.11a under $\lambda_0 = 0.8$. The primary instability of the buckling system is under four wrinkles, switching to three stable crinkles for $b_0 > 0.3$T. The in-plane magnetization m_1 displays antisymmetry already from the pre-bifurcation regime. At the half right (left) plane, the oscillation of m_1 is between positive maxima (negative minima), and minima (maxima) that switch sign from negative (positive) to positive (negative) as the oscillatory pattern approaches the edge. For $b_0 = 0.32$T, the change in the wavenumber is depicted in all fields, although they maintain their reflectional symmetry about $X_1 = 0$. The magnetization m_1 saturates for $b_0 \geq 0.32$T. The field along the positive slope segments of the pattern is piecewise constant. The valleys (peaks) of the pattern at right (left) plane correspond to the small segments of negative slope, alternating magnetized from their neighboring segments. The equilibrated configuration for $\lambda_0 = 0.93$ manifests less crinkles than that of the prior pre-compression, $\lambda_0 = 0.8$. However, these crinkles seem to be more resistant to relaxation versus the magnetic field, than those under the higher axial loading.

Fig.VI.15c,d reports the same fields for applied pre-compression $\lambda_0 = 0.8$ and a higher magnetic contrast $c_s/c_f = 1.25$, so as to illustrate the effect of substrate concentration. Increasing substrate filler leads to lower wavenumbers. The pattern manifests almost eight wrinkles ($b_0 = 0.13$T) that very soon reduce to six ($b_0 = 0.17$T), before turning into two crinkles ($b_0 = 0.2$T). In turn, the pattern finally stabilizes under a single long-wavelength localization ($b_0 = 0.32$T). The equilibrated configuration in Fig.VI.15b is totally different from that under the same loading ($\lambda_0 = 0.8, b_0 = 0.32$T) but lower interlayer magnetic contrast ($c_s/c_f = 0.75$) in Fig.VI.11a. For $b_0 > 0.2$T, the magnetization m_1 relaxes the charges in each half plane. The long-wavelength crinkle is defined by a nearly constant antisymmetric m_1 pattern ($b_0 = 0.32$T). The central joint point (at $X_1 = 0$) of highly

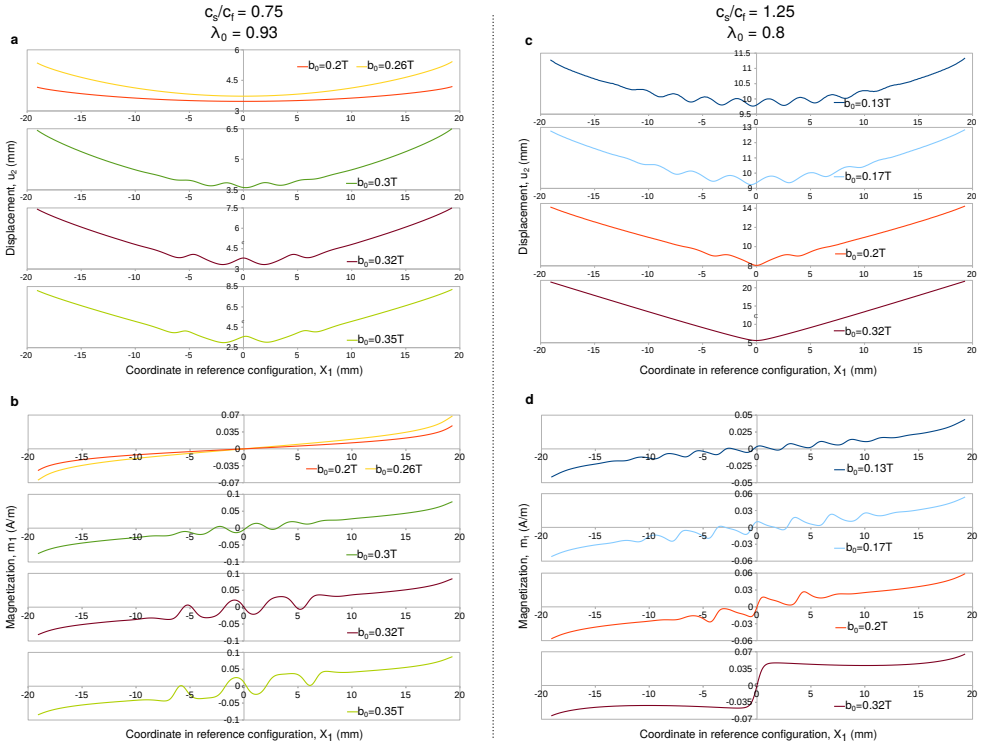

Figure VI.15: Numerical results of the spatial distribution of the **a**,**c**, transverse displacement u_2; **b**,**d**, in-plane magnetization m_1 along a contour line of reference coordinate X_1 within the film. The plots correspond to **a**-**b**, magnetic interlayer contrast $c_s/c_f = 0.75$ and pre-stretch $\lambda_0 = 0.93$; **c**-**d**, magnetic interlayer contrast $c_s/c_f = 1.25$ and pre-stretch $\lambda_0 = 0.8$ under four different applied magnetic fields.

localized curvature connects two regions of uniformly but similarly magnetized domains that repel each other. Now, the field is entirely positively (negatively) magnetized at the right (left) side of the localization (that is a new magnetic pattern). Such a pattern evolution occurs to reduce the total energy. The long-wavelength crinkle has the magnetic charges relaxed at its opposite sides, but concentrated at the joint point in the middle (discontinuity).

VI.4 Concluding remarks

In this chapter, we present the gradual and continuous evolution of wrinkling (sinusoidal) to crinkling (sawtooth) patterns. The analysis of the MRE film/MRE substrate reveals focused distributions of curvature and magnetization spatial oscillations between alternating values. The curvature localization is closely related to magnetostrictive shape effects that lead to symmetry-breaking instabilities. This curvature is a non-local deformation feature, in the sense that it captures the entire length of the surface layer. It also occurs as a result of the high concentration of the magnetic properties at the corners of the film. When the magnetic field is zero, the radius of that curvature is infinite, while as the field increases, the radius decreases to zero. Here, we show that the primary mode for each interlayer contrast is wrinkling, progressively switching to crinkling under the influence of the growing magnetostrictive deflection. Beyond the first bifurcation point, we report sequential bifurcations upon increase of the applied magnetic field. The corresponding complex patterns are

generated by sequential bifurcations of the equilibrated wrinkled state. The wrinkle-crinkle process might provide a fashion of concealing the potential energy.

At the same time, the co-axial magnetization interaction between neighboring segments is penalized by the elastic nature of the substrate and that leads to crinkles. The crinkled film on the top of a magnetostrictive curvature seems to accomodate the potential energy by bending the film with decreasing crinkling (wave)number. The relaxation of the crinkles starts from the edges and gradually spreads to the center of the film. The values of the magnetization dipoles come closer as one approaches the edges, with the smaller (absolute) value switching sign upon further increase of the magnetic field. In that way, the side crinkles pulled by the corners exhibit decay as one approaches the edges. Under high interlayer magnetic contrasts, passing from a crinkled pattern with multiple interfaces to an overall single sharp interface possibly reduces the total energy. To date, the formation mechanisms underlying such large-amplitude crinkle patterns are still not well understood, owing to the broad-scale nonlinear deformation features entailed in the crinkle formation process.

VI.5 Appendix I. Curvature fitting

The curved pre-bifurcated part of the amplitudes is fitted for both $c_s/c_f = 0.75$ and $c_s/c_f = 1.25$ with a fourth-degree polynomial in Fig. VI.16a and b, respectively. The fitting is carried-out by means of polynomial interpolation in Matlab, using the lowest possible degree that passes through the points of the dataset. As seen in the insets of the figures, the quartic functions increase to positive infinity at both ends[13], but are not reflection symmetric. A quadratic function closely fits the bifurcation curve up to 0.14 T and 0.08 T for $c_s/c_f = 0.75$ and $c_s/c_f = 1.25$, respectively. The global amplitude for $c_s/c_f = 1.25$ is observed to grow faster versus the applied magnetic field than that for $c_s/c_f = 0.75$; an indication that a highly magnetic substrate favors the long-wavelength bending mode.

[13] the coefficient of the leading-degree term is positive

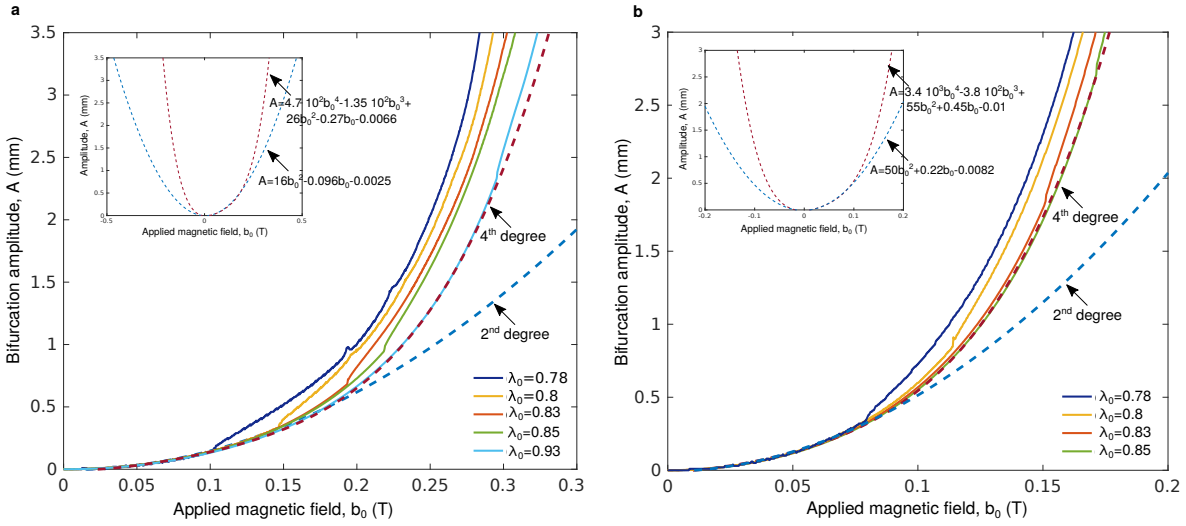

Figure VI.16: Numerical measurements and fitting of the film deflection amplitude A as a function of the applied magnetic field b_0, for four different pre-stretches $\lambda_0 = 0.78, 0.8, 0.83, 0.85$ and two substrate/film magnetic contrasts **a**, $c_s/c_f = 0.75$ and **b**, 1.25. A fourth-degree polynomial fits the entire pre-bifurcated curve as it is insensitive to pre-compression. A quadratic function closely fits the curve up to 0.14T and 0.08T for $c_s/c_f = 0.75$ and 1.25, respectively. Fixed simulation parameters: $H_f = 0.2$mm, $H_s/H_f = 199$, $G_s = 3$KPa, $G_f = 10$KPa, $\chi_f = 0.4$, $\mu_0 m_f^s = 0.5$T ($c_f = 0.2$).

VI.6 Appendix II. Mesh sensitivity on curvature localization

At this point, we should recall that the curvature localization analysis was carried out by means of linear quadrilateral finite elements, see Section III.4. In order to compensate the fact that we try to capture highly localized curves with linear elements, it is evident that we need to use significantly dense meshes. Therefore, a mesh sensitivity study of the curvature localization is necessary to verify convergence on the number of film elements. Following prior mesh convergence studies in Section III.5.2, we recall that the substrate and air have to be also designed in accordance with the film mesh density, respecting good edge seeding and element aspect ratios at the interfaces with the film.

In Fig. VI.17, we show the spatial distribution of the curvature k for different film meshes under a relatively high magnetic field, $b_0 = 0.35$T. Such a magnetic field is considered high within the scale the patterns emerge and thus, it is expected to form a highly localized pattern. The surface modes underneath the labels in color correspond to the curve of the same color. The labels denote the number of film elements along the thickness $\times$ the number of film elements along the length. We observe that the width band, in which curvature localizes, is a decreasing function of the number of elements, as expected. Our simulations are carried out with the mesh (blue curve) of 15 and 350 elements along the thickness and the length of the film, respetively. Presented in Section III.5, this is a mesh already converged in terms of bifurcation modes, loads and amplitudes. This mesh is supplementarily converged on curvature localization with a higher density mesh of 15 and 380 elements along the thickness and the length, respectively.

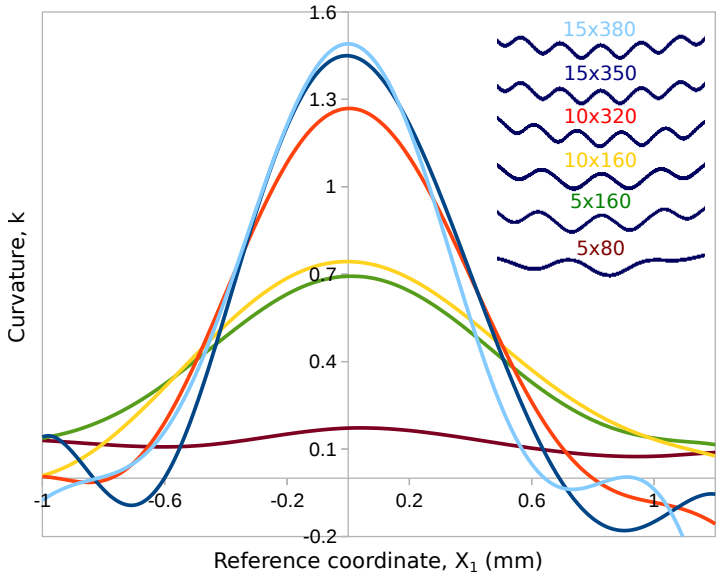

Figure VI.17: Mesh sensitivity study on curvature localization using different film meshes. The surface modes underneath the labels in color correspond to the curvature distribution of that color. The labels denote the number of film elements along the thickness × the number of film elements along the length.

CHAPTER VII

CONCLUSION AND PERSPECTIVES

The magnetorheological elastomers (MREs) are ferromagnetic particle impregnated elastomers whose mechanical (rheological) properties are altered by the application of external magnetic fields. These properties comprise, among others, the high manifestation of elastic strains under a magnetic field and the dependence of the magnetic permeability on stress (see Bednarek, 1999). An interesting feature of such composites is their elastic contraction when placed within a uniform magnetic field, an effect called magnetostiction. To that end, MREs exhibit field-stiffening effects and large magnetostrictive deformations that lead to continuously adjustable hardness upon a fast response to external fields (of the order of milliseconds). When the particle microstructure and macroscopic geometry is unfavorably oriented with respect to the applied magnetic field, magnetically triggered instabilities are possible to emerge in a reversible and repeatable fashion. Such a response is possibly applicable in actively controlled haptic systems and controllable stiffness devices, in order to induce surface patterns by means of external magnetic fields.

Inspired by the concept of combining unstable materials and structures, we investigate experimentally, theoretically and numerically the active control of surface roughness. To do so, we exploit the (post-)bifurcation response of a critically stable MRE film bonded on a nonlinear elastic and highly compliant substrate. As theoretically and numerically shown, such a system can buckle under a) purely mechanical uniaxial compression; b) a purely magnetic field applied perpendicular to the film (compass effect mechanism); or c) a combination of the two above-mentioned loadings. Taken independently, the critical fields needed to trigger the instability are significantly high (see Danas and Triantafyllidis, 2014), however they are reduced when coupled. To that end, the key idea is to mechanically bring the structure near (but not at) a marginally stable state and then destabilize it with relatively small magnetic fields. Such a study provides a proof of concept for operating near marginally stable regimes and passing beyond them with low (path independent) fields. This is attributed to the magnetoresponsive MRE material that is coupled with a prone to mechanical buckling structure.

Following a less common approach, we present experimentally, theoretically and numerically stability phase diagrams in the two-parameter space of applied pre-compression and magnetic field. In virtue of the critical response, we show the monotonic reduction of the critical magnetic field with

increasing pre-compression. The experimental findings are obtained upon fabrication of a MRE film (of volume fraction 20%) on a magnetically insensitive (passive) substrate. Repeatability in response is illustrated for both amplitude measurements and morphological patterns. The fabrication process is novel and allows for the realization of a single material-structure that manifests a variety of surface patterns (e.g., 1D and 2D wrinkling, period-doubling, crinkling, creases) under a large range of applied fields. Such a range of actuation fields owes to the material selection, as the theoretical bifurcation analysis shows.

The purely mechanical and magnetomechanical "bloch-wave" theoretical bifurcation analysis is carried out on a plane-strain infinite magnetoelastic system. Such an approach is an incremental bifurcation analysis that does not incorporate the effects of a boundary value system. The model aims at determining the critical load for the onset of wrinkling and the associated wavelengths (it does not deal with the stability of the bifurcated branches). To that end, we carry out a study on the influence of the material properties of the layers on the critical response. Slightly compressible neo-Hookean and magnetically (non-)saturating materials are employed. The material properties at hand are the compressibility Lamé constants, the shear modulus of the film G_f and substrate G_s respectively, the susceptibility of the film χ_f and their combined interlayer ratios, G_s/G_f, $G_s/(\chi_f \mu_0 m_f^s)$.

By use of different soft materials ranging from MPa (rubbers) to kPa (gels), we find that increasing the material softness permits to trigger instabilities with notably lower magnetic fields and within the sensitivity of realistic compression setups. This is explained by the fact that the softer the layers, the more compliant they are to deform under the same magnetization state. As a result, the most efficient way to decrease the critical fields and expand the range of applied pre-compressions is to use materials as soft as possible, e.g., polymeric gels of shear modulus of order of kPa. In addition, we show that when one makes use of the magnetoelastic nature of the materials under a combined loading, the interlayer stiffness contrast G_s/G_f is no longer sufficient in determining the critical loads and bifurcation modes. In the magnetomechanical bifurcation, the buckling depends on the ratio G_s/G_f, as well as on the absolute shear moduli values, G_s and G_f . This is in contrast with the purely mechanical buckling under incompressibility, where only the relative G_s/G_f ratio drives the response.

The experimental and theoretical critical response are in good agreement for low pre- compressions. However, some non-negligible differences are observed between the experimental findings and the idealized model under finite strains. Such differences are partially related to frictional effects acting at the lateral faces of the film/substrate block, those in contact with the walls of the experimental compression device. To that end, the non-trivial boundary value problem needs to be solved. Within a finite element framework, numerical plane-strain simulations are employed for a finite structure that mimics the experimental specimen and boundary conditions. Following a number of similar works in the literature, we mainly present experimental versus numerical comparisons for the post-bifurcation amplitude and the observed geometrical patterns. The magnetomechanical modeling proposed, albeit simple, captures the morphological response of the experimental samples (even the more complex shape configurations at large strains). The experimental results are probed

successfully with the aid of full-field finite element simulations at finite strains and large magnetic fields. To achieve that, we use a simple nonlinear magnetoelastic Helmholtz free energy with magnetization saturation for the MRE film, a classical nonlinear elastic constitutive law for the substrate and direct simulation of the surrounding air. This allows to reach a quantitatively good agreement between the experimental measurements and the numerical results.

As shown experimentally and numerically, the decrease of the critical magnetic fields is obtained only when the bifurcation modes are cooperative. In simple words, one needs the bifurcation modes triggered by the first field (say the mechanical one) to be the same or very similar to the modes induced by the second field (say the magnetic field). Then, one can achieve a noteworthy reduction of the critical magnetic field with increasing pre-compression. In any other case where the instability patterns are not similar, the two fields act independently. However, even though they do not bring further decrease of the fields, they do lead to an otherwise impressive superposition of different modes (such as wrinkles triggered by the magnetic field and localized modes triggered by the mechanical loading). This non-collaboration of the magnetic and mechanical bifurcation modes in finite pre-compressions with no further reduction of the critical fields is also non-trivial. Such a response is related to the frictional boundary effects. The role of friction in this regime (numerically probed) is an interesting result by itself.

The magnetomechanical modeling of the boundary value problem gives access to the complete contours of the magnetic and mechanical fields. The fields are heterogeneous inside both solids and across the film in the post-bifurcation regime and in principle cannot be resolved analytically. This is because the magnetic field is applied far from the specimen, as it happens in the real experiment. To satisfy magnetic field uniformity far from the specimen, we consider a big free space at whose extremities a magnetic field of Eulerian nature is applied. The numerical simulations allow for the detailed study of the local fields and better understanding of the post-bifurcation response. The concept of the magnetic instability, numerically manifested as patterns of alternating signs in-plane magnetization within the wrinkled film, is novel. The post-bifurcation response is shown to be supercritical both mechanically and magnetically, thus allowing to magnetically load/unload the material system in a cyclic and reversible manner, switching on and off the morphological patterns.

The numerical model can be also used for the systematic study and optimization of the MRE material-systems. To that end, we show the influence of the film slenderness on the magnetoelastic critical response of the system. As expected, a sufficiently large slenderness ratio makes the effect of the boundary conditions on the morphological response less pronounced. The numerical solution is led to higher wavenumbers of notably lower wrinkling amplitude with increasing slenderness ratio. The critical wavenumber is found to be a decreasing function of pre-compression, as theoretically predicted. Such a result is numerically revealed only under favorable (large) slenderness ratios. Similarly, past the mechanical bifurcation point, the magnetic field triggers multi-period superimposed patterns. The long-wavelength wrinkles of these patterns cannot emerge under a low slenderness ratio, if they are comparable (or larger) to the characteristic size of the specimen.

The plane-strain numerical simulations can also uncover advanced post-bifurcation patterns.

The coexistence and coevolution of wrinkling and curvature localization deep in post-bifurcation is experimentally observed and numerically probed. New sawtooth (straight segments) shape configurations, displaying curvature localization, progressively emerge from wrinkling and are called "crinkles". To that end, we carry out a curvature localization analysis in the double parameter space of applied pre-compression and magnetic field and we show that it is an intrinsic feature of MREs. The mechanism of formation of crinkling is strongly related to repelling magnetoelastic interactions. When the magnetoelastic coupling is taken into account, the coupling between surface layer curvature and magnetic macroscopic polarization, is found to lead to the emergence of a boundary layer (band width) in which curvature is highly concentrated.

Finally, we investigate the formation and post-stability evolution of crinkling modes on MRE films bonded on MRE substrates. In virtue of the coupling in material properties, geometry and loading, new contrasts between the mechanical and magnetic properties of the layers take the lead in bifurcation. Therefore, we create different interlayer magnetic ratios and we trigger an extremely wide range of surface patterns. The new features observed for a magnetic substrate are a) a shape-driven curvature along the entire length of the film and b) the significantly high concentration of the magnetic field at the corners of the film. Very large extensive deformations are observed at the lateral edges of the substrate. Such magnetostrictive shape effects pull upwards the corners of the film versus the magnetic field at the pre- and post-bifurcation. As a result, the film is not flat before bifurcation and the principal solution is not defined by uniform fields.

A general and quantitative understanding of the various modes of instabilities given the material properties of the layers is of significant importance. Varying the magnetic properties of the substrate leads to an extremely large range of unique crinkled (primary and sequentially secondary) surface patterns that can be tuned by the magnetomechanical loading. Numerical evidence of crinkling evolution paths are shown in the triple parameter-space of pre-compression, magnetic field and magnetic interlayer contrast (for fixed stiffness ratio). The morphological patterns can be significantly varied from short to long wavelength modes that are sensitive to the parameter fields.

The material-system is found to undergo multiple sequential bifurcations from the primary wrinkles to the crinkles. The evolution of the post-buckling behavior is defined by sequential patterns of reducing wavenumber and curvature localization. This process involves the relaxation of the side crinkles under the influence of the increasing shape effects and magnetic fields, until the equilibrated mode upon saturation magnetization is formed. These features are reflected in the evolution of all mechanical and magnetic local fields. To that end, the numerical analysis of the MRE film/MRE substrate reveals antisymmetric magnetization spatial oscillations between alternating values. The antisymmetry itself implies that apart from the level of oscillatory undulations, a larger-scale magnetic pattern is formed between the two opposite half sides of the pattern. Such a feature is another direct consequence of the magnetic substrate.

The evolution of the local fields in the above-mentioned parameter-space outlines the mechanisms of the gradual pattern change, i.e., curvature localization and gradually sharper magnetic interfaces within the deformed film versus the applied magnetic field. The curvature localization is

closely related to the magnetostrictive shape effects that lead to symmetry-breaking instabilities. The oscillatory (+ and -) in-plane magnetization within the post-bifurcated film illustrates the formation of magnetic walls that decay as one approaches the edges. These walls correspond to the joint points between neighboring crinkled segments and are regimes where rapid spatial variations occur. In such regimes, the continuity is possibly not satisfied and charges are accumulated (not divergence-free points). Consequently, these interfaces of highly localized curvature connect regions of uniformly but similarly magnetized domains that repel each other. In the parameter space of interlayer magnetic contrast, one can pass from a crinkled pattern with multiple interfaces to an overall single sharp interface (wall) that possibly reduces the total energy.

To summarize, this study describes surface instabilities of a stiffer magnetoelastic film on a soft substrate driven by the combined action of magnetic fields and mechanical compression. Although wrinkling of bilayers driven by a variety of factors has been well studied in the literature, the use of magnetic field is particular interesting from the perspective of rapid and non-invasive/non-contact switching of surface morphology. Such a material-structure coupling can produce several surface patterns with one material if properly in-situ adjusted. This is experimentally achieved for the first time. In addition to that, we propose the use of one material (e.g., no need for fabrication under different tensile pre-stretches that rises the number of material samples) that can be seen as a touchable (user-accessible) device. Such a response is scalable and thus, the present system could also be built at the micron-scale by means of more advanced fabrication techniques.

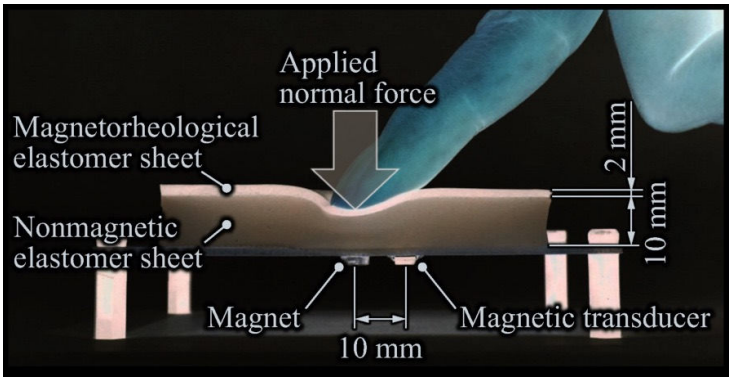

Figure VII.1: Structure of flexible tactile sensor that is able to detect an applied normal force and vertical deformation. To describe the operation principle: in the absence of a contact force, a certain amount of magnetic flux generated by the magnet penetrates the MRE film/substrate and the magnetic transducer. The force applied to the elastomer surface deforms the top MRE film and causes a decrease in the distance between the MRE and the transducer. This distance determines the amount of magnetic flux penetrating the transducer, since the magnetic permeability around the transducer is increased by approaching the MRE. As a consequence, the applied force can be estimated by the amount of magnetic flux penetrating the transducer (Kawasetsu et al., 2018b).

In closing, the present idea of using two (or more) fields to control instabilities in the post-bifurcation regime is more general and can be used in any coupled/active material system if properly designed (e.g., see Bense et al., 2017, Danas, 2017). To that end, this work is able to contribute

to the development of magnetic flexible tactile surfaces/sensors. Even though several types of flexible tactile sensors have been proposed, various technical issues remain, such as a large amount of deformation that fractures the sensing elements and a poor maintainability. Kawasetsu et al. (2018b) recently proposed the use of a MRE film/passive substrate (Fig.VII.1) to design a sensor that can have high sensitivity, extremely low rigidity with respect to the surface deformation and an extremely fast response (in the order of milliseconds). In their case, the sensor was designed to measure the applied forces on the MRE surface by detecting the changes in the magnetic field caused by the displacement of the magnet. We thus believe that the combination of the experiments and numerical simulations presented in this study can pave the way for a realistic instability-triggered polymer-based magnetorheological device for the active control of surface patterns at small magnetic fields.

BIBLIOGRAPHY

Abaqus, D. S. (2009). *ABAQUS/Standard Version 6.9, user manual*. Simulia Corp.

ABAQUS/Explicit (2005). *ABAQUS/Explicit: Advanced topics - Lecture 5: Quasi-static analyses.* Dassault Systems, Simulia Corp, Providence, RI, USA.

Audoly, B. and Boudaoud, A. (2008a). Buckling of a stiff film bound to a compliant substrate–part i:: Formulation, linear stability of cylindrical patterns, secondary bifurcations. *J. Mech. Phys. Solids*, 56(7):2401 – 2421.

Audoly, B. and Boudaoud, A. (2008b). Buckling of a stiff film bound to a compliant substrate–part ii:: A global scenario for the formation of herringbone pattern. *J. Mech. Phys. Solids*, 56(7):2422 – 2443.

Auguste, A., Jin, L., Suo, Z., and Hayward, R. C. (2017). Post-wrinkle bifurcations in elastic bilayers with modest contrast in modulus. *Extr. Mech. Lett.*, 11:30–36.

Barham, M., Steigmann, D. J., McElfresh, M., and Rudd, R. E. (2007). Finite deformation of a pressurized magnetoelastic membrane in a stationary dipole field. *Acta Mechanica*, 191(1):1–19.

Bednarek, S. (1999). The giant magnetostriction in ferromagnetic composites within an elastomer matrix. *Appl Phys A*, 68(1):63–67.

Bellan, C. and Bossis, G. (2002). Field dependence of viscoelastic properties of mr elastomers. *Int. J. Mod. Phys. B*, 16:2447–2453.

Bense, H., Trejo, M., Reyssat, E., Bico, J., and Roman, B. (2017). Buckling of elastomer sheets under non-uniform electro-actuation. *Soft Matter*, 13:2876–2885.

Bertoldi, K., Boyce, M., Deschanel, S., Prange, S., and Mullin, T. (2008). Mechanics of deformation-triggered pattern transformations and superelastic behavior in periodic elastomeric structures. *J. Mech. Phys. Solids*, 56(8):2642–2668.

Bertoldi, K. and Boyce, M. C. (2008). Mechanically triggered transformations of phononic band gaps in periodic elastomeric structures. *Phys. Rev. B*, 77:052105.

Bhattacharya, K. and James, R. (1999). A theory of thin films of martensitic materials withapplications to microactuators. *J. Mech. Phys. Solids*, 47(3):531 – 576.

Bhushan, B. and Jung, Y. C. (2011). Natural and biomimetic artificial surfaces for superhydrophobicity, self-cleaning, low adhesion, and drag reduction. *Progr Mater Sci*, 56(1):1 – 108.

Bica, I. (2009). Influence of the transverse magnetic field intensity upon the electric resistance of the magnetorheological elastomer containing graphite microparticles. *Mat Let*, 63(26):2230–2232.

Biot, M. A. (1965). *Mechanics of Incremental Deformation*. Wiley, New York.

Bodelot, L., Pössinger, T., Danas, K., Triantafyllidis, N., and Bolzmacher, C. (2016). Magnetorheological elastomers: Experimental and modeling aspects. In Ralph, C., Silberstein, M., Thakre, P. R., and Singh, R., editors, *Mechanics of Composite and Multi-functional Materials, Volume 7*, pages 251–256, Cham. Springer International Publishing.

Bodelot, L., Voropaieff, J.-P., and Pössinger, T. (2018). Experimental investigation of the coupled magneto-mechanical response in magnetorheological elastomers. *Exp Mech*, 58(2):207–221.

Borcea, L. and Bruno, O. (2001). On the magneto-elastic properties of elastomer-ferromagnet composites. *J. Mech. Phys. Solids*, 49(12):2877 – 2919.

Bossis, G. and Lemaire, E. (1991). Yield stresses in magnetic suspensions. *J Rheol*, 35:1345–1354.

Bowden, N., Brittain, S., Evans, A. G., Hutchinson, J. W., and Whitesides, G. M. (1998). Spontaneous formation of ordered structures in thin films of metals supported on an elastomeric polymer. *Nature*, 393:146–149.

Brigadnov, I. A. and Dorfmann, A. (2003). Mathematical modeling of magneto-sensitive elastomers. *Int. J. Solids Struc.*, 40(18):4659 – 4674.

Brown, W. F. (1966). *Magnetoelastic interactions*. Springer-Verlag, New York.

Budday, S., Kuhl, E., and Hutchinson, J. W. (2015). Period-doubling and period-tripling in growing bilayered systems. *Philos Mag*, 95(28-30):3208–3224.

Bunoiu, M. and Bica, I. (2016). Magnetorheological elastomer based on silicone rubber, carbonyl iron and rochelle salt: Effects of alternating electric and static magnetic fields intensities. *J Ind Eng Chem*, 37:312–318.

Bustamante, R., Dorfmann, A., and Ogden, R. W. (2007). A nonlinear magnetoelastic tube under extension and inflation in an axial magnetic field: numerical solution. *J Eng Math*, 59(1):139–153.

Cai, S., Breid, D., Crosby, A., Suo, Z., and Hutchinson, J. (2011). Periodic patterns and energy states of buckled films on compliant substrates. *J. Mech. Phys. Solids*, 59(5):1094 – 1114.

Cai, S., Chen, D., Suo, Z., and Hayward, R. C. (2012). Creasing instability of elastomer films. *Soft Matter*, 5:1301–1304.

Cao, C., Chan, H. F., Zang, J., Leong, K. W., and Zhao, X. (2014). Harnessing localized ridges for high-aspect-ratio hierarchical patterns with dynamic tunability and multifunctionality. *Adv Mater*, 26(11):1763–1770.

Cao, Y. and Hutchinson, J. W. (2012a). From wrinkles to creases in elastomers: the instability and imperfection-sensitivity of wrinkling. *P Roy Soc A-Math Phy*, 468(2137):94–115.

Cao, Y. and Hutchinson, J. W. (2012b). Wrinkling phenomena in neo-hookean film/substrate bilayers. *J Appl Mech*, 79(3):031019.

Carlson, J. D. and Jolly, M. R. (2000). Mr fluid, foam and elastomer devices. *Mechatronics*, 10:555–569.

Celli, P., Zhang, W., and Gonella, S. (2018). Pathway towards programmable wave anisotropy in cellular metamaterials. *Phys. Rev. Applied*, 9:014014.

Chan, E. P., Smith, E. J., Hayward, R. C., and Crosby, A. J. (2008). Surface wrinkles for smart adhesion. *Adv Mater*, 20:711–716.

Chen, D., Jin, L., Suo, Z., and Hayward, R. C. (2014). Controlled formation and disappearance of creases. *Mater. Horiz.*, 1:207–213.

Chen, J.-. S. and Lin, J. S. (2005). Exact critical loads for a pinned half- sine arch under end couples. *J Appl Mech*, 72:147–148.

Chen, L., Gong, X. L., and Li, W. H. (2007). Microstructures and viscoelastic properties of anisotropic magnetorheological elastomers. *Smart Mat. Struct.*, 16(6):2645–2650.

Chen, L. and Jerrams, S. (2011). A rheological model of the dynamic behavior of magnetorheological elastomers. *J. Appl. Phys.*, 110(1):13–19.

Chen, Q., Ringleb, S. I., Hulshizer, T., and An, K.-N. (2005). Identification of the testing parameters in high frequency dynamic shear measurement on agarose gels. *J Biomech*, 38(4):959–963.

Chen, X. and Hutchinson, J. W. (2004). Herringbone buckling patterns of compressed thin films on compliant substrate. *J Appl Mech*, 71:597–603.

Coquelle, E., Bossis, G., Szabo, D., and Giulieri, F. (2006). Micromechanical analysis of an elastomer filled with particles organized in chain-like structure. *J. Materials Science*, 41:5941–5953. 10.1007/s10853-006-0329-8.

Corcolle, R., Daniel, L., and Bouillault, F. (2008). Optimal design of magnetostrictive composites: An analytical approach. *IEEE Trans. Magnetics*, 44(1):17 –23.

Cottone, F., Gammaitoni, L., Vocca, H., Ferrari, M., and Ferrari, V. (2012). Piezoelectric buckled beams for random vibration energy harvesting. *Smart Mater Struct*, 21(3):21–35.

Damiani, R. and Sun, L. (2017). Microstructural characterization and effective viscoelastic behavior of magnetorheological elastomers with varying acetone contents. *Int J Dam Mech*, 26(1):104–118.

Danas, K. (2017). Effective response of classical, auxetic and chiral magnetoelastic materials by use of a new variational principle. *J. Mech. Phys. Solids*, 105:25–53.

Danas, K., Kankanala, S., and Triantafyllidis, N. (2012). Experiments and modeling of iron-particle-filled magnetorheological elastomers. *J. Mech. Phys. Solids*, 60(1):120–138.

Danas, K. and Triantafyllidis, N. (2014). Instability of a magnetoelastic layer resting on a non-magnetic substrate. *J. Mech. Phys. Solids*, 69:67 – 83.

Davis, L. C. (1999). Model of magnetorheological elastomers. *J Appl Phys*, 85(6):3348–3351.

dell'Isola, F., Maurini, C., and Porfiri, M. (2004). Passive damping of beam vibrations through distributed electric networks and piezoelectric transducers: prototype design and experimental validation. *Smart Mater Struct*, 13(2):299–305.

Demchuk, S. A. and Kuzmin, V. A. (2002). Viscoelastic properties of magnetorheological elastomers in the regime of dynamic deformation. *J Eng Phys Thermophys*, 75(2):396–400.

Diani, J., Fayolle, B., and Gilormini, P. (2009). A review on the mullins effect. *Eur Pol J*, 45(3):601 – 612.

Diguet, G., Beaugnon, E., and Cavaillé, J. (2010). Shape effect in the magnetostriction of ferromagnetic composite. *J. Magn. Magn. Mater.*, 322(21):3337 – 3341.

Dorfmann, A. and Ogden, R. W. (2003). Magnetoelastic modelling of elastomers. *Eur. J. Mech. A/Solids*, 22(4):497–507.

Dorfmann, A. and Ogden, R. W. (2004). Nonlinear magnetoelastic deformations. *Quart. J. Mech. App. Math.*, 57(4):599–622.

Dorfmann, A. and Ogden, R. W. (2005). Some problems in nonlinear magnetoelasticity. *Zeitschrift für angewandte Mathematik und Physik ZAMP*, 56(4):718–745.

Duenas, T. A. and Carman, G. P. (2000). Large magnetostrictive response of terfenol-d resin composites (invited). *J. Appl. Phys.*, 87(9):4696–4701.

Eem, S., Jung, H., and Koo, J. (2012). Modeling of magneto-rheological elastomers for harmonic shear deformation. *IEEE Trans Magn*, 48(11):3080–3083.

Fan, J. L. and Zhao, F. (2007). Two-dimensional otsu's curve thresholding segmentation method for gray-level images. *Acta Electronica Sinica*.

Fannin, P., Scaife, B., and Charles, S. (1987). A study of the complex susceptibility of ferrofluids and rotational brownian motion. *J Magn Magn Mater*, 65(2):279–281.

Feng, Z., Yiping, L., and Hongjuan, R. (2015). Study of sedimentation stability of magnetorheological fluidz. *Adv Mat*, 4(1):1–5.

Frediani, G., Mazzei, D., De Rossi, D., and Carpi, F. (2014). Wearable wireless tactile display for virtual interactions with soft bodies. *Frontiers Bioeng. Biotech.*, 2:31.

Freund, L. (2000). Substrate curvature due to thin film mismatch strain in the nonlinear deformation range. *J Mech Phys Solids*, 48(6):1159–1174.

Galipeau, E. and Ponte Castañeda, P. (2012). The effect of particle shape and distribution on the macroscopic behavior of magnetoelastic composites. *International Journal of Solids and Structures*, 49(1):1 – 17.

Galipeau, E. and Ponte Castañeda, P. (2013). A finite-strain constitutive model for magnetorheological elastomers: Magnetic torques and fiber rotations. *J Mech Phys Solids*, 61(4):1065–1090.

Gerbal, F., Wang, Y., Lyonnet, F., Bacri, J.-C., Hocquet, T., and Devaud, M. (2015). A refined theory of magnetoelastic buckling matches experiments with ferromagnetic and superparamagnetic rods. *Proc. Nat. Acad. Sci.*, 112(23):7135–7140.

Ginder, J. (1996). Rheology controlled by magnetic fields. *Encyl. Appl. Phys.*, 16:487–503.

Ginder, J., Clark, S., Schlotter, W., and Nichols, M. (2002). Magnetostrictive phenomena in magnetorheological elastomers. *Int. J. Mod. Phys. B*, 16:2412–2418.

Ginder, J., Nichols, M., Elie, L., and Tardiff, J. (1999). Magnetorheological elastomers: properties and applications. *Smart Mater Struct*, 3675:131–138.

Ginder, J. M. (1998). Behavior of magnetorheological fluids. *MRS Bulletin*, 23(8):26–29.

Ginder, J. M., Nichols, M. E., Elie, L. D., and Clark, S. M. (2000). Controllable-stiffness components based on magnetorheological elastomers. *Smart Mater Struct*, 3985:418–423.

Giordano, S., Dusch, Y., Tiercelin, N., Pernod, P., and Preobrazhensky, V. (2012). Combined nanomechanical and nanomagnetic analysis of magnetoelectric memories. *Phys. Rev. B*, 85:155321.

Giordano, S., Goueygou, M., Tiercelin, N., Talbi, A., Pernod, P., and Preobrazhensky, V. (2014). Magneto-electro-elastic effective properties of multilayered artificial multiferroics with arbitrary lamination direction. *Int J Eng Sc*, 78:134–153.

Gong, X. L., Zhang, X. Z., and Zhang, P. Q. (2005). Fabrication and characterization of isotropic magnetorheological elastomers. *Polym Test*, 24(5):669–676.

Gorodkin, S. R., James, R. O., and Kordonski, W. I. (2009). Magnetic properties of carbonyl iron particles in magnetorheological fluids. *Journal of Physics: Conference Series*, 149(1):012051.

Grabovsky, Y. and Truskinovsky, L. (2013). Marginal material stability. *J. Nonlin. Sci.*, 23(5):891–969.

Gripp, J. and Rade, D. (2018). Vibration and noise control using shunted piezoelectric transducers: A review. *Mech Syst Signal Process.*, 112:359–383.

Guan, X., Dong, X., and Ou, J. (2008). Magnetostrictive effect of magnetorheological elastomer. *J. Magn. Magn. Mater.*, 320:158 – 163.

Ha, Q. P., Royel, S., Li, J., and Li, Y. (2016). Hysteresis modeling of smart structure mr devices using describing functions. *IEEE/ASME Trans Mech*, 21(1):44–50.

Hage-Ali, S., Tiercelin, N., Coquet, P., Sauleau, R., Fujita, H., Preobrazhensky, V., and Pernod, P. (2009). A millimeter-wave microstrip antenna array on ultra-flexible micromachined polydimethylsiloxane (pdms) polymer. *IEEE Antennas Wirel Propag Lett*, 8:1306–1309.

Haynes, W. (2013). *CRC Handbook of Chemistry and Physics*. CRC Press.

Horii, T., Kawasetsu, T., Ishihara, H., and Asada, M. (2018). Mexican-hat-like response in a flexible tactile sensor using a magnetorheological elastomer. *Sensors*, 18(2):587.

Hsu, C. S. (1967). The effects of various parameters on the dynamic stability of a shallow arch. *J. Appl. Mech*, 34(2):349–358.

Huang, R. (2005). Kinetic wrinkling of an elastic film on a viscoelastic substrate. *J Mech Phys Solids*, 53(1):63 – 89.

Huang, R. and Im, S. H. (2006). Dynamics of wrinkle growth and coarsening in stressed thin films. *Phys. Rev. E*, 74:026214.

Huang, S., Pessot, G., Cremer, P., Weeber, R., Holm, C., Nowak, J., Odenbach, S., Menzel, A. M., and Auernhammer, G. K. (2016). Buckling of paramagnetic chains in soft gels. *Soft Matter*, 12:228–237.

Huang, Z., Hong, W., and Suo, Z. (2005). Nonlinear analyses of wrinkles in a film bonded to a compliant substrate. *J Mech Phys Solids*, 53(9):2101 – 2118.

Huck, W. T. S., Bowden, N., Onck, P., Pardoen, T., Hutchinson, J. W., and Whitesides, G. M. (2000). Ordering of spontaneously formed buckles on planar surfaces. *Langmuir*, 16:3497–3501.

Hutchinson, J. W. (2013). The role of nonlinear substrate elasticity in the wrinkling of thin films. *Phil. Trans. Royal Soc. A*, 371:0422.

J. Yoon, J. Kim, R. H. (2010). Nucleation, growth, and hysteresis of surface creases on swelled polymer gels. *Soft Matter*, 6:5807.

Jin, L., Auguste, A., Hayward, R. C., and Suo, Z. (2015a). Bifurcation diagrams for the formation of wrinkles or creases in soft bilayers. *J. App. Mech.*, 82(6):061008.

Jin, L. and Suo, Z. (2015). Smoothening creases on surfaces of strain-stiffening materials. *J. Mech. Phys. Solids*, 74:68–79.

Jin, L., Takei, A., and Hutchinson, J. W. (2015b). Mechanics of wrinkle/ridge transitions in thin film/substrate systems. *J Mech Phys Solids*, 81:22 – 40.

Jolly, M. R., Bender, J. W., and Carlson, J. D. (1999). Properties and applications of commercial magnetorheological fluids. *J Intell Mater Syst Struct*, 10(1):5–13.

Jolly, M. R., Carlson, J. D., and Muñoz, B. C. (1996). A model of the behaviour of magnetorheological materials. *Smart Mat. Struct.*, 5(5):607.

Kallio, M., Lindroos, T., Aalto, S., Jarvinen, E., Karna, T., and Meinander, T. (2007). Dynamic compression testing of a tunable spring element consisting of a magnetorheological elastomer. *Smart Mater. Struct.*, 16(2):506.

Kankanala, S. and Triantafyllidis, N. (2008). Magnetoelastic buckling of a rectangular block in plane strain. *J. Mech. Phys. Solids*, 56(4):1147 – 1169.

Kankanala, S. V. (2007). *On Finitely Strained Magnetoelastic Solids*. Doctoral Dissertation, The University of Michigan, Ann Arbor.

Kankanala, S. V. and Triantafyllidis, N. (2004). On finitely strained magnetorheological elastomers. *J. Mech. Phys. Solids*, 52(12):2869 – 2908.

Karadeniz, S., Vahapoglu, V., and Yazici, I. (2011). Uniaxial tensile testing of rubber-like materials. *Exp Tech*, 35(1):17–23.

Kawasetsu, T., Horii, T., Ishihara, H., and Asada, M. (2018a). Flexible tri-axis tactile sensor using spiral inductor and magnetorheological elastomer. *IEEE Sens J*, 18(14):5834–5841.

Kawasetsu, T., Horii, T., Ishihara, H., and Asada, M. (2018b). Mexican-hat-like response in a flexible tactile sensor using a magnetorheological elastomer. *Sensors*, 18(587).

Keip, M.-A. and Rambausek, M. (2015). A multiscale approach to the computational characterization of magnetorheological elastomers. *Int J Numer Methods Eng*, 7:23–32. nme.5178.

Keip, M.-A. and Rambausek, M. (2017). Computational and analytical investigations of shape effects in the experimental characterization of magnetorheological elastomers. *Int. J. Solids Struct.*, 121:1 – 20.

Kim, P., Abkarian, M., and Stone, H. A. (2011). Hierarchical folding of elastic membranes under biaxial compressive stress. *Nat Mater*, 10:952–957.

Kothari, M., Cha, M., and Kim, K. S. (2018). Critical curvature localization in graphene. quantum-flexoelectricity effect. *Proc R Soc Lond A*, 474(2214).

Kusakawa, T. and Otani, T. (1964). Properties of various pure irons : Study on pure iron i. *Tetsu- to- Hagane*, 50(1):42–47.

Lacour, S., Jones, J., Suo, Z., and Wagner, S. (2004). Design and performance of thin metal film interconnects for skin-like electronic circuits. *IEEE Electron Device Lett.*, 25(4):179–181.

Lai, N. D., Liang, W. P., Lin, J. H., Hsu, C. C., and Lin, C. H. (2005). Fabrication of two- and three-dimensional periodic structures by multi-exposure of two-beam interference technique. *Opt. Express*, 13(23):9605–9611.

Lanotte, L., Ausanio, G., Hison, C., Iannotti, V., and Luponio, C. (2003). The potentiality of composite elastic magnets as novel materials for sensors and actuators. *Sens. Actuat. A: Phys.*, 106:56–60. Proceedings of the 4th European Magnetic Sensors and Actuators Conference.

Leblanc, J. L. (2002). RubberâĂŞfiller interactions and rheological properties in filled compounds. *Progress in Polymer Science*, 27(4):627 – 687.

Lee, D., Triantafyllidis, N., Barber, J., and Thouless, M. (2008). Surface instability of an elastic half space with material properties varying with depth. *J Mech Phys Solids*, 56(3):858 – 868.

Lefèvre, V., Danas, K., and Lopez-Pamies, O. (2017). A general result for the magnetoelastic response of isotropic suspensions of iron and ferrofluid particles in rubber, with applications to spherical and cylindrical specimens. *J. Mech. Phys. Solids*, 107:343–364.

Lemaire, E., Meunier, A., Bossis, G., Liu, J., Felt, D., Bashtovoi, P., and Matoussevitch, N. (1995). Influence of the particle size on the rheology of magnetorheological fluids. *J Rheol*, 39(5):1011–1020.

Lestringant, C., Maurini, C., Lazarus, A., and Audoly, B. (2017). Buckling of an elastic ridge: Competition between wrinkles and creases. *Phys. Rev. Lett.*, 118:165501.

Li, R., Kothari, M., Landauer, A. K., Cha, M.-H., Kwon, H., and Kim, K.-S. (2018). A new subcritical nanostructure of graphene crinkle-ruga structure and its novel properties. *MRS Advances*, 3(45-46):2763–2769.

Li, W., Kostidis, K., Zhang, X., and Zhou, Y. (2009). Development of a force sensor working with mr elastomers. In *2009 IEEE/ASME International Conference on Advanced Intelligent Mechatronics*, pages 233–238.

Li, W. H. and Zhang, X. Z. (2010). A study of the magnetorheological effect of bimodal particle based magnetorheological elastomers. *Smart Mater Struct*, 19(3):35–42.

Li, W. H., Zhou, Y., and Tian, T. F. (2010). Viscoelastic properties of mr elastomers under harmonic loading. *Rheologica Acta*, 49(7):733–740.

Lipowsky, R. (2014). Coupling of bending and stretching deformations in vesicle membranes. *Adv Col Inter Sc*, 208:14–24.

Liu, J., Wang, X., Tang, X., Hong, R., Wang, Y., and Feng, W. (2015). Preparation and characterization of carbonyl iron/strontium hexaferrite magnetorheological fluids. *Particuology*, 22:134 – 144.

Liu, L., James, R., and Leo, P. (2006). Magnetostrictive composites in the dilute limit. *J Mech Phys Solids*, 54(5):951 – 974.

Liu, Q., Li, H., and Lam, K. Y. (2018). Transition of magnetic field due to geometry of magneto-active elastomer microactuator with nonlinear deformation. *J Microelectromech Syst*, 27(2):127–135.

Lokander, M. and Stenberg, B. (2003). Improving the magnetorheological effect in isotropic magnetorheological rubber materials. *Polym Test*, 22(6):677 – 680.

Lopez-Pamies, O. (2010). A new i1-based hyperelastic model for rubber elastic materials. *C. R. Mécanique*, 338(1):3 – 11.

Lopez-Pamies, O. (2014). Elastic dielectric composites: Theory and application to particle-filled ideal dielectrics. *J Mech Phys Solids*, 64:61 – 82.

Lopez-Pamies, O., Goudarzi, T., and Danas, K. (2013). The nonlinear elastic response of suspensions of rigid inclusions in rubber: Ii - a simple explicit approximation for finite-concentration suspensions. *J Mech Phys Solids*, 61(1):19 – 37.

Lossouarn, B., Aucejo, M., Deu, J.-F., and Cunefare, K. A. (2018). Design of a passive electrical analogue for piezoelectric damping of a plate. *J. Intell. Mater. Syst. Struct.*, 29(7):1301–1314.

Maugin, G. A. and Eringen, A. C. (1972a). Deformable magnetically saturated media. i. field equations. *J. Math. Phys.*, 13(2):143–155.

Maugin, G. A. and Eringen, A. C. (1972b). Deformable magnetically saturated media. ii. constitutive theory. *J. Math. Phys.*, 13(9):1334–1347.

Maurini, C., Pouget, J., and Vidoli, S. (2007). Distributed piezoelectric actuation of a bistable buckled beam. *Eur J Mech A Solids*.

Maurini, C., Pouget, J., and Vidoli, S. (2009). Bistable buckled beam: Modelling and piezoelectric actuation. In *Smart Materials & Micro/Nanosystems*, volume 54 of *Advances in Science and Technology*, pages 281–286. Trans Tech Publications.

Mitsumata, T., Furukawa, K., Juliac, E., Iwakura, K., and Koyama, K. (2002). Compressive modulus of ferrite containing polymer gels. *Int J Mod Phys B*, 16:2419–2425.

Miya, K., Hara, K., and Someya, K. (1978). Experimental and theoretical study on magnetoelastic buckling of a ferromagnetic cantilevered beam-plate. *J Appl Mech*, 45(2):355–360.

Moon, F. and Hara, K. (1982). Buckling induced stresses in martensitic stainless steels for magnetic fusion reactors. *Nucl. Eng. Des.*, 71(1):27 – 31.

Moon, F. C. and Pao, Y.-H. (1968). Magnetoelastic buckling of a thin plate. *J Appl Mech*, 35(1):53–58.

Moon, J. H., Small, A., Yi, G.-R., Lee, S.-K., Chang, W.-S., Pine, D. J., and Yang, S.-M. (2005). Patterned polymer photonic crystals using soft lithography and holographic lithography. *Synthetic Metals*, 148(1):99 – 102.

Neukirch, S., Frelat, J., Goriely, A., and Maurini, C. (2012). Vibrations of post-buckled rods: The singular inextensible limit. *J Sound Vib*, 331(3):704–720.

Norouzi, M., Alehashem, S. M. S., Vatandoost, H., Ni, Y. Q., and Shahmardan, M. M. (2016). A new approach for modeling of magnetorheological elastomers. *J. Intell. Mater. Syst. Struct.*, 27(8):1121–1135.

Oukhaled, G., Cebers, A., Bacri, J., and Di Meglio, J. (2012). Twisting and buckling: A new undulation mechanism for artificial swimmers. *Eur Phys J E Soft Matter*, 35(11):121.

Pao, Y.-H. (1978). Electromagnetic forces in deformable continua. In *Mechanics today. Ed. by S. Nemat-Nasser, New York, Pergamon Press, Inc.*, volume 4, pages 209–305.

Pao, Y.-H. and Yeh, C.-S. (1973). A linear theory for soft ferromagnetic elastic solids. *Int. J. Eng. Sci.*, 11(4):415 – 436.

Park, H. S., Wang, Q., Zhao, X., and Klein, P. A. (2013). Electromechanical instability on dielectric polymer surface: Modeling and experiment. *Comput Methods Appl Mech Eng*, 260:40–49.

Payne, A. R. The dynamic properties of carbon black-loaded natural rubber vulcanizates. part i. *J Appl Polym Sci*, 6(19):57–63.

Peng, H., Qin, F., Phan, M., Tang, J., Panina, L., Ipatov, M., Zhukova, V., Zhukov, A., and Gonzalez, J. (2009). Co-based magnetic microwire and field-tunable multifunctional macro-composites. *J Non-Cryst Solids*, 355(24):1380–1386. Functional and Nanostructured Materials.

Pipkin, A. C. (1986). *Homogenization and Effective Moduli of Materials and Media - Some Examples of Crinkles*, volume 1. Springer.

Pocivavsek, L., Dellsy, R., Kern, A., Johnson, S., Lin, B., Lee, K. Y. C., and Cerda, E. (2008). Stress and fold localization in thin elastic membranes. *Science*, 320(5878):912–916.

Pössinger, T., Bolzmacher, C., Bodelot, L., and Triantafyllidis, N. (2014). Influence of interfacial adhesion on the mechanical response of magneto-rheological elastomers at high strain. *Microsyst Technol*, 20(4):803–814.

Psarra, E., Bodelot, L., and Danas, K. (2017). Two-field surface pattern control via marginally stable magnetorheological elastomers. *Soft Matter*, 13:6576–6584.

Pye, J. E. and Roth, C. B. (2013). Physical aging of polymer films quenched and measured free-standing via ellipsometry: Controlling stress imparted by thermal expansion mismatch between film and support. *Macromolecules*, 46(23):9455–9463.

Qin, F. and Peng, H.-X. (2013). Ferromagnetic microwires enabled multifunctional composite materials. *Prog Mater Sci*, 58(2):183–259.

Qing, Y., Zhou, W., Luo, F., and Zhu, D. (2010). Epoxy-silicone filled with multi-walled carbon nanotubes and carbonyl iron particles as a microwave absorber. *Carbon*, 48(14):4074 – 4080.

Qiu, J., Lang, J. H., and Slocum, A. H. (2004). A curved-beam bistable mechanism. *J Microelectromech Syst*, 13(2):137–146.

Rabinow, J. (1948). The magnetic fluid clutch. *Elec Eng*, 67(12):1167–1167.

Rambausek, M. and Keip, M.-A. (2018). Magneto-electro-active polymers: material properties and structural effects. *PAMM*, 17(1):545–546.

Ren, H. and Gerhard, E. (1997). Design and fabrication of a current-pulse-excited bistable magnetic microactuator. *Sens Actuators A Phys*, 58(3):259–264.

Schubert, G. (2014). *Manufacture, characterisation and modelling of magneto- rheological elastomers*. PhD thesis, University of Glasgow.

Shan, S., Kang, S. H., Wang, P., Qu, C., Shian, S., Chen, E. R., and Bertoldi, K. (2014). Harnessing multiple folding mechanisms in soft periodic structures for tunable control of elastic waves. *Adv Funct Mater*, 24(31):4935–4942.

Shiga, T., Okada, A., and Kurauchi, T. (1995). Magnetroviscoelastic behavior of composite gels. *J Appl Polym Sci*, 58(4):787–792.

Steigmann, D. J. (2004). Equilibrium theory for magnetic elastomers and magnetoelastic membranes. *Int J Non Linear Mech*, 39(7):1193–1216.

Stoop, N., Lagrange, R., Terwagne, D., Reis, P. M., and Dunkel, J. (2015). Curvature-induced symmetry breaking determines elastic surface patterns. *Nat Mater*, 14(3):337–342.

Streque, J., Talbi, A., Pernod, P., and Preobrazhensky, V. (2010). New magnetic microactuator design based on pdms elastomer and mems technologies for tactile display. *IEEE Trans Haptics*, 3(2):88–97.

Sun, J.-Y., Xia, S., Moon, M.-W., Oh, K. H., and Kim, K.-S. (2012). Folding wrinkles of a thin stiff layer on a soft substrate. *P Roy Soc A-Math Phy*, 468(2140):932–953.

Takagi, T. (1990). A concept of intelligent materials. *J Intell Mater Syst Struct*, 1(2):149–156.

Taylor, R. L. (2011). *FEAP - Finite Element Analysis Program*.

Tian, T. F., Li, W. H., Alici, G., Du, H., and Deng, Y. M. (2011). Microstructure and magnetorheology of graphite-based mr elastomers. *Rheologica Acta*, 50(9):825–836.

Tian, T. F., Zhang, X. Z., Li, W. H., Alici, G., and Ding, J. (2013). Study of pdms based magnetorheological elastomers. *Journal of Physics: Conference Series*, 412(1):012038.

Tiercelin, N., Dusch, Y., Klimov, A., Giordano, S., Preobrazhensky, V., and Pernod, P. (2011a). Room temperature magnetoelectric memory cell using stress-mediated magnetoelastic switching in nanostructured multilayers. *Appl. Phys. Lett.*, 99(19):192–199.

Tiercelin, N., Dusch, Y., Preobrazhensky, V., and Pernod, P. (2011b). Magnetoelectric memory using orthogonal magnetization states and magnetoelastic switching. *J. Appl. Phys.*, 109(7):26–34.

Tiersten, H. F. (1965). Variational principle for saturated magnetoelastic insulators. *J. Math. Phys.*, 6:779–787.

Tipton, C. R., Han, E., and Mullin, T. (2012). Magneto-elastic buckling of a soft cellular solid. *Soft Matter*, 8:6880–6883.

Truesdell, C. and Toupin, R. (1960). The classical field theories. In *Handbuch der Physik. Ed. by S. Flügge*, volume III/I. Springer-Verlag, Berlin.

Trujillo, V., Kim, J., and Hayward, R. C. (2008). Creasing instability of surface-attached hydrogels. *Soft Matter*, 4:564–569.

Vangbo, M. (1998). An analytical analysis of a compressed bistable buckled beam. *Sens Actuators A Phys*, 69(3):212–216.

Vidal-Verdu, F. and Hafez, M. (2007). Graphical tactile displays for visually-impaired people. *IEEE Trans Neural Syst Rehabil Eng*, 15(1):119–130.

Vidoli, S. and Maurini, C. (2008). Tristability of thin orthotropic shells with uniform initial curvature. *P Roy Soc A-Math Phy*, 464(2099):2949–2966.

Vukusic, P. and Sambles, J. R. (2003). Photonic structures in biology. *Nature*, 424:852–855.

Wallerstein, D. V. and Peach, M. O. (1972). Magnetoelastic buckling of beams and thin plates of magnetically soft material. *J Appl Mech*, 39(2):451–455.

Wang, N. and Stamenovic, D. (2000). Contribution of intermediate filaments to cell stiffness, stiffening, and growth. *Am J Physiol Cell Physiol*, 279(1):188–194. PMID: 10898730.

Wang, Q., Robinson, D., and Zhao, X. (2014). On-demand hierarchical patterning with electric fields. *Appl. Phys. Lett.*, 104(23):231–238.

Wang, Q., Zhang, L., and Zhao, X. (2011). Creasing to cratering instability in polymers under ultrahigh electric fields. *Phys. Rev. Lett.*, 106:118301.

Wang, Q. and Zhao, X. (2013a). Creasing-wrinkling transition in elastomer films under electric fields. *Phys. Rev. E*, 88:042403.

Wang, Q. and Zhao, X. (2013b). Phase diagrams of instabilities in compressed film-substrate systems. *J. App. Mech.*, 81(5):051004.

Wang, S., Decker, M., Henann, D. L., and Chester, S. A. (2016). Modeling of dielectric viscoelastomers with application to electromechanical instabilities. *J Mech Phys Solids*, 95:213 – 229.

Wang, X., Xia, Z., Yuan, B., Zhou, H., Li, Z., and Chen, N. (2013). Effect of curing temperature on the properties of conductive silicone rubber filled with carbonyl permalloy powder. *Mater Des*, 51:287 – 292.

Wang, Y., Hu, Y., Chen, L., Gong, X., Jiang, W., Zhang, P., and Chen, Z. (2006). Effects of rubber/magnetic particle interactions on the performance of magnetorheological elastomers. *Polym Test*, 25(2):262–267.

Wilhelm, C., Cebers, A., Bacri, J., and Gazeau, F. (2003). Deformation of intracellular endosomes under a magnetic field. *Eur Biophys J Biophys Lett*, 32((7)):655–660.

Yankin, S., Talbi, A., Du, Y., Gerbedoen, J.-C., Preobrazhensky, V., Pernod, P., and Bou Matar, O. (2014). Finite element analysis and experimental study of surface acoustic wave propagation through two-dimensional pillar-based surface phononic crystal. *J. Appl. Phys.*, 115(24):244–258.

Yin, H., Sun, L., and Chen, J. (2006). Magneto-elastic modeling of composites containing chain-structured magnetostrictive particles. *J. Mech. Phys. Solids*, 54(5):975 – 1003.

Zang, J., Zhao, X., Cao, Y., and Hutchinson, J. W. (2012). Localized ridge wrinkling of stiff films on compliant substrates. *J. Mech. Phys. Solids*, 60(7):1265 – 1279.

Zhang, X., Peng, S., Wen, W., and Li, W. (2008a). Analysis and fabrication of patterned magnetorheological elastomers. *Smart Mater Struct*, 17(4):45–49.

Zhang, Y., Matsumoto, E. A., Peter, A., Lin, P.-C., Kamien, R. D., and Yang, S. (2008b). One-step nanoscale assembly of complex structures via harnessing of an elastic instability. *Nano Letters*, 8(4):1192–1196. PMID: 18333622.

Zhao, X. and Suo, Z. (2009). Electromechanical instability in semicrystalline polymers. *Appl. Phys. Lett.*, 95(3):14–23.

Zhao, Y., Han, X., Li, G., Lu, C., Cao, Y., Feng, X.-Q., and Gao, H. (2015). Effect of lateral dimension on the surface wrinkling of a thin film on compliant substrate induced by differential growth/swelling. *J. Mech. Phys. Solids*, 83:129–145.

Zhu, J.-T., Xu, Z.-D., and Guo, Y.-Q. (2012). Magnetoviscoelasticity parametric model of an mr elastomer vibration mitigation device. *Smart Mater. Struct.*, 21(7):34–39.

Titre : Une étude théorique, éxperimentale et numérique sur des structures magnéto-élastiques

Mots clés : bifurcation, film/substrat, élastomères magnétorhéologiques, magnéto-élasticité

Résumé : Cette étude traite de la stabilité et la post-bifurcation des élastomères magnétorhéologiques isotropes (MRE). Les MRE sont des élastomères comprenant une fraction volumique finie de particules de fer magnétisables, réparties de façon aléatoire dans le volume. Plus précisément, un système de film/substrat magnéto-élastique non linéaire est étudié expérimentalement, numériquement et théoriquement pour obtenir un contrôle actif de la rugosité de la surface du film. L'interaction non-intuitive entre le champ magnétique et la déformation élastique est due au choix des matériaux et de la géométrie du système, à savoir un film composite de particules ferromagnétiques lié à un substrat passif souple. La coopération de deux mécanismes qui sont par ailleurs indépendants, la pré-compression mécanique et le champ magnétique, permet de rapprocher la structure d'un état marginalement stable et puis de la rendre instable par des champs magnétiques ou mécaniques. Nous démontrons pour la première fois que le champ magnétique critique est une fonction décroissante de la pré-compression et vice versa. Les résultats expérimentaux sont ensuite sondés avec succès par des simulations à champs complets par éléments finis en grandes déformations et champs magnétiques. Une analyse théorique de bifurcation magnéto-mécanique sur un système magnéto-élastique infini est également utilisée pour explorer l'effet des propriétés combinées sur la réponse critique.
Dans la perspective d'élargir l'activation de surface à de nouveaux motifs magnéto-mécaniques, nous étudions plus en détail la post-stabilité d'un système film/substrat entièrement magnéto- rhéologique. L'idée sous-jacente est de créer différents contrastes de propriétés magnétiques/mécaniques entre les couches afin de déclencher une gamme de motifs de surface plus riche que celle déjà obtenue en utilisant un film MRE sur un substrat passif. Les calculs post-bifurcation des films MRE liés à des substrats MRE permettent de mettre en évidence de nouveaux motifs qui conduisent à une localisation de courbure très importante et à du "crinkling" (gondolement). Dans tous les cas étudiés, le couplage magnéto-élastique permet le contrôle réversible de l'apparition(/disparition) de motifs de surface sous des champs magnétiques et mécaniques critiques ajustables. Par conséquent, cette étude constitue un premier pas vers des dispositifs haptiques et morphiques actifs.

Title : A study on magnetosensitive solids : Experiments, Theory and Numerics

Keywords : bifurcation, film/substrate, magnetorheological elastomers, magnetoelasticity

Abstract : The present work deals with the stability and post-bifurcation response of isotropic magnetorheological elastomers (MREs). MREs are elastomers comprising a finite volume fraction of magnetizable iron particles distributed randomly in the volume. A nonlinear magnetoelastic film/substrate system is experimentally, numerically and theoretically exploited to obtain active control of surface roughness. The non-intuitive interplay between magnetic field and elastic deformation owes to material and geometry selection, namely, a ferromagnetic particle composite film bonded on a compliant passive foundation. Cooperation of two otherwise independent loading mechanisms–mechanical pre-compression and magnetic field–allows to bring the structure near a marginally stable state and then destabilize it with either magnetic or mechanical fields. We demonstrate for the first time that the critical magnetic field is a decreasing function of pre-compression and vice versa. The experimental results are probed successfully with full-field finite element simulations at large strains and magnetic fields. A theoretical magnetomechanical bifurcation analysis on an infinite magnetoelastic system is employed to explore the effect of the interlayer combined properties on the critical response and is compared with the available numerical results.
With the perspective of applying the principle of surface actuation to new magnetomechanically triggered patterns, we further investigate the post-bifurcation of an entirely magnetorheological bilayer block. The underlying idea is to create different interlayer contrasts of magnetic and mechanical properties allowing us to trigger a larger range of surface patterns than that already obtained when using a MRE film on a passive (magnetically insensitive) foundation. Post-bifurcation calculations of MRE films bonded on MRE substrates allow to reveal novel patterns that lead to significant curvature localisation and crinkling. In all cases studied, the magnetoelastic coupling allows for the reversible on/off control of surface patterning under adjustable critical magnetic and mechanical fields for a single specimen and thus, this study constitutes a first step towards realistic active haptic and morphing devices.

Université Paris-Saclay
Espace Technologique / Immeuble Discovery
Route de l'Orme aux Merisiers RD 128 / 91190 Saint-Aubin, France